Vrije Universiteit Brussel

Faculteit Toegepaste Wetenschappen
Vakgroep Werktuigkunde

A dynamic walking biped actuated by pleated pneumatic artificial muscles: Basic concepts and control issues

Björn Verrelst

Proefschrift voorgelegd tot het behalen van de academische graad
van Doctor in de Toegepaste Wetenschappen

February 2005

Promotor: Prof. dr. ir. Dirk Lefeber

Vrije Universiteit Brussel

Faculteit Toegepaste Wetenschappen
Vakgroep Werktuigkunde

A dynamic walking biped actuated by pleated pneumatic artificial muscles: Basic concepts and control issues

Björn Verrelst

February 2005

Jury:
Prof. dr. ir. D. Lefeber (VUB-WERK), promotor
Prof. dr. ir. A. Cardon (VUB-MEMC), chairman
Prof. dr. ir. J. Vereecken (VUB-META), vice-chairman
dr. ir J. Vermeulen (VUB-WERK), secretary of the chairman
Prof. dr. ir. F. Daerden (VUB-WERK)
Prof. dr. ir. P. Kool (VUB-WERK)
Prof. dr. ir. B. Van Gheluwe (VUB-BIOM)
Prof. dr. ir. Y. Baudoin (Koninklijke Militaire School)
Prof. dr. ir. K. Berns (University of Kaiserslautern)

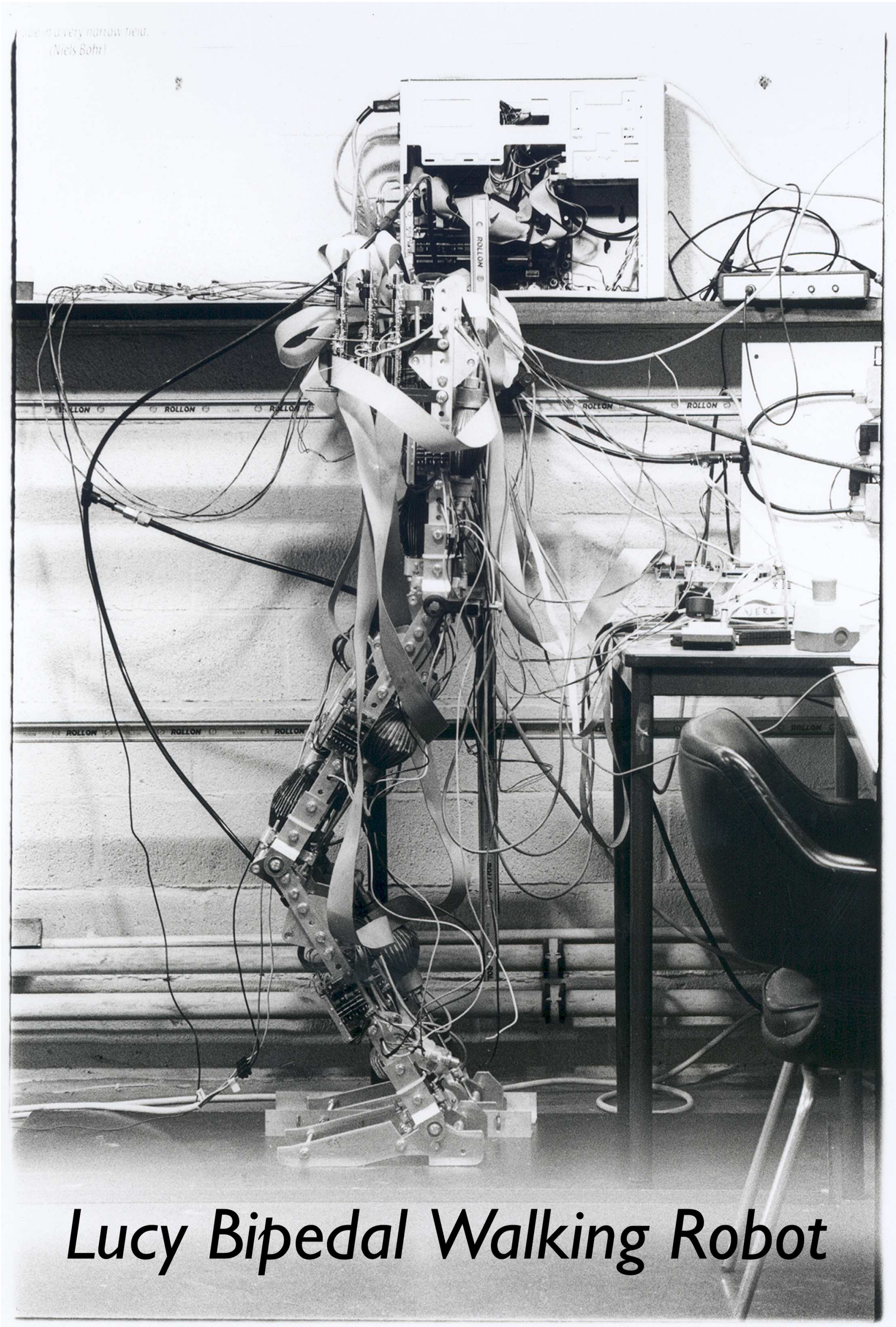

Lucy Bipedal Walking Robot

Contact information:

Vrije Universiteit Brussel
Faculty of Applied Sciences
Department of Mechanical Engineering
Pleinlaan 2
1050 Brussels
Belgium
http://werk.vub.ac.be/multibody_mechanics.htm
http://lucy.vub.ac.be/
bjorn.verrelst@vub.ac.be
dirk.lefeber@vub.ac.be

to Sooi

"The function of muscle is to pull and not to push, except in the case of the genitals and the tongue"

Leonardo Da Vinci

Acknowledgements

The field of robotics, and especially legged robotics, is an extremely multidisciplinary research domain, which demands for the most varying competences. It is thus immensely important to work within a team of enthusiastic people. I was lucky to be in this situation, without it we would never have reached the current state of "Lucy". So, I would like to take this opportunity to thank not only those who assisted in a technical sense but also everyone who has supported.

Special thanks goes to the promotor Dirk Lefeber who has given the opportunity to start this PhD work and who has left the freedom to find my own directions. This work would not have been possible if Frank Daerden did not develop the pleated pneumatic artificial muscle, his ideas about the actuator allowed me to gain some important insights.

I am particulary grateful to have been working with Ronald Van Ham, Bram Vanderborght and Jimmy Vermeulen. Ronald and I started designing and constructing the robot and his practical knowhow was vital for the realization of "Lucy". It is in fact from the moment Bram joined our team that the project gained momentum due to his passion and inexhaustible stamina.
Jimmy is a very close friend who I've met at the beginning of my engineering studies. There have not been many exams for which we didn't study together face to face, hereby having numerous nightly discussions. I was lucky that he also ventured to make a PhD, concerning the theoretical framework of bipedal locomotion and dynamic stability, such that we could continue our fruitful discussions but now mostly during daytime.

Special thanks also to Joris Naudet for his extensive collaboration concerning the simulation model and Michael Van Damme to share his knowledge on C^{++} programming.

A lot of hours were spent on machining and numerous printed circuit boards have been soldered, much of these have been made by Ronald, Bram and myself, but also a lot of people helped with the time consuming construction process. Thanks goes to Jean-Paul Schepens, André Plasschaert, Jean-Pierre Weemaels, Frans Boulpaep and Gabriël Van den Nest.

Hereby I also thank all the other colleagues of the vakgroep WERK and the graduate students who spent hours in the laboratory for there master's thesis.

And I am grateful to have had Willy Cauwerts as mentor in the field of electronics. Although we're not using it anymore, thanks for helping me out with the ISAbus interface card, I really learned a lot spending days and nights in your "Radio Shack".

And of course, I am happy to have had Katrien who not only supported me day and night, but also had the huge task in trying to teach me some basic English writing skills. And not to forget are the continuous influences of all friends and people who I am happy to have with me: Dirk, Dorien, Kas, Stefan, Bert, Nida, Cathy, Joeri, Ilya, Hanne, Amber, Peppie, Tom, Erwin, Frida, Magda, Edwin, Rein, Bomma,..........and surely not to forget my mother.

Brussels
February 2005

Björn Verrelst

Abstract

This thesis reports on the developments of the robot "Lucy", which is a planar walking biped actuated by pleated pneumatic artificial muscles. This type of artificial muscle is designed to overcome some shortcomings associated with existing types. The main purpose of the biped project is to evaluate the implementation of these muscles and to develop some specific control strategies related to legged locomotion with compliant joints. It is believed that pneumatic artificial muscles have some interesting characteristics which are beneficial towards actuation of legged locomotion. They have a high power to weight ratio and can be coupled directly without complex gearing mechanism. Due to the compressibility of air, a joint actuated with these pneumatic actuators shows a compliant behaviour, which can be positively employed to reduce chock effects. Moreover, joint compliance can be adapted while controlling position, when two muscle are positioned antagonistically. This compliance adaptation enhances the possibilities of exploitation of natural dynamics. The main control idea intended for "Lucy" is to combine exploitation of natural dynamics with joint trajectory control. A trajectory generator calculates joint trajectories which ensure dynamically stable walking, and the different joint controllers track the imposed trajectories while adapting the joint compliance, as such that the natural regimes correspond as much as possible to the reference trajectories. This can significantly reduce control effort and energy consumption, while continuously ensuring global dynamical stability.

Currently the biped "Lucy" is assembled and most of its hardware components have been tested. This thesis reports on the design and construction of the biped and on the first developments of the control architecture for "Lucy". So far the control design is focused on trajectory control and dynamic stability. A nonlinear tracking controller for a single and double support phase has been proposed in combination with a joint trajectory generator developed in the framework of a separate doctoral dissertation. A hybrid simulation model, combining the robot link dynamics with the muscle/valve thermodynamics, has been developed to evaluate the proposed control strategy, and to provide an elaborate tool for future research on exploitation of natural dynamics. The basic concepts of exploiting natural dynamics with the proposed pneumatic tracking system, is explained for a simplified model of a robot leg. Additionally, a description is given of a second generation muscle prototype of the pleated pneumatic artificial muscle, which is designed to increase its lifespan.

Contents

Acknowledgements **i**

Abstract **iii**

List of Figures **ix**

List of Tables **xv**

Nomenclature **xvii**

1 Introduction **1**

1.1 Legged locomotion: general discussion 1

1.2 Legged locomotion and pneumatics 3

1.3 Legged locomotion and natural dynamics 7

1.4 Scope of the thesis 9

1.5 Outline 10

2 Pleated pneumatic artificial muscle **13**

2.1 Introduction 13

2.2 PPAM: adapted design 15

2.2.1 Second generation PPAM 16

2.2.2 Mathematical model 21

2.2.3 Characteristic of the PPAM 25

2.3 Static load tests 29

2.4 Summary 34

3 Basic study of a one-dimensional joint setup 37
3.1 Introduction 37
3.2 Kinematics of a revolute joint 39
3.3 Adaptable passive behaviour of a revolute joint 41
3.4 Exploiting natural system dynamics 43
3.5 Trajectory control with adaptable compliance 44
3.5.1 Description of the leg setup 44
3.5.2 Simulation model 45
3.5.3 Joint trajectory tracking controller 47
3.5.4 Simulation results and discussion 49
3.6 Mathematical formulation for compliance adaptation 56
3.7 Energy considerations 58
3.8 Conclusions 61

4 Control architecture for "Lucy" 63
4.1 Introduction 63
4.2 Dynamic balance: zero moment concept 65
4.3 Trajectory generator 68
4.3.1 Phase durations 70
4.3.2 Double support phase 71
4.3.3 Single support phase 74
4.4 Tracking controller 79
4.4.1 Inverse dynamics control during single support 80
4.4.2 Inverse dynamics control during double support 82
4.4.3 Delta-p unit 87
4.4.4 Local PI and bang-bang pressure controller 88
4.5 Conclusion 90

5 Virtual "Lucy": evaluation of the proposed control architecture 93
5.1 Introduction 93
5.2 Mechanics 94
5.2.1 Single support phase 95
5.2.2 Double support phase 96
5.2.3 Impact phase 97
5.3 Thermodynamics 98
5.4 Complete simulation model 99

5.5 Results and discussion 101
5.6 Conclusions 115

6 "Lucy" : design and construction 117

6.1 Introduction 117
6.2 Modular unit 120
6.2.1 Mechanical design 120
6.2.2 Electronic design 124
6.3 Complete biped 131
6.3.1 Mechanical design 131
6.3.2 Electronic design 140
6.4 Preliminary tracking experiments 144
6.5 Conclusion 147

7 General conclusions 149

Appendices 155

A Dynamic model of the basic leg configuration 155

B Thermodynamic model 159

C Kinematics and Dynamics of the biped "Lucy" during a single support phase 163

C.1 Kinematics 163
C.2 Dynamics 165

D Details of the electronics 171

D.1 Joint micro-controller board 171
D.2 Speed-up circuitry 174
D.3 Pressure sensor 176
D.4 Cypress communication interface 178
D.5 Safety board 180

Bibliography 183

List of Figures

1.1 Japanese state-of-the-art robots 3
1.2 The humanoid robot Johnnie 4

2.1 Working principle of a pneumatic artificial muscle [Daerden, 1999] . 14
2.2 Drawing of the McKibben type muscle [Daerden, 1999] 15
2.3 CAD drawing of the deflated and inflated state of the PPAM 15
2.4 Membrane folding 16
2.5 New aluminium end fittings 17
2.6 Photograph of inflated state of the old design 17
2.7 Photograph of a membrane section 18
2.8 Composition of the new muscle prototype 18
2.9 Drawing of the two muscle end connectors 19
2.10 Photograph of inflated state of the second generation PPAM 20
2.11 Meridional and parallel view of the PPAM 21
2.12 3D-view of an infinitesimal section of the membrane 22
2.13 Theoretical forces at pressure levels 1, 2 and 3 bar as a function of contraction 27
2.14 Theoretical enclosed muscle volume as a function of contraction . . . 28
2.15 Theoretical maximum muscle diameter as a function of contraction . 28
2.16 Theoretical function $\zeta(\epsilon)$, which relates F_t to σ, as a function of contraction 29
2.17 Measured forces as a function of contraction for three muscles at pressure levels 1, 2 and 3 bar 30

2.18 Detailed view of measured forces as a function of contraction for three muscles at pressure level 1 bar . . . 31
2.19 Pressure scaled measured forces as a function of contraction compared with theoretical model . . . 31
2.20 Pressure scaled measured forces as a function of contraction compared with polynomial fitted estimation . . . 33
2.21 Scaled measured forces as a function of contraction compared with polynomial fitted estimation and the relative error given for one muscle 33

3.1 Controlling position and stiffness in an antagonistic muscle setup . . 37
3.2 Schematic overview of the antagonistic muscle pull rod system . . . 39
3.3 Schematic overview of the studied model . . . 44
3.4 The applied joint trajectory tracking control scheme . . . 47
3.5 Bang-bang pressure control scheme. . . . 49
3.6 Desired and actual knee angle and angular velocity for $p_s = 16\,\mathrm{Nm}$ and $p_s = 32\,\mathrm{Nm}$. . . . 51
3.7 Required and actual pressure in the extensor muscle for $p_s = 16\,\mathrm{Nm}$ and $p_s = 32\,\mathrm{Nm}$. . . . 52
3.8 Required and actual pressure in the flexor muscle for $p_s = 16\,\mathrm{Nm}$ and $p_s = 32\,\mathrm{Nm}$. . . . 53
3.9 Required and appied knee torque for $p_s = 16\,\mathrm{Nm}$ and $p_s = 32\,\mathrm{Nm}$. . 54
3.10 Actual and desired knee angle with closed muscles for $p_s = 16\,\mathrm{Nm}$ and $p_s = 32\,\mathrm{Nm}$. . . . 55
3.11 Comparison of pressure evolutions for the extensor muscle with supply pressure set at 3 bar and 7 bar. . . . 60

4.1 Global robot control scheme . . . 63
4.2 Forces acting on the foot . . . 66
4.3 Calculation of the ZMP . . . 67
4.4 ZMP during a double support phase . . . 69
4.5 Timing schedule and definitions . . . 70
4.6 Lucy during a double support phase . . . 72
4.7 Free body diagram of the upper body [Vermeulen, 2004] . . . 73
4.8 Lucy during single support phase . . . 74
4.9 Desired upper body angle course [Vermeulen, 2004] . . . 76
4.10 Overview of the joint control architecture . . . 80
4.11 Model of the biped in single support . . . 81

4.12 Definition of net torques and joint torques 82
4.13 Multilevel bang-bang pressure control scheme 89

5.1 Structure of the complete simulation model 100
5.2 Stick diagram of the simulated motion focussing on the left leg . . . 102
5.3 $\alpha_1(°)$ and $\dot{\alpha}_1(°/s)$ left leg 103
5.4 $\alpha_2(°)$ and $\dot{\alpha}_2(°/s)$ left leg 104
5.5 $\alpha_3(°)$ and $\dot{\alpha}_3(°/s)$ left leg 104
5.6 Applied ankle torque left leg 105
5.7 Applied knee torque left leg 105
5.8 Applied hip torque left leg 106
5.9 Ankle front and rear muscle pressures with valve action 107
5.10 Knee front and rear muscle pressures with valve action 108
5.11 Hip front and rear muscle pressures with valve action 109
5.12 Detail of knee front and rear muscle pressures 110
5.13 Horizontal position swing foot 112
5.14 Vertical position swing foot 112
5.15 Horizontal velocity hip 113
5.16 ZMP position 113
5.17 Vertical component of the ground reaction forces in the right and left foot 114
5.18 Comparison of ZMP position during single support between perfect and pneumatic trajectory tracking 114

6.1 One-dimensional joint setup [Daerden, 1999] 118
6.2 One-dimensional leg setup 119
6.3 CAD drawing of the modular unit's basic frame 121
6.4 CAD drawing of the modular unit's basic frame with muscles and connection plates 122
6.5 Picture of the pneumatic solenoid valve 821 2/2 NC made by Matrix 123
6.6 CAD drawing of the valve island 124
6.7 CAD drawing of the complete modular unit 125
6.8 Photograph of a modular unit 126
6.9 Overview of the low-level control hardware 126
6.10 Pressure sensor to be positioned inside the muscle 127
6.11 Essential scheme of the pressure sensor electronics 128

6.12 Essential scheme of valve speed-up circuitry 128
6.13 Valve speed-up circuitry 129
6.14 Essential scheme of micro-controller board 130
6.15 Micro-controller board 131
6.16 Schematic overview of the complete pneumatic circuit 133
6.17 CAD drawing of the robot "Lucy" 134
6.18 Photograph of the robot "Lucy" 135
6.19 Photograph of the leg of "Lucy" attached to the guiding vertical XY-frame 136
6.20 CAD drawing with side view of a modular unit, showing the kinematical joint design parameters 136
6.21 Definition of the oriented relative joint angles (counterclockwise positive) 138
6.22 Generated flexor and extensor torque in the ankle joint for 1, 2 and 3 bar 138
6.23 Generated flexor and extensor torque in the knee joint for 1, 2 and 3 bar 139
6.24 Generated flexor and extensor torque in the hip joint for 1, 2 and 3 bar 139
6.25 Schematic overview of the robot electronics 140
6.26 Communication interface overview scheme 141
6.27 EZ-USB FX2 communication interface 142
6.28 Desired and measured angles β_i ($^\circ$) for the ankle, knee and hip joint 145
6.29 Required and measured pressure (bar) in the front muscle for the knee joint 146
6.30 Required and measured pressure (bar) in the rear muscle for the knee joint 146
6.31 Detail of required and measured pressure (bar) in the front muscle for the knee joint 147

A.1 schematic overview of the studied model 155

B.1 Muscle and valves on time step t and $t + dt$ 159

C.1 Model of the biped during a single support phase 163
C.2 Definition of net torques and joint torques 166

D.1 Electronic scheme of joint microcontroller board 173

D.2 Electronic scheme of the speed-up circuitry 175
D.3 Electronic scheme of the pressure sensor 177
D.4 Electronic scheme of the cypress communication interface 179
D.5 Electronic scheme of the safety board 181

List of Tables

2.1 Coefficients of the polynomial force function approximation 34
2.2 Coefficients of the polynomial volume function fitting 34

3.1 Inertial parameters of the leg model 45
3.2 Air mass flows entering the system for one cycle 58
3.3 Exergy associated with air mass flows entering and leaving the system for one cycle with $p_{supply} = 7\,\text{bar}$ 59
3.4 Air mass flows with associated exergy level, entering the system for one cycle with $p_{supply} = 3\,\text{bar}$ 59

4.1 Currently applied reaction levels of the multilevel bang-bang pressure controlscheme 90

5.1 Inertial parameters of the robot 94
5.2 Objective locomotion parameters 101

Nomenclature

Acronyms

COG	Center Of Gravity
COP	Center Of Pressure
CPU	Central Processor Unit
DAE	Differential Algebraic Equations
DOF	Degrees Of Freedom
IRQ	Interrupt Request
FRI	Foot Rotation Indicator
GUI	Graphical User Interface
ODE	Ordinary Differential Equations
PD	Proportional Derivative
PID	Proportional Integral Derivative
PAM	Pneumatic Artificial Muscle
$PPAM$	Pleated Pneumatic Artificial Muscle
RAM	Random Accessible Memory
SDI	Serial Debugger Interface
SPI	Serial Peripheral Interface
TPU	Timer Processor Unit
USB	Universal Serial Bus controller
ZMP	Zero Moment Point

Abbreviations

lhs	left hand side
rhs	right hand side
td	touch-down

Greek

α	coefficient denoting COG of lower leg	
α_i	angular design parameters of the joint muscle setup	rad
	absolute angular position of link i of the left leg	$^\circ$
β	oriented angle between $\bar{1}_r$ and $d\bar{F}_p$	rad
	coefficient denoting COG of upper leg	
β_i	relative joint angle	rad($^\circ$)
γ	coefficient denoting COG of upper body	
ϵ	muscle contraction	
ϵ_i^c	contraction of muscle i at a chosen central position θ^c	
ρ_0	air density at standard conditions	kg/m^3
$\epsilon_i(\theta)$	contraction of muscle i in a joint setup	
σ	tensile stress	Pa
φ	elliptical integral amplitude	rad
$\zeta(\epsilon)$	stress related function	N
θ	angular joint position	rad($^\circ$)
θ^c	chosen central position in a joint setup	rad
θ_i	absolute angle related to link i	rad($^\circ$)
$\Delta\tilde{p}$	control variable of delta-p control unit	bar
τ	actuator torque	Nm
$\bar{\boldsymbol{\tau}}$	torque vector	Nm
ν	mean horizontal hip velocity	m/s
λ	step length	m
λ_i	Lagrange multipliers	
δ	step height	m
κ	foot lift/clearance	m
Δ	variation	
μ	angular momentum	kgm^2/s
$\boldsymbol{\Lambda}$	vector of Lagrange multipliers	
$\boldsymbol{\omega}$	generalized velocity vector	
η_i	mass of link i relative to total robot mass	

Roman

a	reaction level of bang-bang pressure controller	bar
b	pneumatic valve critical pressure ratio	
	reaction level of bang-bang pressure controller	bar
b_i	distance between origin O and points B_i	m
B_i	fixed base points of a joint muscle setup	
c	reaction level of bang-bang pressure controller	bar
c_i	constant transformations	
c_p	constant pressure specific heat	J/kg/K

c_v	constant volume specific heat	J/kg/K
C	pneumatic valve flow constant	Std.l/min/bar
$C(\mathbf{q}, \dot{\mathbf{q}})$	centrifugal/coriolis matrix	
d_i	distance between R and points D_i	m
$d\left(\epsilon, \frac{l_0}{R}\right)$	dimensionless muscle diameter function	
D	muscle diameter	m
D_i	moving points of a joint muscle setup	
$D(\mathbf{q})$	inertia matrix	
dA	elementary surface associated with w and dL	m^2
dL	infinitesimal muscle fibre length	m
e	reaction level of bang-bang pressure controller	bar
f	reaction level of bang-bang pressure controller	bar
$f_i(\theta)$	dimensionless force function of muscle i in a joint setup	
$f\left(\epsilon, \frac{l_0}{R}\right)$	dimensionless muscle force function	
f_i	coefficients of a polynomial force fitting	
F	foot point	
$\bar{F}_p$	force transferred by muscle membrane	N
$\bar{F}_t$	muscle traction force	N
g	acceleration of gravity	$\mathrm{m/s}^2$
G_i	COG of robot link i	
$G(\mathbf{q})$	gravitational torque/force vector	
I_i	moment of inertia of robot link i	kgm^2
$J(q)$	Jacobian matrix	
$k_i(\theta)$	joint stiffness function for a joint setup	Nm/bar
K	joint stiffness	Nm
	kinetic energy	J
	feedback gain	
l_0	initial muscle/fibre length	m
l_b	base suspension bar length a muscle joint setup	m
l_i	length of robot link i	m
l_{m_i}	actual length of muscle i in a joint setup	m
m	elliptical integral parameter	
$\dot{m}_{air_i}$	air mass flow through valves of muscle i	kg/s
m_i	mass of robot link i	kg
M	total mass	kg
n	number of used fibres	
	polytropic exponent	
p	gauge pressure	bar
p_m	stiffness variable of delta-p control unit	bar
p_s	stiffness variable of delta-p control unit	Nm
P	absolute pressure	bar
p_{i_0}	initial gauge pressure when muscle i was closed	bar
P_{i_0}	initial absolute pressure when muscle i was closed	bar

q_i	generalized coordinate	
Q_i	generalized torque/force associated to q_i	
$\mathbf{q}$	generalized coordinate vector	
r	radial distance from fibre to central muscle axis	m
	dry air gas constant	J/kg/K
r_0	largest muscle radius at each contraction	m
$r_i(\theta)$	leverage arm of muscle i in a joint setup	m
R	unpressurized muscle radius	m
	rotation point of a joint muscle setup	
$\bar{R}$	reaction force vector	N
s	fibre section	m^2
	sampling counter	
t	time	s
$t_i(\theta)$	torque function of muscle i in a joint setup	Nm/bar
T	joint torque	Nm
	time duration	s
	temperature	K
T_i	torque generated by muscle i in a joint setup	Nm
U	potential energy	J
$v\left(\epsilon, \frac{l_0}{R}\right)$	dimensionless volume function	
v_i	coefficients of polynomial muscle volume fitting	
V	enclosed muscle volume	m^3
V_{i_0}	initial volume when muscle i was closed	m^3
w	half the distance between two neigbouring fibres	m
W	work	J
x_0	x coordinate of extreme end of muscle volume	m
$\bar{1}_r$	unity vector corresponding radial direction	
$\bar{1}_x$	unity vector corresponding axial direction	
$\bar{1}_z$	unit vector corresponding to z-axis	

Subscript

a	in the air
A	of ankle
air	of compressed air
B	back
atm	atmospheric
d	downstream
	derivative
D	of double support
f	of foot
F	front
gr	ground
H	of hip

i	integral
	muscle number
	link number
	joint number
	counter
$isotherm$	at isothermal conditions
j	joint number
	counter
k	counter
K	of knee
p	proportional
R	rear
s	stance
S	of single support
tot	total
u	upstream
$+$	at touchdown
$-$	instance just before impact

Superscript

D	of double support
ex	of exhaust valve
in	of inlet valve
nat	natural function
sup	of compressed air supply
S	of single support
T	transpose
y	along y-axis
$\tilde{}$	required value
$\hat{}$	calculated with estimated parameter values
$+$	psuedo inverse
$\dot{}$	derivative with respect to time
$\bar{}$	vector
-1	inverse

Chapter 1

Introduction

1.1 Legged locomotion: general discussion

An important motivation for research and development of legged robots is their potential for high mobility. Since these machines only need a discrete number of isolated footholds, their mobility in unstructured environments is much higher than their wheeled counterparts, which require a more or less continuous path of support. For outdoor environments, such as minefields [Habumuremyi and Doroftei, 2001], volcanos [Bares and Wettergreen, 1999] and forests [Plustech, 2004], legged machines can serve a useful purpose. Legged inspection robots could e.g. be of great use examining disaster areas, or inspection and maintenance robots can be used in contaminated areas which are found in nuclear or chemical plants. But especially with regard to an environment close to humans, legged machines increase in versatility towards navigation. In such an environment, wheeled machines continuously encounter obstacles, as a wheelchair user will surely testify. In our increasingly aging society, the demand for medical care and assistance is growing while the desire to maintain a high living standard is all the more felt. This societal evolution opens a potential market for many automation applications. The dream application in such a context is of course a humanoid robot who assists in the repetitive and time-consuming household chores. Particularly these contexts require a biped much more than a multi-legged robot, since humans will probably prefer a robot resembling ones own image, over a spiderlike eight-legged machine crawling around in the house. Another motivation for many researchers to built legged machines and especially bipedal robots is to understand the mechanisms behind human walking and locomotion of legged species in general. The mechanical counterparts with reduced complexity can give some essential insights in the biomechanics of walking. Such insights are required e.g. in the field of rehabilitation in order to design proper protheses and orthoses. Contrary to the older designs based on passive motion, recent devices are designed with active control. One extremely innovative example of active control in orthoses is a robotic exoskeleton used for the rehabilitation of paraplegic persons [Colombo et al., 2000], commercialized by Hocoma AG[1]

Since the second half of the previous century, research on legged machines is increasingly gaining interest. Many research groups have been tackling the very complex task of making robots walk. Besides artificial intelligence, one of the biggest challenges is balancing these machines during fast motion. This poses high demands on the actuation system together with specific sensory equipment in general. Difficulties associated with legged locomotion such as the different phases in the walking and running motions, the high degrees of freedom (DOF) and the unilateral nature of the foot/ground contact require advanced control strategies in order to maintain balance and achieve prescribed robot motions. Many robot models have been studied and built in the past, and several surveys reporting on the most common robots have been published, such as by Regele et al. [2003] and Ridderström [1999]. Nevertheless, the greatest efforts and most substantial progress in the field of legged robots has been made during the last decade. One of the most significant events has been the presentation of the humanoid robot P2 by Honda Motor Corporation in Tokyo in 1996 [Hirai et al., 1998], after ten years of undisclosed research. This autonomous humanoid was able to walk smoothly on level ground and even to climb stairs. This event triggered fierce competition in the research and development of legged robots among the major Japanese technology concerns. Honda has already built several humanoids of which the latest model is ASIMO [Hirose et al., 2001]. Recently an astonishing version of ASIMO performed a smooth running motion at 3 km/h [Honda, 2004]. Sony put the well-known pet-robot AIBO on the market and revealed their running robot QRIO [Kuroki et al., 2001]. Toyota Motor Corporation announced its "Partner Robot" [Toyota, 2004a] and revealed a two legged walking chair [Toyota, 2004b]. Fujitsu introduced a miniature humanoid robot HOAP-1 [Fujitsu, 2001] and Kawada Industries developed the prototype of the H series humanoids for the university of Tokyo [Nishiwaki et al., 2000] and the state of the art HRP-2 [Kaneko et al., 2004] humanoid platform for the HRP-project [Yokoi and al., 2003] of the Japanese government. This last project attempts to promote ready-to-use industrial, domotic and health-care applications for humanoid robots. Figure 1.1 shows pictures of P2[2], Asimo[3], I-foot[4], Partner Robot[5], Qrio[6], Hoap-I[7], Hrp-2[8], and H7[9]. Japan is definitely the leading country on legged robotics, an important and comparable European humanoid robot is Johnnie [Pfeiffer et al., 2003] from the Technical University of Munich in

[1] http://www.hocoma.ch/
[2] source: http://www.plyojump.com/pseries.html
[3] source: http://world.honda.com/news/2001/c011112_1.html
[4] source: http://www.toyota.co.jp/en/news/04/1203_1d.html
[5] source: http://www.plyojump.com/toyota.html
[6] source: http://www.hindustantimes.com/news/
[7] source: http://pr.fujitsu.com/en/news/2001/09/10.html
[8] source: http://www.kawada.co.jp/global/ams/hrp_2.html
[9] source: http://www.jsk.t.u-tokyo.ac.jp/research/h6/H6_H7.html

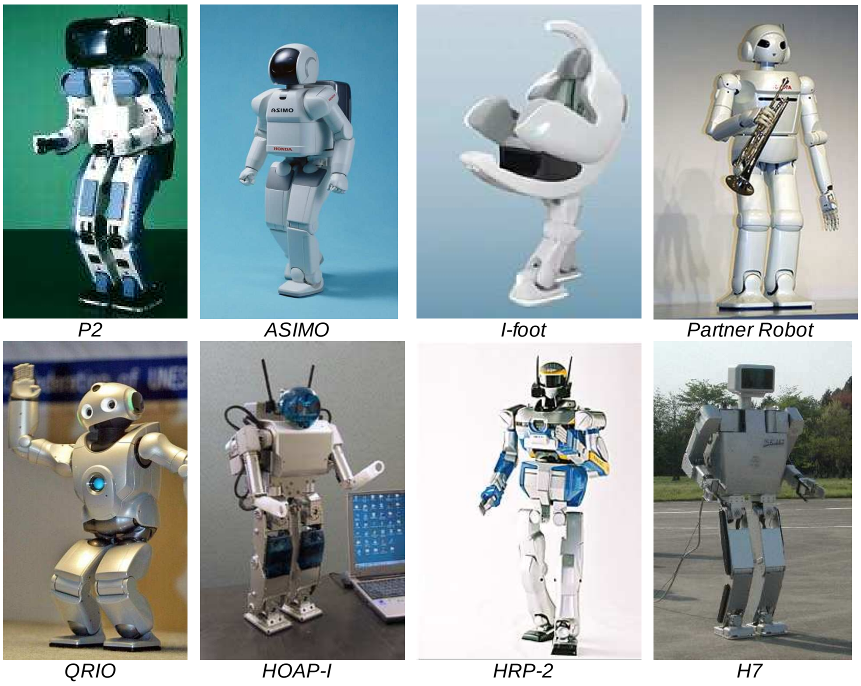

Figure 1.1: Japanese state-of-the-art robots

Germany. A picture of this robot is given in figure 1.2[10].

1.2 Legged locomotion and pneumatics

The current enormous evolution brings the idea of humanoid robots out of science fiction into the real world and stimulates research institutes all over the world to invest in this highly multi-disciplinary research area. The number of robots built by universities and governmental technology centers is rapidly growing. Each of these models focus on their own specific implementations, ranging from biological mimic for control purposes to autonomous navigation by means of 3D camera vision. Despite the diverging goals of these projects, they usually share one common feature, namely electrical actuation. Since motor drives and their attributes are widely available and the control aspects of such actuation is well-known, this type of actuation is extensively used. Nevertheless there are some important limitations to this kind of actuation in legged machines. Since rotational speeds of the inter limb joints are much lower than nominal speeds of most electrical motors, transmission units are required. These increase the weight and complexity of the actuation

[10]source: http://www.amm.mw.tu-muenchen.de/index_e.html

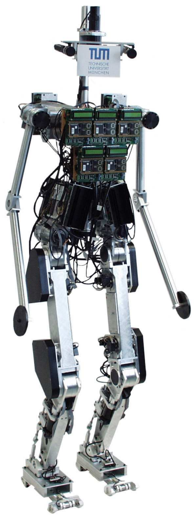

Figure 1.2: The humanoid robot Johnnie

system and induce high reflected inertia. The latter is inconvenient for shock absorbance, especially when robots are expected to improve in velocity and mobility. For manipulator robot implementation, stiff joints have always been preferred to compliant joints since they increase tracking precision. For legged robots however, tracking precision is not that stringent as overall dynamic stability. Elastic joint properties can then be exploited to store potential energy and reduce control effort.

In this context pneumatic systems are an interesting alternative for the actuation of legged robots. Mainly two types of pneumatic actuation are used: pneumatic cylinders and pneumatic artificial muscles. A pneumatic artificial muscle is essentially a volume, enclosed by a reinforced membrane, that expands radially and contracts axially when inflated with pressurized air. Hereby the muscle generates a uni-directional pulling force along the longitudinal axis. Standard pneumatic cylinders are well known and available off-the-shelf but, contrary to pneumatic cylinders, these artificial muscles do not have the troublesome stick-slip phenomenon and are controlled by pressure levels instead of air flows to influence position. Pneumatic artificial muscles have a very high power to weight ratio and both pneumatic systems can be coupled directly without complex gearing mechanisms. Due to the compressibility of air, a pneumatic actuation system inherently possesses a compliant behaviour, which can be exploited to reduce shock effects at touch-down of a leg. In some pneumatic configurations, joint compliance can be adjusted by applying appropriate pressure combinations. This compliance adjustment can positively influence energy consumption and control effort by adapting the natural dynamics of the system as a function of the desired robot motion. This topic is discussed in the next section. In spite of these benefits, however, pneumatic actuation has not been widely used as an actuation system for legged locomotion, mainly because of the extra design effort needed to control these systems when used for a dynamic application.

The number of pneumatic legged robots built worldwide up till now is rather limited compared to the amount of robots with electrical actuation. Since this thesis concerns a pneumatic biped, an extensive enumeration of projects involved in pneumatic legged robots is given below. One of the first to incorporate pneumatics is the Japanese pioneer for legged locomotion Kato. During the sixties and seventies he has built several statically balanced walking bipeds such as WAP I, II and III [Kato et al., 1972]. These machines where actuated by different types of pneumatic artificial muscles and were able to move very slowly. Another pioneer in legged robotics is Raibert, who has built several hopping and running machines during the eighties at the Massachusetts Institute of Technology. His mono-, bi- and quadruped robots used pneumatic cylinders to actuate the telescopic legs [Raibert, 1986]. Raibert implemented decoupled control for body pitch and forward speed. The latter was controlled with an intuitive law for foot placement during touch-down. The pneumatic cylinders were used to provide thrust action and were exploited as compliant elements. At the university of Paris, two pneumatic robots were developed: the quadruped robot "Ralphy" [Villard et al., 1993] and the hybrid wheeled-leg robot "Sapphyr" [Guihard et al., 1995]. Also in Paris the pneumatic biped "Bipman" [Guihard and Gorce, 2001] has been developed at INSERM, and now resides at the university of Toulon. The main objective of this project is to develop a hierarchic and modular architecture able to deal with the different stages of control. Similar to "Ralphy" and "Sapphyr", this architecture is based on a biomechanic analysis of humans at a high control level and on computed torque techniques in combination with an estimated force model of the pneumatic actuators at the low control level. At the Laboratoire de Robotique de Versailles, the pneumatic biped "STEP" [Nadjar-Gauthier et al., 2002] was built with pneumatic cylinders. This robot is underactuated and its main focus is the implementation of a new sliding mode control scheme. In Great Britain the spider-like pneumatic robot ROBUG IV [Cooke et al., 1998] was created at the university of Portsmouth and focused on modularity. The group of Caldwell, at the university of Salford, developed the biped "Salford Lady" [Artrit and Caldwell, 2001] and a gorilla like robot [Davis and Caldwell, 2001], both actuated with McKibben artificial muscles. The local joint control directly calculates desired pressure levels with a PID position feedback loop. The pressure itself is regulated with fast switching pulse-width modulated on/off valves. At FZI Karlsruhe, Germany, a stick-insect-like robot "Airbug" [Kerscher et al., 2002] has been built and its successor "AirInsect" [Kerscher et al., 2004] is being developed. As the former two, the mammal-like robot "Panter" [Albiez et al., 2003] at FZI is actuated with Fluidic Muscles, which is a type of pneumatic artificial muscle commercialized by Festo. The local control of the antagonistic muscle setup is a series of different controllers. A pure PID position feedback control dictates the necessary contractions, which results in two desired pressures based on a muscle force feedback. The forces are not directly measured, but estimated with a linearized model of the static-force-to-contraction muscle characteristic in combination with pressure measurements. The desired pressures of both muscles are then set by a PI controlled pressure feedback loop. Additionally, the stiffness of a joint can be adapted. Festo itself developed a full scale humanoid "TronX"[11] which is actuated with pneumatic cylinders. Although this robot has two actuated legs, it is not able to walk. Also in Germany, at the university of Lübeck, different pneumatic robots with standard cylinders as FRED II [Brockmann and Huwendiek, 1998] have been built and studied. The robot's motion is achieved by orthogonally moving frames. The low-level position control of the pneumatic cylinders is achieved with a specific neuro-fuzzy method, the NetFAN approach, in order to cope with the complicated control characteristics of pneumatic cylinders. In the nineties, three generations of bipeds [Einstein and Pawlik, 1995] driven by pneumatic cylinders have been built at the polytechnic institute of Czestochowa in Poland. These models were statically balanced and the research focused on simplicity and incorporation of higher level pneumatic control hardware. At the university of Lódź in Poland the small, simple and extremely low cost pneumatically driven quadruped "Spike" [Dabrowski et al., 2001] has been developed. This robot is actuated with only two pneumatic cylinders and tries to mimic turtle movement. The pneumatics are driven with a simple open loop structure, using pulse-width modulated valve regulation. In Italy at the university of Cassino the pneumatic biped EP-WAR3 [Figliolini and Ceccarelli, 2003] has been developed, this is already the third version of a biped actuated with pneumatic cylinders. Exceptional for this biped is the discrete number of postural positions since the cylinders are used in a binary way. Dynamic postural stability is simplified by using suction caps which fix the feet to the ground at each step. In Catania, an articulated pneumatic robot leg [Guccione et al., 2003] with two pneumatic cylinders actuating the ankle joint and one cylinder to rotate the knee joint has been developed. A fuzzy controller, which mimics a PID position feedback control, is implemented to regulate the position of the pneumatic cylinders. In the Netherlands at the university of Delft several biped models have been developed by van der Linde [1998] and Wisse and van Frankenhuyzen [2003]. These robots incorporate passive behaviour by exploiting the compliance of the pneumatic artificial muscle actuation system. Active control is added by using so called phasic activation. At certain phases during a walking cycle pneumatic energy is added to the system by temporarily increasing pressure levels. Analogous to the robots of Delft, the Shadow Robot Company[12] implemented McKibben type pneumatic artificial muscle in a bipedal robot. In the United States at Case Western Reserve University R. Quinn and his team have built several pneumatically powered robots. The first is "Robot III" [Quinn and Ritzmann, 1998] which is actuated by pneumatic cylinders. For its successors "Robot IV" [Quinn et al., 2001] and "Ajax" [Kingsley et al., 2003] the standard cylinders are replaced by pneumatic artificial muscles. All

[11] http://www.gizmodo.com/archives/festos-humanoid-robot-015276.php
[12] source: http://www.shadow.org.uk

three robot designs are inspired by a cockroach. The swing leg control consists of three different stages. The lowest trajectory tracking is achieved with a local proportional feedback controller and the inverse leg kinematics is implemented with a neural network that coordinates the different joints in a leg. Finally, a distributed network is used to control the different legs, which results in a tripod gait similar to a real cockroach. The same insect also inspired researchers at the university of Illinois to develop the hexapod robot "Mark I" [Delcomyn and Nelson, 2000]. This robot is actuated with pneumatic cylinders which are controlled by a kind of pulse-width modulation in order to mimic several features of nerve impulse control for insect muscles. Overall coordination of the legs is done by PID trajectory tracking for which the desired trajectories are constructed with captured data of real cockroaches. A tiny hexapod robot "Sprawlita" [Clark et al., 2001] has been designed at Stanford University, trying to mimic several features of the same cockroach. This robot uses small pneumatic cylinders for primary thrust action. The cylinders are attached to the hip by a passive element, while small motors rotate the legs to direct the thrust action. The control counts on the tuned passive self stabilizing visco-elastic mechanical system of the legs, while gait characteristics such as forward speed are controlled in a feedforward manner by foothold placement at touch-down. Recently, a pneumatic jumping quadruped [Kikuchi et al., 2003] has been developed at the Hirose-Yoneda lab in Tokyo. This robot is actuated by pneumatic cylinders and is able to jump quite far. The purpose of this robot lies in the field of rescue operations in disaster areas. Its control currently focusses on the exhaust flows in order to influence impact behaviour.

1.3 Legged locomotion and natural dynamics

Legged robots can be classified in terms of the applied overall control strategy. The more recent robots are dynamically balanced machines, whereas the older machines were statically balanced. Statically balanced robots keep the center of mass within the polygon of support in order to maintain postural stability. To avoid inertial effects these machines move rather slowly, contrary to dynamically balanced robots where the inertial effects are taken into account in the different control strategies. When the control unit not only takes these inertial effects into account but also exploits them, the term natural dynamics in legged robotics arises.

Natural dynamics or passive dynamics is the unforced response of a system under a set of initial conditions. In general, in legged locomotion, natural dynamics is not or only partially exploited. Examples of exploitation of the natural dynamics are the swing-leg swinging freely without hip actuation or the body and stance-leg pivoting as an inverted pendulum around an unactuated ankle. Legged systems that walk completely without actuation are the so called "Passive Walkers". These machines are only powered by gravity and they are mechanically tuned in order to walk down a sloped surface. These "Passive Walkers" could be pointed out as highly energy efficient but unfortunately they are of little practical use. A minimum actuation should be provided to walk on level ground to overcome friction and impact losses. However it remains important to exploit the natural dynamics by trying to incorporate the unforced motion of a system instead of ignoring or avoiding it. Doing so could positively affect energy consumption and control efforts.

One of the first to incorporate passive dynamics for legged locomotion was Matsuoka [1980], and later Raibert [1986]. The pneumatic cylinders in the telescopic legs of Raibert's hopping robots were used as a pneumatic spring to influence and exploit the passive dynamics in the vertical direction. Exploiting passive dynamics by means of the stance leg pivoting freely as an inverted pendulum was incorporated in the biped walkers of Takanishi et al. [1985] and Lee and Liao [1988]. At the end of the eighties Thompson and Raibert [1989] studied additional exploitation of natural dynamics of the hip motion by placing a torsional spring. At the same time McGeer [1990] built and studied a "Passive Walker" without compliant elements. During the nineties the group of Andy Ruina [Garcia et al., 1998] studied the models of McGeer in more detail and extended the two dimensional model to three dimensions while building several "Passive Walkers". Kuo [1999] studied the lateral motion of a 3D "Passive Walker", and investigated methods to stabilize motion. In the second half of the nineties Gregorio et al. [1997] built a legged hopping monoped following the examples of Raibert using electrical actuation combined with a torsional spring in the hip and a linear spring in the telescopic leg. The control strategy was to calculate the passive dynamic trajectories with the correct initial conditions as a function of the desired forward speed while in parallel with these trajectories standard active control was used to cope with modelling imperfections. A more intuitive control, but still focussing on exploiting natural dynamics, was done at MIT by Pratt et al., by implementing "Series Elastic Actuators" [Pratt and Williamson, 1995]. These devices were used for the two legged "Spring Flamingo" [Pratt and Pratt, 1998] and consist of a motor drive connected in series with a linear elastic element. After 2000, Quartet III was built by Osuka and Saruta [2000], this quadruped starts walking down a sloped surface in an active way and gradually decreases control input to transfer to passive walking. Asano et al. [2000] introduced the "virtual gravity field" for horizontal walking in order to exhibit virtual passive walking based on McGeer's models but with hip and ankle actuation. Finally, Wisse et al. [2001] studied a 3D Passive Walker with a pelvic body.

Most of these models use inertial properties to determine the eigenfrequency and additionally fixed compliance of mechanical linear or rotational springs. As a result the eigenfrequency of these systems is set during construction which limits the different passive walking patterns and walking speeds. Flexibility, with the ability to change this natural frequency, is increased by implementing passive elements with variable compliance. In this context the group of Takanishi developed the two-legged walker WL-14 [Yamguschi et al., 1998], where a complex non-linear spring mechanism makes changes in stiffness possible. At Carnegie Mellon University, Hurst et al. [2004] focus on the use of variable compliance for legged locomotion, with an analogous complex mechanical joint construction. A more elegant way to implement variable compliance is to use pneumatic artificial muscles, where the applied pressures determine stiffness. Research on this topic was done by van der Linde [1998], Wisse [2001], Davis and Caldwell [2001] through implementation of McKibben type pneumatic artificial muscles.

1.4 Scope of the thesis

Some ten years ago the Multibody Mechanics Research Group of the Vrije Universiteit Brussel began research in the domain of legged robots by focussing on footless hopping monopods. Strategies were developed by De Man et al. [1996] to control these underactuated mechanisms for hopping on irregular terrain, hereby formulating a joint trajectory generator based on objective locomotion parameters. This formulation allowed to adjust foothold placement and forward speed from one hop to another. After evaluating the developed theories in simulation, a real robot model, actuated by electrical drives, was built [De Man et al., 1998]. But the experimental process failed due to the high demands of the algorithm, required to control the fast dynamics associated with hopping. Moreover, the electrical drives were found far to heavy for this application, and the impact chocks at touch-down put a substantial load on the drive mechanism. Vermeulen [2004] fine-tuned the developed theories and implemented them for a hopping robot with an actuated foot, in order to be able to give small correcting ankle torques [Vermeulen et al., 2003]. The same principle was extended to control a planar biped with quasi zero ankle torques in order to position the zero moment point (ZMP) in the vicinity of the ankle joint, resulting in dynamically stable walking [Vermeulen et al., 2005]. The developed trajectory generator is based on fast converging iteration loops, which makes the method suitable for real-time applications.

At the same time, research was started on a novel lightweight actuator; the pleated pneumatic artificial muscle, which is a type of artificial muscle developed by Daerden [1999], designed to overcome some shortcomings of the McKibben pneumatic artificial muscle. The muscle membrane layout was arranged into radially laid out folds that can unfurl free of radial stress when inflated. It is believed that these pneumatic actuators have interesting characteristics which can be used in the field of legged robotics. As was already pointed out in the introduction on legged robots, these pneumatic drives are lightweight and can be coupled directly to drive a robot joint without any complex gearing mechanism. The air compressibility makes these actuators compliant, which can reduce chock effects and, when using two muscles to drive a one-dimensional rotating joint, can adapt the compliance characteristics of such a joint. This compliance adaptability can be used to alter natural frequencies of the system in order to create more flexibility towards exploitation of natural dynamics.

In this context, the development of a planar robot actuated with pleated pneumatic artificial muscles (PPAM), which is the main topic of this PhD and the research work of Van Ham and Vanderborght, was started. The robot has been given the name "Lucy", and its main purpose is to create an elaborate experimental platform to evaluate the implementation of the PPAM. The control goal for this biped is to combine exploitation of natural dynamics with the concept of trajectory tracking. For a "Passive Walker", the inertia properties and compliance characteristics are designed in such a way that it can walk within a certain rhythmic motion, but its dynamically feasible walking patterns are situated within a small range of possible motions. Such a system is highly energy efficient, but an actively controlled biped has, however, much more versatility towards different walking patterns. Moreover, a trajectory generator, and possible dynamic stability feedback control, ensures better conditions for dynamically stable walking. The proposed joint trajectories are then tracked by the pneumatic artificial muscle actuation system. But the tracking controller is designed so that the compliance of the different joints can be altered while tracking position in order to reduce control activity. Hereby adapting the natural dynamics as a function of the imposed trajectories, such that these active trajectories have a resemblance with the passive trajectories associated with the controlled joint compliances.

The research associated with the design and construction of the biped "Lucy" and its control algorithms will entail three doctoral dissertations, of which this is the first one to be submitted. The present study describes the design and construction of the complete biped. The overall research is carried out in collaboration with the above-mentioned colleagues Van Ham and Vanderborght. This work points out some conceptual ideas about tracking control with adapted compliance and proposes a multilevel nonlinear tracking controller for the complete biped which is balanced by the trajectory generator developed by Vermeulen. The feasibility of the proposed control structure is evaluated with an elaborate simulation model of the biped "Lucy", which incorporates the specific nature and limitations associated with the pneumatic actuation system. This simulation model will be an important tool when the proposed control algorithms are being extended towards exploitation of natural dynamics and fine-tuned for the actual robot. At this stage of development, some preliminary tracking results of leg motions are shown while the robot is suspended in the air. Additionally, the prototype of the PPAM, as developed by Daerden was substantially redesigned for this thesis.

1.5 Outline

Chapter 2 discusses the second generation PPAM, which is an adaptation of the first prototype in order to extend the muscle lifespan and to simplify construction of the muscles. This chapter describes the new design and gives a reformulation of the mathematical model, developed by Daerden, which describes the actuator characteristics. The mathematical force model is compared with measurements of static load tests carried out on the type of muscle which is currently implemented in the robot "Lucy". Chapter 3 reports on a one-dimensional joint setup controlled by two antagonistically positioned muscles. The kinematics describing angular displacement and joint generation are given, with additionally a formal discussion on the adaptability of joint compliance. The basic control strategy intended for "Lucy" is to combine the exploitation of natural dynamics and trajectory control. This concept is illustrated by means of a simulation of a simplified one-dimensional leg model. Chapter 4 discusses the control architecture designed to steer the biped. An introduction is given on the ZMP concept, followed by a recapitulation of the trajectory generation method developed by Vermeulen. Subsequently, a multilevel nonlinear tracking controller is proposed, which deals with the system nonlinearities, introduced by the robot mechanics and the muscle characteristics at separate levels. The proposed control architecture, formulated for single and double support, is then evaluated with a hybrid simulation model in chapter 5. A specific description of the modelling of the robot dynamics and the thermodynamics of the muscle/valve system is given, followed by an overview of the complete simulator, while showing the incorporation of some hardware limitations associated with the real robot design. The simulation model incorporates three different phases: a single support phase, an impact phase and a double support phase. A specific simulation shows that tracking performance is adequate at the cost of control activity because optimization of control parameters and exploitation of natural dynamics is not yet considered. The most important result points out that dynamic stability, as prescribed by the trajectory generator, is still guaranteed with the proposed pneumatic actuation system and the introduction of some model parameter estimation errors. The design and construction of the biped "Lucy" is discussed in chapter 6. An extensive description of the mechanical and electronic design is given. Hereby showing the robots modularity and sophisticated control hardware. Some flexibility towards simple changes on torque characteristics is incorporated in order to meet the needs of specific experiments. It is expected that further research on the exploitation of natural dynamics will require specific joint characteristics, which are not yet known in the current phase of research. Additionally, some preliminary results of tracking experiments, with the robot suspended in the air, are given. Finally, in chapter 7 some overall conclusions are drawn, followed by the planning of future research concerning the biped "Lucy".

Chapter 2

Pleated pneumatic artificial muscle

2.1 Introduction

A pneumatic artificial muscle (PAM) is essentially a volume, enclosed by a reinforced membrane, that expands radially and contracts axially when inflated with pressurized air. Hereby the muscle generates a uni-directional pulling force along the longitudinal axis. When neglecting the membrane's material deformation and the low inertial muscle properties, the generated force is expressed as [Chou and Hannaford, 1996; Daerden, 1999]:

$$F = -p\frac{dV}{dl} \tag{2.1}$$

with p the gauge pressure inside the muscle, dV enclosed muscle volume changes and dl actuator length changes. The volume of the actuator increases with decreasing length until a maximum volume is reached. At maximum contraction, forces become zero, and at low contraction these forces can be very high. Figure 2.1 gives the working principle of a PAM at constant pressure. The changing force as a function of contraction at constant pressure is essentially different compared to standard pneumatic cylinders, for which the generated force does not change at constant pressure. For these devices the generated force is proportional to the piston area on which the internal pressure works, consequently the force does not change with piston position at constant pressure.

Depending on the geometry and type of the membrane, the specific force characteristic alters. Several concepts of PAM have been developed over time, some examples are the Romac muscle [Immega, 1987], the Baldwin muscle type [Baldwin, 1969], and the best know type is the so called McKibben muscle. This muscle was introduced by McKibben for orthotic applications in the fifties [Schulte, 1961]. Several forms of this type of muscle have actually been commercialized by different companies such as Bridgestone Co. [Inoue, 1987], the Shadow Robot Company [Shadow Robot Company, 2003], Merlin Systems Coorporation [Merlin Systems

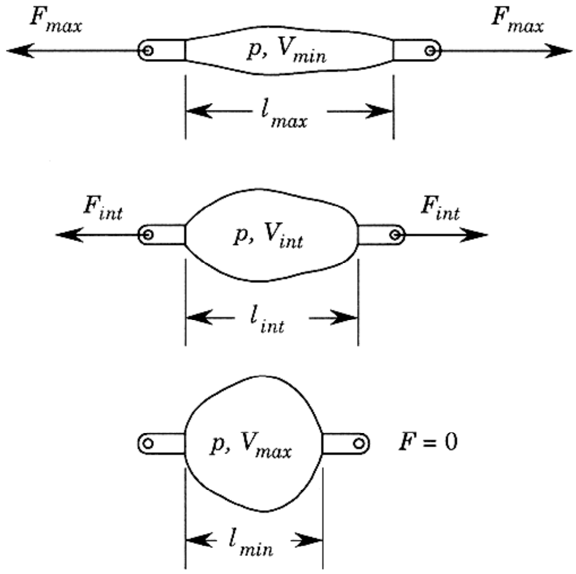

Figure 2.1: Working principle of a pneumatic artificial muscle [Daerden, 1999]

Coorporation, 2003] and Festo [Festo, 2004]. More and more interest for these actuators is growing and several groups all over the world use McKibben like muscles in various robotic and medical applications [Raparelli et al., 2000; Eskiizmiler et al., 2001; Klute et al., 2002; Berns et al., 2001; Davis et al., 2003; Kingsley et al., 2003; Pomiers, 2003; Kawashima et al., 2004; Wisse, 2004].

In figure 2.2 the concept of the McKibben muscle is given. It contains a rubber inner tube which will expand when inflated, while a braided sleeving transfers tension. Inherent to this design are dry friction between the netting and the inner tube and deformation of the rubber tube. Typical working pressure values range from 1 to 5 bar and more. Due to a threshold of pressure which depends on the rubber characteristics, these muscles do not function properly at low pressures.

To avoid friction and deformation of the rubber material, the Pleated Pneumatic Artificial Muscle (PPAM) has been designed by Daerden [1999]. The membrane of this muscle is arranged into radially laid out folds that can unfurl free of radial stress when inflated. Figure 2.3 shows the working principle of the PPAM. The membrane is a fabric made of an aromatic polyamide such as Kevlar to which a thin liner is attached in order to make the membrane airtight. The high tensile longitudinal fibres of the membrane transfer tension, while the folded structure allows the muscle to expand radially. The folded membrane is positioned into two end fittings which close the muscle and provide tubing to inflate and deflate the enclosed volume. The end fittings are constructed with a circular inner teeth structure to position and align each fold of the membrane, while an outer aluminium

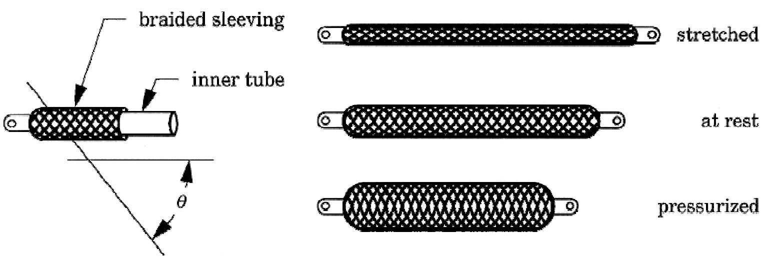

Figure 2.2: Drawing of the McKibben type muscle [Daerden, 1999]

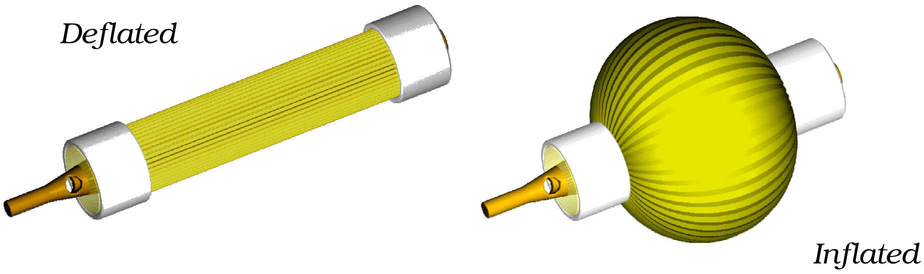

Figure 2.3: CAD drawing of the deflated and inflated state of the PPAM

ring prevents the membrane of expanding at the end fittings. An epoxy resin fixes the membrane to the end fittings.

Due to its specific design, the PPAM can easily work at pressures as low as 20 mbar. For lifetime considerations of the membrane, the upper limit of the working pressure is set to a maximum 4 bar gauge pressure. Muscle contraction can be more than 40 %, depending on its original dimensions (theoretically 54 % for a infinitely thin muscle). The muscle prototype built by Daerden [1999] has a weight of about 100 gr while it can generate forces up to 5 kN.

In this chapter a second generation of the PPAM is discussed. A new design has been introduced to extend the muscle lifespan and to simplify construction of the muscles. Section 2.2.1 discusses the adapted design and a mathematical model of the new muscle is given in section 2.2.2. This mathematical model is used to determine muscle characteristics which are given in section 2.2.3. Finally, in section 2.3, static load tests on muscles used for the biped "Lucy" are discussed.

2.2 PPAM: adapted design

One of the drawbacks of the first PPAM prototype is its limited lifetime. In Daerden's work, the PPAM design focussed on improving the muscle performance, while studying basic control techniques for an unloaded rotative joint. Extensive usage of the muscles, for example as an actuator for a bipedal walking robot, was however not immediately considered. For any experimental platform the lifespan of the muscle is crucial for obvious reasons. Apart of the interesting scientific aspects related to a study of the PPAM, such a muscle will be economically lucrative, if it can be produced at a reasonable price and has a sufficient lifespan.

2.2.1 Second generation PPAM

One of the causes of the limited muscle lifespan is the overlap used to make a cylindrical pleated membrane. The membrane of the former prototype is folded while starting from a flat woven fabric. The result of the folding process was a flat pleated membrane, and to create a circular shape, one or two folds are glued together with an overlap. During operation, stresses on the interface between the two overlapped membrane pieces create weakened attachments. The pressurized air finds its way through these weakened spots, which results in leakage. To avoid this, the folding production process was changed. Instead of the folded overlap, the folding now starts from an airtight cylindrical fabric in which the folds are created afterwards, as in figure 2.4.

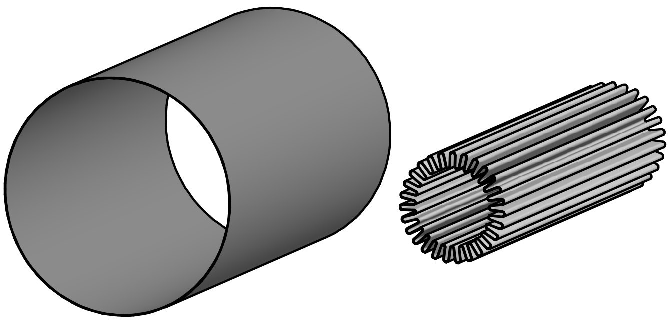

Figure 2.4: Membrane folding

The toothed inner metal tube of the end fittings requires a lot of machining. Additionally, a large amount of operations are required to position the pleated membrane, fold by fold, in the tooth holes. The idea is to replace this complex end fitting by a straightforward aluminium basin in which the membrane is fixed by the same epoxy resin. The folds are not deliberately aligned, but are assumed to lie already parallel after the improved folding process. The epoxy keeps the pleated membrane in place. Figure 2.5 gives a drawing of the new end fittings. These are made of two parts to facilitate production. Several grooves at the inner and outer side improve the epoxy to aluminium fixing.

One of the major changes is made to the membrane layout itself. The most

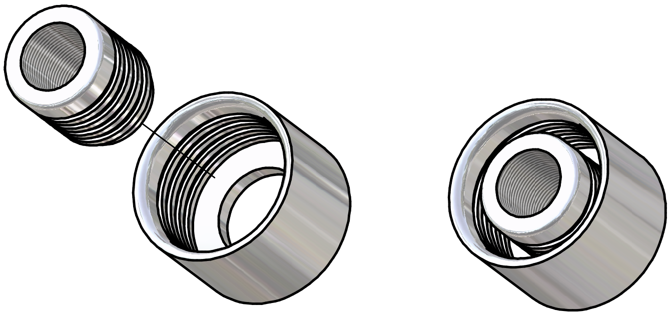

Figure 2.5: New aluminium end fittings

important reason for a shorter lifespan, was an incorrect bulging of the pleated membrane. In figure 2.3 the folds are assumed to unfold evenly, but for a real muscle this was hardly the case. The photograph in figure 2.6 shows the inflated state of a muscle with new end fittings, but with the old membrane structure. It is

Figure 2.6: Photograph of inflated state of the old design

seen that the membrane is not evenly unfolded, which causes extra parallel stresses on the Kevlar fabric and its airtight coating, especially at the top of each fold. It is observed that the axial Kevlar fibres on each top tend to move towards the bottom of its respective crease, leaving a gap at the top. This of course weakens these spots and facilitates the pressurized air to induce leakage. As a solution to this is then to change the membrane composition by only using high tensile stiffness fibres positioned at the bottom of each crease, while another more flexible fabric is used to create the folded membrane structure and keep the pressurized air inside the muscle. The flexible fabric is a simple woven polyester cloth, which is made airtight by a polymer liner. This structure is folded and in each crease a yarn of high-tensile Kevlar fibres is responsible for transferring the large axial tension.

Figure 2.7 shows a photograph of a membrane cross-section and figure 2.8 depicts the complete straightforward construction of the new muscle.

Figure 2.7: Photograph of a membrane section

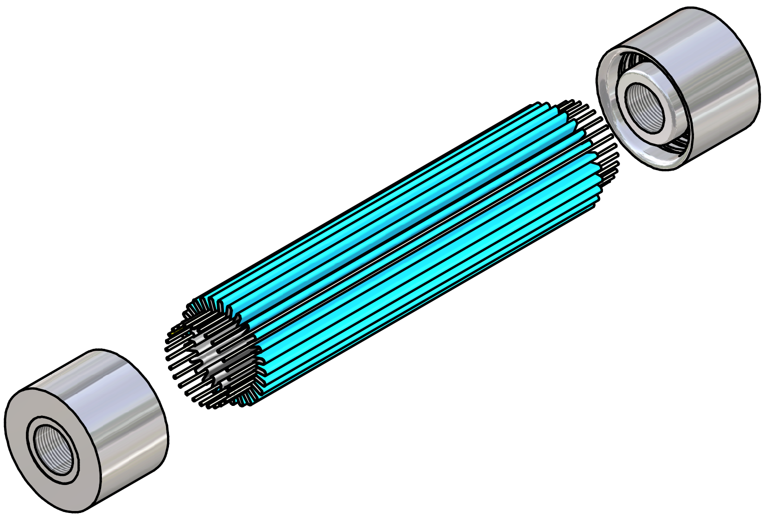

Figure 2.8: Composition of the new muscle prototype

Contrary to the former design, this muscle prototype does not incorporate air connectors. The end fittings have a treated hole in which additional muscle connectors can be screwed. An advantage of this setup is that a broken muscle can be replaced easily, without having to change the more complex muscle connectors.

These connectors incorporate three functions: guiding the pressurized air in and out the enclosed volume, creating the interface for the connection to the specific application frame, and providing an attachment for a pressure sensor positioned inside the muscle. Figure 2.9 shows the two different connectors to be fixed at each side of the muscle. The left side drawing of figure 2.9 shows the connector

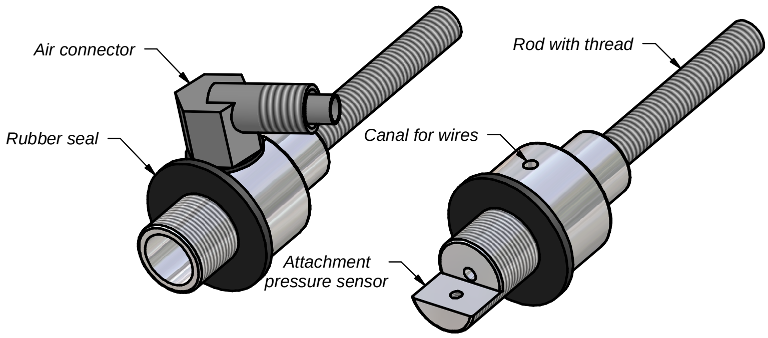

Figure 2.9: Drawing of the two muscle end connectors

which allows the air to flow in and out of the muscle, while the right side drawing depicts the connector with the attachment for a pressure sensor. Both connectors are made of aluminium and have a rubber sealing. At the back of each connector a threaded rod forms the interface to the application frame. In the muscle connector on the left of figure 2.9, a standard air tube connector can be fixed. In the muscle connector for the pressure sensor a small borehole has been drilled to guide the wires of the electronics needed for the pressure sensor, which is positioned inside the muscle. Once this sensor and its wiring are positioned, the borehole is filled with epoxy resin to prevent the air from escaping from the enclosed volume.

Finally, figure 2.10 shows a photograph of the new muscle prototype. The muscle is shown in its inflated state. Note the regular unfolding of the flexible membrane while the Kevlar fibres stay positioned at equal distances. A lifespan test was performed, at which a muscle moves up and down a load of 130 kg by a slow varying gauge pressure between 1 and 3 bar. About 400.000 cycles have been reached before the test was ended. At this large number of cycles a few Kevlar fibres were broken somewhere in the end fittings. At these spots the epoxy resin makes the fibres fragile. Although movements of the fibres in the end fittings are small, due the large number of cycles, the fibres will break eventually. Although the reached number of cycles is already a significant improvement, currently, a third generation of muscle is being studied.

Figure 2.10: Photograph of inflated state of the second generation PPAM

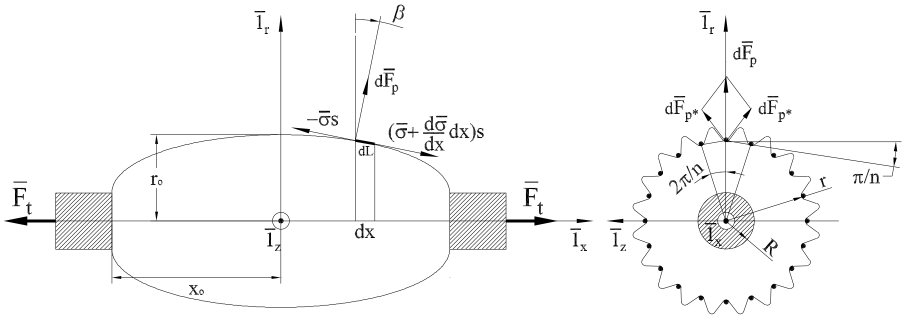

Figure 2.11: Meridional and parallel view of the PPAM

2.2.2 Mathematical model

In this section, the mathematical model describing the muscle characteristics, developed by Daerden [1999], is adapted according to the new membrane design. The original model assumed a continuous axisymmetrical circular membrane, while for this model the focus lies on the discrete number of high tensile longitudinal fibres. The initial assumptions of the model are different, but the resulting analytical solution is almost identical. Therefore, only the starting point for the model is established here, while the elaboration on the analytical solution can be found in [Daerden, 1999].

In figure 2.11 a meridional and parallel section of the new muscle is given. The muscle is pressurized and subjected to a longitudinal traction force $\bar{F}_t$. For the mathematical formulation it is assumed that longitudinal tension is only transferred by the high tensile fibres which are positioned in each crease. Any influence of the more flexible longitudinal fibres of the airtight polyester membrane is thus neglected. The membrane transfers the forces $\bar{F}_p$, that are generated on it by the pressurized air, to the high tensile longitudinal fibres. In figure 2.12 a 3D-view of an infinitesimal section of the membrane is depicted with the forces acting on the longitudinal fibre.

At the left and right side of the fibre, part of the membrane transfers a force $d\bar{F}_{p*}$. Due to the axisymmetrical situation of the closing membrane, the parallel components of these forces, which are tangent to the perpendicular circle running through the longitudinal fibres, compensate each other. Consequently, only the resultant force, $d\bar{F}_p$, is taken into account. The magnitude of this is calculated as:

$$\left|d\bar{F}_p\right| = 2p\cos\frac{\pi}{n}dA = 2pw\cos\frac{\pi}{n}dL \tag{2.2}$$

with p the gauge pressure inside the enclosed volume, n the number of longitudinal fibres, evenly distributed over the membrane, w representing half the distance

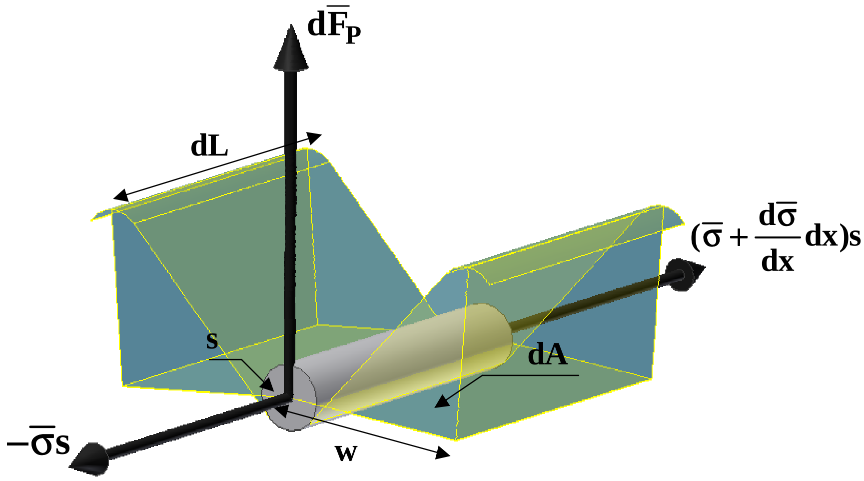

Figure 2.12: 3D-view of an infinitesimal section of the membrane

between two neighbouring longitudinal fibres and dA the elementary surface associated with w and the infinitesimal section length dL. If β defines the oriented angle (counter-clockwise positive) between the radial direction $\bar{1}_r$ and the force vector $d\bar{F}_p$, the components of this vector are represented by:

$$d\bar{F}_p = \left(-2pw\cos\frac{\pi}{n}dL\sin\beta\right)\bar{1}_x + \left(2pw\cos\frac{\pi}{n}dL\cos\beta\right)\bar{1}_r \tag{2.3}$$

$$= \left(-2pr\sin\frac{\pi}{n}\cos\frac{\pi}{n}\tan\beta dx\right)\bar{1}_x + \left(2pr\sin\frac{\pi}{n}\cos\frac{\pi}{n}dx\right)\bar{1}_r \tag{2.4}$$

$$= \left(-pr\sin\frac{2\pi}{n}\tan\beta dx\right)\bar{1}_x + \left(pr\sin\frac{2\pi}{n}dx\right)\bar{1}_r \tag{2.5}$$

Hereby using following transformations:

$$\cos\beta = \frac{dx}{dL} \tag{2.6}$$

$$w = r\sin\frac{\pi}{n} \tag{2.7}$$

with r the radial distance from the fibre to the central muscle axis $\bar{1}_x$ and dx the projection of the infinitesimal fibre length dL on to the same axis.

Assuming the tensile stress σ, generated in the high tensile longitudinal fibre, constant over the fibre section s, the force associated with this stress is given by:

$$\bar{\sigma}s = (\sigma s\cos\beta)\,\bar{1}_x + (\sigma s\sin\beta)\,\bar{1}_r \tag{2.8}$$

Shear stresses are neglected since the longitudinal fibre is extremely flexible in the perpendicular direction. If additionally the gravitational force associated with the weight of the membrane and high tensile fibres are neglected with respect to the much higher tensile forces, the equilibrium of forces acting on the infinitesimal fibre piece dL can be expressed along the directions $\bar{1}_x$ and $\bar{1}_r$:

$$\bar{1}_x : \qquad -pr\sin\frac{2\pi}{n}\tan\beta dx + \frac{d(\sigma s\cos\beta)}{dx}dx = 0 \tag{2.9}$$

$$\bar{1}_r : \qquad pr\sin\frac{2\pi}{n}dx + \frac{d(\sigma s\sin\beta)}{dx}dx = 0 \tag{2.10}$$

Eliminating $pr\sin\frac{2\pi}{n}$ from equations (2.9) and (2.10) leads to:

$$\frac{d(\sigma s\sin\beta)}{dx}\tan\beta + \frac{d(\sigma s\cos\beta)}{dx} = 0 \tag{2.11}$$

Rearranging the differentials and multiplying 2.11 with $\cos\beta$ leads to:

$$\frac{d(\sigma s)}{dx} = 0 \tag{2.12}$$

which results in:

$$\sigma s = c \tag{2.13}$$

with c an integration constant.

And substituting $\tan\beta = \frac{dr}{dx}$ in (2.9), while integrating gives:

$$\frac{r^2}{2}p\sin\frac{2\pi}{n} + c' = \sigma s\cos\beta \tag{2.14}$$

with c' an integration constant. Assuming that the traction force F_t is equally distributed over the n different longitudinal fibres, this integration constant can be interpreted as $c' = \frac{F_t}{n}$ [Daerden, 1999].

If the longitudinal high tensile fibres are assumed to be inelastic (a special case of the discussion in [Daerden, 1999]) the following geometrical constraint on the fibre length l_0 has to be taken into account:

$$\int_{x=0}^{x=x_0} dL = \int_{x=0}^{x=x_0} \sqrt{1+\left(\frac{dr}{dx}\right)^2}dx = \frac{l_0}{2} \tag{2.15}$$

with x_0 being the extreme ends of the enclosed volume of the muscle. Using the relation $\sqrt{1+\left(\frac{dr}{dx}\right)^2} = \frac{1}{\cos\beta}$ and $c' = \frac{F_t}{n}$, equation (2.14) can be transformed to the following differential equation:

$$dx = -\frac{c_2 r^2 + c_3}{\sqrt{1-(c_2 r^2 + c_3)^2}}dr \tag{2.16}$$

with:

$$c_2 = \frac{p \sin \frac{2\pi}{n}}{2\sigma s} \tag{2.17}$$

$$c_3 = \frac{F_t}{n\sigma s} \tag{2.18}$$

Given a pressure p and traction F_t, as a consequence of equation (2.13), c_2 and c_3 are constant. Finally, the differential equation (2.16) can be integrated from $x = 0$ to $x(r)$, in order to determine the shape of the curved fibres with each pressure level p and traction F_t. This integration is not straightforward but has been analytically described by Daerden. Only the solution is repeated here, a detailed discussion can be found in [Daerden, 1999].

For the analytical solution two new constants, m and φ_R were introduced. These relate to c_2 and c_3 as follows:

$$c_2 = 2m\frac{\cos^2 \varphi_R}{R^2} \tag{2.19}$$

$$c_3 = 1 - 2m \tag{2.20}$$

and their values are bounded as $(0 \leq m \leq 1/2)$ and $(0 \leq \varphi_R \leq \pi/2)$. The symbol R represents the unpressurized muscle radius.

Defining the muscle contraction ϵ as:

$$\epsilon = 1 - \frac{2x_0}{l_0} \tag{2.21}$$

and after introducing the running coordinate φ, the shape of the longitudinal fibres, at contraction ϵ, can be found from the following set of equations:

$$x = \frac{R}{\sqrt{m}\cos\varphi_R}\left(E\left(\varphi \setminus m\right) - \frac{1}{2}F\left(\varphi \setminus m\right)\right) \qquad 0 \leq \varphi \leq \varphi_R \tag{2.22}$$

$$r = \frac{R}{\cos\varphi_R}\cos\varphi \qquad 0 \leq \varphi \leq \varphi_R \tag{2.23}$$

$$\frac{E\left(\varphi_R \setminus m\right) - \frac{1}{2}F\left(\varphi_R \setminus m\right)}{\sqrt{m}\cos\varphi_R} = \frac{l_0}{2R}\left(1 - \epsilon\right) \tag{2.24}$$

$$\frac{F\left(\varphi_R \setminus m\right)}{\sqrt{m}\cos\varphi_R} = \frac{l_0}{R} \tag{2.25}$$

with $E\left(\varphi \setminus m\right)$ and $F\left(\varphi \setminus m\right)$ elliptical integrals of the first and second kind.

For each contraction ϵ, a combination of the constants m and φ_R have to be calculated from equations (2.24) and (2.25). With these values, equations (2.22) and (2.23) fully characterize the shape $x(\varphi)-r(\varphi)$ of the fibres at each contraction. From this set of equations, valid only with the assumption of inelastic fibres, it is seen that the solution is characterized by the muscle slenderness l_0/R. At this point there is no difference with the solution of Daerden, the shape at which the longitudinal fibres position at each contraction ϵ is the same. The difference arises when expressing the force generated with each contraction. This force is dependent on the number of fibres as is shown in the next section.

2.2.3 Characteristic of the PPAM

Daerden [1999] extensively discusses several characteristics concerning the PPAM, for inelastic as well as elastic membranes. Hereby giving for each contraction the characteristics of the membrane shape, muscle traction, enclosed volume, maximum muscle diameter, and fibre stress and strain values. In this work mainly two characteristics are important: generated traction and enclosed volume for each contraction. The first is used for joint torque dimensioning and control purposes, while the latter is incorporated in the simulation models, used to evaluate the controller designs (chapters 3 and 5), and to predict joint compliance with closed muscles (chapter 3). Furthermore, maximum stresses generated in the kevlar fibres and maximum diameter when the muscle is fully bulged should be taken into account. The first is required to dimension the thickness of the kevlar yarn used for the muscles, the second information should be considered when designing the different joints of the robot in order to provide enough space for the muscle to bulge.

To determine the traction characteristics, equations (2.17) and (2.18) are combined with the parameter transformations (2.19) and (2.20):

$$F_t = n\sigma s c_3 = pn\sin\left(\frac{2\pi}{n}\right)\frac{c_3}{2c_2} = pn\sin\left(\frac{2\pi}{n}\right)\frac{(1-2m)\,R^2}{4m\cos^2\varphi_R} \tag{2.26}$$

And using equation (2.24) gives:

$$F_t = pn\sin\left(\frac{2\pi}{n}\right)l_0^2\frac{(1-2m)\,(1-\epsilon)^2}{16\left[E\left(\varphi_R\setminus m\right)-\frac{1}{2}F\left(\varphi_R\setminus m\right)\right]^2} \tag{2.27}$$

$$= p\frac{n}{2\pi}\sin\left(\frac{2\pi}{n}\right)l_0^2 f\left(\epsilon,\frac{l_0}{R}\right) \tag{2.28}$$

with $f\left(\epsilon,\frac{l_0}{R}\right)$ the dimensionless force function as defined by Daerden [1999]. Expression (2.28) shows the difference between the current model and the one of Daerden, namely a term $\frac{n}{2\pi}\sin\frac{2\pi}{n}$ appears. This term lowers the generated traction compared to the model of Daerden when the number of fibres is decreased. When increasing the number of fibres, the difference between the traction models becomes smaller. As the number of used fibres (n) increase to infinity, the model should corresponds to the case of a closed circular membrane, as was assumed by Daerden:

$$\lim_{n\to\infty} \frac{n}{2\pi} \sin \frac{2\pi}{n} = 1 \tag{2.29}$$

Thus the two models are the same for large numbers of discrete fibres. The limit in equation 2.29 converges fast to 1, if the number of used fibres is greater then 15 the difference between the two models is less then 3 %. Generally, if the number of fibres is large enough, the generated muscle force depends on the applied gauge pressure (p), the contraction (ϵ) and the two parameters, initial muscle length (l_0) and slenderness ($\frac{l_0}{R}$). The latter two are important during the joint design process, where these parameters are chosen as a function of the desired joint torque characteristics.

For the mathematical description of the enclosed volume, the pleated polyester membrane is approximated by considering at each parallel section a circular membrane pattern instead of the pleated structure. These calculations are identical as in the work of Daerden [1999] and resulted in the following expression:

$$V = l_0^3 v \left(\epsilon, \frac{l_0}{R}\right) \tag{2.30}$$

with v a dimensionless function of the contraction and the slenderness only.

Using equations (2.18) and (2.20), stress in the fibres can be related to the traction F_t as follows:

$$\sigma = \frac{F_t}{nsc_3} = \frac{1}{ns}\frac{F_t}{1-2m} = \frac{1}{ns}\zeta\left(\epsilon\right) \tag{2.31}$$

The parameter m has a minimum value, $m = 0$, at zero contraction and varies to $m = 0.5$ at maximum contraction.

The muscles largest diameter at each contraction ($2r_0$) is obtained with equation (2.23) while substituting $\varphi = 0$ [Daerden, 1999]:

$$D = 2r_0 = \frac{2R}{cos\varphi_R} = l_0 d \left(\epsilon, \frac{l_0}{R}\right) \tag{2.32}$$

For the practical realization of the robot identical muscles are used in order to simplify the robot's construction process by having a modular structure. The specific muscles have a physical membrane length $l_0 = 110$ mm and an unpressurized radius $R = 11.5$ mm for the position of the Kevlar fibres and a radius of 16 mm at the top of the polyester fabric pleats. These specific dimensions result from the standard tools used for the fabrication of the muscles, and the unloaded radius takes into account the dimensions of the pressure sensor which is positioned inside the muscle. The muscle used for the biped is constructed with 40 aligned fibre yarns. The extra term (2.29), distinguishing this specific force model, is 0.996 for this number of fibres. So the predicted forces generated by this muscle are almost

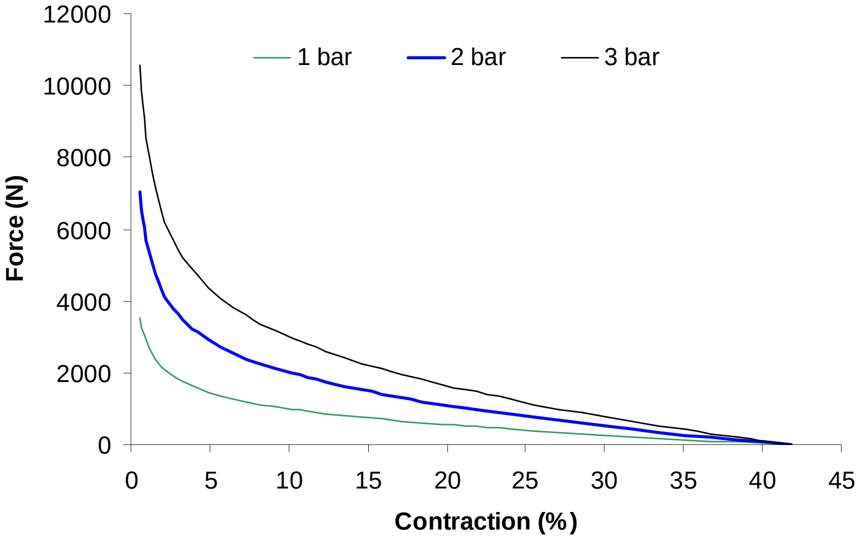

Figure 2.13: Theoretical forces at pressure levels 1, 2 and 3 bar as a function of contraction

identical for both models. Using $l_0 = 110\,\mathrm{mm}$, $R = 11.5\,\mathrm{mm}$ and $n = 40$ in equation (2.28), results in the force characteristics depicted in figure 2.13. The traction as a function of contraction is drawn for different applied gauge pressures: 1, 2 and 3 bar. The graph shows the nonlinear character of the generated muscle force. For small contractions, the forces are extremely high, while for large contractions, the forces drop to zero. For the practical robot application, contractions will be bounded somewhere between 5 and 35 %. The first limit is set to bound the stresses on the fibres and consequently extend the lifetime of the muscle. And beyond 35 % contraction, forces drop too low to be of practical use. In figure 2.14 the volume characteristic is given for the considered muscle dimensions. The volume ranges from a dead volume of approximately 100 ml at zero contraction to a volume of about 400 ml at maximum contraction. To the dead volume, the volumes of the end fittings and tubing should be added. Figure 2.15 depicts this diameter to contraction for the considered muscle. The maximum diameter when the muscle is fully bulged equals approximately the initial muscle length ($l_0 = 110\,\mathrm{mm}$). This approximated maximum diameter is used to find the initial diameter of the cylindrical polyester muscle membrane and it should be taken into account during the design of the joints of the robot in order to provide enough space for the muscle to bulge. In figure 2.16 the function $\zeta(\epsilon)$ which relates F_t to σ for the considered muscle is given. Although traction tends to zero at large contraction, stresses in the fibres always remain. The fibre section s is dimensioned at 5 % contraction at 3 bar.

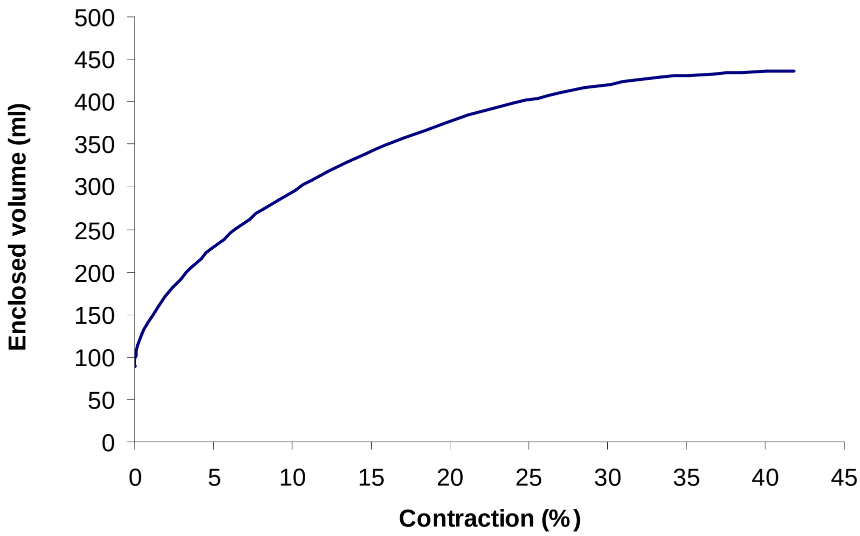

Figure 2.14: Theoretical enclosed muscle volume as a function of contraction

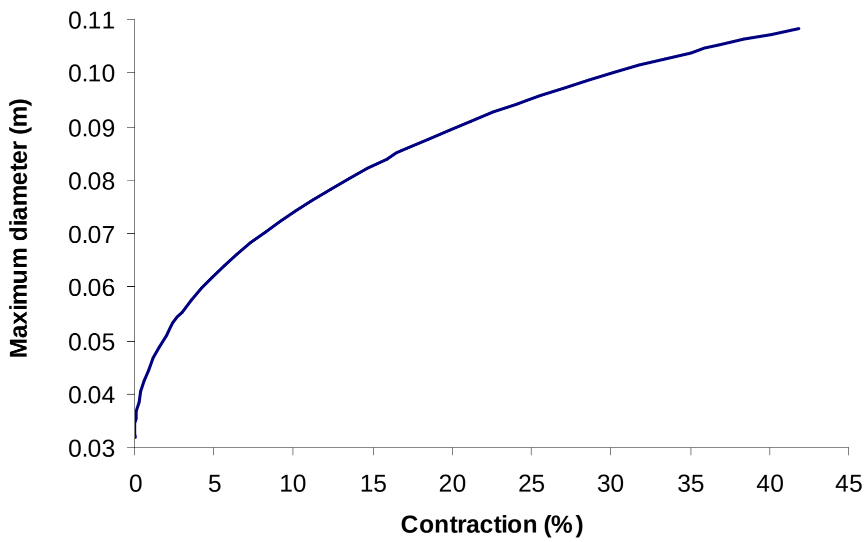

Figure 2.15: Theoretical maximum muscle diameter as a function of contraction

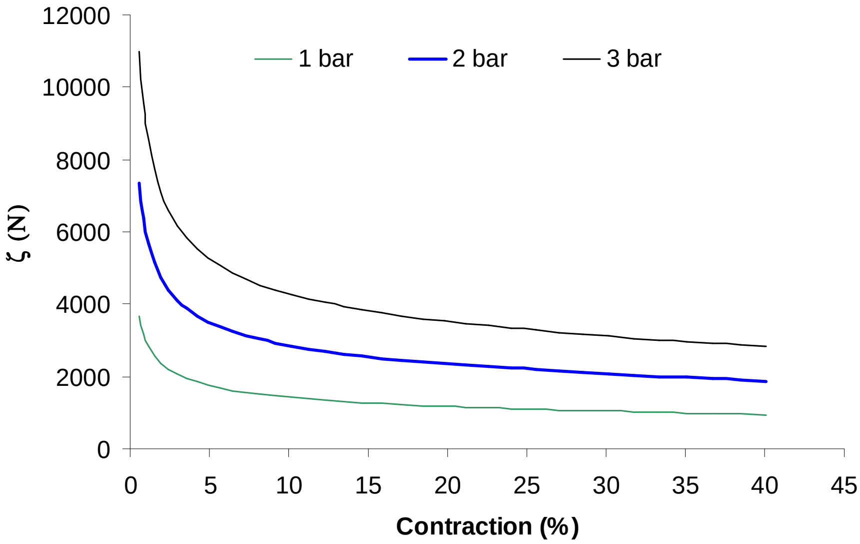

Figure 2.16: Theoretical function $\zeta(\epsilon)$, which relates F_t to σ, as a function of contraction

2.3 Static load tests

As was done by Daerden [1999], static load tests on real muscles are carried out to validate the proposed mathematical model of equation (2.28). Three different muscles are tested with an Intron test bench (model 4505) at isobaric conditions, while applying three different gauge pressures: 1, 2 and 3 bar. The forces are recorded with a load cell of 10 kN (accuracy $\pm 0.05\%$) and the pressure inside the muscle is regulated with a Kolvenbach pressure servo-valve, KPS3/4. In order to increase accuracy, the pressure inside the muscle is separately measured with a silicon gauge pressure sensor, XCA5-60GN, from Data Instruments (accuracy $\pm 0.5\%$ of 60 psi span). This sensor is placed as close as possible to the inlet of the muscle. One side of the muscle is fixed to the load cell, while the other side is attached to a movable frame. The tests are performed by changing the displacement of this frame. During each test, frame position, muscle force and applied gauge pressure are recorded.

For each test, the voltage controlling the servo-valve is set at the beginning of each run to regulate the pressure in the muscle for a constant level. Subsequently, the moving part of the test bench displaces in such a way that the generated force of the muscle ranges between 100 N and 3000 N, hereby following a slow sine-wave path of 0.005 Hz such that the pressure is stabilized at each measurement. Figure 2.17 gives the results of these tests by depicting force as a function of contraction for each of the three muscles at the three different gauge pressures. Although the muscles

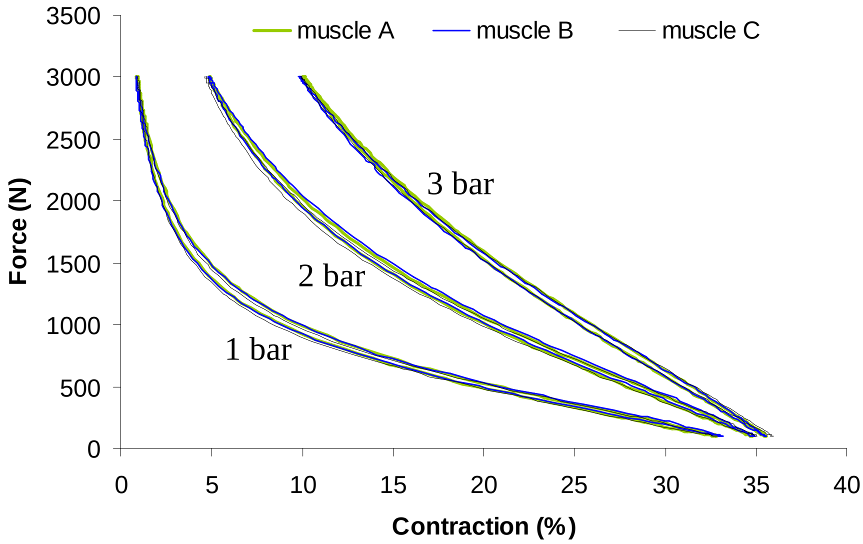

Figure 2.17: Measured forces as a function of contraction for three muscles at pressure levels 1, 2 and 3 bar

are handmade, the repeatability seems satisfactory. On the graph, an un-modelled hysteresis effect on the actual force as a function of contraction curve is noticed. Figure 2.18 gives a detailed view of the hysteresis and the displacement direction information for the case of 1 bar gauge pressure. It is seen that the different curves show a more or less comparable hysteresis width. Due to the pressure regulating valve, the actual pressure during each test run is not exactly the same. To overcome this, it is better to compare the test results by dividing the measured forces by the measured pressures. Figure 2.19 shows all the pressure scaled measurements together with estimated theoretical force functions of equation (2.28). These two theoretical graphs are calculated with $R = 11.5$ mm and $R = 16$ mm respectively. The first compares to the actual radius at which the Kevlar fibres are positioned during construction of the muscles. The radius equal to 16 mm corresponds to the radius of the top of the pleats, which is the same as the outer radius of the enclosed volume at the aluminium end fittings. It is seen that the theoretical model with $R = 11.5$ mm does not fit the measured data, while the other graph with $R = 16$ mm is much more suited to represent the actual generated force. Since the epoxy resin reaches to only about a centimeter away from the edge of the end fitting, the Kevlar fibres tend to be positioned at the outer radius of the aluminium basin, immediately after the muscle is pressurized. At all contractions the fibres at the end fittings stay at this radius, as if the initial radius was $R = 16$ mm. This explains why the theoretical function with the larger radius fits the measured data much better. For full bulging of the muscle the initial diameter of the cylindrical polyester membrane should be taken higher then the initial length of the muscle

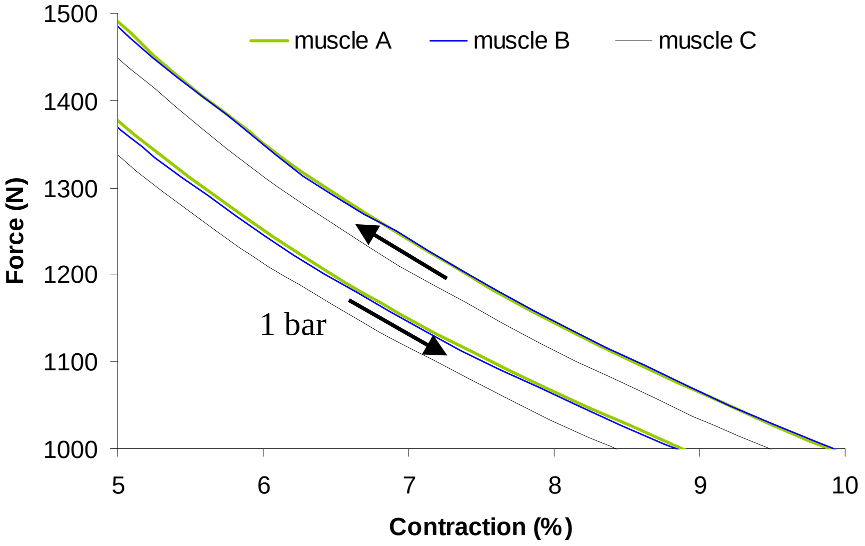

Figure 2.18: Detailed view of measured forces as a function of contraction for three muscles at pressure level 1 bar

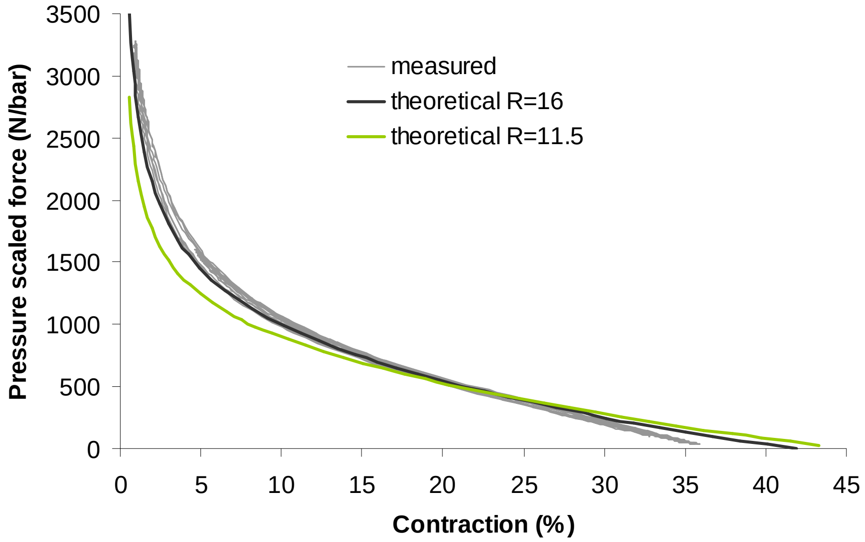

Figure 2.19: Pressure scaled measured forces as a function of contraction compared with theoretical model

(figure 2.15). But it has been observed, for a muscle with not fully unfolded pleats at maximum contraction, that the unfolding process is less regular as with the previous muscle design. So the initial diameter of the cylindrical polyester tube is taken smaller. Consequently, the muscle can not fully bulge and at certain contraction level, radial stresses in the polyester membrane start influencing the traction characteristic. This explains why the theoretical model deviates from the measured data (see figure 2.19) at large contractions.

The approximation of the real force with the theoretical model is sufficient enough such that it can be used for dimensioning purposes. An accurate estimation of the force function however is also required for a feedforward joint tracking control structure. Since the force functions of the different muscles are very similar, a polynomial function fit on the pressure scaled measured data is performed in order to achieve a better force estimation. The nonlinear nature of the force function attains extremely large values at small contractions, therefore it is more suitable to perform a polynomial fit on the scaled force function multiplied with contraction. This lowers after all the extreme values at small contractions. A 4th order polynomial fit on these data is performed. With the incorporation of pressure p and the square of the initial muscle length l_0^2, as was described by the theoretical model, the polynomial fit of the force function can be expressed as:

$$F_t = pl_0^2 f(\epsilon) = pl_0^2 \left(f_4\epsilon^3 + f_3\epsilon^2 + f_2\epsilon + f_1 + f_0\epsilon^{-1}\right) \tag{2.33}$$

with f_0 to f_4 the 5 coefficients resulting from a 4th order polynomial approximation. Figure 2.20 shows all the pressure scaled force measurements in comparison with the estimated force function. This polynomial force function is used by a feedforward control structure, of which a detailed discussion is found in chapter 4. With such a control structure, it is important to evaluate the influence of possible estimation errors, due to hysteresis and repeatability, on the control performance. The control performance evaluation is done with a full hybrid simulation model of the robot as is discussed in chapter 5. Therefore, figure 2.21 shows a detailed picture of the force estimation, compared to the force measurements of one muscle, and depicts the relative error between measurement and estimation. It is seen that a substantial error is present due to the hysteresis. When evaluating the proposed control structure on its robustness by means of the simulation model in chapter 5, roughly, an error of $\pm 5\%$ on the estimated force function is taken into account. The coefficients of the fitting process for the force function, following the structure of equation (2.33), are given in table (2.1). The values are valid when the generated force F_t is expressed in N, the initial muscle length l_0 in m, the pressure expressed in bar and the contraction ϵ expressed in %.

Finally, for the same simulation purposes, a polynomial fitting is performed on the theoretical data for the enclosed muscle volume depicted in figure 2.14:

$$V(\epsilon) = l_0^3 v(\epsilon) = l_0^3 \left(v_5\epsilon^5 + v_4\epsilon^4 + v_3\epsilon^3 + v_2\epsilon^2 + v_1\epsilon + v_0\right) \tag{2.34}$$

with v_0 to v_5 the 6 coefficients resulting from a 5th order polynomial approxima-

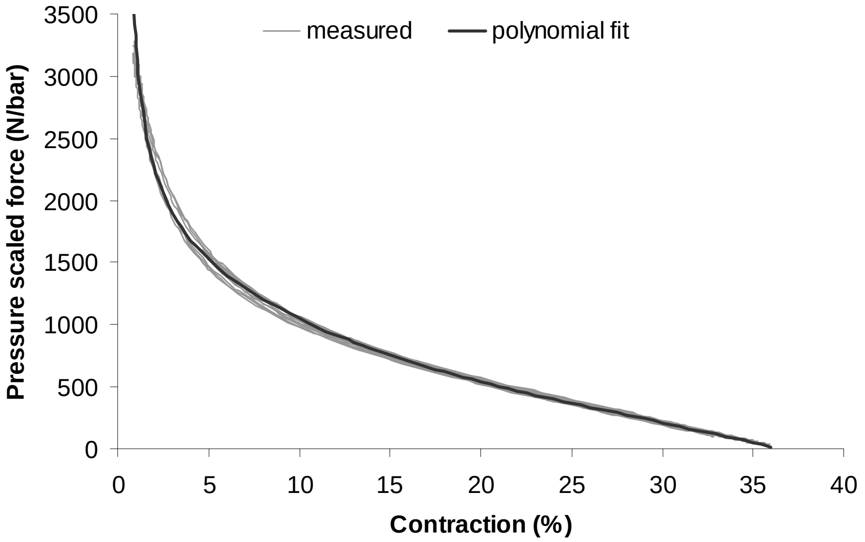

Figure 2.20: Pressure scaled measured forces as a function of contraction compared with polynomial fitted estimation

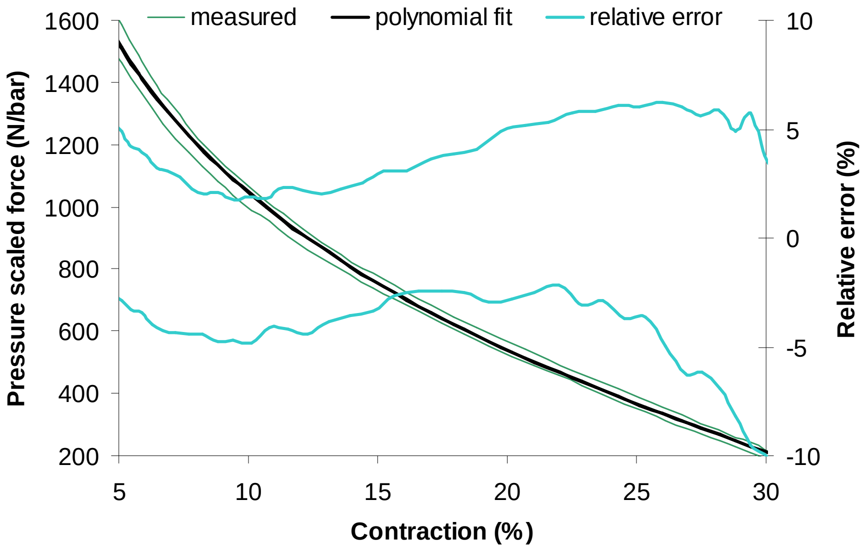

Figure 2.21: Scaled measured forces as a function of contraction compared with polynomial fitted estimation and the relative error given for one muscle

f_4	f_3	f_2	f_1	f_0
−2.0413	171.623	−7178.93	128611.6	146099

Table 2.1: Coefficients of the polynomial force function approximation

v_5	v_4	v_3	v_2	v_1	v_0
0.02254	−2.6296	113.82	−2386.3	30080	71728

Table 2.2: Coefficients of the polynomial volume function fitting

tion. Equation (2.34) is much easier to handle than the numerical solution derived from the mathematical model represented by expression (2.30). In table 2.2 the coefficients of the volume fitting, following equation (2.34), are given. The values are valid for the volume given in ml, the initial length expressed in m and the contraction ϵ expressed in %. The data in table 2.1 and 2.2, together with equations (2.33) and (2.34), can also be used to generate an approximation of the force and volume characteristics for muscles with lengths different from $l_0 = 110\,\text{mm}$. But the values in these tables are only valid for muscles with a specific slenderness ($l_0/R = 110/16 = 6.9$), as is explained by the theoretical model with equations (2.30) and (2.28). So, whenever the polynomial fitting is used for a muscle with different initial length, the unloaded radius of that muscle has to be adapted, otherwise the force and volume approximations are not valid.

2.4 Summary

In this chapter the pleated pneumatic artificial muscle, as designed by Daerden was introduced. This type of artificial was developed to overcome dry friction and material deformation which is present in the widely used McKibben type of artificial muscle. The essence of the PPAM is its pleated membrane structure which enables the muscle to work at low pressures and at large contractions. In order to deal with some limitations of the PPAM design of Daerden, a second generation of PPAM was proposed. A redesign of the pleated membrane structure resulted in a much higher muscle lifespan which is an essential property if the muscle is used for an elaborate experimental setup, such as a biped. Additionally, some changes made to the end fitting design simplified machining of the muscle and provided possible reuse of some muscle parts.

The new membrane layout differs from the previous design mainly due to usage of a discrete number of high tensile fibres instead of a complete high tensile stiff fabric. Therefore the mathematical model of the muscle, introduced by Daerden, was reformulated. This model describes the shape of the muscle bulging at each contraction, and gives essential characteristics such as muscle traction, enclosed volume, maximum diameter and tension in the fibres. The difference in the adapted mathematical model is seen in the formulation for the generated muscle force, which becomes dependent on the discrete number of high tensile fibres used to contract the muscle. Several graphs depicting the essential characteristic of the muscle used for the biped "Lucy" have been given. This clearly showed the nonlinear character of the force generation, which has extreme high values at low contractions and almost zero values at full bulging.

In order to validate the theoretical traction function with the real force generation of the muscle used for "Lucy", static load test on this specific muscle were carried out. It was found that the mathematical model gives a good approximation for the force function such that it can be used for dimensioning purposes. Since the generated force function will also be used in a feedforward control structure, a polynomial fit on the measured force data was carried out to have a more accurate force estimate. Due to a hysteresis on the muscle force function, a substantial approximation error up to $\pm 5\,\%$ is made with the polynomial force estimation function. This error is taken into account in chapter 5, which handles a simulation model built to evaluate the robustness of the biped's control strategy developed in chapter 4.

Chapter 3

Basic study of a one-dimensional joint setup

3.1 Introduction

Pneumatic artificial muscles can only exert a pulling force. In order to have a bidirectionally working revolute joint, two muscles are coupled antagonistically as is depicted in figure 3.1. While one muscle contracts and rotates the joint in its direction, the other muscle will elongate. The gauge pressure difference between the two muscles determines the generated torque (T), and consequently also angular position (θ). Furthermore, both pressures can be increased (decreased) in such a

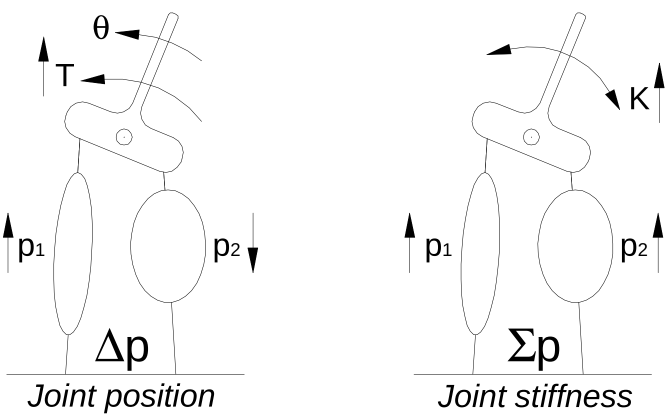

Figure 3.1: Controlling position and stiffness in an antagonistic muscle setup

way that joint stiffness (K) raises (lowers) without affecting angular position. Thus both position and compliance can be controlled independently.

Many research groups investigated different control strategies for such a one-dimensional antagonistic setup. E.g. Daerden et al. [1999], and Tondu et al. [1994], used linear control techniques and defined an open loop control to be able to exploit compliance and switched to closed loop techniques to perform accurate position control. In the Netherlands van der Linde [1999] focussed on inverted pendulum motion with compliance adaptation by varying equal pressures in both muscles. Kawashima et al. [2004], and Pomiers [2003], used a cascade of several standard PID control stages and Schröder et al. [2003] combined a muscle actuator model with these linear control techniques to enhance position control. Analogously, Albiez et al. [2003] incorporated a muscle force model with PID position feedback to regulate joint stiffness. Caldwell et al. [1995] applied adaptive control techniques using a polynomial estimation model of the complete joint muscle/valve system. Hesselroth et al. [1994] used feedforward neural net control and Mattiazzo et al. [1998], and Raparelli et al. [2001], introduced fuzzy control techniques. Carbonell et al. [2001] compared, through simulations, several nonlinear control techniques including sliding-mode control.

As in van der Linde [2001] and Wisse [2004], this work is not trying to incorporate explicit force control, but aims at exploiting natural dynamics by adapting joint stiffness, and specifically in combination with trajectory tracking. The developed position control incorporates modularity, which means that it can be easily adapted for different multi-joint configurations. Therefore a multilevel controller was constructed which allows to deal with the different system nonlinearities separately. One level handles the nonlinear behaviour of the robot dynamics, followed by a control level which incorporates the nonlinear joint characteristics. Finally, at pressure level the controller design allows to exploit natural dynamics.

In this chapter fundamental aspects concerning a one-dimensional joint setup are discussed. The focus lies on simulations which are used to clarify the concept of exploiting natural dynamics by compliance adaptation. In section 3.2, the kinematic relations, linking the generated joint to the applied muscle forces, are given. These are required for dimensioning purposes, but are also used in the design of the tracking controller. Section 3.3 describes the adaptability of the passive behaviour which can be exploited to influence natural dynamics as will be discussed in section 3.4. A simulation model of a basic leg configuration with one antagonistic muscle pair actuating the knee joint is presented in section 3.5. This model is used to show the importance of appropriate stiffness selection in order to reduce control activity. A joint tracking controller, that forms the basis for the tracking controller design of the complete biped, is incorporated in the simulation model. Section 3.5.4 discusses two simulation results which clearly demonstrate the influence of adapted compliance, for which a basic mathematical formulation is given in section 3.6. Finally, some energy considerations concerning the proposed control strategy are given in section 3.7.

3.2 Kinematics of a revolute joint

In order to have a bidirectionally working revolute joint, two muscles are coupled antagonistically as was shown in figure 3.1. In fact only one muscle e.g. in combination with a mechanical return spring could be used, but in order to be able to control joint compliance, this option is not chosen (see section 3.3). The antagonistic coupling of two muscles could be achieved with either a pulley mechanism or a pull rod and leverage mechanism. The latter is chosen since the lever arm can be varied such that the highly nonlinear force-length characteristic of the PPAM is transformed to a more flattened torque-angle relation. The basic configuration of the pull rod and leverage mechanism is depicted in figure 3.2. Two muscles, muscle

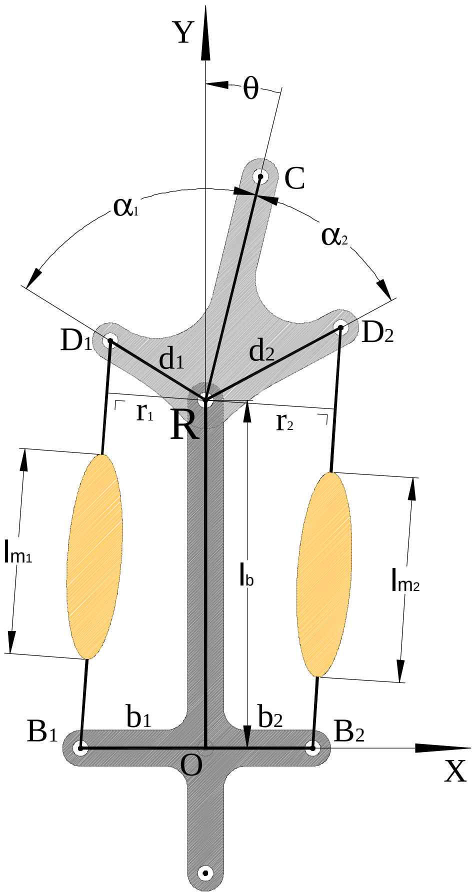

Figure 3.2: Schematic overview of the antagonistic muscle pull rod system

1 and 2, are connected at one side of the system to a fixed base in the points B_1

and B_2 respectively. The other ends of the muscles are attached to a pivoting part at the points D_1 and D_2, of which the rotation axis passes through a point R. The rods are assumed to be rigid.

To determine the kinematic expressions of the joint system, an orthogonal X, Y-coordinate system is defined. The X-axis is aligned with the base points B_1 and B_2, while the vertical Y-axis intersects the physical pivoting point R and lies along the base suspension bar of the pull rod mechanism. The essential parameters to be determined during the design process of the joint are the following:

- b_i is the distance between the origin O and the point B_i.
- d_i is the distance between the pivoting point R and the point D_i.
- α_i is the angle between the vector $\overline{RD_i}$ and $\overline{RC}$, with C a point on the rotating part. (α_i is not oriented and always positive)
- l_{m_i} is the actual length of muscle i
- l_b is the length of the base suspension bar, measured between the origin O and the pivot point R.
- θ represents the rotation angle, measured between $\overline{RC}$ and the Y-axis. (θ is oriented, counter-clockwise is positive)

Combining equation (2.28) with r_1 and r_2, which define the orthogonal leverage arms of muscles 1 and 2 respectively, the joint torque is given by following expression:

$$\begin{aligned} T(\theta) = T_1(\theta) - T_2(\theta) &= p_1 l_{0_1}^2 r_1(\theta) f_1(\theta) - p_2 l_{0_2}^2 r_2(\theta) f_2(\theta) && (3.1) \\ &= p_1 t_1(\theta) - p_2 t_2(\theta) && (3.2) \end{aligned}$$

with $T_i(\theta)$ the torque generated by muscle i and p_i the applied gauge pressure in the respective muscle with initial unpressurized length l_{0_i}. The dimensionless force functions $f_i(\theta)$ are determined by the mathematical model (2.28) or with the polynomial function (2.33) fitted on the measured force data. Note that equation (3.2) is valid in case that the inertial properties of muscle membrane and attachments are neglected. The torque functions $t_1(\theta)$ and $t_2(\theta)$, in equation (3.2), are determined during the design phase and depend on the angular position of the joint.
The vectors $\overline{B_i D_i}$ and $\overline{RD_i}$ are expressed in the proposed coordinate system as follows:

$$\overline{B_1 D_1} = [b_1 - d_1 \sin(\alpha_1 - \theta), l_b + d_1 \cos(\alpha_1 - \theta)] \quad (3.3)$$

$$\overline{B_2 D_2} = [d_2 \sin(\alpha_2 + \theta) - b_2, l_b + d_2 \cos(\alpha_2 + \theta)] \quad (3.4)$$

$$\overline{RD_1} = [-d_1 \sin(\alpha_1 - \theta), d_1 \cos(\alpha_1 - \theta)] \quad (3.5)$$

$$\overline{RD}_2 = \left[d_2 \sin\left(\alpha_2 + \theta\right), d_2 \cos\left(\alpha_2 + \theta\right)\right] \tag{3.6}$$

The expression for $r_i\left(\theta\right)$ can then be found as:

$$r_i\left(\theta\right) = \frac{\left|\overline{B_i D}_i \times \overline{RD}_i\right|}{\left|\overline{B_i D}_i\right|} \tag{3.7}$$

The muscle contraction ϵ_i relates to the rotation angle θ as:

$$\epsilon_i\left(\theta\right) = 1 - \frac{l_{m_i}}{l_{0_i}} = \epsilon_i^c + \frac{l_{m_i}^c - l_{m_i}}{l_{0_i}} = \epsilon_i^c + \frac{|\overline{B_i D}_i^c| - |\overline{B_i D}_i|}{l_{0_i}} \tag{3.8}$$

The contraction $\epsilon_i\left(\theta\right)$ is defined with respect to ϵ_i^c, which is the contraction of muscle i at a chosen central position θ^c. The parameters ϵ_i^c and θ^c are fixed during the joint design process.

Equations (3.1) to (3.6), in combination with the muscle force function (2.28) or (2.33), are used to design the characteristics of the joints for "Lucy" and are incorporated in the joint tracking control structure. These parameters determine torque characteristics and angle range. Important are not only the generated torque levels, but also the specific shape of the torque characteristics, which influences joint stiffness and consequently passive behaviour. The joint range is determined via the two angle as a function of contraction relations and the minimum and maximum contraction of the muscles. Angle range and torque characteristics are determined as a function of the specific joint application. The design of all these functionalities is complex and is linked to the specific motion of the robot. In chapter 6 a discussion is given concerning this dimensioning process. An important conclusion of this section is that joint angular position is influenced by weighted differences in gauge pressures of both muscles of an antagonistic setup.

3.3 Adaptable passive behaviour of a revolute joint

A PPAM has two sources of compliance, being gas compressibility, and the dropping force to contraction characteristic [Daerden, 1999]. The latter effect is typical for pneumatic artificial muscles while the first is similar to standard pneumatic cylinders. Joint stiffness, the inverse of compliance, for the considered revolute joint, can be obtained by the angular derivative of the torque characteristic in equation (3.2):

$$\begin{aligned} K &= \frac{dT}{d\theta} = \frac{dT_1}{d\theta} - \frac{dT_2}{d\theta} \\ &= \frac{dp_1}{d\theta} t_1 + p_1 \frac{dt_1}{d\theta} - \frac{dp_2}{d\theta} t_2 - p_2 \frac{dt_2}{d\theta} \end{aligned} \tag{3.9}$$

The terms $dp_i/d\theta$ represent the share in stiffness of changing pressure with contraction, which is determined by the action of the valves controlling the joint and by the thermodynamic processes taking place. If the valves are closed and if we assume polytropic compression/expansion, the pressure changes inside a muscle are a function of volume changes [Rogers and Mayhew, 1992]:

$$P_i V_i^n = P_{i_o} V_{i_o}^n \tag{3.10}$$

with:

$$P_i = P_{atm} + p_i \tag{3.11}$$

leading to:

$$\frac{dp_i}{d\theta} = -n\left(P_{atm} + p_{i_o}\right)\frac{V_{i_o}^n}{V_i^{n+1}}\frac{dV_i}{d\theta} \tag{3.12}$$

With P_i, V_i the absolute pressure and volume of muscle i, P_{i_o} the absolute initial pressure, V_{i_o} the initial volume when the valves of muscle i were closed, p_i and p_{i_o} the gauge pressure and initial gauge pressure respectively, P_{atm} the atmospheric pressure and n is a polytropic exponent. The value of the latter should be experimentally estimated and may depend on the specific process. The polytropic exponent is introduced to describe deviations from the isentropic expansion/compression. An isentropic process assumes reversible adiabatic thermodynamic conditions and the exponent in equation 3.10 becomes in this case $n = \gamma = c_p/c_v = 1.4$ for dry air [Rogers and Mayhew, 1992].

During the joint design process, it is ensured that the torque to angle and the volume to angle characteristics of a joint are monotonous functions. Meaning that the derivatives $dt_i/d\theta$ and $dV_i/d\theta$ keep the same sign within the range of motion for which the joint was designed. Thus, referring to figure 3.2, it can be understood that the torque function $t_1(\theta)$ is increasing with increasing joint angle θ, while its volume is decreasing. Indeed the larger θ, the lesser muscle 1 is contracted and consequently the generated force is bigger. On the contrary, less contraction means that the muscle gets thinner and that volume decreases. Thus $dt_1/d\theta > 0$ and $dV_1/d\theta < 0$. For the other muscle 2 in the antagonistic setup, the actions are opposite: $dt_2/d\theta < 0$ and $dV_2/d\theta > 0$. Combining equation (3.9), (3.10) and (3.12) with this information gives:

$$K = k_1(\theta)\, p_{1_o} + k_2(\theta)\, p_{2_o} + k_{atm}(\theta)\, P_{atm} \tag{3.13}$$

with:

$$\begin{aligned}
k_1(\theta) &= t_1(\theta)\, n \frac{V_{1_o}^n}{V_1^{n+1}} \left|\frac{dV_1}{d\theta}\right| + \frac{V_{1_o}^n}{V_1^n}\left|\frac{dt_1}{d\theta}\right| && > 0 \\
k_2(\theta) &= t_2(\theta)\, n \frac{V_{2_o}^n}{V_2^{n+1}} \left|\frac{dV_2}{d\theta}\right| + \frac{V_{2_o}^n}{V_2^n}\left|\frac{dt_2}{d\theta}\right| && > 0 \\
k_{atm}(\theta) &= k_1(\theta) + k_2(\theta) - \left|\frac{dt_1}{d\theta}\right| - \left|\frac{dt_2}{d\theta}\right|
\end{aligned}$$

The coefficients $k_1(\theta)$, $k_2(\theta)$, $k_{atm}(\theta)$ are determined by the geometry of the joint and its muscles.

From equation (3.13) the conclusion is drawn that closed muscles in an antagonistic joint setup create a passive spring element with an adaptable stiffness which is controlled by a weighted sum of both initial gauge pressures, i.e. when closing the muscles. Since stiffness depends on a sum of gauge pressures while position is determined by differences in gauge pressure, the angular position can be controlled while setting stiffness.

3.4 Exploiting natural system dynamics

As was mentioned in chapter 1, natural or passive dynamics is the unforced response of a system under a set of initial conditions. In fact, a pseudo-periodic movement of the different robotic limbs, caused by inertial forces and a gravity field, can be exploited such that energy consumption and control activity is decreased. An extreme example of such a system is a "Passive Walker", which doesn't require any other actuation than gravity. The inertial properties are determined in such a way that the system walks down a sloped surface. To enhance the performance of such robots, actuators are added. This however can disturb the exploitation of passive dynamics, since controlling actuated joints generally makes the joints stiffer [Pratt et al., 1995]. Thus, if exploitation of passive dynamics is combined with controlled actuation, special attention should be given to the implementation of the actuation system. Two interesting examples in this context, where actuation is combined with passive dynamics, have been created by Pratt and Pratt [1998] and Gregorio et al. [1997]. Both groups used a compliant element in series with a motor drive such that the motors are able to influence the passive motion resulting from the compliant element. Since the compliant element consists of a mechanical spring with constant compliance characteristics, the eigenfrequencies of the system are fixed. This limits the applicability of this type of actuation system for different periodic walking patterns.

Pneumatic artificial muscles have the possibility to adapt the stiffness while controlling position, as was shown in the previous sections. Exploitation of the natural dynamics by varying the compliance characteristics can be approached in two ways. A first option is to design a robot, taking into account all the inertial and compliance parameters, such that the system performs a motion close to walking without actuation, by making the system oscillate at its natural frequency. By controlling the joint compliance, the motion characteristics are then adapted. Concerning dynamic robot stability, this is however a complex task and will probably result in a small range of feasible motion patterns. A second approach is to design joint trajectories for a specific robot configuration, such that dynamic stability is ensured if these trajectories are tracked by a trajectory tracking controller. In order to reduce valve control activity, the joint trajectory tracking unit then adapts the

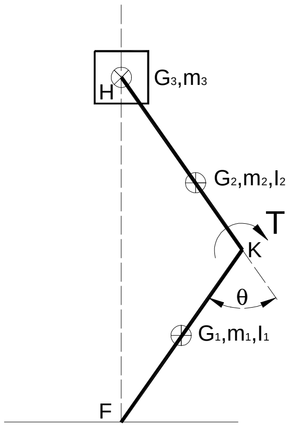

Figure 3.3: Schematic overview of the studied model

compliance of the different joints, so that the natural motion "best" fits the given trajectories. As a result the global stability is ensured due to the calculated trajectories, while energy consumption is lowered by adapting the joint compliances. But of course, setting the ranges in which the natural motion corresponds to the calculated trajectories, required for dynamic stability, asks for a proper design of all inertial and joint design parameters. So in the end, a combination of these two different approaches will give interesting results.

3.5 Trajectory control with adaptable compliance

In this section the proposed strategy of combining adaptable passive behaviour with trajectory control is illustrated. The effect on valve control activity and energy consumption by changing the compliance characteristics are shown on a simplified model of a leg by means of a simulation.

3.5.1 Description of the leg setup

The leg consists of three parts (fig. 3.3): lower leg, upper leg and upper body. The Hip (**H**) and Foot (**F**) are attached to a vertical slider and the body is modelled as a point mass. The knee (**K**) is powered by a joint mechanism as described in section 3.2. The length of the i-th link is l_i, its mass is m_i and the moment of inertia about its center of mass G_i is I_i. The location of the center of mass G_1 of the lower leg and G_2 of the upper leg are given by $FG_1 = \alpha l_1$, $KG_2 = \beta l_2$ with $0 < \alpha, \beta < 1$. For this simulation $\alpha = \beta = 0.5$. The parameter values are given in table 3.1

i	l_i (m)	m_i (kg)	I_i (kgm^2)
1	0.4	2	0.014
2	0.4	3.5	0.022
3	/	10	/

Table 3.1: Inertial parameters of the leg model

While the foot is in contact with the ground, this model has one degree of freedom (DOF) which is represented by the relative knee angle θ.

3.5.2 Simulation model

A prescribed motion is imposed on the knee joint and a joint tracking controller commands the pneumatic system to follow this trajectory. The controller has a specific architecture which allows the joint stiffness to be altered in order to exploit natural dynamics. The effect on the control activity is analyzed for different joint compliance settings. The strategy is illustrated by means of a simulation. The differential equations for this simulation are divided into two parts: a mechanical part representing the motion of the leg in the gravity field actuated by a knee torque T, and a pneumatic part describing the thermodynamic processes in the two muscle/valve systems. The motion is described by a second order differential equation. The pneumatics are described by four first order differential equations. Two equations determine the pressure changes in both muscles of the antagonistic setup and the remaining two describe conservation of mass in the respective muscle volumes. Additionally, in the assumption that the pressurized air in the muscles behaves as a perfect gas, the perfect gas law completes the set of equations, required to perform the simulation. The generated knee torque T links the mechanic model to the pneumatic model, and is given by equation (3.2).

Mechanics

If the joints are assumed to be frictionless, the equation of motion describing the movement of the leg due to the applied knee torque T is given by (appendix A):

$$D\big(\theta\big)\ddot{\theta} + C\big(\theta,\dot{\theta}\big)\dot{\theta} + G\big(\theta\big) = T \tag{3.14}$$

with:

$$\begin{aligned} D\big(\theta\big) = \frac{1}{4}\big[&I_1 + I_2 + m_1\alpha^2 l^2 + m_2\left(1+\beta^2\right) l^2 \\ &+ 2m_3 l^2 - 2l^2\left(m_2\beta + m_3\right)\cos\theta\big] \end{aligned} \tag{3.14a}$$

$$C\big(\theta,\dot{\theta}\big) = \frac{1}{4} l^2\left[\left(m_2\beta + m_3\right)\sin\theta\right]\dot{\theta} \tag{3.14b}$$

$$G(\theta) = -g\frac{l}{2}\left[\alpha m_1 + (1+\beta)\, m_2 + 2m_3\right]\sin\frac{\theta}{2} \tag{3.14c}$$

with l the length of upper and lower leg.

Thermodynamics

The pressure inside a muscle is influenced by its volume changes resulting from a variation of the joint angle and by the air flow through the valves. Assuming a polytropic thermodynamic process, and assuming that the compressed air inside each muscle behaves as a perfect gas, the first law of thermodynamics, while neglecting the fluid's kinetic and potential energy, can be written for each muscle of the antagonistic setup in the following differential form (appendix B):

$$\dot{p}_i = \frac{n}{V_i}\left(rT_{air}^{sup}\dot{m}_{air_i}^{in} - rT_{air_i}\dot{m}_{air_i}^{ex} - (P_{atm} + p_i)\,\dot{V}_i\right) \tag{3.15}$$

with r the dry air gas constant. T_{air}^{sup} is the temperature of the supply air and T_{air_i} the temperature in muscle i. The total orifice flow through the opened inlet valves and exhaust valves of muscle i are given by $\dot{m}_{air_i}^{in}$ and $\dot{m}_{air_i}^{ex}$ respectively. The latter two can be calculated with the following equations which represents a normalized approximation of a valve orifice flow defined by the International Standard ISO6358 [1989]:

$$\dot{m}_{air} = CP_u\rho_0\sqrt{\frac{293}{T_{air}^u}}\sqrt{1-\left(\frac{P_d/P_u - b}{1-b}\right)^2} \qquad \text{if} \qquad \frac{P_d}{P_u} \geq b \tag{3.16}$$

$$\dot{m}_{air} = CP_u\rho_0\sqrt{\frac{293}{T_{air}^u}} \qquad \text{if} \qquad \frac{P_d}{P_u} \leq b \tag{3.17}$$

with ρ_0 the air density at standard conditions. C and b are two flow constants characterizing the valve system. The constant C is associated with the amount of air flowing through the valve orifice, while b represents the critical pressure ratio at which orifice air flows become maximal. P_u and P_d are the upstream and downstream absolute pressures, while T_{air}^u is the upstream temperature. When choking occurs, equation (3.17) is valid, otherwise equation (3.16) is used.

The muscles are controlled by a number of fast switching on/off valves. More information on the valve system used for "Lucy" will be given in the next chapters. For this simulation one inlet and one exhaust valve is used. Once the actions (opening or closing) of the valves are known, all the air flows can be calculated in order to be substituted in (3.15). The temperature in the muscle is calculated with the perfect gas law:

$$T_{air_i} = \frac{P_iV_i}{m_{air_i}r} \tag{3.18}$$

with $P_i(= p_i + P_{atm})$ the absolute pressure in muscle i. The total air mass m_{air_i} is given by integration of the net mass flow entering muscle i:

$$\dot{m}_{air_i} = \dot{m}^{in}_{air_i} - \dot{m}^{ex}_{air_i} \tag{3.19}$$

The volumes and their time derivatives are given by kinematical expressions as a function of the joint angle and joint angular velocity. These functions are determined with the fitted polynomial volume function (2.34) and the link between contraction and joint angle, represented by the kinematic expression (3.8) of the pull rod system.

3.5.3 Joint trajectory tracking controller

The joint tracking controller has to command the valves of the two muscles in order to track an imposed desired trajectory. The complete system incorporates several nonlinearities such as the nonlinear behaviour of the robot configuration and the nonlinearities introduced by the antagonistic muscle setup. The tracking controller is designed in a modular way, which means that the controller can be easily adapted for an application with another mechanical configuration, but with an analogues antagonistic muscle actuator setup. Therefore, the controller is multistage, of which each stage deals with the different nonlinearities separately. A schematic overview of the proposed control structure is given in figure 3.4. The controller consists of three parts: a feedback linearization module, a delta-p unit and a bang-bang pressure controller. The feedback linearization module is a standard nonlinear control technique which deals with the nonlinear behaviour of the mechanical robot configuration (cfr. [Slotine and Li, 1991]). The delta-p unit translates calculated torques into desired muscle pressure levels, coping with the nonlinearities introduced by the muscle actuation system. Finally, the bang-bang pressure controller commands the valves in order to set the required pressures in the muscles.

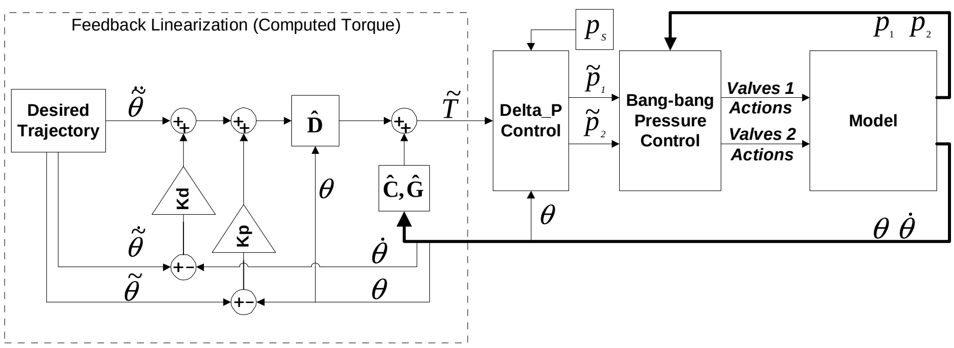

Figure 3.4: The applied joint trajectory tracking control scheme

In the first module, the computed torque $\tilde{T}$ is composed of the feedforward term $\hat{D}(\theta)\,\ddot{\tilde{\theta}}$, the centrifugal/gravitational compensation term $\hat{C}(\theta,\dot{\theta})\dot{\theta}+\hat{G}(\theta)$ and a proportional and derivative feedback part for which the gains K_p and K_d are tuned in order for the mechanical system to behave critically damped, in case the modelling would be perfect. The following expression is thus obtained:

$$\tilde{T} = \hat{C}(\theta,\dot{\theta})\dot{\theta} + \hat{G}(\theta) + \hat{D}(\theta)\left[\ddot{\tilde{\theta}} - K_d(\dot{\theta} - \dot{\tilde{\theta}}) - K_p(\theta - \tilde{\theta})\right] \tag{3.20}$$

The symbol ˜ represents required values, and the symbol ˆ denotes that the respective expressions are calculated with estimated parameter values.

The computed torque $\tilde{T}$ is then fed to the delta-p control unit, which calculates the required pressure values to be set in the muscles. These two gauge pressures are generated as follows:

$$\tilde{p}_1 = \frac{p_s}{\hat{t}_1(\theta)} + \Delta\tilde{p} \tag{3.21a}$$

$$\tilde{p}_2 = \frac{p_s}{\hat{t}_2(\theta)} - \Delta\tilde{p} \tag{3.21b}$$

with p_s a parameter that is used to influence the sum of pressures and consequently the joint stiffness, $\Delta\tilde{p}$ influences the difference in pressure of the two muscles in order to control the generated torque. The functions $\hat{t}_1(\theta)$ and $\hat{t}_2(\theta)$ represent the torque characteristics of the antagonistic muscle setup and are calculated with estimated values of the muscle force functions and geometrical parameters. Expression (3.2) allows to link the required torque to the required pressure values in the muscles:

$$\tilde{T} = \tilde{p}_1\hat{t}_1(\theta) - \tilde{p}_2\hat{t}_2(\theta) = \left(\hat{t}_1(\theta) + \hat{t}_2(\theta)\right)\Delta\tilde{p} \tag{3.22}$$

If the calculated pressure values $\tilde{p}_1$ and $\tilde{p}_2$ of equations (3.21) are set in the muscles, the generated torque depends only on $\Delta\tilde{p}$ and is independent of the joint stiffness parameter p_s, in case the modelling would be perfect. This means that joint stiffness is changed without affecting the joint angular position.

Feeding back the knee angle θ and introducing the torque $\tilde{T}$, expression (3.22) can be used to determine the required $\Delta\tilde{p}$:

$$\Delta\tilde{p} = \frac{\tilde{T}}{\hat{t}_1(\theta) + \hat{t}_2(\theta)} \tag{3.23}$$

The delta-p unit is actually a feedforward calculation from torque level to pressure level, using the kinematic model of the muscle actuation system. The calculated $\Delta\tilde{p}$ affects the torque required to track the desired trajectory, while p_s is introduced to determine the sum of pressures which influences the stiffness of the joint as was discussed in section 3.3. Increasing p_s lowers the compliance of the joint.

In the last control block the desired gauge pressures calculated by the delta-p unit are compared with the measured gauge pressure values after which appropriate

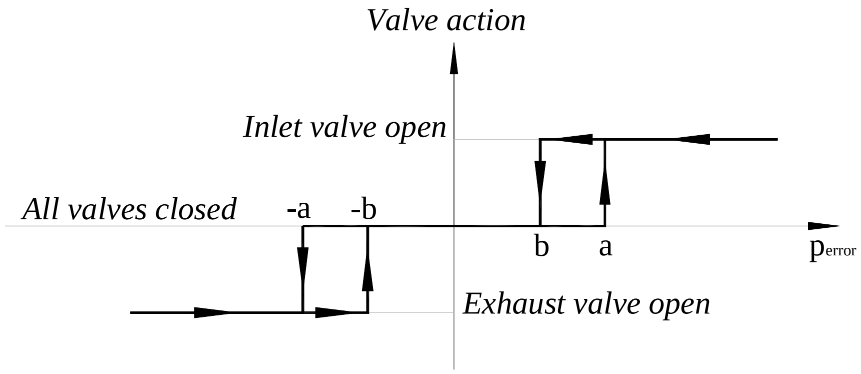

Figure 3.5: Bang-bang pressure control scheme.

valve actions are taken by a bang-bang pressure controller. One inlet or exhaust valve is opened if the pressure difference, between required and measured pressure ($p_{error} = \tilde{p} - p$)), exceeds level a. Figure 3.5 gives an overview of the control principle. The valves are closed again when the difference drops below level b. If the pressure difference is small enough, no valve action takes place (dead zone) and the muscle stays closed. In this situation the muscle is acting as a compliant passive element.

The simulation includes a delay time for opening or closing a valve of 1 ms and a controller sampling time of 2 ms. The valve delay time corresponds to real data, recorded with the valves used for "Lucy". A sampling time of 2 ms was used in an older version of the communication protocol, but currently fairly higher sampling rates are attained, as is discussed in chapter 6. The bang-bang reaction levels are set at $a = 20$ mbar and $b = 15$ mbar. Parameter deviations are not introduced. The scope of this chapter is to show the principle and the importance of adapting the compliance and not to check on controller robustness.

3.5.4 Simulation results and discussion

Releasing the leg from a position different from the static balance configuration with pressurized closed muscles, the system starts to oscillate at a specific natural frequency. This frequency depends on the mean pressure and on the initial conditions, due to the nonlinearity of the passive compliance characteristic. If this passive trajectory is equal to a desired trajectory and the compliance and initial conditions correspond, then no valve action is required. Increasing or decreasing the mean pressure in this situation results in more control activity and consequently more power consumption. When, on the other hand, an arbitrary trajectory is imposed (e.g. a sine-wave at a certain frequency) it is important to select an appropriate stiffness, influenced by the parameter p_s, in order to reduce the amount of valve switching. This is shown by the following two simulation results.

A sine wave of 2 Hz is imposed as a knee angle trajectory, with θ ranging from $35\,^\circ$ to $45\,^\circ$. A first simulation is performed with $p_s = 16\,\mathrm{Nm}$ and a second one is done with $p_s = 32\,\mathrm{Nm}$ The following figures (3.6 to 3.10) each compare both simulations for different characteristics. The graphs represent one period with the initial pressures and torques calculated dynamically to fit the sine wave in order to represent steady state motion. Comparing angle and angular velocity in figure 3.6, no substantial difference can be noticed between the two simulations. With p_s set at 32, small deviations between desired and measured trajectory can be seen, but for both simulations tracking performance is very good.

An important difference between the simulations is seen on the graphs representing pressures and valve actions. Figure 3.7 shows required and actual pressure, together with valve switching, for the extensor muscle (1). Figure 3.8 shows the same information for the flexor muscle (2). A closed muscle in these graphs is represented by a horizontal line depicted at the level of the initial pressure while a peak upwards represents one opened inlet valve and a peak downwards corresponds to one opened exhaust valve. In the second simulation, the mean pressure of both flexor and extensor muscle is set higher due to the higher p_s value. Based on the valve actions, it is clear that a p_s value of 16 is more suitable to track a sine-wave of 2 Hz. The control activity in the case of $p_s = 32\,\mathrm{Nm}$ is considerably higher. For example, in figure 3.7 for $p_s = 16$ it is seen that no valve action is taken between 0.06 s and 0.14 s because the slope of the pressure course induced by the natural dynamics fits the one of the imposed pressure course, required to track the sine-wave. On the contrary, the results for the same time interval with $p_s = 32\,\mathrm{Nm}$ show that opening an inlet valve is needed to compensate pressure drops, induced by the natural dynamics with closed muscles. These pressure drops, resulting from volume changes due to the leg movement, are too high compared to the imposed pressure course.

The desired pressure courses originate from the delta-p unit, which determines the pressures in function of the required torque, calculated by the computed torque unit. Therefore, the same behaviour is observed at the graphs depicting the torque values. Figure 3.9 gives required and applied torques for both simulations. In the case of $p_s = 16\,\mathrm{Nm}$ the slopes between desired and applied torque are comparable, while in the other case they do not match.

Another way to visualize the influence of p_s, is by an uncontrolled oscillation of the leg. Figure 3.10 shows again desired and actual knee angle for both simulations with the same initial conditions and respective p_s values, but with the muscles closed all the time. The imposed sine-wave of 2 Hz is also depicted on the graphs. None of the two passive trajectories fits the sine-wave exactly, but the base frequency of the actual passive trajectory with $p_s = 16$ approximates 2 Hz, while in the other case, the base frequency is situated around 2.7 Hz, since the stiffness of the joint is higher. Due to the nonlinear torque to angle relation, the shape of the passive trajectory deviates from a pure sine-wave. The deviation from the sine-

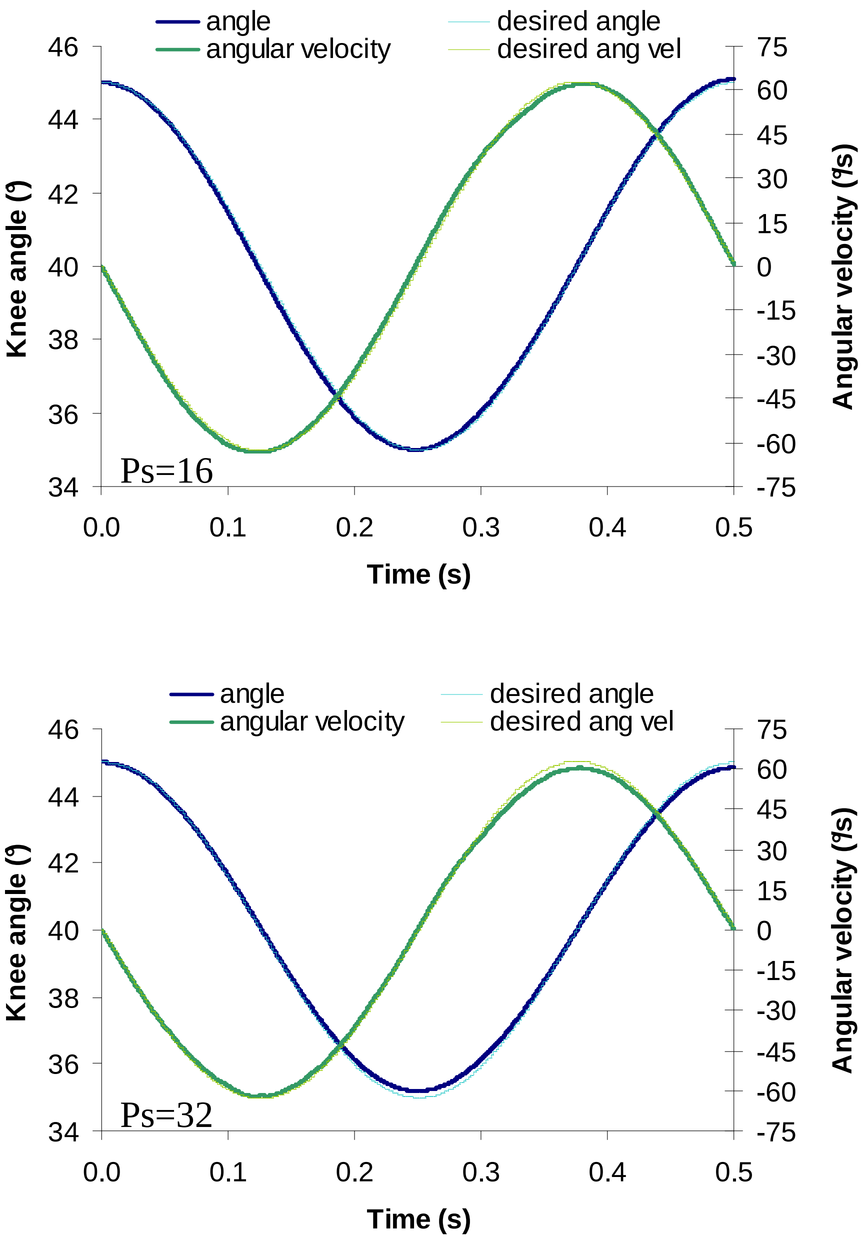

Figure 3.6: Desired and actual knee angle and angular velocity for $p_s = 16\,\mathrm{Nm}$ and $p_s = 32\,\mathrm{Nm}$.

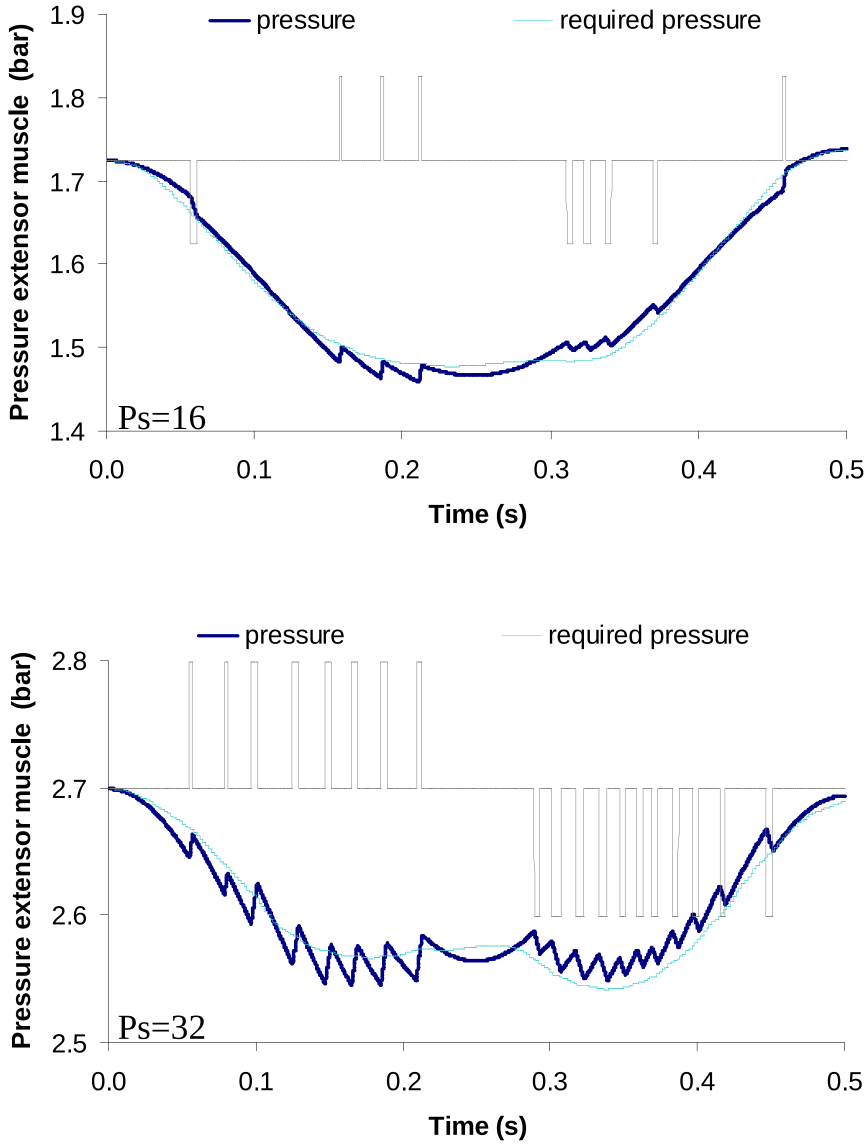

Figure 3.7: Required and actual pressure in the extensor muscle for $p_s = 16\,\mathrm{Nm}$ and $p_s = 32\,\mathrm{Nm}$.

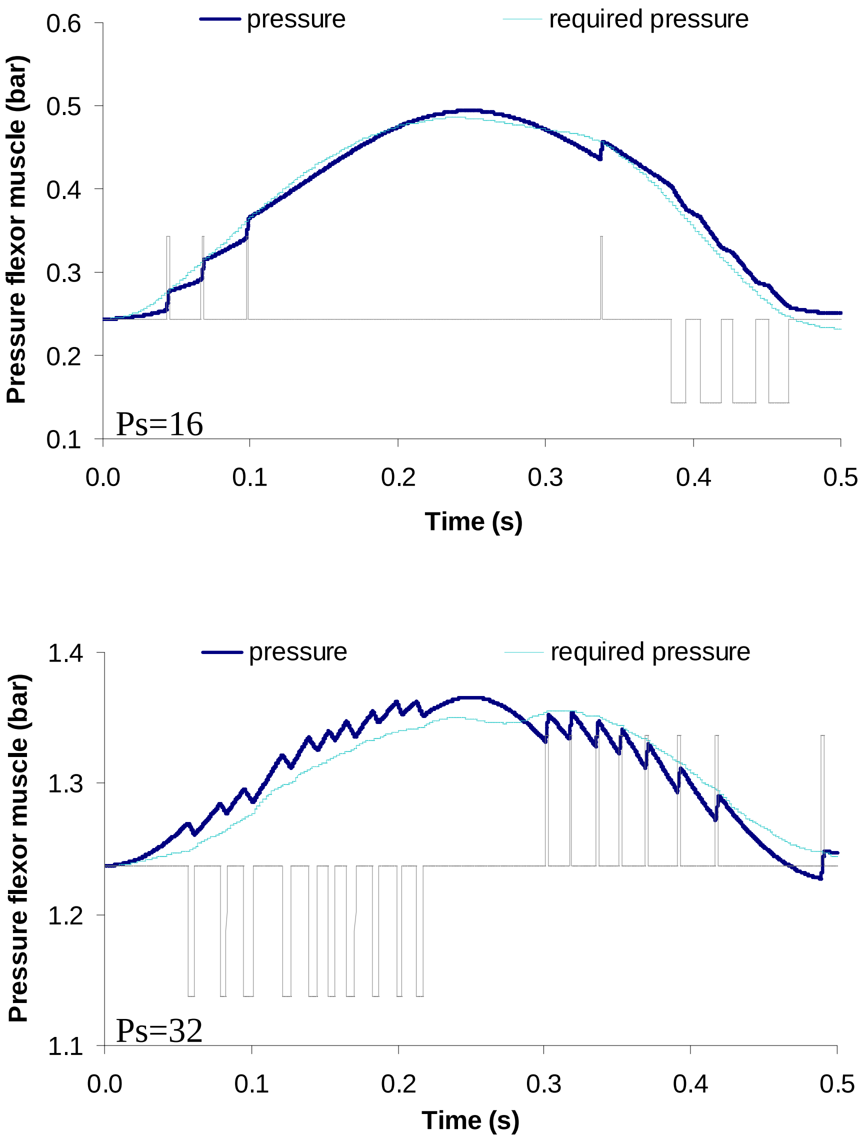

Figure 3.8: Required and actual pressure in the flexor muscle for $p_s = 16\,\mathrm{Nm}$ and $p_s = 32\,\mathrm{Nm}$.

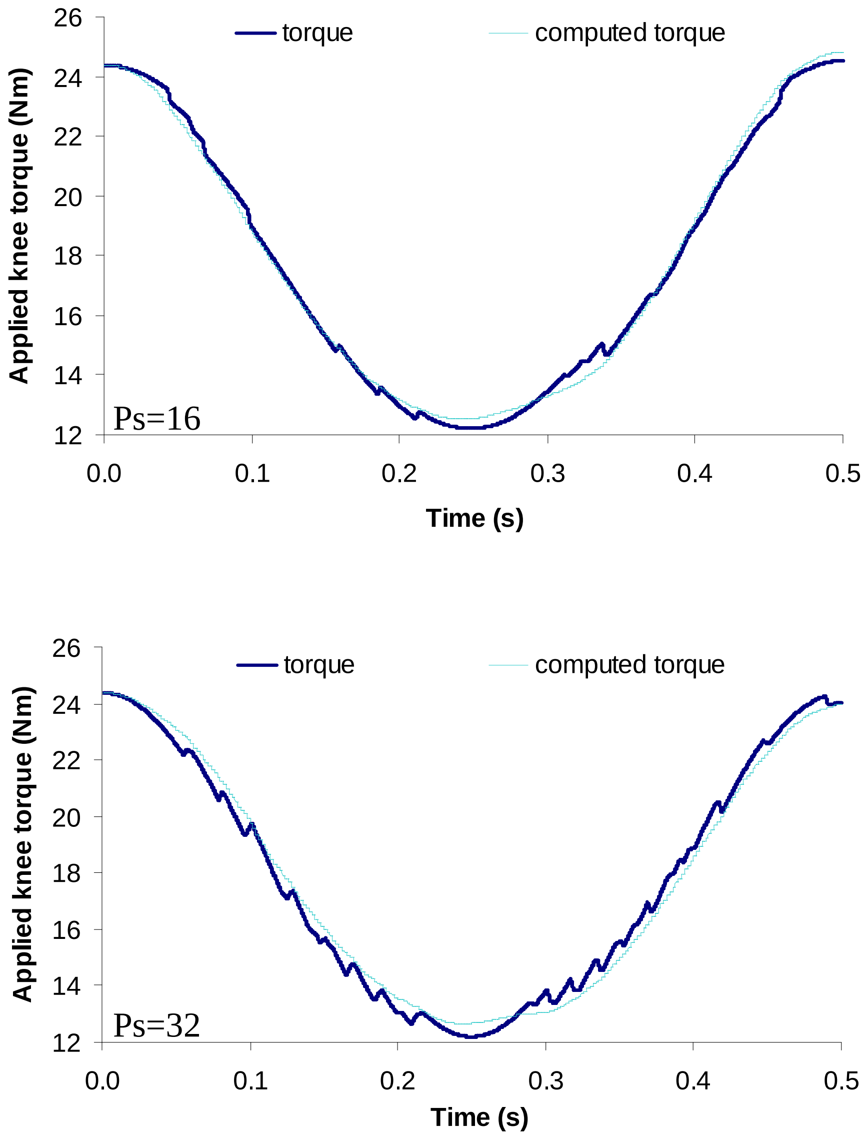

Figure 3.9: Required and appied knee torque for $p_s = 16\,\mathrm{Nm}$ and $p_s = 32\,\mathrm{Nm}$.

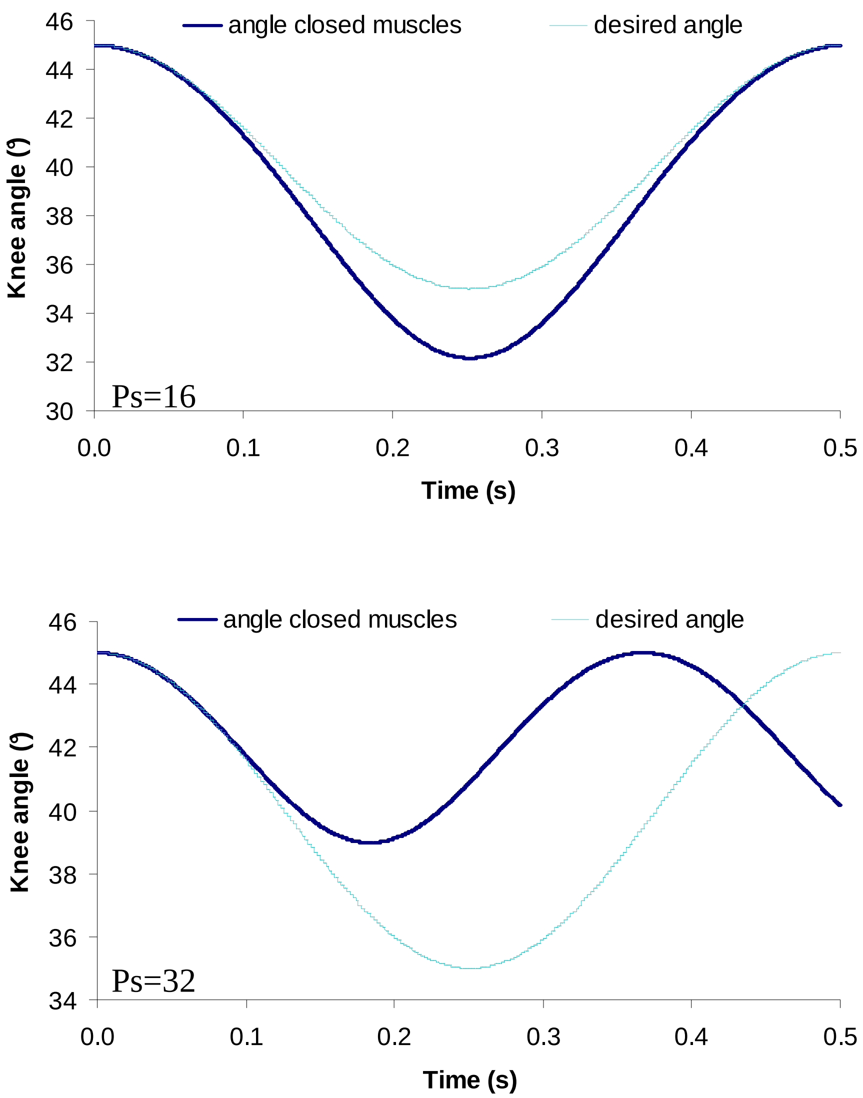

Figure 3.10: Actual and desired knee angle with closed muscles for $p_s = 16\,\mathrm{Nm}$ and $p_s = 32\,\mathrm{Nm}$.

wave increases for larger amplitudes. Consequently, more valve switching is needed for larger movements.

These simulation results show the importance of selecting an appropriate p_s value in order to exploit the natural dynamics of the system. Moreover, it is clear that the dead-zone, introduced in the pressure bang-bang controller, plays a crucial role.

Decreasing the margins on the pressure deviations for which valves are opening, as was introduced with the bang-bang controller, increases valve switching. On the contrary, enlarging these margins facilitates the exploitation of the passive behaviour, when an appropriate p_s value is selected. However, this deteriorates the tracking performance, which indicates that a compromise between control effort and tracking error will have to be made.

3.6 Mathematical formulation for compliance adaptation

In the previous section it was shown that choosing an appropriate joint stiffness reduces control activity while tracking a desired trajectory. Depending on the specific shape and base frequency component of the desired trajectory, the p_s value introduced in equations (4.74) has to be chosen.

This section describes a mathematical formulation for estimating an appropriate value of p_s, for the case p_s is constant. Note that when controlling the biped "Lucy", a constant value of p_s will probably not be suitable, and that other strategies for setting p_s will have to be formulated. In the previous simulation a sine-wave was selected as desired trajectory. For small oscillations the passive behaviour fits a sine-wave. So in this case a constant p_s value is justified. But, in general, the trajectories for the biped joints are not sine functions with only one frequency component. For such situations, a varying p_s value will be more interesting. Apart from selecting an appropriate joint stiffness as a function of the desired joint trajectory, it is also important to take this joint stiffness into account while calculating the joint trajectories.

The starting-point for the estimation procedure is to fit the natural pressure slopes with the required ones. The required pressure slopes are determined by the delta-p unit in combination with the computed torque module and depend on the desired trajectory. Pressure changes with closed muscles are influenced by p_s. The required pressure slopes are obtained by deriving equations (3.21) with respect to the trajectory $\tilde{\theta}$:

$$\frac{d\tilde{p}_1}{d\tilde{\theta}} = -\frac{p_s}{t_1^2}\frac{dt_1}{d\tilde{\theta}} + \frac{d\Delta\tilde{p}}{d\tilde{\theta}} \tag{3.24a}$$

$$\frac{d\tilde{p}_2}{d\tilde{\theta}} = -\frac{p_s}{t_2^2}\frac{dt_2}{d\tilde{\theta}} - \frac{d\Delta\tilde{p}}{d\tilde{\theta}} \tag{3.24b}$$

Taking into account equation (3.23), the derivatives can be expanded by:

$$\frac{d\Delta\tilde{p}}{d\tilde{\theta}} = \frac{1}{(t_1+t_2)^2}\left[(t_1+t_2)\,\tilde{K} - \left(\frac{dt_1}{d\tilde{\theta}} + \frac{dt_2}{d\tilde{\theta}}\right)\tilde{T}\right] \tag{3.25}$$

with $\tilde{K}$ (equation (3.9)) representing the stiffness associated with the desired trajectory and $\tilde{T}$ the torque calculated by the computed torque module. On the other hand, combining equation (3.12), valid for closed muscles, with equations (3.21) yields:

$$\frac{d\tilde{p}_1}{d\tilde{\theta}} = -p_s \left(\frac{n}{t_1} \frac{V_{1_o}^n}{V_1^{n+1}} \frac{dV_1}{d\tilde{\theta}} \right) - (P_{atm} + \Delta\tilde{p}) \left(n \frac{V_{1_o}^n}{V_1^{n+1}} \frac{dV_1}{d\tilde{\theta}} \right) \tag{3.26a}$$

$$\frac{d\tilde{p}_2}{d\tilde{\theta}} = -p_s \left(\frac{n}{t_2} \frac{V_{2_o}^n}{V_2^{n+1}} \frac{dV_2}{d\tilde{\theta}} \right) - (P_{atm} - \Delta\tilde{p}) \left(n \frac{V_{2_o}^n}{V_2^{n+1}} \frac{dV_2}{d\tilde{\theta}} \right) \tag{3.26b}$$

The idea is to match for each muscle the required pressure slope with the slope associated with the natural dynamics, by selecting an appropriate p_s value. Once the desired trajectory is known, expressions (3.24) and (3.26) can be evaluated at a number of points θ_i, separated by equal time intervals along the trajectory. Subsequently a p_s value is searched in order to match as much as possible both pressure slopes. For each θ_i, equations (3.24a) and (3.26a) and equations (3.24b) and (3.26b) are thus respectively combined and each solved for a value $p_{s_j}^i$.

$$p_{s_1}^i = \left[\left(\frac{1}{t_1^2} \frac{dt_1}{d\tilde{\theta}} - \frac{1}{t_1} \frac{n}{V_1} \frac{dV_1}{d\tilde{\theta}} \right)^{-1} \left((P_{atm} + \Delta\tilde{p}) \left(\frac{n}{V_1} \frac{dV_1}{d\tilde{\theta}} \right) + \frac{d\Delta\tilde{p}}{d\tilde{\theta}} \right) \right]_{\theta_i} \tag{3.27a}$$

$$p_{s_2}^i = \left[\left(\frac{1}{t_2^2} \frac{dt_2}{d\tilde{\theta}} - \frac{1}{t_2} \frac{n}{V_2} \frac{dV_2}{d\tilde{\theta}} \right)^{-1} \left((P_{atm} - \Delta\tilde{p}) \left(\frac{n}{V_2} \frac{dV_2}{d\tilde{\theta}} \right) - \frac{d\Delta\tilde{p}}{d\tilde{\theta}} \right) \right]_{\theta_i} \tag{3.27b}$$

Note that the initial volume V_{j_o}, when closing a muscle, is set equal to the actual volume V_j. To select one p_s value, a mean of all calculated $p_{s_j}^i$ values is defined:

$$p_s = \frac{1}{2z} \sum_{i=1}^{z} \left[p_{s_1}^i + p_{s_2}^i \right] \tag{3.28}$$

with z the number of points chosen to evaluate equations (3.27). Applying this formulation to the desired trajectory of 2 Hz of section 3.5.4 results in an estimate of $p_s = 16.5$ Nm. Note that this result is only an indication and does not give a p_s value for which valve action or energy consumption is extremely minimized. There still exists a strong dependence on the controller parameters, such as bang-bang pressure control reaction levels and feedback gains of the computed torque controller. E.g. decreasing the reaction levels of the bang-bang controller for opening a valve would increase valve switching. Moreover, the thermodynamics are assumed to be polytropic, following equation (3.10), thus a realistic value has to be provided for the polytropic exponent n. Furthermore, modelling errors exist on the dynamic model concerning mechanics comprised within $\tilde{T}$ and on the kinematic muscle torque prediction with $\hat{t}_1$ and $\hat{t}_2$. As was already mentioned, depending on the specific joint trajectories, a varying p_s can be more suitable. The same idea of comparing the pressure slopes might then be used, but for the calculations a differential formulation on p_s has to be solved.

3.7 Energy considerations

It was shown that less valve switching is needed to track a specified trajectory, when an appropriate p_s value is selected. Besides the valve switching, the thermodynamic conditions of the pressurized air also determine energy consumption. Since these thermodynamic conditions in the muscles for both simulations are completely different, the air mass flowing through an opened valve differs a lot. So apart from valve actions, it is interesting to consider actual air mass entering and leaving the total system. In table (3.2) the total air mass inflow of the two muscles is given for both simulations. These values give the airflow over one period. Due to the

	$p_s = 16\,\mathrm{Nm}$	$p_s = 32\,\mathrm{Nm}$
airflow input muscle 1	25.7 mg	77.9 mg
airflow input muscle 2	23.7 mg	47.8 mg
total airflow input	49.4 mg	125.7 mg

Table 3.2: Air mass flows entering the system for one cycle

law of conservation of mass, the total air mass leaving the system is equal to the one entering the system over a complete period during regime motion. Comparing both simulations, it is seen that the situation with the unsuitable p_s value demands more than double air mass consumption!

Based on the previous findings, the amount of energy consumption is also calculated. This energy consumption depends not only on the air mass flows but is related to the thermodynamic conditions of the compressed air supply source. It is not straightforward to calculate the actual energy needed to power the leg, since this depends on how the pressurized air of the pneumatic supply source has been created. One way to give an idea of energy consumption is to calculate the exergy associated with the particular pneumatic air mass flow. Exergy is in fact the maximum amount of energy, with respect to the surrounding environment, which can be transformed into useful work. For example, the air mass flow entering the muscle system comes from a compressed air reservoir at certain temperature and pressure level. The surrounding environment is regarded as the atmosphere. The exergy of the pneumatic power supply is then calculated as the minimal work needed to compress the atmospheric air to the pressure supply conditions. For a compressor, the minimal work needed to compress air from pressure level p_{atm} to p_1 is done at isothermal conditions and can be calculated as follows [Rogers and Mayhew, 1992]:

$$W_{isotherm} = \dot{m}_{air} r T_{atm} \ln \frac{p_1}{p_{atm}} \tag{3.29}$$

hereby assuming the air to behave as a perfect gas. The symbol $\dot{m}_{air}$ represents the total air mass flowing through the compressor, r is the dry air gas constant and T_{atm} is the temperature of the atmosphere expressed in Kelvin.

	$p_s = 16\,\mathrm{Nm}$	$p_s = 32\,\mathrm{Nm}$
exergy inlet muscle 1	4.2 J	12.7 J
exergy inlet muscle 2	3.9 J	7.8 J
total exergy inlet	8.1 J	20.5 J
exergy exhaust muscle 1	2.0 J	8.3 J
exergy exhaust muscle 2	0.6 J	3.4 J
total exergy exhaust	2.6 J	11.7 J

Table 3.3: Exergy associated with air mass flows entering and leaving the system for one cycle with $p_{supply} = 7\,\mathrm{bar}$

	$p_s = 16\,\mathrm{Nm}$
airflow input muscle 1	24.9 mg
airflow input muscle 2	25.3 mg
total airflow input	50.3 mg
exergy inlet muscle 1	2.29 J
exergy inlet muscle 2	2.34 J
total exergy inlet	4.63 J

Table 3.4: Air mass flows with associated exergy level, entering the system for one cycle with $p_{supply} = 3\,\mathrm{bar}$

Equation (3.29) can be used to calculate the exergy of the supply source as well as the exergy associated with the air leaving the muscles. Contrary to the air mass flows, the exergy values are not the same for inlet and exhaust. Table 3.3 gives an overview of the respective exergy levels for both simulations. The absolute supply pressure level is set at 7 bar, the atmospheric absolute pressure at 1 bar and the atmospheric temperature is 293 K.

The most interesting value is the exergy consumption of the inlet, since this gives an indication of the energy consumption of the system. The exergy level at inlet for $p_s = 16\,\mathrm{Nm}$ is 8.1 J, which is much lower than 20.5 J for the other case. Also important to notice is the exergy level of the exhaust which is 2.6 J for the simulation with $p_s = 16\,\mathrm{Nm}$. Due to the nature of the pneumatic drive mechanism this energy is wasted since it is rejected to the atmosphere. The higher the pressure inside the muscle, the more exergy is wasted. This shows the importance of low working pressures which emphasizes the advantage of the PPAM compared to other pneumatic artificial muscles. The same discussion can be held regarding the pressure level of the supply source. Tabel 3.4 gives total air mass flow and exergy levels at inlet only for a simulation with $p_s = 16\,\mathrm{Nm}$ and when the supply pressure is set at 3 bar. It is observed that, in spite of almost identical air mass consumption at inlet, the exergy associated with this flow is lowered from 8.1 J to

4.6 J. When the pressure supply is set at 7 bar, this inlet pressure is expanded to the muscle working pressure over the inlet valve while loosing a lot of exergy in the air mass flow swirl. This energy is not recuperated. At this point e.g. an exergy discussion can be made to argue the choice between an onboard compressor and a high pressure supply tank in order to create an autonomous robot. Of course, several other practical implications should be taken into account.

Since the pressure gradient depends on the pressure difference over the valves, the slope of the pressure evolution when opening an inlet valve for the situation with the supply set at 3 bar decreases in comparison with higher supply pressures (see equations (5.18) and (5.19)). Consequently, different valve actions are taken by the bang-bang controller. Figure 3.11 gives pressure values inside the extensor muscle at the time interval 0.10 s to 0.25 s for both pressure supply source conditions. It

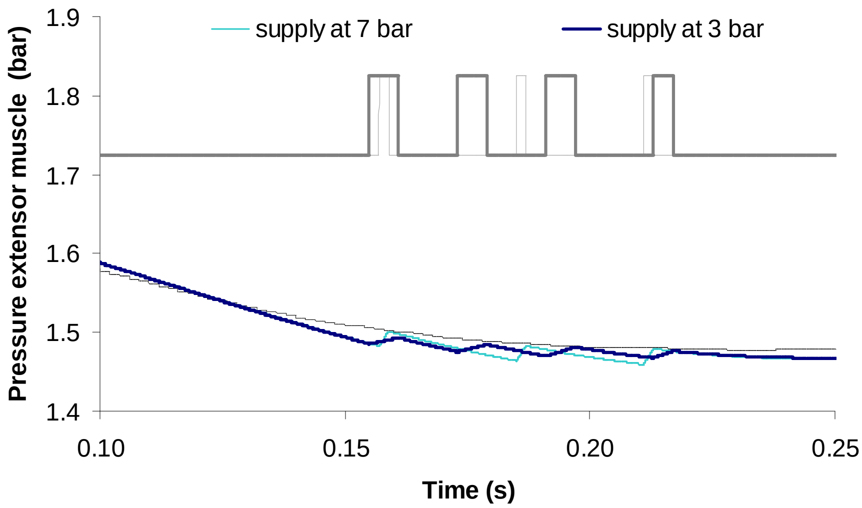

Figure 3.11: Comparison of pressure evolutions for the extensor muscle with supply pressure set at 3 bar and 7 bar.

is seen that the effect of an opened inlet valve is much lower in case of the reduced supply pressure level but that the tracking of the desired pressure is still guaranteed with adapted valve switching. Note that the slope of the pressure is the same when the muscle is closed, which is expected since the conditions for closed muscles are independent from the used pressure supply level.

The supply pressure set at 3 bar is a limiting situation since higher muscle pressures become impossible for these supply source conditions. But towards the autonomous navigation, all these energy considerations should be taken into account. Not only torque characteristics but also pressure level conditions in combination with desired robot motion should be involved during the design process. Due to the extreme complexity of such a design, it is not possible and wise to take into account all these considerations at once. The first version of the robot "Lucy" is of course designed with a limited set of conditions. But the ability to allow easy changes in torque characteristics is foreseen, such that a flexible experimental setup is created. This topic is handled in chapter 6, where the design of the robot is discussed.

3.8 Conclusions

In this chapter a one dimensional setup has been discussed, since this forms the basis for the complete biped. First, the antagonistic muscle setup was introduced to power a joint bidirectionally. The kinematic expressions, which link the generated torques to the muscle forces and the geometry of the setup, were developed. These expressions are used for joint dimensioning purposes and are incorporated in the joint tracking control structure.

An important element in this chapter is the compliance adaptation. Therefore a formulation of the compliance was given for closed muscles. It was shown that a weighted sum of both pressures in the antagonistic muscle setup determines the joint compliance, while pressure differences determine the generated torque and consequently also the joint position. This means that compliance can be set while controlling position.

In this context a discussion was given concerning exploitation of natural dynamics. Joint compliance setting should be done in an appropriate way, such that the natural movement of the setup corresponds to the imposed movement. A simulation model was presented to show the effect of adapted compliance. This model represents a simplified leg configuration with the knee joint actuated by an antagonistic muscle pair. The simulation incorporates modelling of the mechanics as well as the thermodynamic processes, which take place in the muscle/valve systems. Additionally, a joint tracking control structure has been presented in order to perform the simulations. This control structure, which forms the basis for the controller of the complete biped, is multilayered. The controller has a computed torque module which copes with nonlinearities associated with the robot configuration. The nonlinear behaviour of the actuation system is dealt with by the delta-p unit. This unit translates the required torque into required pressure levels, using the muscle force characteristics and geometrical relations of the antagonistic setup. Finally, the required pressures are set in the muscles by a bang-bang pressure controller, which commands discrete the pneumatic on/off valves.

Simulations with an imposed knee joint trajectory were carried out for two different joint stiffness settings. It was clearly shown that control activity, represented by the valve switching, could be reduced substantially when selecting an appropriate stiffness. In this context a mathematical formulation was given to predict a suitable stiffness setting for a simplified case. And finally, some considerations about pneumatic energy consumption were given.

Chapter 4

Control architecture for "Lucy"

4.1 Introduction

Figure 4.1 shows a schematic overview, depicting several essential control blocks, of a possible overall control structure required to steer a biped. A task manager commands the robot to execute a particular task at a specific moment. Depending on

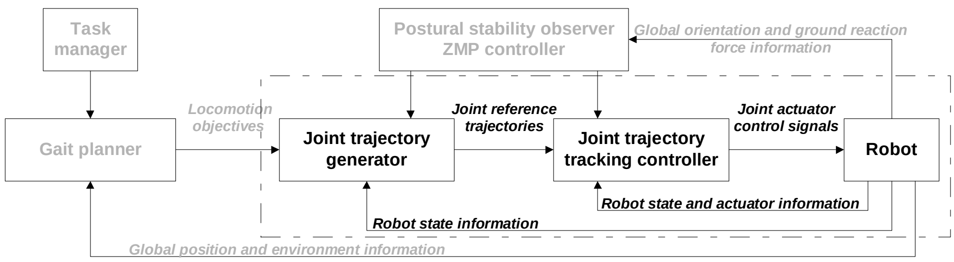

Figure 4.1: Global robot control scheme

the current global robot position and information about its direct environment, a gait planner produces specific objectives for the global robot motion. According to these objectives, while taking into account the biped's configuration, a joint trajectory generator calculates desired trajectories for each joint of the robot. Finally, a tracking controller determines the necessary control actions to be carried out by the different joint actuator units in order to track the trajectories. A joint trajectory generator generally calculates trajectories which incorporate global dynamic postural stability e.g. based on ZMP [Vukobratovic and Borovac, 2004] placement. Since this feedforward ZMP placement is however based on estimated robot parameters and approximated dynamics, an extra feedback loop controlling the ZMP, should be provided. This control block commands deviations for the trajectory controller and/or tracking controller, based on ground reaction force measurements in the feet and global orientation information of the robot.

Due to the current impressive state of the research on locomotion and postural control of legged robots, more and more research groups start to focus on the complex task of gait planning in a real environment. This unit is task dependent and incorporates several research domains such as vision recognition, artificial intelligence, path planning, collision detection, force control, etc. . . . A few examples are vision guided path planning and obstacle avoidance on the humanoid platform "Johnnie" [Cupec et al., 2003] and the biped robot BARt-UH [Seara et al., 2003]. On the humanoid platform HRP-2 several research on gait planning is under taken: locomotion planning to pass through narrow spaces [Kanehiro et al., 2004], gait planning for force controlled manipulation [Harada et al., 2004] and teleoperation [Yokoi et al., 2004]. On the biped robot "H7", research is going on concerning navigation through complex environments [Chestnutt et al., 2003].

A popular method for motion control of humanoids is defining prescribed joint trajectories. This research area can be split into two major categories: off-line and on-line techniques. With off-line techniques joint trajectories, which ensure stable walking, are calculated in advance based on some kind of optimization criteria. E.g. Chevallereau and Aoustin [2001] and Denk and Schmidt [2001] define energy optimized reference trajectories for 2D bipedal walking, Kagami et al. [2002] determine joint trajectories which combine predefined ZMP trajectories with desired robot motion. On-line techniques, on the other hand, generate joint trajectories in real-time, while using actual robot feedback information. Generally, for this purpose, the robot is modelled by simplified dynamics such as inverted pendulum dynamics. An important method in this context is the "Three-Dimensional Inverted Pendulum Mode" [Kajita et al., 2001], which is used to control the humanoid robot HRP-2. Analogously, simplified dynamics are used to generate joint trajectories for the biped "Johnnie" [Löffler et al., 2002].

In order to track given joint reference trajectories for a nonlinear system, such as a biped robot, nonlinear tracking control techniques are often used. A computed torque method is implemented in the robot "Johnnie" [Pfeiffer et al., 2003] and Pratt combines computed torque with an adaptive control technique to enhance the performance of the swing leg in the robot "Spring Flamingo" [Pratt, 2000]. Tzafestas et al. [1996] compare a computed torque method with sliding mode control for a 5-link biped in simulation. Regarding robustness against parameter and modelling deviations, sliding mode control was found superior to a computed torque method at the cost of actuator control activity. Unfortunately, in this study actuator dynamics were not taken into account. Gorce and Guihard [1998], on the other hand propose a two level control method which combines a computed torque method with a dynamic control model of the pneumatic actuators in order to perform position and impedance control on the legs of the biped "Bipman".

The last control block concerning feedback of the ZMP position has been implemented on "HRP-2" [Yokoi et al., 2001] and "Johnnie" [Pfeiffer et al., 2003]. For both robots, control of the horizontal position of the robot torso is used to adjust the ZMP position. E.g. tracking of the desired horizontal motion of "Johnnie" is suspended whenever the ZMP approaches instability regions. A ZMP feedback control on the hip is then used to correct the ZMP position. Another interesting work is conducted by Mitobe et al. [2004], here ZMP manipulation is used to control the angular momentum of a walking robot.

The current research on "Lucy" focusses on the two control blocks depicted in boldface in figure 4.1: joint trajectory generator and joint tracking controller. The trajectory generator has been developed by Vermeulen et al. [2005]. For the sake of completeness, the technique is explained in this chapter. The main focus of this work is the development of a tracking controller, which incorporates the actuator characteristics and dynamic model of the robot. The proposed control strategy is a multilevel construction of several essential blocks, trying to cope with the nonlinear structure by using model-based feedforward techniques. The control concept has been developed from an engineering point of view, meaning that existing techniques are gathered to create a smooth working trajectory controller, rather than searching for optimal control performance.

4.2 Dynamic balance: zero moment concept

One of the most important tasks of the control algorithm for bipeds, and legged robots in general, is maintaining postural stability. As was mentioned in the introduction, one can distinguish two major kinds of control regarding stability: statically and dynamically balanced robots.

Statical stability is ensured by keeping the projection of the global COG of the robot on the supporting plane within the convex hull of the supporting area of the robot [Song and Waldron, 1989; McGhee and Frank, 1968]. Applying statical balance conditions, one assumes the motion of the robot to be slow, in fact quasi-static, so that the inertial forces are negligible. When these inertial forces have non-negligible proportions due to increased robot speed, static balance conditions are no longer valid and dynamic balance control techniques are used. Contrary to static stability, the term dynamic stability is very loosely interpreted and often dynamic gaits are referred to as not statically balanced at all times [Ridderström, 1999]. One of the most important criteria for dynamic balance is the concept of the zero moment point, which was introduced by Vukobratovic [1975]. The ZMP can be referred to as "*an overall indicator of the mechanism behaviour, and is the point where the influence of all forces acting on the mechanism can be replaced by one single force*" [Vukobratovic and Borovac, 2004]. Or as interpreted by Dasgupta and Nakamura [1999]: *The ZMP is defined as that point on the ground at which the net moment of the inertial forces and the gravity forces has no component along the horizontal axis.* For a better comprehension, the ZMP formulation is given here for a planar robot system.

During the single support phase, the ZMP concept is about avoiding tipping over of the stance foot. After all, it is important to be able to use the total supporting foot area in order to influence the robot's behaviour. In figure 4.2, all the forces, inertial and ground reaction forces, which act on the foot are depicted. The influence of the dynamics of the complete robot on the foot are replaced by the torque $\bar{\boldsymbol{\tau}}_{\mathbf{A}}$ (exerted by the ankle actuator) and the force $\bar{\mathbf{F}}_{\mathbf{A}}$, acting at the ankle point A. The total resultant of the ground reaction force $\bar{\mathbf{R}}$ works at point P and gravity acts on the foot in the center of gravity G_f. Note that for the sake of clearness the discussion is restricted to a 2D problem representation with the foot aligned to the horizontal ground. In the vertical direction, the ground reaction

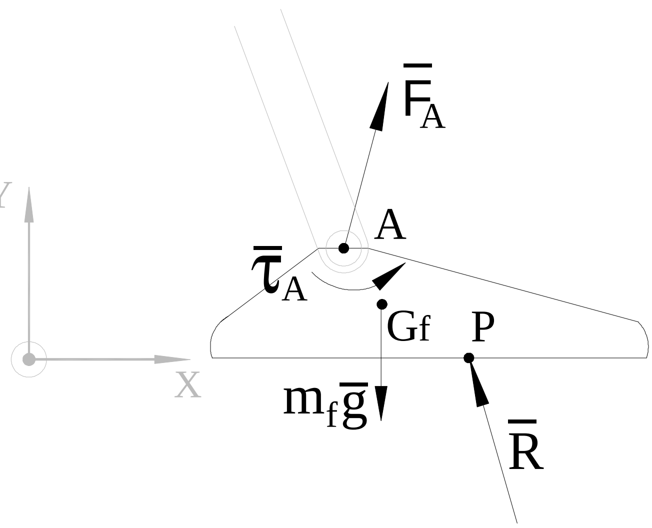

Figure 4.2: Forces acting on the foot

force $\bar{\mathbf{R}}$ compensates the vertical component of $\bar{\mathbf{F}}_{\mathbf{A}}$ and the weight of the foot $\mathbf{m_f}\bar{\mathbf{g}}$. The horizontal component of $\bar{\mathbf{R}}$, generated by friction forces, only compensates the horizontal component of $\bar{\mathbf{F}}_{\mathbf{A}}$. Note that, besides the robot stability criteria on rotation, friction between foot sole and ground has to be sufficient in order to have a non-slipping foot condition. To prevent the foot from rotating around one of its edges, the ground reacting forces will also counteract the moment induced by gravity and the inertial forces:

$$\overline{\mathbf{OP}} \times \bar{\mathbf{R}} + \overline{\mathbf{OG_f}} \times \mathbf{m_f}\bar{\mathbf{g}} + \overline{\mathbf{OA}} \times \bar{\mathbf{F}}_{\mathbf{A}} + \bar{\boldsymbol{\tau}}_{\mathbf{A}} = 0 \tag{4.1}$$

Writing equation 4.1 with respect to point P, the ground reaction force $\bar{\mathbf{R}}$ disappaers from the equation. So with respect to this point the moment of the inertial and gravitational forces acting on the robot has to be zero. This explains the name of point P, zero moment point, and clarifies the equality between ZMP and COP, centre of pressure. The centre of pressure is defined as the distance-weighted average location of the individual pressures on the foot [Pratt, 2000], thus the point P where the resultant $\bar{\mathbf{R}}$ of the ground reaction forces acts. The ZMP and COP are frequently mixed up in the legged robotics community, the ZMP can be seen as defined from the robot dynamic's point of view, while the COP is determined by the ground reaction forces. Whenever, the moment generated by the inertial and gravitational forces is too large for the unilateral ground reaction force $\bar{\mathbf{R}}$ to compensate, the force $\bar{\mathbf{R}}$ will act on one of the foot edges, while an uncompensated part of the force moment will cause the robot to start tipping over. This means that, in this undesirable situation, the COP is located at the foot edge, but that the ZMP actually, doesn't exist anymore. In this context, Goswami [1999] defined the foot-rotation index, FRI. This index creates a quantitative representation of the amount of postural instability by defining a virtual ZMP outside the foot supporting area.

In a further development of the control strategy in this chapter an approximation is made by neglecting the weight of the foot and the height of the ankle point. In figure 4.3 the origin is placed at the ankle point A and τ_A is the applied ankle

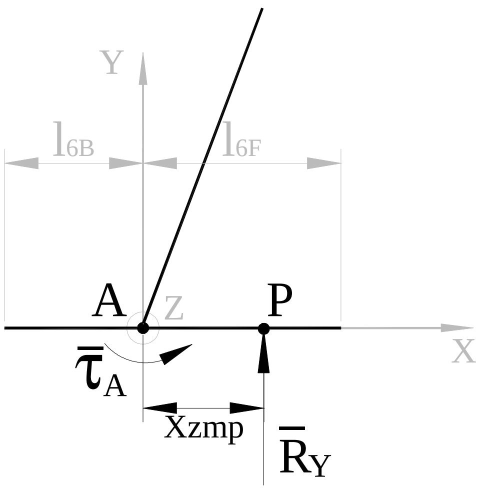

Figure 4.3: Calculation of the ZMP

torque in the ankle joint of the supporting foot, during the single support phase. The horizontal ZMP position, X_{zmp}, is then defined as:

$$R_y X_{zmp} + \tau_A = 0 \tag{4.2}$$

$$R_y = m_{tot}\left(\ddot{Y}_G + g\right) > 0 \tag{4.3}$$

with m_{tot} the total mass of the robot and $\ddot{Y}_G$ the vertical acceleration of the global

COG, which can be calculated with equation (C.3b) of appendix C, which represents the vertical position of the COG. Equation (4.3) is a result of the vertical component of the linear momentum theorem expressed for the global COG of the robot. Combining (4.2) and (4.3) gives:

$$X_{zmp} = \frac{-\tau_A}{m_{tot}\left(\ddot{Y}_G + g\right)} \tag{4.4}$$

with

$$\ddot{Y}_G > -g \tag{4.5}$$

To ensure dynamic stability during the single support phase $|X_{zmp}|$ has to be respectively smaller than the distances l_{6B} and l_{6F}, which are the respective distances from the heel and from the toe to the ankle point. A straightforward way to ensure dynamic stability is to locate the ZMP at the ankle point by applying zero ankle torque (τ_A) during a single support phase. A trajectory generator developed for the robot "Lucy", discussed in the next section, uses this strategy.

For the double support phase, instead of calculating the ZMP with the inertial and gravitational forces, the ground reaction forces are used to calculate the COP. In figure 4.4 the robot is depicted during a double support phase. At the front foot (F_F) the ground reaction force $\bar{\mathbf{R}}_{\mathbf{F}}$ is acting, and at the rear foot $\bar{\mathbf{R}}_{\mathbf{R}}$. In the absence of ankle torques, the total reaction forces on both feet act at the ankle points. The COP, or ZMP, location P is then found as:

$$X_{zmp} = \frac{R_F^y X_{A_F}}{R_F^y + R_R^y} \tag{4.6}$$

with X_{A_F} the distance between both ankle points during double support. Contrary to the single support phase, the ZMP stability margin is generally much larger and does not imply the same critical situation towards postural stability. During double support, the ZMP will have to be shifted from the rear to the front foot by gradually changing the "weight" of the robot from the back to the front. The ZMP will be located at the front foot when the rear foot is about to be lifted to start the next single support phase.

4.3 Trajectory generator

In this section a trajectory generator developed for the biped "Lucy" is described. The work on this topic has been performed by Vermeulen [2004], for the sake of completeness, the trajectory generation strategy is explained in this section. The developed trajectory tracking controller, after all, takes into account specific elements of the proposed joint motion planner. Moreover, results of a simulation model (see chapter 5), with the trajectory generator incorporated, discusses the effectiveness of the tracking controller with respect to the dynamic robot stability.

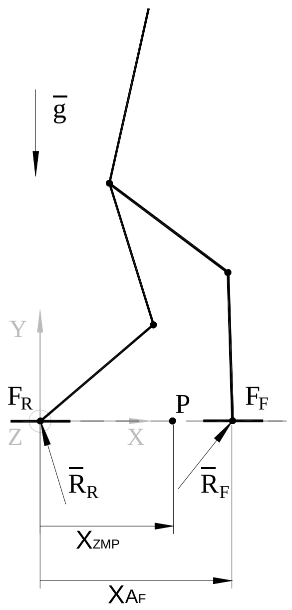

Figure 4.4: ZMP during a double support phase

A complete and a more elaborate discussion on the real-time dynamic trajectory generator can be found in [Vermeulen, 2004; Vermeulen et al., 2004, 2005].

The trajectory planning unit generates joint motion patterns based on two specific concepts, being the use of objective locomotion parameters, and the exploitation of the natural upper body dynamics by manipulating the angular momentum equation. The objective locomotion parameters are average forward speed of the hip, step-length, step-height and intermediate foot-lift. These parameters are calculated by a higher level gait planning control unit, which is beyond the scope of this work. It is important to mention that the trajectory generator ensures dynamically stable walking for a wide range of objective locomotion parameter combinations. For the calculation of the joint trajectories, the motion of the swing foot during the single support phase is not considered, it is kept in a horizontal position.

A biped robot step generally contains a single support phase and a double support phase. During single support the trajectories of the leg joints, represented by polynomials, are planned in such a way that the upper body motion is "naturally steered". This means that the rotation of the upper body due to the hip motion coincides with a desired upper body behaviour. The trajectory generator assures that practically no ankle torque is required on the supporting leg, only small ankle torques must be provided to compensate for modelling and approximation errors. Doing so, the ZMP is kept in the vicinity of the ankle joint and thus away from the supporting foot edges, resulting in a dynamically stable walking motion. The polynomials are established by manipulating the angular momentum equation to determine suitable boundary conditions for the hip and upper body motion. A short double support phase is used to ensure the necessary initial conditions for the next single support phase. The boundary acceleration conditions for double support phase are chosen in such a way that the ZMP switches from the rear foot to the next supporting front foot during the double support phase.

An interesting aspect of this method is that it is based on fast converging iteration loops, requiring only a limited number of elementary calculations. The computation time needed for generating feasible trajectories is low, which makes this strategy suitable for real-time application on "Lucy".

4.3.1 Phase durations

The single support phase is chosen to cover 80 % of a total step duration, while the double support phase lasts for the remaining 20 %. This corresponds to low-speed human walking [Hardt et al., 1999]. In order to calculate the different phase durations, first the steady-state objective parameters are defined:

- ν: mean horizontal hip velocity during a single support phase
- λ: step length, defined as the horizontal distance between both ankle points during a double support phase
- δ: step height, being the vertical distance between both ankle points during a double support phase
- κ: intermediate foot lift, imposing a specific vertical position of the swing foot at a given time instance during a single support phase

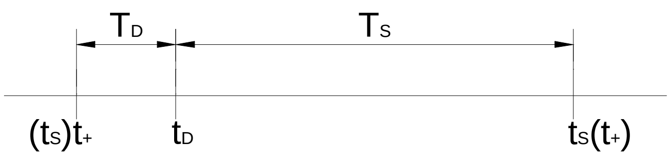

Figure 4.5: Timing schedule and definitions

If ΔX_H^S represents total horizontal hip displacement during single support, then the duration of this phase is defined as :

$$T_S = \frac{\Delta X_H^S}{\nu} \tag{4.7}$$

During single support, the biped can be seen as an inverted pendulum rotating around the ZMP point, which is comprehensibly discussed by Pratt [2000]. Since in the first half of this phase, the COG is located behind the pivoting point, the horizontal motion is decelerated by gravity. During the second half of the single support phase, the horizontal motion is accelerated, since then the COG is located in front of the pivoting point. The boundary values of the horizontal hip velocity in single support are therefore chosen larger than the mean horizontal velocity ν.

During a double support phase it is assumed that the horizontal hip velocity is approximately a constant. The duration of the double support phase can be defined as :

$$T_D = \frac{\Delta X_H^D}{\dot{X}_H^D\,(t^+)} \tag{4.8}$$

With ΔX_H^D being the horizontal hip displacement during double support and $\dot{X}_H^D\,(t^+)$ being the initial horizontal hip velocity, resulting from an inelastic impulsive impact model (see 5.2.3). During steady-state walking, the horizontal hip displacement equals the step length:

$$\lambda = \Delta X_H^S + \Delta X_H^D \tag{4.9}$$

Taking the $20 - 80\,\%$ time distribution into account, the phase durations can be calculated with:

$$T_S = 4T_D = \frac{4\lambda}{4\nu + \dot{X}_H^D\,(t^+)} \tag{4.10}$$

In the following sections, the time definitions of figure 4.5 are used. The start time of a double support phase is given by t_+, which is the instance of the touch-down of the swing leg. The end time of a double support phase is given by t_D, which is also the start time of a next single support phase. The end time of a single support phase is given by t_S. Note that in theory the impact phase is infinitely small, and that therefore t_+ actually has the same value as t_S of the preceding single support phase.

4.3.2 Double support phase

In figure 4.6 the model of the planar biped Lucy is depicted during a double support phase. In this picture the R stands for Rear, whereas the F stands for Front. Since both feet are in contact with the ground, a closed kinematic chain is formed by the two legs and the ground. Thus two holonomic constraints are imposed and the robot's number of DOF is equal to three.

$$l_1cos(\theta_1) + l_2cos(\theta_2) - l_2cos(\theta_4) - l_1cos(\theta_5) = \lambda \tag{4.11a}$$

$$l_1sin(\theta_1) + l_2sin(\theta_2) - l_2sin(\theta_4) - l_1sin(\theta_5) = \delta \tag{4.11b}$$

with l_1 and l_2 being the length of lower leg and upper leg respectively, θ_i is the absolute angle of joint i measured with respect to the horizontal axis.

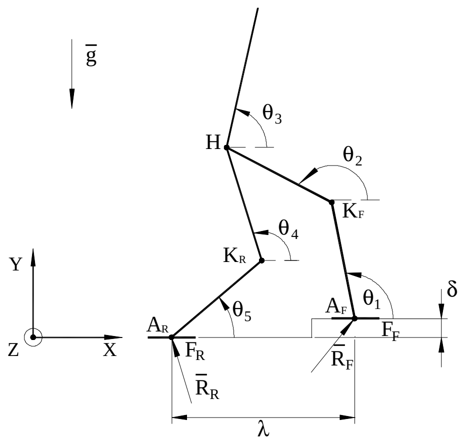

Figure 4.6: Lucy during a double support phase

Hip motion during the double support phase

Suppose that the following Lagrange coordinates are chosen to describe the motion during a double support phase:

$$\mathbf{q_D} = [X_H \, Y_H \, \theta_3]^T \tag{4.12}$$

where X_H and Y_H respectively represents the horizontal and vertical position of the hip joint and θ_3 the absolute upper body angle. The trajectory generator establishes fifth order polynomial functions for the different leg link angles. These polynomials ensure a horizontal and vertical hip motion satisfying the following boundary conditions:

$$\begin{aligned} X_H(t_+), \quad \dot{X}_H(t_+), \quad \ddot{X}_H(t_+) \quad &\rightarrow \quad X_H(t_D), \quad \dot{X}_H(t_D), \quad \ddot{X}_H(t_D) \\ Y_H(t_+), \quad \dot{Y}_H(t_+), \quad \ddot{Y}_H(t_+) \quad &\rightarrow \quad Y_H(t_D), \quad \dot{Y}_H(t_D), \quad \ddot{Y}_H(t_D) \end{aligned}$$

The boundary conditions at t_+ are calculated by an impact model, whereas those at t_D influence the values of the objective locomotion parameters as well as the natural upper body motion. In fact, polynomials for two leg links are established while the two remaining joint trajectories of the leg links are determined with the constraint equations (4.11).

Upper body motion during the double support phase

In order to derive the natural motion of the upper body during the double support phase, it is assumed that no actuator torque is acting on it. In that case, the upper body behaves as an inverted pendulum with a moving supporting point, being the

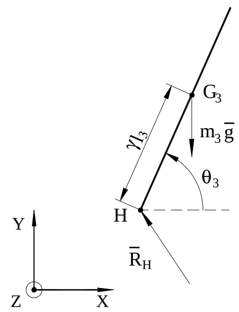

Figure 4.7: Free body diagram of the upper body [Vermeulen, 2004]

hip point H. Considering the free body diagram of the upper body in figure 4.7, and applying the angular momentum theorem with respect to the hip point H, yields:

$$\dot{\bar{\mu}}_H = \overline{HG}_3 \times m_3 \bar{g} + m_3 \left(\bar{v}_{G_3} \times \bar{v}_H \right) \tag{4.13}$$

Vermeulen [2004] showed that under the assumption of small rotations of the pendulum, equation (4.13) results in the following differential equation:

$$\ddot{\theta}_3 \approx C \left[\ddot{X}_H - \left(\ddot{Y}_H + g \right) \left(\frac{\pi}{2} - \theta_3 \right) \right] \tag{4.14}$$

with

$$C = \frac{m_3 \gamma l_3}{I_3 + \gamma^2 l_3^2 m_3} \tag{4.15}$$

and I_3 is the moment of inertia of the upper body with respect to its COG.

If the upper body is assumed to be close to an upright position, meaning $\theta_3 \approx \frac{\pi}{2}$, equation 4.14 can be further simplified:

$$\ddot{\theta}_3 \approx C \ddot{X}_H \tag{4.16}$$

A rough approximation of the natural upper body motion during double support is thus determined by the horizontal hip motion only. Integrating twice over time equation (4.16) yields:

$$\begin{aligned} \theta_3^{nat}(t) \approx\ & \theta_3(t_+) + (t - t_+)\dot{\theta}_3(t_+) \\ & + C \left[X_H(t) - X_H(t_+) - (t - t_+)\dot{X}_H(t_+) \right] \end{aligned} \tag{4.17}$$

Using expression 4.8, which defines T_D, an approximation of the upper body angle at the end of the double support phase is given by:

$$\theta_3^{nat}(t_D) \approx \theta_3(t_+) + T_D \dot{\theta}_3(t_+) \tag{4.18}$$

Next a fifth order polynomial function is established for the upper body angle, connecting the following initial and final boundary values:

$$\theta_3(t_+), \quad \dot{\theta}_3(t_+), \quad \ddot{\theta}_3(t_+) \quad \rightarrow \quad \theta_3(t_D), \quad \dot{\theta}_3(t_D), \quad \ddot{\theta}_3(t_D)$$

The boundary conditions at t_+ are determined by the impact model. Angular position and angular acceleration are calculated according to the previous discussion:

$$\theta_3\left(t_D\right) = \theta_3^{nat}(t_D) \tag{4.19}$$

$$\ddot{\theta}_3\left(t_D\right) = C\left[\ddot{X}_H\left(t_D\right) - \left(\ddot{Y}_H\left(t_D\right) + g\right)\left(\frac{\pi}{2} - \theta_3^{nat}\left(t_D\right)\right)\right] \tag{4.20}$$

The angular velocity $\dot{\theta}_3(t_D)$ is determined by the calculations for the natural upper body motion of the next single support phase.

4.3.3 Single support phase

In figure 4.8 the biped Lucy is depicted during a single support phase. Since it

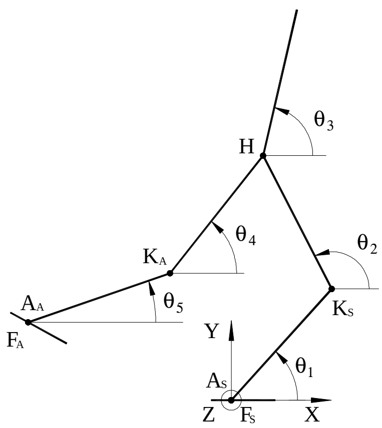

Figure 4.8: Lucy during single support phase

is assumed that the supporting foot stays in contact with the ground and does not slip during a single support phase, the number of DOF is equal to five when disregarding the dimensions of the swing foot. The upper body motion is treated separately from the hip and swing foot motion, but a dependance between these two demands for an iterative procedure. During this procedure the following three items are considered with respect to a natural (unactuated) upper body motion.

- the initial angular velocity, $\dot{\theta}_3\left(t_D\right)$, is determined such that the natural upper body rotation during single support compensates for the upper body rotation of the double support phase.

- the initial horizontal hip position, $X_H\,(t_D)$, is calculated such that the upper body angular velocity at the end of the single support phase equals the initial angular velocity.
- the initial and final horizontal hip acceleration, $\ddot{X}_H\,(t_D)$ and $\ddot{X}_H\,(t_S)$, are determined in order to have a smooth transition, at acceleration level, between successive single support and double support phases.

Hip and swing foot motion during the single support phase

Suppose that the following Lagrange coordinates are chosen to describe the motion:

$$\mathbf{q_S} = [X_H\,Y_H\,X_{F_A}\,Y_{F_A}\,\theta_3]^T \tag{4.21}$$

Assuming initially that no external ankle torque in supporting leg is exerted, so that only the knee and hip actuators are used, the robot is an underactuated mechanism. This fact is used later when writing the angular momentum equation. Two fifth order polynomial functions for the leg links of the supporting leg are established, which connect the following initial and final boundary values for the hip motion:

$$\begin{array}{ccccccc} X_H(t_D), & \dot{X}_H(t_D), & \ddot{X}_H(t_D) & \rightarrow & X_H(t_S), & \dot{X}_H(t_S), & \ddot{X}_H(t_S) \\ Y_H(t_D), & \dot{Y}_H(t_D), & \ddot{Y}_H(t_D) & \rightarrow & Y_H(t_S), & \dot{Y}_H(t_S), & \ddot{Y}_H(t_S) \end{array}$$

Two sixth order polynomial functions for the leg links of the swing leg are established, which connect the following initial, intermediate and final boundary values for the swing foot motion:

$$\begin{array}{ccc} X_{F_A}(t_D), \dot{X}_{F_A}(t_D), \ddot{X}_{F_A}(t_D) \rightarrow & X_{F_A}(t_i) \rightarrow & X_{F_A}(t_S), \dot{X}_{F_A}(t_S), \ddot{X}_{F_A}(t_S) \\ Y_{F_A}(t_D), \dot{Y}_{F_A}(t_D), \ddot{Y}_{F_A}(t_D) \rightarrow & Y_{F_A}(t_i) \rightarrow & Y_{F_A}(t_S), \dot{Y}_{F_A}(t_S), \ddot{Y}_{F_A}(t_S) \end{array}$$

The intermediate condition at $t = t_i$ is used to lift the foot, with height κ, whenever an obstacle has to be avoided during the swing phase. Note that in all cases

$$\dot{X}_{F_A}(t_D) = \ddot{X}_{F_A}(t_D) = 0 = \dot{Y}_{F_A}(t_D) = \ddot{Y}_{F_A}(t_D)$$

Which is partly a choice and partly a consequence of the feet remaining fixed to the ground during the double support phase.

Upper body motion during the single support phase

In order to obtain a natural upper body motion, it is initially assumed that the ankle actuator is not used. In that case one can write the angular momentum equation with respect to the ankle joint of the supporting foot as follows:

$$\dot{\bar{\mu}}_{F_S} = \overline{FG} \times M\bar{g} = -Mg\,(X_G - X_{F_S})\,\bar{1}_z \tag{4.22}$$

where X_G is the horizontal position of the global COG.

The kinematical expression of the angular momentum is calculated as:

$$\bar{\mu}_{F_S} = \sum_{i=1}^{5} \left(\overline{F_S G}_i \times m_i \dot{\overline{F_S G}}_i + I_i \dot{\theta}_i \bar{1}_z \right) = \left(A_3 \dot{\theta}_3 + h \right) \bar{1}_z \tag{4.23}$$

with the function h being independent of the angular velocity of the upper body $\dot{\theta}_3$. The complete expressions for the functions h and A_3 can be found in [Vermeulen, 2004].

Figure 4.9 depicts an example of how the upper body angle should evolve during both single and double support phases. The natural upper body angle rotation

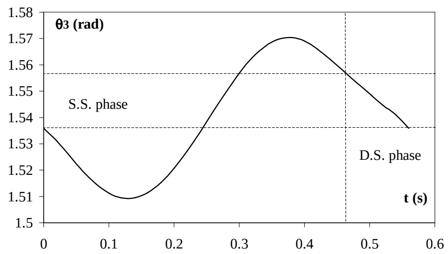

Figure 4.9: Desired upper body angle course [Vermeulen, 2004]

during single support should compensate the rotation induced during double support. Since in the short double support phase the upper body angular velocity does not vary much, the initial and final angular velocity during single support should be equalized by the natural upper body motion.

Naturally achieving upper body angle

If the origin of the coordinate system is placed at the ankle joint of the supporting foot, X_{F_S} becomes zero. Then integrating (4.22) from $u = t_D$ to $u = t$, gives:

$$\mu_{F_S}(t) - \mu_{F_S}(t_D) = -Mg \int_{t_D}^{t} X_G \, du \tag{4.24}$$

A second integration from $t = t_D$ to $t = t_S$ yields:

$$\int_{t_D}^{t_S} \mu_{F_S}(t) \, dt - \mu_{F_S}(t_D) T_S = -Mg \int_{t_D}^{t_S} (T_S - t) \, X_G \, dt \tag{4.25}$$

Now introducing (4.23) into the lhs of (4.25) and solving for $\dot{\theta}_3\,(t_D)$ gives:

$$\dot{\theta}_3\,(t_D) = F + \frac{1}{T_S A_3\,(t_D)} \int_{t_D}^{t_S} A_3 \dot{\theta}_3\,dt \tag{4.26}$$

with

$$F = \frac{1}{A_3(t_D)} \Big[-Mg \int_{t_D}^{t_S} (T_S - t)\, X_G\,dt + h\,(t_D)\, T_S - \int_{t_D}^{t_S} h\,dt \Big] \tag{4.27}$$

It has been shown by Vermeulen [2004] that, when assuming small rotations of the upper body in the neighborhood of $\frac{\pi}{2}$, as well as small vertical motions of the hip point, the function A_3 can be approximated as a constant:

$$A_3(t) \approx I_3 + m_3\gamma^2 l_3^2 + m_3\gamma l_3 Y_H(t) \approx A_3(t_D) \quad (t_D \leq t \leq t_S) \tag{4.28}$$

Expression (4.26) then becomes:

$$\dot{\theta}_3\,(t_D) = F + \frac{\theta_3(t_S) - \theta_3(t_D)}{T_S} = F + \frac{\Delta\theta_3^S}{T_S} \tag{4.29}$$

Now recalling expression (4.18), which calculates the upper body rotation during the double support phase:

$$\Delta\theta_3^D = T_D \dot{\theta}_3(t_+) \tag{4.30}$$

with $\dot{\theta}_3(t_+)$ the initial upper body angular velocity of the preceding double support phase. Demanding that $\Delta\theta_3^D + \Delta\theta_3^S = 0$ allows one to determine a necessary initial value for the upper body angular velocity during single support:

$$\dot{\theta}_3\,(t_D) = F - \frac{T_D}{T_S} \dot{\theta}_3\,(t_+) \tag{4.31}$$

This specific value for the upper body angular velocity has to be used as end boundary value to construct the polynomial function for the upper body during the preceding double support phase (see section 4.3.2). In this way the upper body rotation of the double support phase is compensated during the next single support phase, without the use of an ankle actuator.

Naturally achieving upper body angular velocity

Evaluating (4.24) at $t = t_S$ and introducing the kinematical expression (4.23) yields:

$$\dot{\theta}_3(t_S) = \dot{\theta}_3(t_D) + \frac{1}{A_3(t_D)} \Big[h(t_D) - h(t_S) - Mg \int_{t_D}^{t_S} X_G\,dt \Big] \tag{4.32}$$

This equation is used to manipulate the final value of the angular velocity $\dot{\theta}_3(t_S)$ which is chosen such that:

$$\dot{\theta}_3(t_S) = \dot{\theta}_3(t_D) \tag{4.33}$$

Figure 4.9 shows that during double support $\dot{\theta}_3$ after all does not vary much. Condition (4.33) can be achieved by manipulating the rhs of equation (4.32) by iteratively shifting the horizontal position of the hip point $X_H(t_D)$ at the end of the double support phase. This means that the configuration of the robot at the end of the double support phase is determined by the succeeding single support phase.

Smooth Transition Single Support to Double Support

Evaluating (4.22) at $t = t_D$ and introducing the kinematical expression (4.23), gives:

$$A_3(t_D)\ddot{\theta}_3(t_D) + \dot{A}_3(t_D)\dot{\theta}_3(t_D) + \dot{h}(t_D) = -Mg\big[X_G(t_D) - X_{F_S}(t_D)\big] \tag{4.34}$$

Note that this equation corresponds to a zero ankle torque, or in other words to a ZMP located exactly at the ankle joint. Since $\ddot{\theta}_3(t_D)$ is imposed by the polynomial function during the double support phase, introducing expression (4.20) in (4.34) yields a condition which has to be satisfied at the beginning of the single support phase. Satisfying this equation results in a transition from double to single support phase with a ZMP coinciding with the ankle joint. In practice this can be achieved e.g. by tuning the hip accelerations $\ddot{X}_H(t_D)$ and $\ddot{Y}_H(t_D)$. The value for $\ddot{Y}_H(t_D)$ is chosen while $\ddot{X}_H(t_D)$ is calculated by combining (4.34) with (4.20).

An analogous reasoning can be done at the end of the single support phase $t = t_S$, yielding a condition on $\ddot{X}_H(t_S)$ and $\ddot{Y}_H(t_S)$. This condition has to be satisfied in order to have the ZMP located at the ankle joint of the supporting foot before the impact occurs.

Upper body tracking function

In the preceding paragraphs, conditions on boundary values were formulated based on natural upper body motion, such that the upper body is steered without requiring an ankle actuator. Next a fifth order polynomial function for the upper body absolute rotation is constructed with :

$$\theta_3(t_D), \quad \dot{\theta}_3(t_D), \quad \ddot{\theta}_3(t_D) \quad \rightarrow \quad \theta_3(t_S), \quad \dot{\theta}_3(t_S), \quad \ddot{\theta}_3(t_S)$$

Here, $\theta_3(t_D)$, $\ddot{\theta}_3(t_D)$ and $\ddot{\theta}_3(t_S)$ directly result from the equations during double support. While $\theta_3(t_S)$ and $\dot{\theta}_3(t_S)$ result from the expected natural upper body rotation during single support and $\dot{\theta}_3(t_S)$ was calculated in order to induce this natural motion. The constructed polynomial function is a good approximation of the natural upper body motion. Consequently, only low ankle joint torques are required to track this function, resulting in a ZMP which stays in the vicinity of the ankle joint.

Note also that due to the developed strategy during the double support phase, the ZMP automatically transfers from the rear ankle to the front ankle, without requiring external torques. Indeed, polynomial trajectories are constructed, connecting two successive single support phases, each with the ZMP located exactly at the ankle joint of its supporting foot.

4.4 Tracking controller

The task of a tracking controller is to apply joint torques such that the robot follows the trajectories as imposed by a trajectory generator. Due to the specific nature of the pneumatic actuation system, this tracking controller has several essential blocks which are depicted in figure 4.10. The scheme presented in this figure is an extension of the controller as was proposed in chapter 3. The inverse dynamics unit determines the torque values required to track the desired joint trajectories. These feedforward torque calculations are based on the robot dynamics for the single and double support phase. The calculations demand a different approach for each phase.

For each joint a delta-p unit translates the required torques into desired pressure levels for the two muscles of the antagonistic set-up. Additionally, a correction Δp_{pi}, calculated by a local PI controller, provides a local position feedback to cope with modelling errors. Finally, a bang-bang controller determines the necessary valve actions to set the correct pressures in the muscles. The trajectory generator, inverse dynamics and delta-p unit are implemented on a central PC, since these controllers require a substantial computational effort. The PI controller and the bang-bang pressure controller are locally implemented on micro-controller units (see chapter 6). In the next sections the different elements of the control structure are discussed in more detail.

As was mentioned before, the swing foot is kept horizontally during the leg swing. Since this foot has to be controlled by a muscle pair, the dynamics of this link are taken into account. The muscle pressure courses should be defined during the swing phase according to an applied ankle joint torque on the swing foot. The stance foot on the other hand is not included, since this foot is on the ground and only has a marginal influence on the ground reaction forces and the ZMP position. Thus during the single support phase the robot has now 6 DOF. The following Lagrange coordinates are used to describe the motion of the robot.

$$\mathbf{q} = \left[\theta_1\, \theta_2\, \theta_3\, \theta_4\, \theta_5\, \theta_6\right]^T \tag{4.35}$$

These coordinates are the absolute angles of each link of the robot, apart from the stance foot, measured with respect to the horizontal axis.

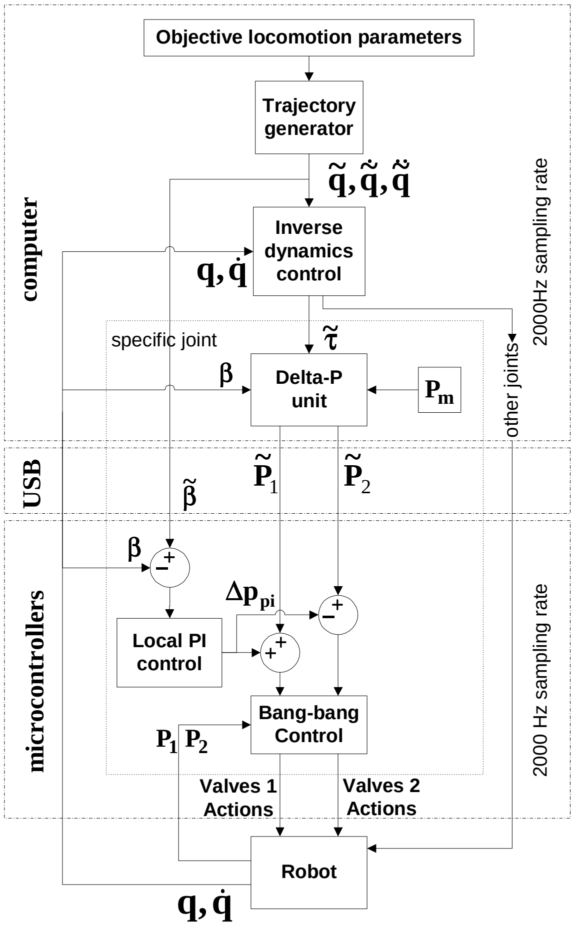

Figure 4.10: Overview of the joint control architecture

Figure 4.11 shows the definition of the chosen Lagrange coordinates on the robot depicted during a single support phase. For the double support phase the same Lagrange coordinates are used, but the swing foot stands in front of the stance foot and the coordinate θ_6 of this link is a constant.

4.4.1 Inverse dynamics control during single support

During the single support phase the robot's supporting foot is assumed to remain in full contact with the ground. This condition is guaranteed as long as the ZMP stays within the physical boundaries of the supporting foot and if the acceleration of the COG of the robot does not reach $-g$. Successful tracking of the generated joint

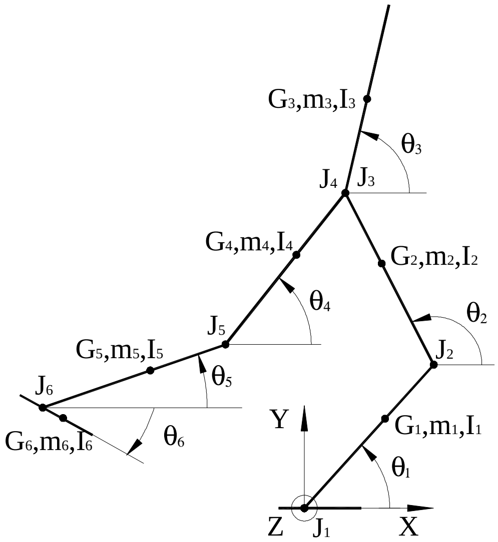

Figure 4.11: Model of the biped in single support

trajectories should implicitly ensure the correct ZMP location, since the dynamics of the robot were taken into account by the trajectory generator. So during single support, the robot can be seen as a multi-link serial robot for which standard nonlinear tracking techniques of manipulator control are utilized. Here a computed torque method as described by Slotine and Li [1991] is proposed. This method, also called feedback linearization, linearizes the nonlinear input-output relation for the mechanical dynamic equations, describing the robot motion. These dynamic equations are written as [Spong and Vidyasagar, 1989]:

$$D(\mathbf{q})\ddot{\mathbf{q}} + C(\mathbf{q},\dot{\mathbf{q}})\dot{\mathbf{q}} + G(\mathbf{q}) = \boldsymbol{\tau} \tag{4.36}$$

with $D(\mathbf{q})$ the inertia matrix, $C(\mathbf{q},\dot{\mathbf{q}})$ the centrifugal/coriolis matrix, $G(\mathbf{q})$ the gravitational torque/force vector. The torque vector $\boldsymbol{\tau}$ contains the net torques acting on each link of the robot since the equations of motion are written in absolute coordinates (see figure 4.12):

$$\boldsymbol{\tau} = \begin{bmatrix} \tau_1 \\ \tau_2 \\ \tau_3 \\ \tau_4 \\ \tau_5 \\ \tau_6 \end{bmatrix} = \begin{bmatrix} \tau_{K_s} - \tau_{A_s} \\ \tau_{H_s} - \tau_{K_s} \\ -\tau_{H_s} - \tau_{H_a} \\ \tau_{H_a} - \tau_{K_a} \\ \tau_{K_a} - \tau_{A_a} \\ \tau_{A_a} \end{bmatrix} \tag{4.37}$$

The H, K and A stands for "Hip", "Knee" and "Ankle" respectively, a stands for "air", and s for "stance". Expression (4.37) gives the relations between the net

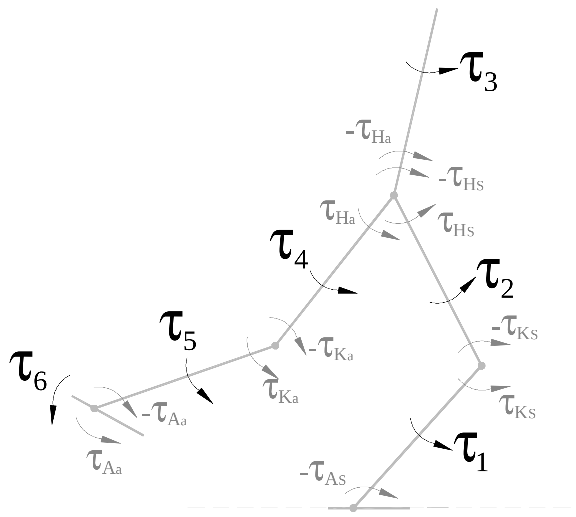

Figure 4.12: Definition of net torques and joint torques

torques and the applied joint torques. The complete derivation of the dynamic model of "Lucy" can be found in appendix C.

The computed torque method determines the torque vector $\tilde{\boldsymbol{\tau}}$. The calculation of these torques is performed by feeding forward the desired trajectory accelerations $\ddot{\tilde{\mathbf{q}}}$ and by feeding back measured positions $\mathbf{q}$ and velocities $\dot{\mathbf{q}}$ in order to cancel the nonlinear centrifugal and gravitational terms in (4.36). A secondary PD-feedback loop is added to improve control performance. This results in the following calculation:

$$\tilde{\boldsymbol{\tau}} = \hat{C}(\mathbf{q}, \dot{\mathbf{q}})\dot{\mathbf{q}} + \hat{G}(\mathbf{q}) + \hat{D}(\mathbf{q})\left[\ddot{\tilde{\mathbf{q}}} - K_d(\dot{\mathbf{q}} - \dot{\tilde{\mathbf{q}}}) - K_p(\mathbf{q} - \tilde{\mathbf{q}})\right] \tag{4.38}$$

The matrices $\hat{D}$, $\hat{C}$ and $\hat{G}$ contain estimated values of the inertia, centrifugal and gravitational parameters. The feedback diagonal gain matrices K_d and K_p are tuned in order to make each mechanical link behave as critically damped, in case the modelling would be perfect. Since unavoidable modelling errors of the mechanics such as parameter estimation errors, friction and the actuator limitations occur, the tracking performance will differ in reality. Therefore the feedback gains will have to be manually adjusted afterwards.

4.4.2 Inverse dynamics control during double support

Immediately after impact of the swing leg, three geometrical constraints are imposed on the motion of the system. Two of them have already been introduced for the closed kinematic chain of the leg links by equations (4.11). The third constraint expresses that the swing foot stays on the ground, with θ_6 being a constant. The three constraints are summarized as follows :

$$l_1cos(\theta_1) + l_2cos(\theta_2) - l_2cos(\theta_4) - l_1cos(\theta_5) - X_{A_F}^{td} = 0 \tag{4.39a}$$

$$l_1sin(\theta_1) + l_2sin(\theta_2) - l_2sin(\theta_4) - l_1sin(\theta_5) - Y_{A_F}^{td} = 0 \tag{4.39b}$$

$$\theta_6 - C^{te} = 0 \tag{4.39c}$$

with $X_{A_F}^{td}$ and $Y_{A_F}^{td}$ the actual horizontal and vertical position of the front ankle point at touch down. The number of DOF during double support is reduced to 3, but the same 6 Lagrange coordinates (4.35) are used. The equations of motion of single support are adapted with the three geometrical constraints as follows [Jalón and Bayo, 1994]:

$$D\big(\mathbf{q}\big)\ddot{\mathbf{q}} + C\big(\mathbf{q}, \dot{\mathbf{q}}\big)\dot{\mathbf{q}} + G\big(\mathbf{q}\big) = \boldsymbol{\tau} + J^T\big(\mathbf{q}\big)\boldsymbol{\Lambda} \tag{4.40}$$

with $J\big(\mathbf{q}\big)$ the Jacobian matrix, which is calculated by taking the derivative of the constraint equations with respect to the generalized Lagrange coordinates:

$$J\big(\mathbf{q}\big) = \begin{bmatrix} -l_1sin(\theta_1) & -l_2sin(\theta_2) & 0 & l_2sin(\theta_4) & l_1sin(\theta_5) & 0 \\ l_1cos(\theta_1) & l_2cos(\theta_2) & 0 & -l_2cos(\theta_4) & -l_1cos(\theta_5) & 0 \\ 0 & 0 & 0 & 0 & 0 & 1 \end{bmatrix} \tag{4.41}$$

and $\boldsymbol{\Lambda}$ the vector of Lagrange multipliers:

$$\boldsymbol{\Lambda} = \big[\lambda_1\, \lambda_2\, \lambda_3\big]^T \tag{4.42}$$

Since each joint is actuated, the number of applied joint torques is 6. The number of DOF during double support is however reduced to 3, which makes the system overactuated during this phase. An infinite combination of torques can be applied to realize a trajectory tracking. In the following calculations one specific solution is selected. These calculations are based on an extended version of the method proposed by Shih and Gruver [1992]. The latter omitted the centrifugal and coriolis terms, which are taken into account in this work. Also, an adaptation of their pseudo-inverse calculation is proposed in function of the specific goals of the trajectory generator.

The 6 Lagrange coordinates can be divided into dependent and independent coordinates as follows:

$$\mathbf{q_1} = \big[\theta_1\, \theta_2\, \theta_3\big]^T \qquad \mathbf{q_2} = \big[\theta_4\, \theta_5\, \theta_6\big]^T \tag{4.43}$$

where $\mathbf{q_1}$ are the independent and $\mathbf{q_2}$ the dependent coordinates. The independent coordinates describe the absolute angle of the upper body and the orientation of the rear leg, while the dependent coordinates describe the front leg and the front foot orientation. With these separate coordinates the constraints (4.39) can be rewritten in the following form:

$$Z(\mathbf{q}) = Z_1(\mathbf{q_1}) + Z_2(\mathbf{q_2}) = \mathbf{0} \tag{4.44}$$

with:

$$Z_1(\mathbf{q_1}) = \begin{bmatrix} l_1 cos(\theta_1) + l_2 cos(\theta_2) \\ l_1 sin(\theta_1) + l_2 sin(\theta_2) \\ 0 \end{bmatrix} \tag{4.45}$$

and

$$Z_2(\mathbf{q_2}) = \begin{bmatrix} -l_2 cos(\theta_4) - l_1 cos(\theta_5) - X_{A_F}^{td} \\ -l_2 sin(\theta_4) - l_1 sin(\theta_5) - Y_{A_F}^{td} \\ \theta_6 - C^{te} \end{bmatrix} \tag{4.46}$$

Analogously, the Jacobian matrix is also divided into two different parts J_1 and J_2:

$$J(\mathbf{q}) = \frac{\partial Z}{\partial \mathbf{q}} = (J_1\, J_2) \tag{4.47}$$

with

$$J_1(\mathbf{q_1}) = \frac{\partial Z_1}{\partial \mathbf{q_1}} = \begin{bmatrix} -l_1 sin(\theta_1) & -l_2 sin(\theta_2) & 0 \\ l_1 cos(\theta_1) & l_2 cos(\theta_2) & 0 \\ 0 & 0 & 0 \end{bmatrix} \tag{4.48}$$

and

$$J_2(\mathbf{q_2}) = \frac{\partial Z_2}{\partial \mathbf{q_2}} = \begin{bmatrix} l_2 sin(\theta_4) & l_1 sin(\theta_5) & 0 \\ -l_2 cos(\theta_4) & -l_1 cos(\theta_5) & 0 \\ 0 & 0 & 1 \end{bmatrix} \tag{4.49}$$

The constraint equation and the Jacobian matrix (4.47) are used to write the derivatives of the dependant coordinates as a function of the independent coordinates. Differentiating the constraint equation gives

$$\dot{Z}(\mathbf{q}) = \mathbf{0} \Leftrightarrow J_1(\mathbf{q_1})\,\dot{\mathbf{q}}_\mathbf{1} + J_2(\mathbf{q_2})\,\dot{\mathbf{q}}_\mathbf{2} = \mathbf{0} \tag{4.50}$$

The first derivatives of the dependent coordinates are then obtained:

$$\dot{\mathbf{q}}_\mathbf{2} = -J_2^{-1} J_1 \dot{\mathbf{q}}_\mathbf{1} \tag{4.51}$$

The Jacobian matrix J_2 is invertible when det $J_2 \neq 0$, or:

$$det(J_2) = l_1 sin(\theta_5)\, l_2 cos(\theta_4) - l_2 sin(\theta_4)\, l_1 cos(\theta_5) \neq 0 \tag{4.52}$$

Or, if both lengths of upper and lower leg (l_1 and l_2) are identical, which is the case for the robot "Lucy":

$$det(J_2) = l^2 sin(\theta_5 - \theta_4) \neq 0 \tag{4.53}$$

meaning that a fully stretched front leg corresponds to a singular configuration. For biped robots this situation can be avoided by walking with sufficiently bent knees [Kajita et al., 2001].

Differentiating again (4.50) once more gives

$$\dot{J}_1\dot{\mathbf{q}}_\mathbf{1} + J_1\ddot{\mathbf{q}}_\mathbf{1} + \dot{J}_2\dot{\mathbf{q}}_\mathbf{2} + J_2\ddot{\mathbf{q}}_\mathbf{2} = 0 \tag{4.54}$$

The second derivatives of the dependent coordinates are then obtained:

$$\begin{aligned}\ddot{\mathbf{q}}_\mathbf{2} &= J_2^{-1}\left(-\dot{J}_1\dot{\mathbf{q}}_\mathbf{1} - J_1\ddot{\mathbf{q}}_\mathbf{1} - \dot{J}_2\dot{\mathbf{q}}_\mathbf{2}\right) \\ &= \left(-J_2^{-1}\dot{J}_1 + J_2^{-1}\dot{J}_2 J_2^{-1}J_1\right)\dot{\mathbf{q}}_\mathbf{1} - J_2^{-1}J_1\ddot{\mathbf{q}}_\mathbf{1}\end{aligned} \tag{4.55}$$

Additionally, the equations of motion (4.40) can be divided as follows:

$$\begin{cases} D_{11}\ddot{\mathbf{q}}_\mathbf{1} + D_{12}\ddot{\mathbf{q}}_\mathbf{2} + C_{11}\dot{\mathbf{q}}_\mathbf{1} + C_{12}\dot{\mathbf{q}}_\mathbf{2} + G_1 = J_1^T\mathbf{\Lambda} + \boldsymbol{\tau}_\mathbf{1} \\ D_{21}\ddot{\mathbf{q}}_\mathbf{1} + D_{22}\ddot{\mathbf{q}}_\mathbf{2} + C_{21}\dot{\mathbf{q}}_\mathbf{1} + C_{22}\dot{\mathbf{q}}_\mathbf{2} + G_2 = J_2^T\mathbf{\Lambda} + \boldsymbol{\tau}_\mathbf{2} \end{cases} \tag{4.56}$$

where

$$\hat{D}(\mathbf{q}) = \begin{bmatrix} D_{11} & D_{12} \\ D_{21} & D_{22} \end{bmatrix} \tag{4.57}$$

$$\hat{C}(\mathbf{q}, \dot{\mathbf{q}}) = \begin{bmatrix} C_{11} & C_{12} \\ C_{21} & C_{22} \end{bmatrix} \tag{4.58}$$

$$\hat{G}(\mathbf{q}) = \begin{bmatrix} G_1 \\ G_2 \end{bmatrix} \tag{4.59}$$

and

$$\boldsymbol{\tau}_\mathbf{1} = \left[\tau_1\,\tau_2\,\tau_3\right]^T \qquad \boldsymbol{\tau}_\mathbf{2} = \left[\tau_4\,\tau_5\,\tau_6\right]^T \tag{4.60}$$

Note that, since these calculations are used to define a feedforward control loop, the matrices D, C and G, which contain dynamical expressions, are replaced by $\hat{D}$, $\hat{C}$ and $\hat{G}$ respectively. These are calculated by using estimated values of the inertial parameters. The equations of motion (4.56) are a set of 6 differential equations, containing 3 additional unknown variables of the Lagrange multiplier $\mathbf{\Lambda}$. This set is transformed into three equations by eliminating the Lagrange multipliers in (4.56):

$$\begin{aligned} D_{11}\ddot{\mathbf{q}}_\mathbf{1} + D_{12}\ddot{\mathbf{q}}_\mathbf{2} - J_1^T(J_2^T)^{-1}D_{21}\ddot{\mathbf{q}}_\mathbf{1} - J_1^T(J_2^T)^{-1}D_{22}\ddot{\mathbf{q}}_\mathbf{2} \\ +C_{11}\dot{\mathbf{q}}_\mathbf{1} + C_{12}\dot{\mathbf{q}}_\mathbf{2} + G_1 - J_1^T\left(J_2^T\right)^{-1}(C_{21}\dot{\mathbf{q}}_\mathbf{1} + C_{22}\dot{\mathbf{q}}_\mathbf{2} + G_2) \\ = \boldsymbol{\tau}_\mathbf{1} - J_1^T(J_2^T)^{-1}\boldsymbol{\tau}_\mathbf{2} \end{aligned} \tag{4.61}$$

Next, the derivatives of the dependent coordinates are eliminated by substituting (4.51) and (4.55) in equation (4.61):

$$\hat{D}'(\mathbf{q})\,\ddot{\mathbf{q}}_\mathbf{1} + \hat{C}'(\mathbf{q}, \dot{\mathbf{q}}_\mathbf{1})\,\dot{\mathbf{q}}_\mathbf{1} + \hat{G}'(\mathbf{q}) = \boldsymbol{\tau}_\mathbf{1} - J_1^T(J_2^T)^{-1}\boldsymbol{\tau}_\mathbf{2} \tag{4.62}$$

with

$$\hat{D}'(\mathbf{q}) = D_{11} - D_{12}J_2^{-1}J_1 - J_1^T(J_2^T)^{-1}D_{21} + J_1^T(J_2^T)^{-1}D_{22}J_2^{-1}J_1 \tag{4.63}$$

$$\begin{aligned}\hat{C}'(\mathbf{q}, \dot{\mathbf{q}}_1) &= -D_{12}J_2^{-1}\dot{J}_1 + D_{12}J_2^{-1}\dot{J}_2J_2^{-1}J_1 \\ &\quad - J_1^T(J_2^T)^{-1}\left(-D_{22}J_2^{-1}\dot{J}_1 + D_{22}J_2^{-1}\dot{J}_2J_2^{-1}J_1 + C_{21} - C_{22}J_2^{-1}J_1\right) \\ &\quad + C_{11} - C_{12}J_2^{-1}J_1 \end{aligned}\tag{4.64}$$

$$\hat{G}'(\mathbf{q}) = G_1 - J_1^T(J_2^T)^{-1}G_2 \tag{4.65}$$

In (4.62) $\mathbf{q}$, $\dot{\mathbf{q}}_1$ and $\ddot{\mathbf{q}}_1$ are replaced by their desired values, $\tilde{\mathbf{q}}$, $\dot{\tilde{\mathbf{q}}}_1$ and $\ddot{\tilde{\mathbf{q}}}_1$, computed by the trajectory generator. The three independent coordinates $\tilde{\mathbf{q}}_1$ and their first and second derivatives are obtained by using the polynomial functions for these coordinates. The dependent coordinates $\tilde{\mathbf{q}}_2$ are obtained from the geometrical constraint equations (4.39). Next, a feedforward torque $\tilde{\boldsymbol{\tau}}_\mathbf{f}$, required to track these desired reference trajectories, is calculated.

The rhs of equation (4.62) can be rewritten as:

$$\tilde{\boldsymbol{\tau}}_1 - J_1^T(J_2^T)^{-1}\tilde{\boldsymbol{\tau}}_2 = \{W_1 - J_1^T(J_2^T)^{-1}W_2\}\tilde{\boldsymbol{\tau}}_\mathbf{f} = W\tilde{\boldsymbol{\tau}}_\mathbf{f} \tag{4.66}$$

with

$$W_1 = [I_{3x3}\, 0_{3x3}] \qquad W_2 = [0_{3x3}\, I_{3x3}] \tag{4.67}$$

and

$$\tilde{\boldsymbol{\tau}}_\mathbf{f} = \left[\tilde{\boldsymbol{\tau}}_1\, \tilde{\boldsymbol{\tau}}_2\right]^T \tag{4.68}$$

Since W has dimensions 3×6 and the lhs of equation (4.62) is a three dimensional vector, the computed torque is calculated with a pseudo-inverse of matrix W:

$$\tilde{\boldsymbol{\tau}}_\mathbf{f} = W^+\left[\hat{D}'(\tilde{\mathbf{q}})\,\ddot{\tilde{\mathbf{q}}}_1 + \hat{C}'\left(\tilde{\mathbf{q}}, \dot{\tilde{\mathbf{q}}}_1\right)\dot{\tilde{\mathbf{q}}}_1 + \hat{G}'(\tilde{\mathbf{q}})\right] \tag{4.69}$$

Expression (4.69) selects a certain solution, but it is not an appropriate one, since the ankle torques are not demanded to be zero during the double support phase. The strategy of the joint trajectory generator was to achieve small ankle torques during single support. It is therefore desirable to have the same condition during double support. Moreover, small ankle torques allow these joints to be used by the ZMP observer as depicted in figure 4.1. This module can adapt the ZMP trajectory by applying extra ankle torques in order to influence ground reaction forces, but this issue is beyond the scope of this work. So before applying a psuedo inverse in (4.69), the Moore-Penrose inverse [Rao and Mitra, 1971], an extra condition is added which expresses zero ankle torques during the double support phase. The front foot is taken into account in the equations of motion and this foot is forced to stay on the ground ($\theta_6 = C^{st}$). Consequently the calculated ankle torque of the front foot, represented by $\tilde{\boldsymbol{\tau}}_{\mathbf{f}}(6)$, is already zero. Note that $\tilde{\boldsymbol{\tau}}_{\mathbf{f}}$ represents net torques acting on each link. Thus, recalling (4.37), the ankle torque of the rear foot can be calculated by adding all the net torques. Demanding that the rear ankle torque has to be zero, is thus expressed by including the following expression:

$$\sum_{i=1}^{5} \tilde{\boldsymbol{\tau}}_{\mathbf{f}}(i) = 0 \tag{4.70}$$

This results in the following calculation:

$$\tilde{\boldsymbol{\tau}}_{\mathbf{f}} = \begin{bmatrix} 1 & 1 & 1 & 1 & 1 & 0 \\ W_{11} & & & & & \\ & & \ldots & & & \\ & & & & & W_{36} \end{bmatrix}^{+} \begin{bmatrix} 0 \\ \hat{D}'(\tilde{\mathbf{q}})\ddot{\tilde{\mathbf{q}}}_{\mathbf{1}} + \hat{C}'\left(\tilde{\mathbf{q}}, \dot{\tilde{\mathbf{q}}}_{\mathbf{1}}\right)\dot{\tilde{\mathbf{q}}}_{\mathbf{1}} + \hat{G}'(\tilde{\mathbf{q}}) \end{bmatrix} \tag{4.71}$$

And finally, as was done for the computed torque during the single support phase, a PD-feedback loop is added to cope with modelling errors and influence the tracking performance.

$$\tilde{\boldsymbol{\tau}} = \tilde{\boldsymbol{\tau}}_{\mathbf{f}} - K_d\big(\dot{\mathbf{q}} - \dot{\tilde{\mathbf{q}}}\big) - K_p\big(\mathbf{q} - \tilde{\mathbf{q}}\big) \tag{4.72}$$

The parameters of the diagonal gain matrices K_d and K_p of the feedback loop are manually tuned.

4.4.3 Delta-p unit

In the previous section the net torque values for each link were calculated. These net torques can be transformed into the required joint torques with (4.37). On the other hand, the torques generated by each joint are determined by the pressures in the antagonistic muscle system. Therefore the delta-p unit is used to transform the calculated torques into required pressure levels. For each muscle pair, such a controller is provided and dimensioned according to its specific torque characteristic.

The generated torque in an antagonistic muscle setup was already discussed in 3.2. For the sake of convenience, the formulation is repeated here. The generated torque is calculated with the kinematical model of the leverage and rod mechanism, combined with the estimated force function of the muscles (2.33) and the applied gauge pressures. This can be represented by the following calculation:

$$\begin{aligned} \tau &= p_1 l_{0_1}^2 r_1(\beta) f_1(\beta) - p_2 l_{0_2}^2 r_2(\beta) f_2(\beta) \\ &= p_1 t_1(\beta) - p_2 t_2(\beta) \end{aligned} \tag{4.73}$$

with τ the generated torque and β the locally defined relative joint angle. p_i is the applied gauge pressure in the respective muscle with initial unpressurized length l_{0_i} and $f_i(\beta)$ characterizes the force function of the respective muscle. The kinematical transformation from forces to torques are represented by $r_1(\beta)$ and $r_2(\beta)$ which results, together with the muscle force characteristics, in the torque functions $t_1(\beta)$ and $t_2(\beta)$. These nonlinear functions are determined by the choices made during the design phase and depend on the specific joint angle β.

Equation (4.73) is used to determine the two desired gauge pressure $\tilde{p}_1$ and $\tilde{p}_2$ for each muscle pair. These two pressures are generated starting from a mean pressure value p_m while adding and subtracting a $\Delta\tilde{p}$ value:

$$\tilde{p}_1 = p_m + \Delta\tilde{p} \tag{4.74a}$$

$$\tilde{p}_2 = p_m - \Delta\tilde{p} \tag{4.74b}$$

The mean value p_m normally influences the joint stiffness and can be controlled in order to influence the natural dynamics of the system. Note that the structure of (4.74) slightly differs from (3.21). Here a simplified version of the delta-p unit is implemented, combined with a chosen constant p_m value for each joint. At this moment the controller of the complete biped does not yet incorporate the exploitation of natural dynamics as was discussed in chapter 3. Combining the equations (4.74) with equation (4.73), allows one to calculate the $\Delta\tilde{p}$ value required to generate the torque originating from the inverse dynamics control module:

$$\Delta\tilde{p} = \frac{\tilde{\tau} + p_m\left[\left(\hat{t}_2(\beta) - \hat{t}_1(\beta)\right]\right.}{\hat{t}_2(\beta) + \hat{t}_1(\beta)} \tag{4.75}$$

For each joint a delta-p unit performs a feedforward calculation from torque to pressure level and uses estimated values of the respective muscle force function and kinematic data of the pull rod mechanism. The force as a function of contraction curve of the PPAM shows a hysteresis (see 2.3) which can result in a non-negligible force estimation error of up to 5 %. Measurements of the kinematic data of the different pull rod systems create additional errors for the estimated torque functions $\hat{t}_1$ and $\hat{t}_2$. A local PI-feedback controller is implemented to cope with the effect of these estimation errors on the pressure difference $\Delta\tilde{p}$.

4.4.4 Local PI and bang-bang pressure controller

Errors induced by the delta-p unit specifically act at joint level, therefore an extra local position feedback structure per joint is added to the global feedback, which is implemented in the inverse dynamics controller. Thus, for each joint a position feedback structure is directly acting at pressure level by adding and subtracting an additional Δp_{pi} in equations (4.74):

$$\tilde{p}_1 = p_m + \Delta\tilde{p} + \Delta p_{pi} \tag{4.76a}$$

$$\tilde{p}_2 = p_m - \Delta\tilde{p} - \Delta p_{pi} \tag{4.76b}$$

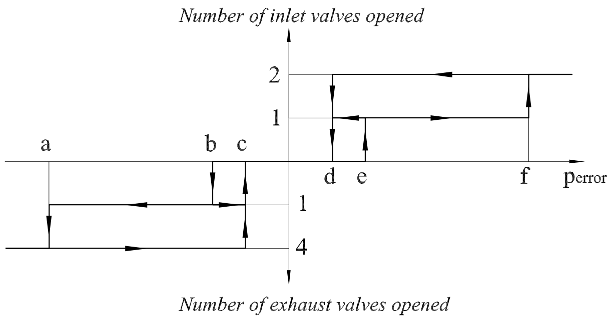

Figure 4.13: Multilevel bang-bang pressure control scheme

The value of Δp_{pi} is determined by a proportional and integral feedback part, calculated at position level:

$$\Delta p_{pi} = K_{p_{local}} \big(\beta - \tilde{\beta}\big) + K_{i_{local}} \sum_{s} \big(\beta - \tilde{\beta}\big) \Delta t_{local} \tag{4.77}$$

with $K_{p_{local}}$ and $K_{i_{local}}$ the local feedback gains, β the joint angle measured each sample s and $\tilde{\beta}$ the desired joint angle originating from the calculated reference functions. The sampling time Δt_{local} is currently set at 0.5 ms because of the refresh rate of 2000 Hz on the micro-controller units. There is no derivative part in the local feedback structure due to the limited computational capacity of the micro-controller units. Calculations of derivatives demand a substantial computational effort in comparison with the calculations for the pure proportional integral part since the angular velocity is not measured directly.

For each joint the two desired pressure values $\tilde{p}_1$ and $\tilde{p}_2$ are sent to the respective local muscle pressure controller, which is responsible for tracking the required muscle pressure. In order to realize a lightweight rapid and accurate pressure control, fast switching on-off valves are used. For the inlet and the exhaust of a muscle respectively 2 and 4 valves are placed in a parallel configuration. The hardware of this valve system is described in chapter 6. The pressure controller itself is achieved by a multilevel bang-bang structure with various reaction levels depending on the pressure error. Figure 4.13 depicts the working principle of this control scheme and table 4.1 gives the currently applied reaction levels and the respective valve actions. The reaction levels have to be manually tuned. The pressure error is defined as $p_{error} = \tilde{p} - p$, with $\tilde{p}$ the desired pressure calculated by the delta-p unit and p the pressure measured inside the muscle. If this pressure error is small and stays within the boundaries b and e, no valve action is taken and the muscle volume stays closed. If p_{error} increases and reaches level e, one inlet valve is opened in order to make the pressure rise to the required level. If one opened inlet valve is not enough to track the required pressure and p_{error} becomes larger than f, a second inlet valve

	$p_{error}(mbar)$	valve action
a	-60	open all exhaust valves
b	-25	open only one exhaust valve
c	-20	close all exhaust valves
d	20	close all inlet valves
e	25	open only one inlet valve
f	60	open all inlet valves

Table 4.1: Currently applied reaction levels of the multilevel bang-bang pressure controlscheme

is opened. Whenever p_{error} drops again, the opened valves are closed only if the error drops below level d. This has been introduced since a considerable time delay exists to set pressures. The same approach is used for negative values of p_{error}, but beyond level a 4 exhaust valves are opened instead of 2. This asymmetrical situation is introduced since asymmetrical pneumatic conditions exist between exhaust and inlet. The orifice airflow though a valve is characterized by the pressure difference over the valve. The gauge pressure inside the muscle generally varies between 0 and 3 bar, while the pressure of the inlet is set at 6 to 7 bar. This means that the maximum pressure difference over the exhaust valves is 3 bar and over the inlet valves 6 to 7 bar. Consequently, the orifice airflow through valves with the same opening section is much lower for exhaust compared to the inlet. This means that the time required to set the pressure inside a muscle differs significantly between inflation and deflation of a muscle. In order to level this difference, the number of exhaust valves has been doubled. Of course, increasing the number of valves and reaction levels ameliorates and fastens the pressure tracking, but on the other hand increases the weight of the pneumatic valve system and the electronic power consumption, required to switch the valves. Simulations and tests on a robot arm with one pair of comparable artificial muscles, which are not discussed in this work, have lead to the current compromise of 2 inlet and 4 outlet valves. For more information about this topic one is referred to [Van Ham et al., 2002].

4.5 Conclusion

In this chapter a control structure for the biped "Lucy" was discussed. The presented structure covers joint trajectory generation and joint trajectory tracking. The trajectory generator unit determines joint motion patterns based on two specific concepts, being the use of objective locomotion parameters, and the exploitation of the natural upper body dynamics by manipulating the angular momentum equation. The objective locomotion parameters are the average forward speed of the hip, step-length, step-height and intermediate foot-lift. The leg links move the hip point in such a way that the upper body is "naturally steered", which means that an unactuated movement of the upper body coincides with a desired movement. Hereby making use of the angular momentum equation expressed with zero ankle torque. As a result, quasi no ankle torque is required in the supporting foot during the single support in order to track the generated joint trajectories. Consequently, the ZMP is kept in the vicinity of the ankle point and thus away from the foot edges, which results in a dynamically stable walking motion.

The tracking controller controls the pressure in each muscle of the robot in order to track the different joint trajectories. This controller is multilayered and incorporates several feedforward structures in order to cope with the highly nonlinear behaviour of the complete system. An inverse dynamic controller calculates required torques, based on a dynamic model of the robot link mechanics for single and double support phase separately. For the single support phase a computed torque method is used, and for the double support phase a feedforward torque selection procedure is presented. Since the system is overactuated in the double support phase, an infinite choice of actuation combinations can be made. One solution with zero ankle torques is selected, apart from a PD feedback part. This is in accordance with the zero ankle torque strategy for the single support phase, as is applied by the trajectory generator. For each joint a delta-p unit then translates the calculated torques into two required muscle pressure levels. This unit utilizes the nonlinear torque to angle relation as presented in chapter 3. Additional to the delta-p unit, a local PI feedback loop is implemented to adjust the calculated pressures in order to cope with modelling errors. Finally, a local multilevel pressure bang-bang controller commands the several on/off valves to set the required pressure in the respective muscle. The proposed control structure is evaluated in the next chapter by means of a simulation.

Chapter 5

Virtual "Lucy": evaluation of the proposed control architecture

5.1 Introduction

After discussing, in chapter 4, the elaborate control architecture for dynamic walking the question whether the designed trajectories can be tracked with sufficient accuracy and stability remains. This question is especially important with respect to the time delays introduced at several levels: sampling time of the computer system, time delay of the valve switching and the time constant due to the restricted air flows through the valves. Beside the expected inaccuracies due to the discrete pneumatic valve control system, and parameter estimation and modelling errors for the feedforward trajectory control system, also the different phase transitions in the walking motion might jeopardize the dynamic stability of the robot. In this chapter these issues are being tackled by means of a simulation model of the complete robotic system. Hereby incorporating the link dynamics with the thermodynamic effects of the muscle valve/system, as was already introduced in chapter 3. The simulation model in this chapter differs substantially regarding augmented complexity due to the increased number of DOF and the several different phases in the walking motion.

The first concern at this moment is to show by means of a simulation that dynamic stable walking can be achieved with the proposed pneumatic control system. But the simulation model is also intended for future use when the real robot is being fine-tuned towards its control parameters. The model can then be exploited to qualitatively help understand the influence of the different control parameters such as feedback gains and reaction levels of the bang-bang pressure controller. Moreover, it can be used to fine-tune the model parameters of the feedforward control system in an adaptive structure using measured data during the experimental process. Furthermore, the simulation model will be an important tool for the design of new control strategies regarding the exploitation of natural dynamics. Besides giving insight on the functional passive behaviour of the compliant joints under all the different loading conditions, the simulation model will be important to redesign the joint characteristics while optimizing towards exploitation of passive behaviour.

The simulation model is conceived with the largest possible amount of adaptability of all kind of parameters, not only towards the essential control parameters, but also regarding the joint design parameters and parameters related to the pneumatics of the valve system. It will be important to validate the simulation model during the experimental process not only regarding parameter values, but also towards modelling insufficiencies, e.g. leakage in the muscles and pneumatic tubing. It is therefore not the purpose of this chapter to give results with optimized control parameters, but in a first instance to show that the pneumatic tracking system in combination with the proposed trajectory generator can ensure dynamic stable walking.

5.2 Mechanics

The biped model during a single support phase is depicted in figure 4.11, with G_i the COG of each link, and m_i and I_i being respectively the link mass and the link inertia. J_i represents the rotation axis between two connected links. The inertial and geometrical parameters of the simulation model are summarized in table 5.1 with l_i the length of link i. For the upper body, the measured inertial parameters are adapted to include a possible payload which can be carried by the robot. The

i	l_i (m)	J_iG_i (m)	m_i (kg)	I_i (kgm^2)
1	0.45	0.260	3.61	0.060
2	0.45	0.261	3.69	0.062
3	0.45	0.200	18.0	0.600
4	0.45	0.189	3.66	0.060
5	0.45	0.192	3.53	0.058
6	0.30	0.046	1.15	0.005

Table 5.1: Inertial parameters of the robot

mechanical part of the simulation model contains three different phases: a single support phase, a double support phase and an instantaneous impact phase. During single support, the robot's equations of motion (4.36) are used, while for a double support phase the equations of motion (4.40) together with the constraint equations (4.39) are used. As was mentioned before, the inertial parameters of the swing foot are taken into account, while the influence of the supporting foot is neglected, since this foot is not moving. The origin of the coordinate system is positioned at the supporting ankle point during single support and at the rear ankle point during double support, which is physically the same point. Each time a transition from double support to single support occurs, the origin of the coordinate system is shifted. In order to have a realistic simulation, the impact phase at touch-down of the swing leg is considered. This impact phase is modelled as an inelastic impulsive impact of the front foot.

5.2.1 Single support phase

The simulation kernel integrates first order differential equations only. Since the equations of motion (4.36) are of second order, these equations have to be transformed into a first order formulation. This can be done by introducing $\boldsymbol{\omega}$ for the angular velocity:

$$\boldsymbol{\omega} = \dot{\mathbf{q}} = \left[\omega_1\, \omega_2\, \omega_3\, \omega_4\, \omega_5\, \omega_6\right]^T \tag{5.1}$$

The equations of motion can then be rewritten as:

$$\begin{cases} \dot{\boldsymbol{\omega}} = D(\mathbf{q})^{-1}\left[\boldsymbol{\tau} - C(\mathbf{q}, \boldsymbol{\omega}) - G(\mathbf{q})\right] \\ \dot{\mathbf{q}} = \boldsymbol{\omega} \end{cases} \tag{5.2}$$

Note that the inertia matrix $D(\mathbf{q})$ is symmetric and positive definite and can be inverted. Equations (5.2) represent a set of 12 first order differential equations for which the torques $\boldsymbol{\tau}$ depend on the angular positions $\mathbf{q}$ and the pressure values in the muscles of all joints (4.73).

During the simulation process, several conditions need to be observed to check for phase transitions. Whenever the ankle of the swing foot hits the ground, an impact phase will occur, immediately followed by the next double support phase, i.e. if the foot does not bounce. If the coordinates of the front foot are given by:

$$X_{A_F} = l_1 \cos\theta_1 + l_2 \cos\theta_2 - l_2 \cos\theta_4 - l_1 \cos\theta_5 \tag{5.3a}$$

$$Y_{A_F} = l_1 \sin\theta_1 + l_2 \sin\theta_2 - l_2 \sin\theta_4 - l_1 \sin\theta_5 \tag{5.3b}$$

than the condition for phase transition is formulated as:

$$Y_{A_F} < Y_{gr}\left(X_{AF}\right) \tag{5.4}$$

With $Y_{gr}(X)$ representing the specific shape of the ground. In this work simulations only consider walking on flat terrain, thus $Y_{gr}(X) = 0$. Note that an approximation is made by expressing this condition on the ankle point and not including foot dimensions, neither are taken into account specific shapes of obstacles which could obstruct the walking motion.

Other phase transitions occur when the stance foot during single support looses contact with the ground, this happens when conditions on the ground reaction force and the ZMP terminate the simulation. One of the difficulties of controlling legged robots is the unilateral nature of this foot/ground contact. The vertical acceleration of the global COG, $\ddot{Y}_G$, has to be higher than $-g$, otherwise the total ground reaction force will switch sign and the robot starts a flight phase which is not foreseen in the control algorithm. Thus a necessary condition for foot/ground contact is:

$$R_y = m_{tot}\left(\ddot{Y}_G + g\right) > 0 \tag{5.5}$$

if the vertical positive direction is defined upwards. Furthermore, the ZMP position (4.4) has to stay within the physical boundaries of the foot, otherwise the robot starts to tip over while rotating around one of the supporting foot edges:

$$-l_{6B} < -\frac{\tau_A}{m_{tot}\left(\ddot{Y}_G + g\right)} < l_{6F} \tag{5.6}$$

This situation is undesirable and is described by totally different equations of motion, so the simulation should be stopped at this point. It is furthermore assumed that the stance foot of the robot does not slip, meaning that friction between the foot sole and the ground is high enough.

5.2.2 Double support phase

The equations of motion for the double support phase (4.40) represents 6 equations in 9 unknowns: 6 unknowns for $\ddot{\mathbf{q}}$ and 3 for the Lagrange multipliers $\mathbf{\Lambda}$. This should be solved by additionally using the three constraint equations (4.39), which constitute a total set of differential algebraic equations (DAE). In order to transform this into a set of ordinary differential equations (ODE), the second derivative of the kinematic constraint equation with respect to time is used [Jalón and Bayo, 1994]:

$$J(\mathbf{q})\ddot{\mathbf{q}} + \dot{J}(\mathbf{q})\dot{\mathbf{q}} = 0 \tag{5.7}$$

Combining (4.40) and (5.7) results in:

$$\begin{bmatrix} D(\mathbf{q}) & J^T(\mathbf{q}) \\ J(\mathbf{q}) & 0 \end{bmatrix} \begin{bmatrix} \ddot{\mathbf{q}} \\ \mathbf{\Lambda} \end{bmatrix} = \begin{bmatrix} \boldsymbol{\tau} - C(\mathbf{q},\dot{\mathbf{q}})\dot{\mathbf{q}} - G(\mathbf{q}) \\ -\dot{J}(\mathbf{q})\dot{\mathbf{q}} \end{bmatrix} \tag{5.8}$$

Equations (5.8) are then solved for the 9 unknowns. After introducing $\boldsymbol{\omega}$, the following set of 12 first ODE is formed, which have to be integrated numerically:

$$\begin{cases} \dot{\boldsymbol{\omega}} = \mathbf{f}(\mathbf{q},\boldsymbol{\omega}) \\ \dot{\mathbf{q}} = \boldsymbol{\omega} \end{cases} \tag{5.9}$$

with $\mathbf{f}$ being a result of solving (5.8).

When describing the equations of motion with dependent coordinates and Lagrange multipliers, the forces associated with the constraints can be calculated in a straightforward way. In this case, the ground reaction force $\bar{\mathbf{R}}_{\mathbf{F}}$ of the front foot (see figure (4.4)) is linked with the two first constraints of (4.39) by Lagrange multipliers λ_1 and λ_2. The constraint equations can be written in such a way that the horizontal and vertical components of the ground reaction force acting at the front ankle point are found as:

$$R_F^x = \lambda_1 \tag{5.10a}$$

$$R_F^y = \lambda_2 \tag{5.10b}$$

Writing the linear momentum theorem with respect to the global COG allows one to calculate the total ground reaction forces:

$$R_{tot}^x = m_{tot}\ddot{X}_G \tag{5.11a}$$

$$R_{tot}^y = m_{tot}\left(\ddot{Y}_G + g\right) \tag{5.11b}$$

with m_{tot} the total mass of the robot, $\ddot{X}_G$ and $\ddot{Y}_G$ the horizontal and vertical acceleration of the global COG, which can be calculated with equations (C.3) of appendix C. Combining (5.10) with (5.11) allows one to find the ground reaction force acting at the rear ankle point:

$$R_R^x = R_{tot}^x - R_F^x = m_{tot}\ddot{X}_G - \lambda_1 \tag{5.12a}$$

$$R_R^y = R_{tot}^y - R_F^y = m_{tot}\left(\ddot{Y}_G + g\right) - \lambda_2 \tag{5.12b}$$

Whenever the vertical component of the ground reaction force acting at the rear foot (5.12b) becomes negative, the double support phase should be terminated since this means that the rear foot is lifted of the ground. Apart from the rear foot ground reaction force, the vertical component of the front foot ground reaction force is checked if it becomes negative during the double support phase. If so, the simulation should be terminated, since this means that the robot tends to move in the opposite direction, apart from bouncing effects just after impact. Based on the values of the vertical ground reaction forces of the feet, the ZMP position during double support is obtained with equation (4.6).

5.2.3 Impact phase

After the single support phase, an impact occurs when the swing foot touches the ground. This impact causes jumps on the joint angular velocities. The values of these velocity changes become starting conditions for the numerical integrator of the next double support phase. The touch-down of the front foot is modelled as an inelastic impulsive impact only on the ankle point. Thereby ignoring the impact on rotation of the foot itself, thus only the two first equation (4.39a) and (4.39b) are taken into account.

The relation between front foot ankle point velocity and angular velocities of each link, apart from the feet, is given by:

$$\dot{\mathbf{q}}_{\mathbf{A_F}} = J\dot{\mathbf{q}} \tag{5.13}$$

with

$$\mathbf{q_{A_F}} = \begin{bmatrix} X_{A_F} \\ Y_{A_F} \end{bmatrix} \tag{5.14}$$

and the Jacobian matrix J:

$$J(\mathbf{q}) = \begin{bmatrix} -l_1 sin(\theta_1) & -l_2 sin(\theta_2) & 0 & l_2 sin(\theta_4) & l_1 sin(\theta_5) \\ l_1 cos(\theta_1) & l_2 cos(\theta_2) & 0 & -l_2 cos(\theta_4) & -l_1 cos(\theta_5) \end{bmatrix} \tag{5.15}$$

Since the Jacobian matrix is non-square it can not be inverted. Zheng and Hemami [1985] derived the following expression, which calculates the angular velocity jumps $\Delta\dot{\mathbf{q}}$ using the dynamic model of the robot (4.36). It is assumed that the robot configuration and applied torques remain unchanged during the infinitesimal short impact phase.

$$\Delta\dot{\mathbf{q}} = D^{-1} J^T \left(J D^{-1} J^T \right)^{-1} \Delta\dot{\mathbf{q}}_{\mathbf{A_F}} \tag{5.16}$$

with:

$$\Delta\dot{\mathbf{q}}_{\mathbf{A_F}} = \begin{bmatrix} -\dot{X}^-_{A_F} \\ -\dot{Y}^-_{A_F} \end{bmatrix} \tag{5.17}$$

$\dot{X}^-_{A_F}$ and $\dot{Y}^-_{A_F}$ are the horizontal and vertical velocity of the front foot ankle point just before impact.

5.3 Thermodynamics

The thermodynamic processes which take place in the antagonistic muscle setup of each joint are described by four first order differential equations. Two equations determine the pressure changes in both muscles of the antagonistic setup and the remaining two describe conservation of mass in the respective muscle volumes. Additionally to these differential equations the perfect gas law is used to determine temperature values. These equations have been discussed in chapter 3 for the simulation of the one-dimensional leg configuration. In this chapter, 6 sets of these equations are used to describe the thermodynamics taking place in all the muscles of the biped. For the sake of convenience the same discussion on the thermodynamics is repeated here.

The pressure inside a muscle is influenced by its volume changes resulting from a variation of the joint angle and by the air flows through the valves which have been activated by the bang-bang pressure controller. Assuming a polytropic thermodynamic process, and assuming that the compressed air inside each muscle behaves as a perfect gas, the first law of thermodynamics, while neglecting the fluid's kinetic and potential energy, can be written for each muscle of the antagonistic setup in the following differential form (appendix B):

$$\dot{p}_i = \frac{n}{V_i} \left(r T^{sup}_{air} \dot{m}^{in}_{air_i} - r T_{air_i} \dot{m}^{ex}_{air_i} - (P_{atm} + p_i) \dot{V}_i \right) \tag{5.18}$$

The total orifice flow through opened inlet valves or exhaust valves can be calculated with the following equations which represents a normalized approximation of a valve orifice flow defined by the International Standard ISO6358 [1989]:

$$\dot{m}_{air} = C P_u \rho_0 \sqrt{\frac{293}{T^u_{air}}} \sqrt{1 - \left(\frac{P_d/P_u - b}{1-b}\right)^2} \qquad \text{if} \qquad \frac{P_d}{P_u} \geq b \tag{5.19}$$

$$\dot{m}_{air} = C P_u \rho_0 \sqrt{\frac{293}{T^u_{air}}} \qquad \text{if} \qquad \frac{P_d}{P_u} \leq b \tag{5.20}$$

C and b are two flow constants characterizing the valve. The constant C is associated with the amount of air flowing through the valve orifice, while b represents the critical pressure ratio at which orifice air flows become maximal. Both coefficients have been experimentally determined for the used Matrix valves (see chapter 6), which resulted in $C = 22\,\mathrm{Std.l/\min/\,bar}$ and $b = 0.16$. When choking occurs, equation (5.20) is valid, otherwise equation (5.19) is used.

Once the actions (opening and closing of the valves) for the different inlet and exhaust valves are known, all the air flows can be calculated in order to be substituted in (5.18). The temperature in the muscle is calculated with the perfect gas law:

$$T_{air_i} = \frac{P_i V_i}{m_{air_i} r} \tag{5.21}$$

The total air mass m_{air_i} is given by integration of the net mass flow entering muscle i:

$$\dot{m}_{air_i} = \dot{m}^{in}_{air_i} - \dot{m}^{ex}_{air_i} \tag{5.22}$$

The volumes and their time derivatives are given by kinematical expressions as a function of the joint angle and joint angular velocity. These functions are determined with the fitted polynomial volume function (2.34) and the link between contraction and joint angle, represented by the kinematic expression (3.8) of the pull rod system. The link at torque level between the mechanical equations of motion and these thermodynamic differential equation systems is provided by equation (4.73) which characterizes joint torque as a function of pressures and joint angle.

5.4 Complete simulation model

In figure 5.1 an overview is given of the complete simulation model. The kernel of this simulator is based on three equation blocks, as depicted in the center of the figure. The 12 first order differential equations (5.2) or (5.9) describe the motion during single support and double support respectively, with addition of the constraint equations for double support. The thermodynamics of each joint are characterized by four first order differential equations on pressure (5.18) and air mass (5.22). This gives in a set of 24 differential equations for the thermodynamic differential equation block. Finally, the 12 thermodynamic state equations (5.21) complete the set.

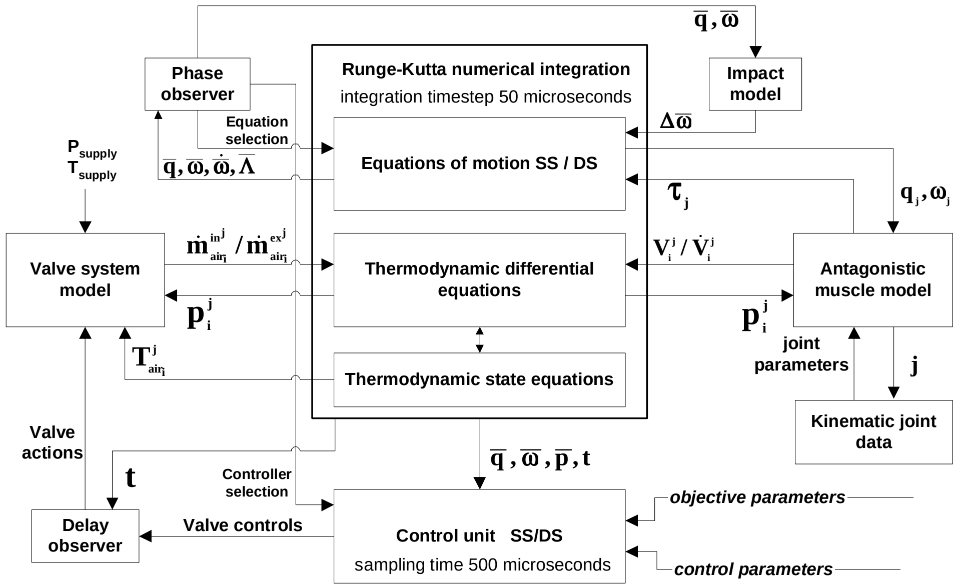

Figure 5.1: Structure of the complete simulation model

The antagonistic muscle model block creates the link between the mechanics and the thermodynamics by calculating the torque for each joint (j) with the pressure information of the thermodynamic block. Therefore it needs angle information from the integrated equations of motion. This information allows to calculate the contraction of each muscle (i) within the antagonistic setup (3.8), while using the kinematic data of the pull-rod mechanism of the specific joint. With the contraction values, the linear forces (2.33) of the two muscles can be calculated in order to determine the applied torque with equation (4.73). Additionally, to determine the pressure changes in the thermodynamic differential equation block, muscle volume and volume changes are calculated with (2.34). For the volume changes angular velocity information is required from the integrated equations of motion.

The valve system block determines the air mass flow rates (5.19 or 5.20) for each muscle, depending on the actual pressure and temperature in the muscle and the action taken by the valves. This action is determined by the valve control signals of the control unit. These signals pass through the delay observer, which requires the time instant of the integrator to determine whether the valve may be switched or not. Hereby a valve delay of 1 ms is used.

Finally, the phase observer calculates the vertical ground reaction forces (5.5 or

5.10b, 5.12b) and the position of the front foot (5.3) to check whether the robot is in a single support phase or a double support phase. At touch-down of the front foot, this module commands the impact module to calculate the velocity jumps (5.16). The phase observer requires angles, angular velocities and accelerations and the Lagrange multipliers to determine the ground reaction forces.

The differential equations are numerically integrated using a $4th$ order Runge-Kutta method with an integration time step of $50\,\mu s$, which is ten times less than the sample time of the control unit. In order to evaluate robustness of the controller with respect to parameter estimation, two systematic errors are introduced. Firstly, the inverse dynamics control unit calculates with deviations on the inertia parameters : 5 % for center of gravity and mass and 10 % for the inertia of each link. These deviations are applied by increasing the inertia parameters with the respective deviation. Secondly, the reported ±5 % for the hysteresis on both force functions (see 2.3) of the antagonistic set-up is taken into account. This is particularly achieved by adding 5 % to the estimated force for one muscle and subtracting the same deviation for the other muscle before calculating the applied joint torque with (4.73). Both muscles of an antagonistic setup, after all move in opposite directions.

5.5 Results and discussion

In this section the results of a simulation are discussed. The objective locomotion parameters for the presented walking motion are given in table 5.2. The calculated

mean forward velocity	ν	0.20	m/s
step length	λ	0.15	m
step height	δ	0.00	m
foot lift	γ	0.02	m

Table 5.2: Objective locomotion parameters

phase durations for the single support T_S (4.7) and double support T_D (4.8) are respectively 0.59 s and 0.15 s. The results shown in this section are valid for a steady state walking pattern and the following graphs depict a sequence of 3 double support phases and 2 single support phases. The presented graphs show only data for the left leg, since each leg takes all essential configurations of a walking pattern over the complete time course of the simulation. Figure 5.2 gives a stick diagram of the presented robot motion, hereby focusing on the different configurations of the left leg. The simulation starts with a double support phase with the left leg as the rear leg. Next, this leg is shifted to the front during a single support on the right leg. The left leg becomes the front leg during the following double support phase. Successively, another single support phase on the left leg brings the right leg back to the front for the last double support phase. The total simulation time

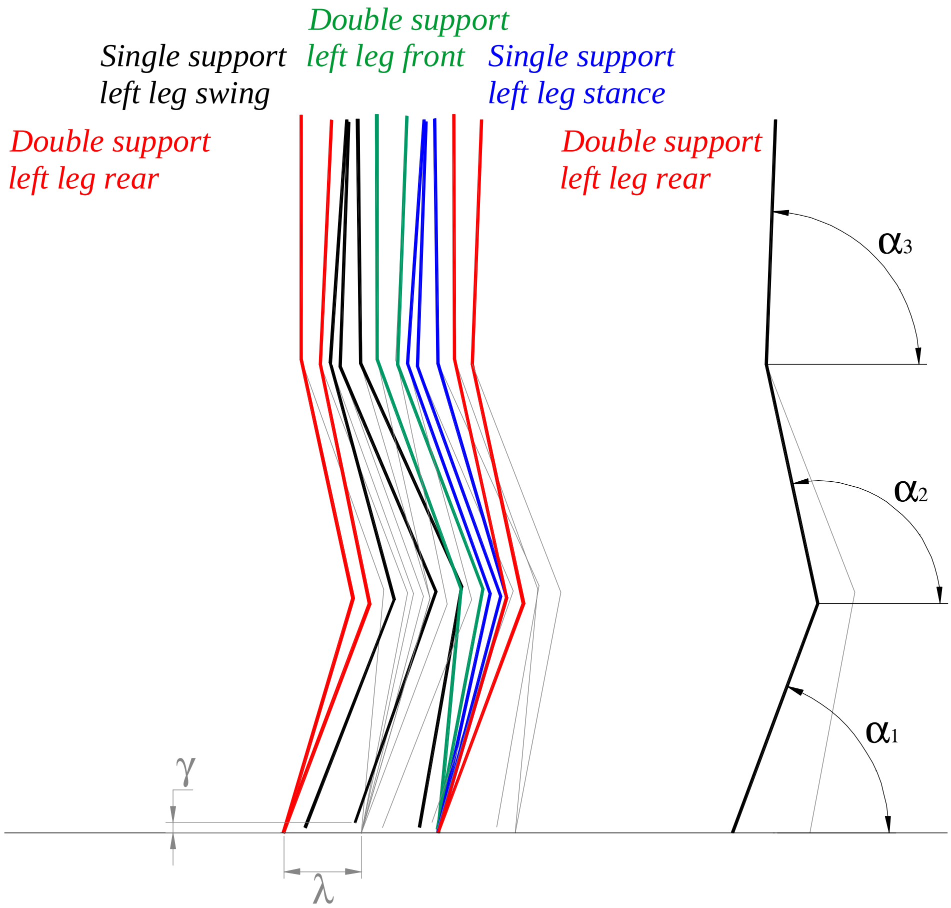

Figure 5.2: Stick diagram of the simulated motion focussing on the left leg

is 1.6 s. Due to approximation and tracking errors, the different phase transitions do not occur exactly at the calculated instants. This means that, while tracking the desired trajectories, the double and single support phases are not terminated as expected. For this reason, intermediate conditions are foreseen in the control structure. If a double support phase ends too early, the trajectories calculated for this phase are still sent to the tracking controller of the next single support phase, before calculating new trajectories. When a double support phase takes too long, the trajectories for the following single support phase are imposed on the system during this double support phase. The nature of these trajectories force the rear foot to be lifted of the ground and thus end the double support phase. If the front foot does not touch the ground in time, the polynomial trajectories for single support phase are extended until touch-down occurs. Steady state simulations show that all these special transition phases are very short, so they are not explicitly marked on the graphs. Additionally, one transition is introduced artificially. Due to tracking imprecision, the orientation of the swing foot is not exactly parallel to the ground at the end of the single support phase. In the simulation, the orientation of the foot is therefore forced to align with the ground at touch-down, as is the case in a real robot.

In figure 5.2 the three angles α_1, α_2 and α_3 are defined for the left leg. They describe respectively the absolute orientation of the lower leg, upper leg and upper body with respect to the horizontal direction. Figures 5.3, 5.4 and 5.5 depict the graphs of the absolute angles α_i and the angular velocities $\dot{\alpha}_i$ of the left leg. The

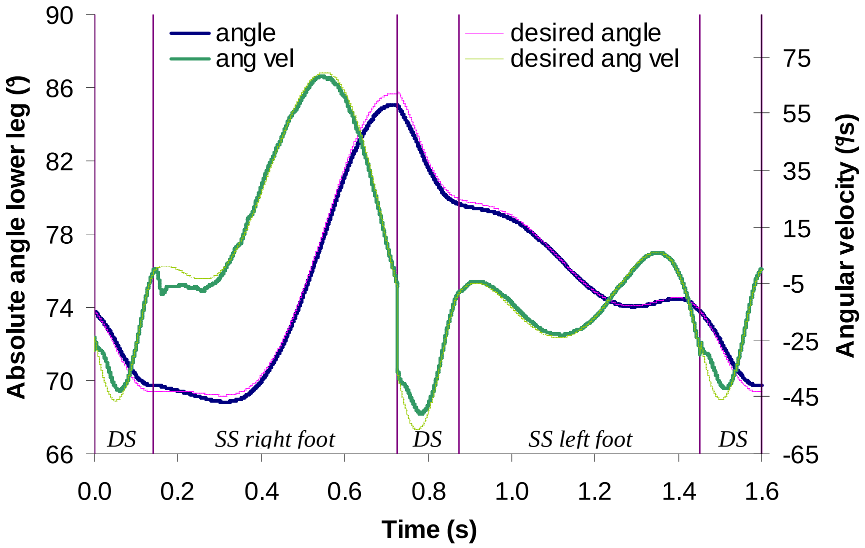

Figure 5.3: $\alpha_1(°)$ and $\dot{\alpha}_1(°/\mathrm{s})$ left leg

vertical lines on all graphs indicate when a phase transition occurs. Due to the nature of the bang-bang pneumatic drive units and the imperfections introduced in the control loops, tracking errors can be observed at position and velocity level, especially when transitions occur, since these introduce severe changes for the control signals. But these tracking errors are limited and do not jeopardize the overall dynamic robot stability as is shown below. Figure 5.5 shows clearly the steady state oscillation of the upper body as was imposed by the trajectory generator control unit. It also shows that the upper body oscillates with only small amplitude about the upright position.

The incorporated estimation error of $\pm 5\,\%$ for the force functions of the different antagonistic setups has an important negative influence on the performance of the torque-pressure feedforward controller. In figure 5.6, 5.7 and 5.8 the required torque

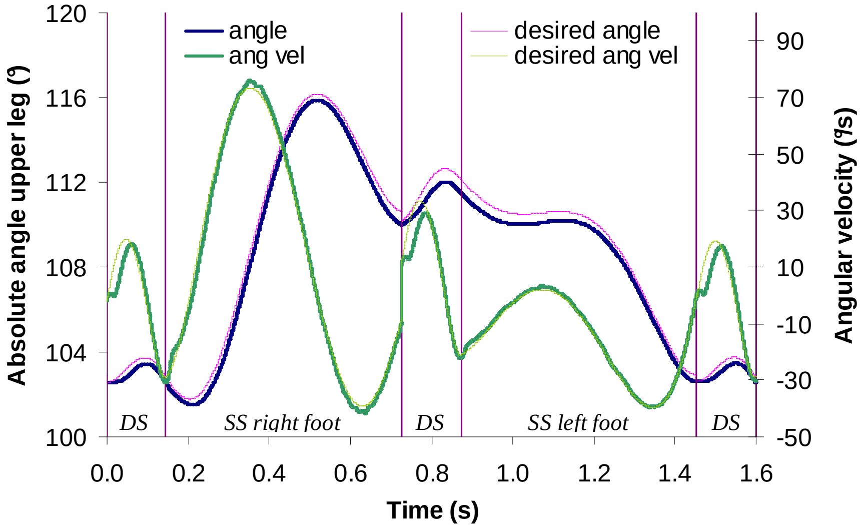

Figure 5.4: $\alpha_2(°)$ and $\dot{\alpha}_2(°/\mathrm{s})$ left leg

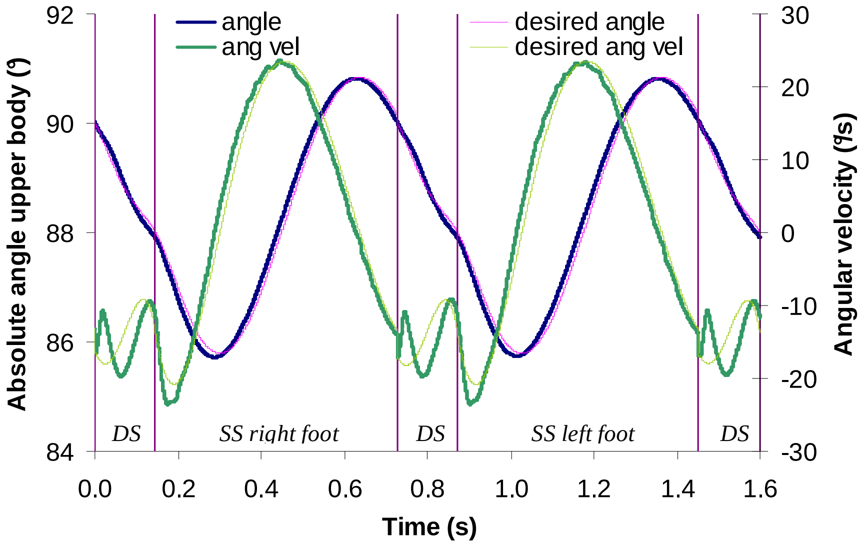

Figure 5.5: $\alpha_3(°)$ and $\dot{\alpha}_3(°/\mathrm{s})$ left leg

values, as calculated by the inverse dynamics control block, and the actual applied torques for the ankle, knee and hip of the left leg are depicted. The computed torque values (see 4.4.1 and 4.4.2) are used by the delta-p unit (see 4.4.3). The influence of the force function errors can be clearly seen at the graph for the ankle torque in figure 5.6, the difference between computed torque and actual applied torque is

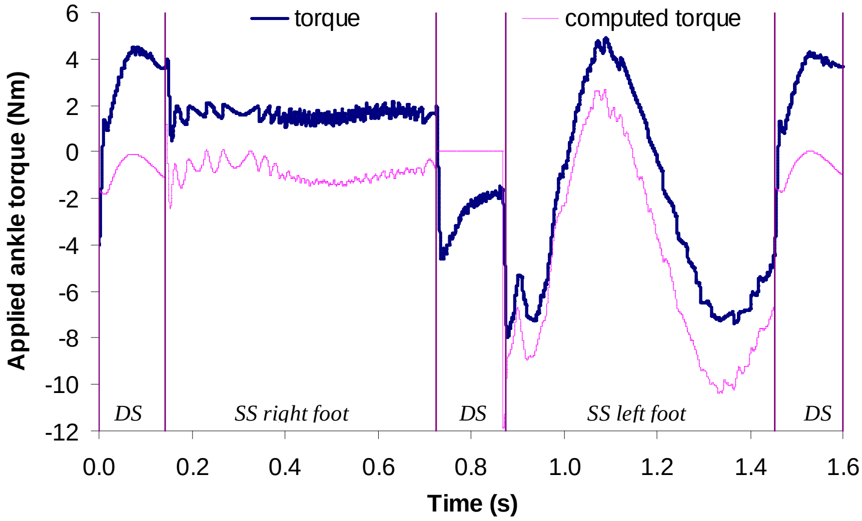

Figure 5.6: Applied ankle torque left leg

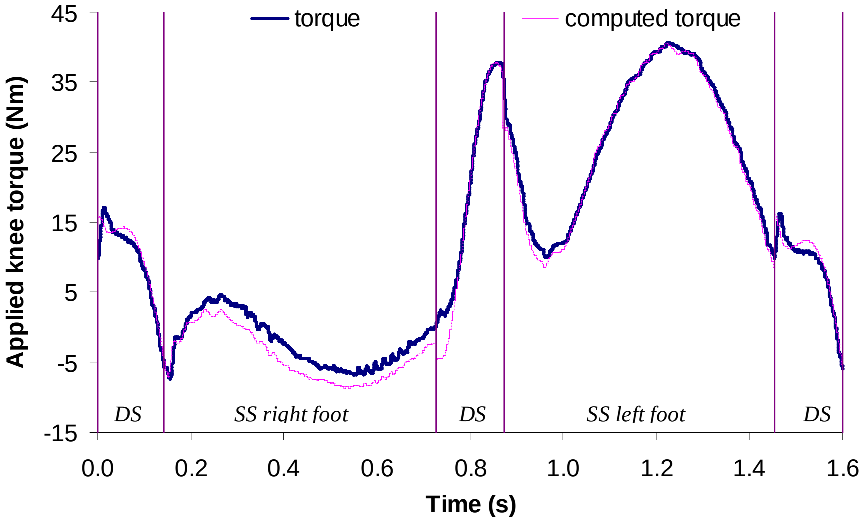

Figure 5.7: Applied knee torque left leg

clearly visualized due to the low torque values. E.g. when the foot of the left leg is in the air (SS right foot), the inverse dynamics control block calculates negative ankle torques, while the actually applied ankle torques, required to hold the foot horizontally, are positive. Actually, it is the feedback part that is responsible for this difference. Note that the effect of the low-level feedback PI controller (see 4.4.4) is not depicted separately, since this is included in the required pressure

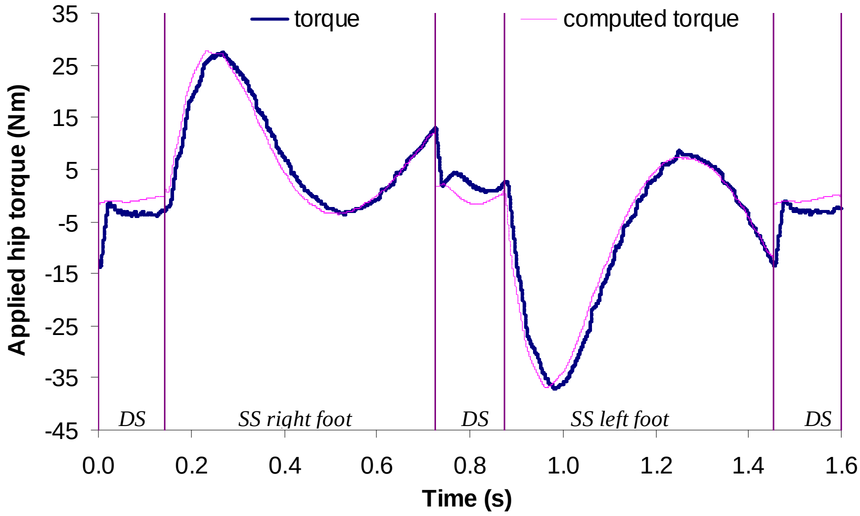

Figure 5.8: Applied hip torque left leg

values. The graphs show furthermore that the torques exerted in the knee and hip are smaller than 40 Nm. The highest torque values for the knee and hip are recorded when the respective leg is acting as supporting leg, just as one could expect.

The pneumatics are characterized by pressure courses in both muscles of each joint. Figures 5.9, 5.10 and 5.11 depict required and actual pressures for the front and rear muscles of respectively ankle, knee and hip of the left leg. All these graphs additionally show the valve actions taken by the respective bang-bang pressure controllers. Note that in these figures a muscle with closed valves is represented by a horizontal line depicted at the 2 bar pressure level, while a small peak upwards represents one opened inlet valve, a small peak downwards one opened exhaust valve and the larger peaks represent two opened inlet or four opened outlet valves. The required pressures are calculated by the delta-p unit and corrected by the local PI-controller. For this simulation, the mean pressure p_m is set at 2 bar for all joints. Consequently, the sum of the pressures in each pair of graphs, drawing the front and rear muscle pressures, is always approximately 4 bar. It can be observed that the bang-bang pressure controller is very adequate for tracking the desired pressures. Although a lot of valve switching is required to achieve this result. But as was already mentioned, at this moment the goal is to validate on dynamic stability and not on energy consumption, neither are the control parameters optimized.

An important factor, for the valve system to be able to track the required pressure courses, is the frequency contents of these courses. These frequency components are not too high in this simulation, since the walking speed of the robot is moderate. For increased walking speeds, the pressure gradient over some valves might

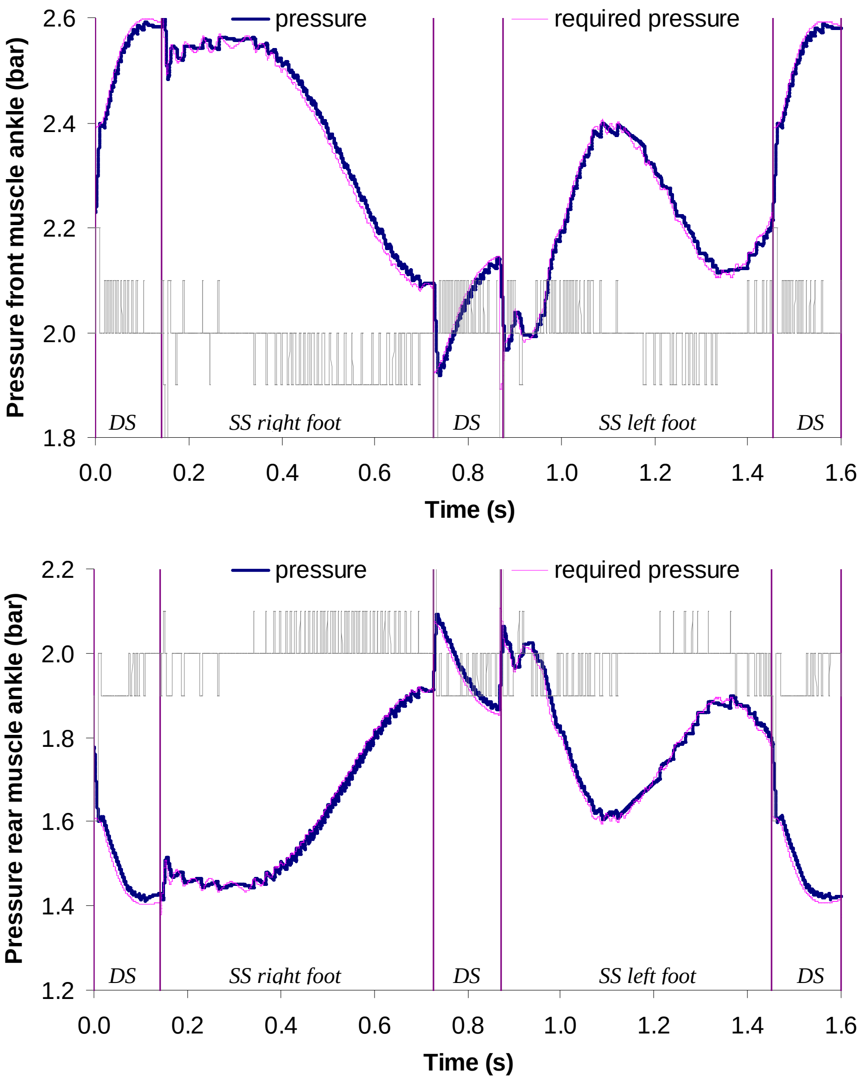

Figure 5.9: Ankle front and rear muscle pressures with valve action

become insufficient, such that the time constant of muscle inflation/deflation becomes too large in comparison to the requirements associated with the imposed pressure course. It is hereby expected that especially the exhaust valves will pose this specific limitation, since the pressure gradient between muscle and atmosphere can be low. This all can lead to a deterioration of the pressure tracking performance. If higher walking speeds would be considered, then the number of valves has to be increased in order to obtain the necessary air mass flow rates in all cases,

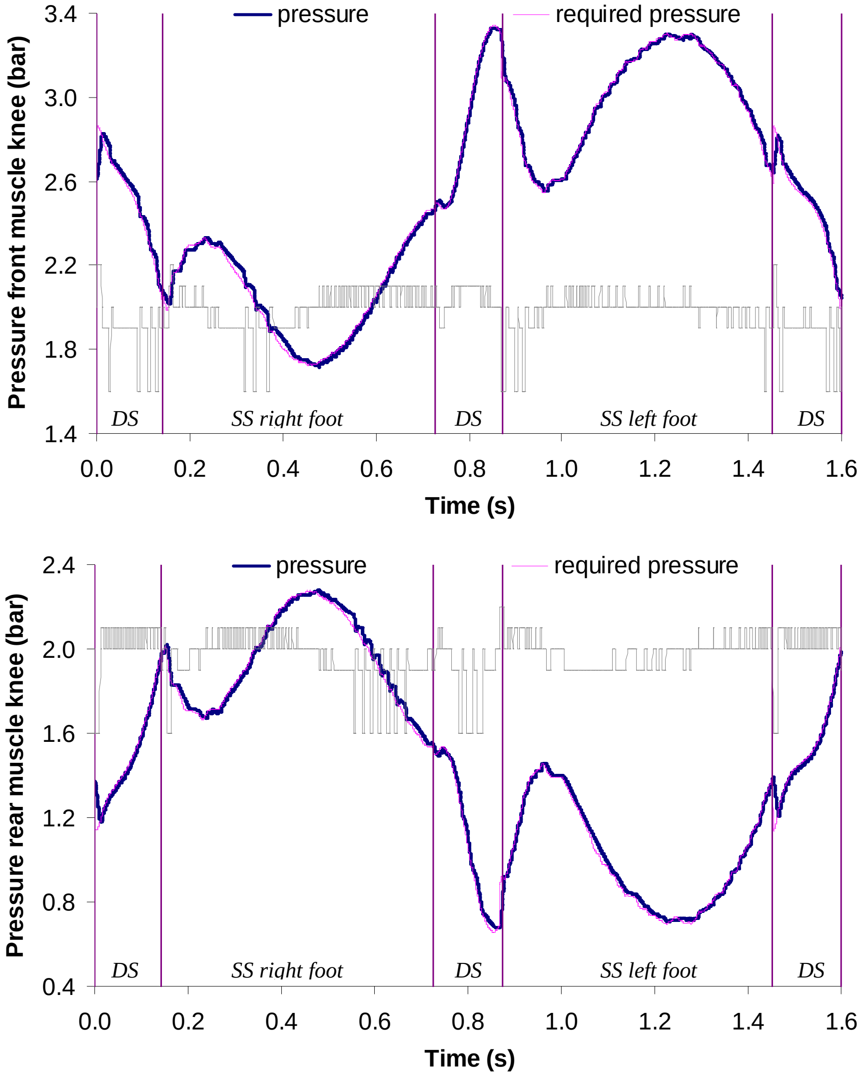

Figure 5.10: Knee front and rear muscle pressures with valve action

hereby also increasing the number of discrete reaction levels in the pressure bang-bang controller. It may also be a solution to use valves with larger orifice section, but, in general, this influences the valve switching time in a negative way. With the current design of the pressure regulating valve system (6 on/off valves, see chapter 6) and the current controller as proposed in chapter 4, a speed of about 0.3 m/s can be attained, but it is observed that deflating the muscles becomes critical at certain moments. Furthermore, if the natural dynamics as discussed in chapter

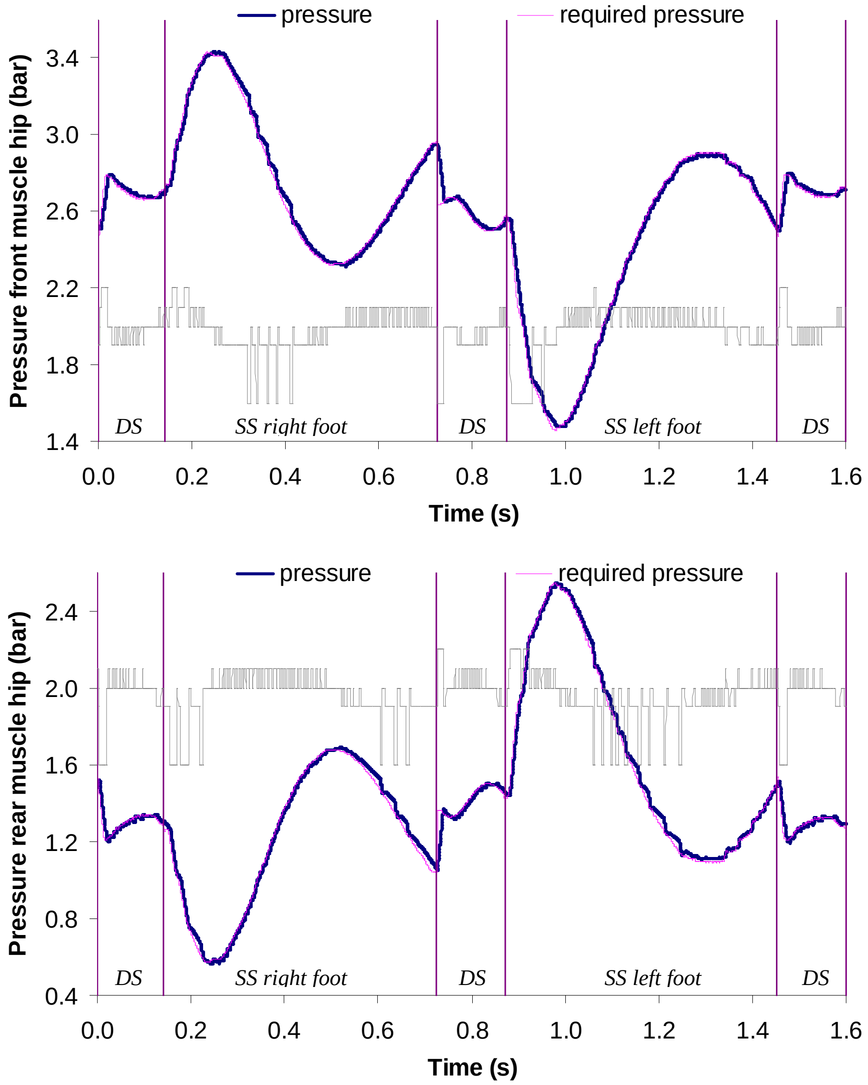

Figure 5.11: Hip front and rear muscle pressures with valve action

3, would be exploited properly, it is expected that higher walking speed could be achieved since less control could be necessary. The natural pressure changes, due to proper natural volume changes, could contribute to better muscle inflate and deflate conditions.

To have a clearer view on the bang-bang pressure controller, figure 5.12 gives pressure information for front and rear muscle of the knee for a smaller time interval.

Due to the discrete levels of the bang-bang pressure controller, its dead zone, the

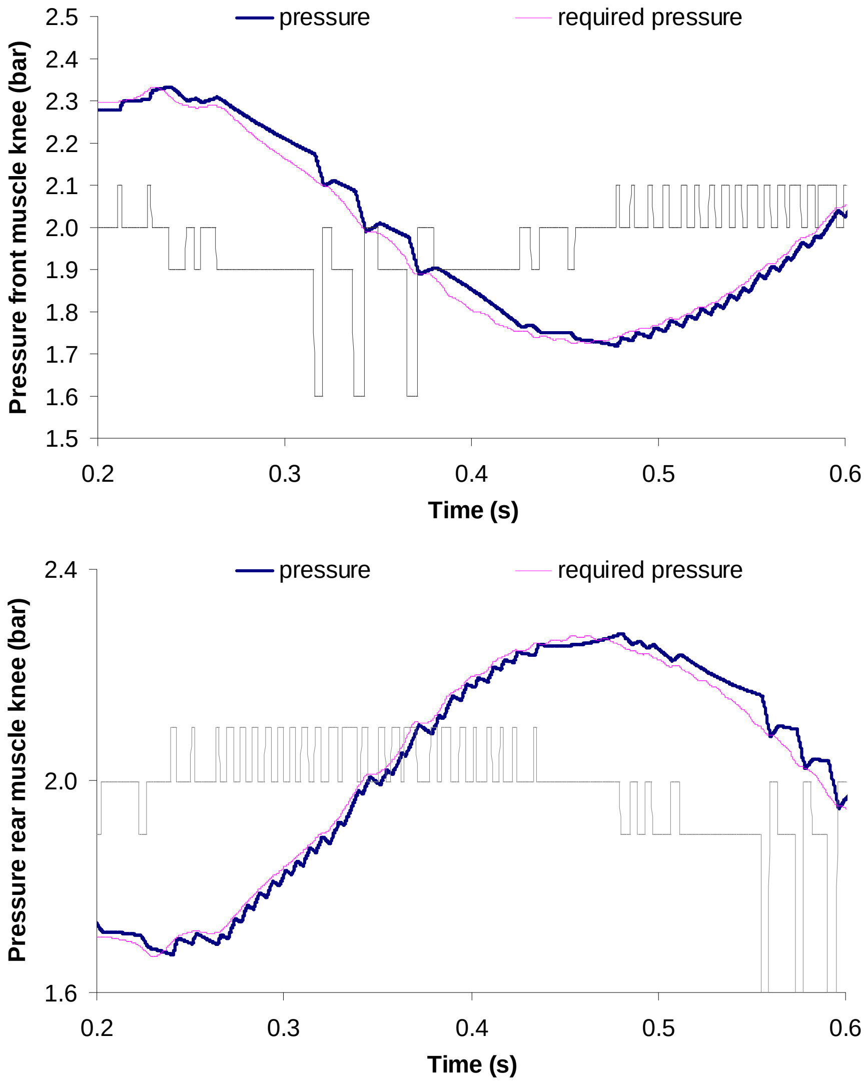

Figure 5.12: Detail of knee front and rear muscle pressures

delay times of the valves and the sampling time, the latter are not switching continuously. In figure 5.12, around 0.3 s, opening one outlet valve of the front muscle is not enough to track the desired pressure course for this muscle, since the flow rate through one valve is not enough to deflate the muscle. Therefore the other three valves are opened, at a certain maximum pressure error, to increase the flow rate and consequently track the required pressure course more accurately. When valves are closed, the pressure generally does not remain constant, as the volumes change according to the leg movements. Taking a close look at a same time interval for both closed rear and front muscle, the directions of pressure changes are opposite. This is due to opposite volume changes for both muscles in an antagonistic setup. The dead zone introduced in the bang-bang controller will be of great importance towards energy consumption but has evident reflections on the tracking error. The trajectories, calculated by the trajectory generator, and the mean pressure values of the tracking controller have to be manipulated in such a way that pressure changes with closed muscles can be exploited as much as possible. But as was mentioned at the beginning of this section, the control unit does currently not take energy considerations into account, but focuses on dynamic stability and desired robot motion with this kind of pneumatic actuation system.

The remaining graphs depict the several objective locomotion parameters and the ZMP position. These reflect the global performance of the proposed control strategy. Figures 5.13 and 5.14 depict horizontal and vertical position of the swing foot. Only small deviations on the step length and the step height can be observed. In figure 5.15 the horizontal velocity of the hip is given. It can be seen that the mean value of the forward velocity is about 0.2 m/s, as was desired. In the same graph, the inverted pendulum principle during single support can be verified. The hip first decelerates and then re-accelerates again. Note that at the beginning of each double support phase a discontinuity occurs in the velocity pattern. This is due to the impact of the swing foot which can also be seen at the angular velocity patterns of the different leg links. But, of course, a big difference exists between the angular velocity jumps for a stance leg and a swing leg.

The small ankle torque during single support has an important reflection on the ZMP which is depicted in figure 5.16. The ZMP moves around the ankle point during single support and switches from the rear to the front ankle point during the double support phase. The switching of the weight can also be seen at the graph in figure 5.17, which depicts the vertical component of the ground reaction force on the left and right foot. Since the total weight of the simulated robot is about 33 kg, the vertical component of the total ground reaction force is about 330 N.

One of the main purposes of the simulation model at this moment is to investigate the effect of the proposed pneumatic tracking control system on the dynamic stability of the biped. The single support phase is the most critical one regarding the dynamic stability. In figure 5.18 the ZMP position is isolated and depicted for a single support phase only (SS left foot), with the origin of the coordinate system in the ankle point of the stance foot. The actual ZMP position is compared to the one if the calculated joint trajectories were perfectly tracked. These trajectories (see 4.3) are calculated such that the ZMP is located at the ankle point as a consequence of zero stance foot ankle torques. Due to approximations made during the calculations of the trajectory generator, the calculated ZMP oscillates with a small

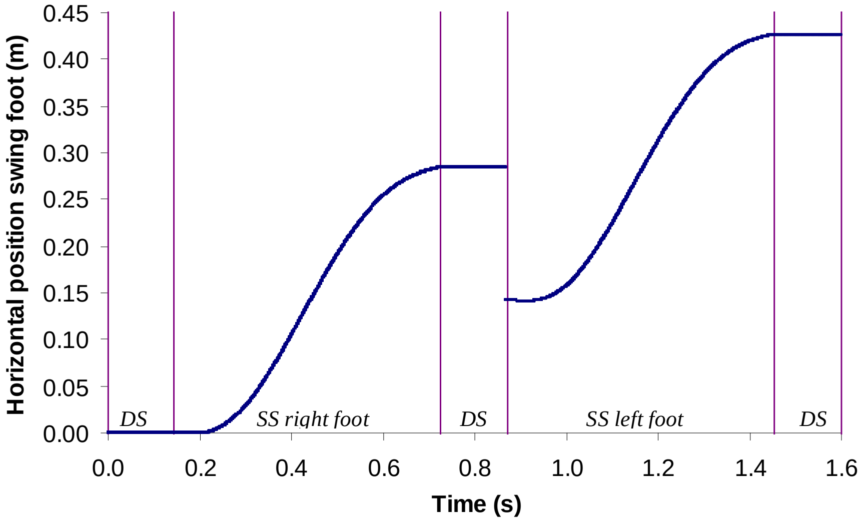

Figure 5.13: Horizontal position swing foot

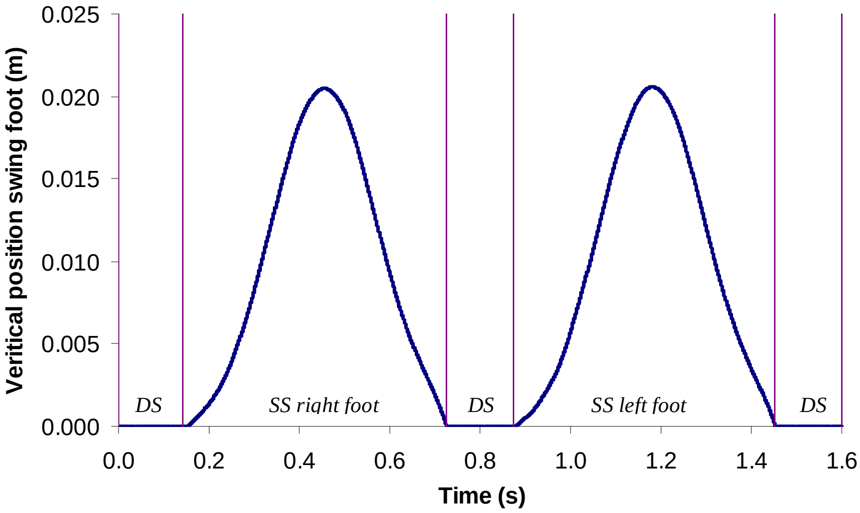

Figure 5.14: Vertical position swing foot

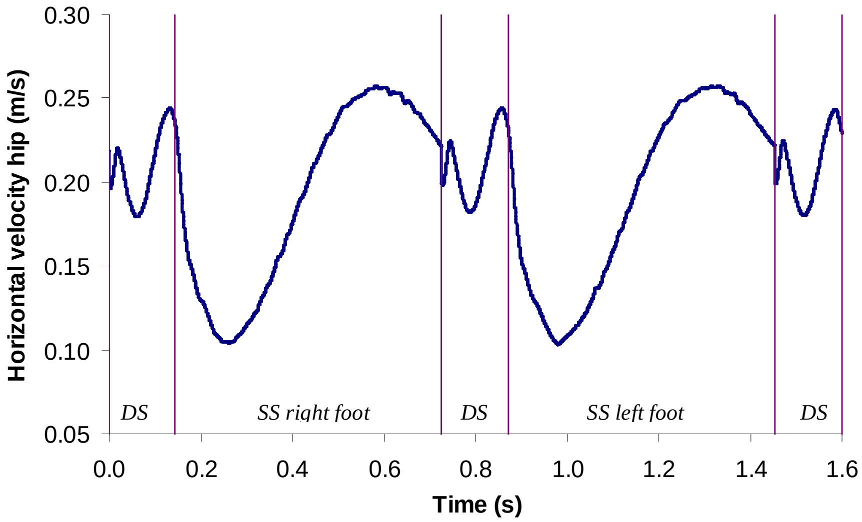

Figure 5.15: Horizontal velocity hip

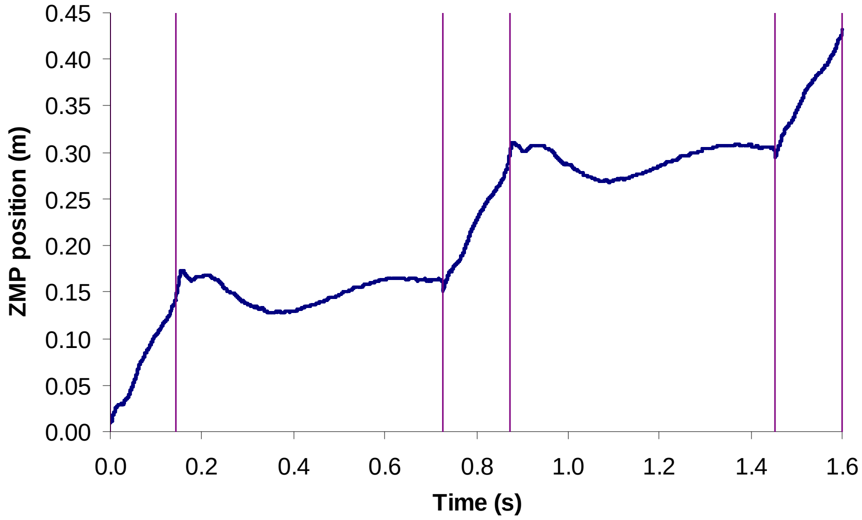

Figure 5.16: ZMP position

amplitude of 1 cm about the ankle point. When the pneumatic tracking controller is considered, these deviations get larger and more irregular, but stay within a limit of about 2 cm. A ZMP that reaches the physical boundary of the supporting foot during single support will make the robot tip over in the sagittal plane. This has to be prevented in order to ensure postural stability. The feet of "Lucy" have respective lengths of 20 cm to the tip and 10 cm to the heel of the foot, so the

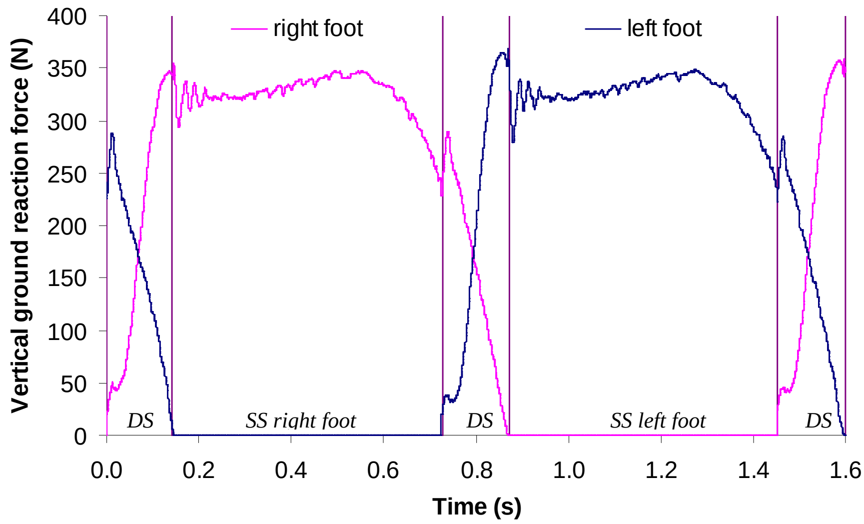

Figure 5.17: Vertical component of the ground reaction forces in the right and left foot

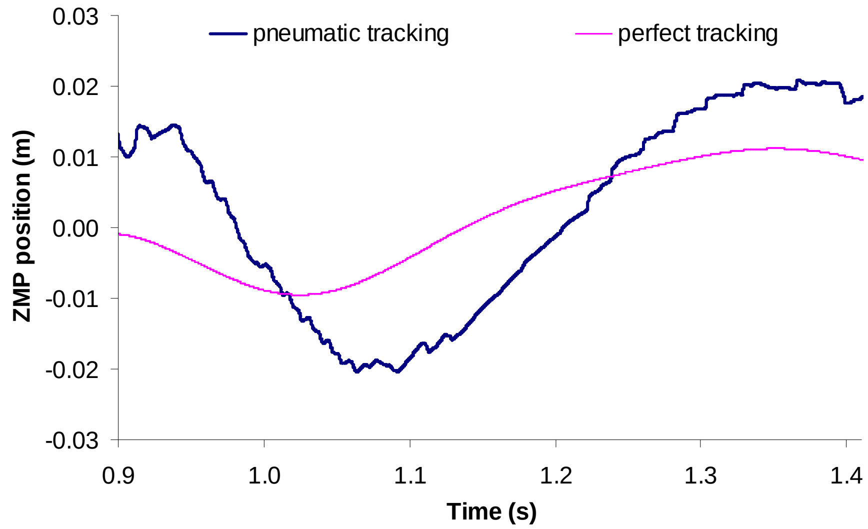

Figure 5.18: Comparison of ZMP position during single support between perfect and pneumatic trajectory tracking

overall stability is guaranteed, even with the introduced parameter deviations and imperfect pneumatic tracking system. Note that the prescribed ZMP strategy is actually a feedforward ZMP placement and that the simulation do not regard any external disturbance. In a real application, a feedback structure, while observing the ZMP by means of force measurements in the feet, should be provided to adapt the robot's motion in order to secure dynamic stability at all times. But this is beyond the scope of the presented work.

5.6 Conclusions

In this chapter an elaborate simulation model of the biped lucy was presented. The model combines mechanical and thermodynamical differential formulations to describe the link motions on the one hand, and the actuator torque generation on the other hand. Doing so allows to evaluate the proposed control strategy of chapter 4 under actuator limitations.

The simulation model allows to simulate a single as well as a double support phase, and in order to have a realistic evaluation, an impact phase when the swing foot touches the ground is also modelled. These phase transitions after all have a strong influence on the tracking performance. Not only phase transitions and the pneumatic nature of the drive mechanism have their influence, estimation errors of parameters, used within the control algorithm, also determine tracking performance. The simulation model therefore includes estimation errors on the inertial parameters of the robot links and errors on the estimated force function of the pneumatic muscles.

The purpose of the simulation model at this moment was to evaluate if dynamic stable walking, as proposed by the trajectory generator, is possible with the pneumatic tracking system. Hereby not considering control parameter optimization and energy consumption. A simulation of a walking motion at a moderate speed of 0.2 m/s was shown. An elaborate discussion concerning the different characteristics of the walking system was presented. Tracking performance was shown to be very good, at the expense of substantial valve switching. It was shown that even with imperfections introduced at several levels, the ZMP was located within a range of about 2 cm around the ankle point of the stance foot during single support. The ZMP located around the ankle point was planned by the trajectory generator. Due to the pneumatic drive mechanism, the ZMP moves in a wider range around the ankle point, but this range is bounded such that the ZMP stays far away from the foot edges, thus resulting in dynamically stable walking.

The simulation model is also intended for future use when implementing the control design in the real robot. The model then allows fast evaluations of parameter influences in order to help tuning the control performance. Furthermore, will the simulation model be used to give insights concerning exploitation of natural dynamics. It provides an important tool to search for suitable joint design parameter values and specific trajectories, all as a function of minimization of control activity by exploitating the natural dynamics.

Chapter 6

"Lucy" : design and construction

6.1 Introduction

The main goal of the biped "Lucy" is to investigate whether the PPAM can be an interesting alternative to the electric drive generally used for walking robots. Hereby focusing on the exploitation of compliance characteristics in combination with trajectory tracking. The compliance can be used in a first instance to reduce chock effects during touch-down of the swing leg, but as was already argued, the adaptability of the compliance can also be exploited to change the natural dynamics of the system in order to reduce control activity. Thus creating walking patterns analogous to passive walking. Trajectory tracking on the other hand is important towards dynamic stability, regarding ZMP conditions, in combination with a wide range of possible walking patterns. Thereby arguing that a robot, which can only walk within one fixed walking rhythm, is of no practical use. Thus the practical setup should be suitable to experiment on the following main items:

- Investigation of the influence of natural dynamics with adapted compliance for biped walking.
- Evaluation in a practical setup of a trajectory generator which ensures dynamic stability in combination with the pneumatic drive mechanism.
- Evaluation of a trajectory tracking control strategy with the specific pneumatic system.

In a first attempt to study trajectory tracking, a practical setup consisting of a one-dimensional joint had been built by Daerden. Figure 6.1 shows a picture of this setup. A position controller, with simple PI control techniques, was developed for an unloaded joint [Daerden et al., 1998] and the first elementary tests were performed to study joint compliance [Daerden et al., 1999]. Despite the good results for the unloaded case, several hardware limitations resulted in poor performance

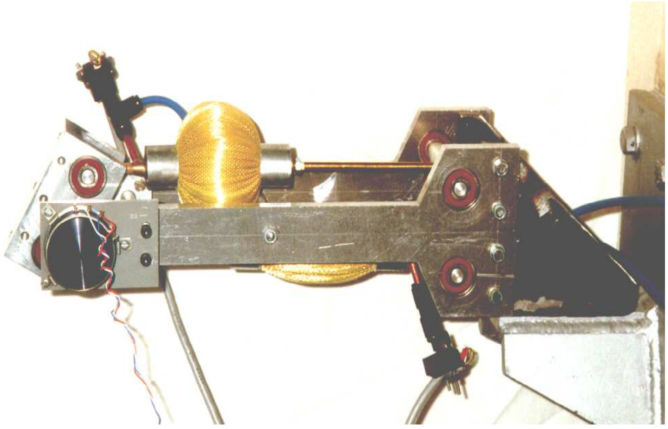

Figure 6.1: One-dimensional joint setup [Daerden, 1999]

when load was added. The most important limitation was the slow pneumatic valve system and the insufficient sampling rate of the computer hardware. The same mechanical setup, with renewed controlling hardware, was recuperated to test a newly designed pneumatic valve system [Van Ham et al., 2002], which resulted in a fast and accurate pressure control with on/off valves. This valve system forms the basis for an adequate trajectory tracking control system. At the same time a new setup, representing a one-dimensional leg as discussed in chapter 3, was built in order to study the basics of impact and energy recuperation with two PPAMs actuating the knee joint [Verrelst et al., 2000]. A picture of this setup is given in figure 6.2. Due to large friction in the actuated joint, this setup was not used to study trajectory tracking. Besides, it did not allow to study the effects on tracking performance of the dynamic effects induced by more than one activated joint.

Instead of building a new basic setup with two links and two actuated joints, such as a double pendulum structure, a two-dimensional walking biped was built. This setup is after all required to validate the trajectory generator (chapter 4) developed and evaluated so far only by means of simulations [Vermeulen et al., 2004, 2003]. Furthermore, the robot structure is designed in a modular way, such that separate parts of the robot can be used in order to perform experiments with reduced complexity. Parallel to the construction of the real biped model, a complete simulation model was developed (chapter 5), in order to introduce practical considerations into the computer model. But since simulations are also used for dimensioning purposes, such as joint actuator dimensions, the real experimental platform incorporates versatility towards possible joint design changes.

Due to the modular structure each elementary unit, such as a lower leg, an upper leg and an upper body, is almost mechanically and electronically identical. The latter means that each modular element is controlled by its own control hardware

Figure 6.2: One-dimensional leg setup

such that these elements have identical types of signal flows. Thereby allows the overall communication protocol easy reconfiguration of the control setup. The flexibility towards mechanical changes to the experimental platform is foreseen at joint torque level and recombination of the modular units. The joint torque characteristics can easily be altered by either replacing the pneumatic artificial muscles or by changing the actuator connecting interface. Furthermore, the frame of the robot has been designed in a straightforward manner to facilitate machining and it also allows easy attachment of additional parts, which could be required in a later phase. The design of the robot and its sophisticated hardware is discussed in the next sections. And, at the end this chapter, the first experimental results are briefly discussed.

Constructing a biped such as "Lucy" would have been impossible for just one person. Together with two colleagues, Ronald Van Ham and Bram Vanderborght, we worked as a team. As a consequence, all the work referred to in this chapter is not of my sole doing, but the result of a smoothly cooperating team.

6.2 Modular unit

6.2.1 Mechanical design

Each modular unit represents a link of the robot and drives one joint, e.g. the upper leg drives the knee joint. The mechanical setup of a modular unit incorporates a basic frame, two muscles attached to the frame via a pull rod mechanism, a leverage mechanism creating the interface to the neighboring unit and a pneumatic valve system which regulates the pressure inside both muscles.

Basic frame

As was already argued in chapter 3, a pull rod and leverage mechanism was selected to position two muscles in an antagonistic setup. The basic frame in which this system is incorporated is depicted in figure 6.3. The CAD drawing shows both assembled and exploded view of the basic frame. The modular unit is made of two slats at the side, which are connected parallel to each other by two linking bars. A joint rotary part, provided with roller bearings, is foreseen for the connection with an other modular unit. The fixed base for the pull rods mechanism includes two rotary axes at which the muscles are attached. The small rotations of these axes are guided by sliding bearings positioned in the frame. As can be seen in the exploded view, the basic frame is created by assembling several elementary parts. All these parts are made of a high grade aluminium alloy, AlSiMg1, apart from the bolts and nuts, required to assemble the frame. The cross sectional dimensions of the frame are determined to withstand buckling due to the load set by the muscles in the antagonistic setup. Forces generated by the muscles can easily go up to 5000 N.

Figure 6.4 shows a CAD drawing with the muscles attached to the frame by the pull rods and lever mechanism. The muscles are positioned crosswise to allow complete bulging. At one side they are attached to the frame via the fixed rotary base and at the other side the interface to the next modular unit is provided via the leverage mechanism. Two connection plates, joined together with two rotary axes, are fixed to the next modular unit and incorporate the leverage mechanism. Again sliding bearings are used to guide the rotations of both rotary axes. The position of the rotation points determine the dimensions of the leverage mechanism and consequently joint torque characteristics. The mathematical formulation of the torque as a function of force relation was given in section 3.2. The connection plates incorporate the parameters α_1, α_2, d_1 and d_2 of the leverage mechanism for both muscles. Since these parameters have a large influence, the connection plate system is the one which can be changed easily, besides muscle dimensions, to alter joint torque characteristics. Therefore the two plates have to be replaced with only different positioned holes for the sliding bearings.

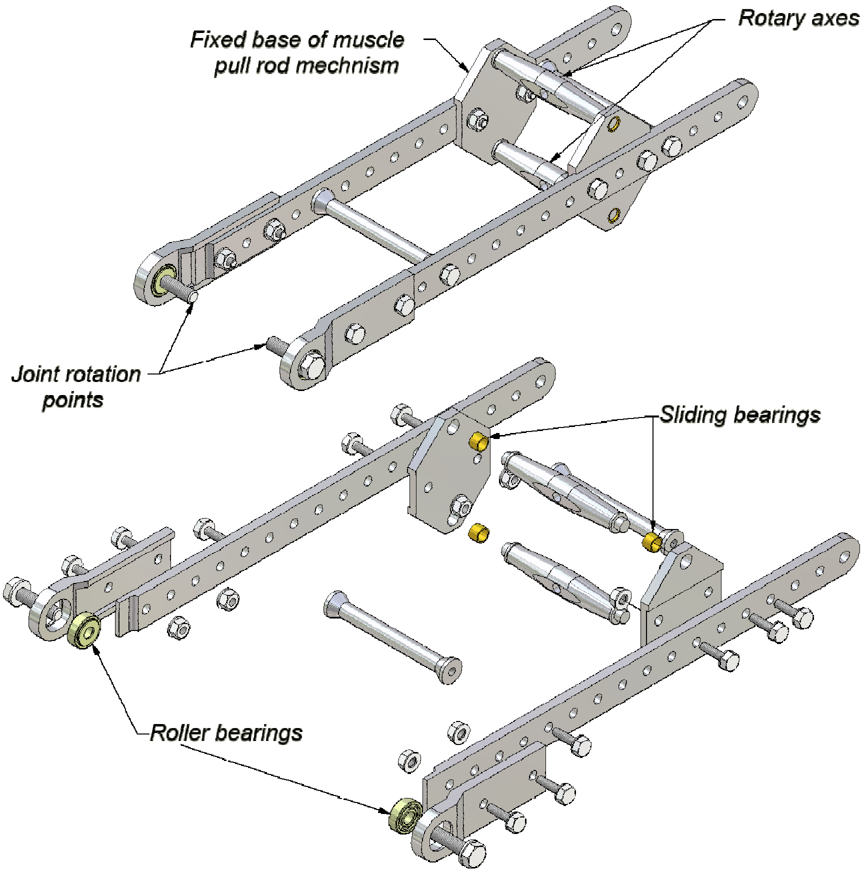

Figure 6.3: CAD drawing of the modular unit's basic frame

Valve system

Pneumatic artificial muscles have a high power to weight ratio which makes them suitable for legged robots. But for a pneumatic system a pressure control device should be taken into account to evaluate this ratio if the valve system is on board of the robot. So the weight of the valves controlling the muscles should be taken as low as possible without compromising too much on performance. Since most pneumatic systems are designed for fixed automation purposes where weight is not an issue at all, most off-the-shelf proportional valves are far too heavy for this application.

In order to realize a lightweight rapid and accurate pressure control, fast switching on/off valves are used. The pneumatic solenoid valve 821 2/2 NC made by Matrix weighs only 25 g. They have a reported switching time of about 1 ms and flow rate

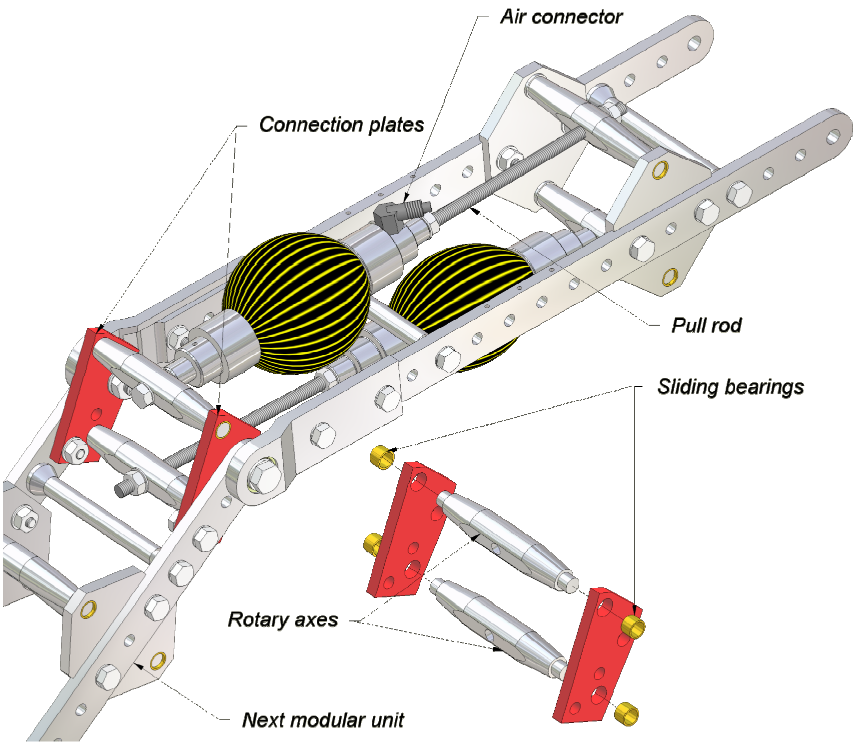

Figure 6.4: CAD drawing of the modular unit's basic frame with muscles and connection plates

of 180 Std.l/ min. Figure 6.5 shows a picture of the selected valve. The valves come with two different types, one with and one without return spring which acts on the air flow interrupting flapper inside the valve. The permitted pressure difference over the valve ranges, for each type, between $0 \ldots 6$ bar and $2 \ldots 8$ bar respectively.

To pressurize and depressurize the muscle which has a varying volume up to 400 ml, it is best to place a number of these small on/off valves in parallel. Obviously the more valves used, the higher electric power consumption, price and weight will be. Simulations of the pressure control on a constant volume led to the compromise of 2 inlet and 4 outlet valves. The different number between inlet and outlet comes from the asymmetric pressure conditions between inlet and outlet and the aim to create equal muscle's inflation and deflation flows. This was already argued in section 4.4.4 and for detailed information on the simulations is referred to [Van Ham et al., 2002].

The 6 valves are brought together in a valve island with special designed inlet and outlet collectors after removing parts of the original housing material. A CAD

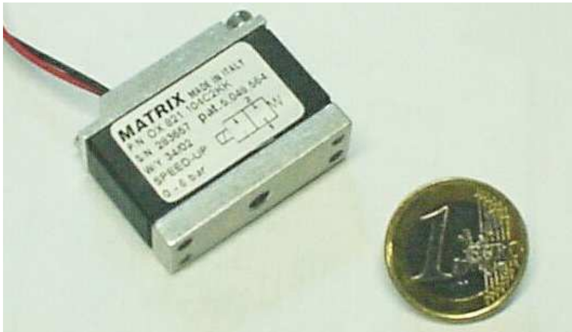

Figure 6.5: Picture of the pneumatic solenoid valve 821 2/2 NC made by Matrix

drawing of the valve island is given in figure 6.6. The total weight of this device is less than 150 g. The two valves at inlet are of the type without spring, while the four valves responsible to deflate the muscle are with the internal return spring. The pressure inside the muscle generally ranges from 0 to 3 bar gauge pressure, while the supply pressure level is set at about 7 bar. This leads to a pressure difference over the valves of minimum 4 bar for the inlet valves and 0 bar for the exhaust valves. Removing a spring significantly decreases opening times of the valve, while on the other hand the presence of the spring decreases closing times of the valves. Contrary, a large pressure difference over the valves increases opening times, while a small pressure difference increases closing times of the valves. So, due to the opposite pressure difference conditions over the inlet and exhaust valves, both situations concerning the return spring are exploited positively. For more detailed experimental information on this topic is referred to [Van Ham et al., 2002].

Complete mechanical setup of a modular unit

In figure 6.7 a final CAD drawing is given of the complete modular unit. The two valve islands are mounted at each side of the basic frame. The muscles are connected with the valves and the latter with a compressed air buffer. This buffer is required to avoid the pressure fluctuations in the compressed air supply tubes while controlling the complete biped. The volume of this buffer is comparable to the volume of one muscle. In normal operation, only one muscle of the antagonistic setup is inflated. The other muscle is deflated, except when the controller decides to increase the stiffness of the joint by increasing the mean pressure of both muscles. Additionally, a silencer is added at the exhaust of each valve island of the modular unit. Without a silencer, the immediate expansion to atmospheric conditions of the compressed air at the exhaust creates a lot of noise. A silencers consists of a closed permeable tube which makes the pressurized air leave the volume slowly, resulting in a strongly reduced noise generation. But generally, a silencer also obstructs the dynamic performance of muscle deflation, since a pressure rise in the silencer

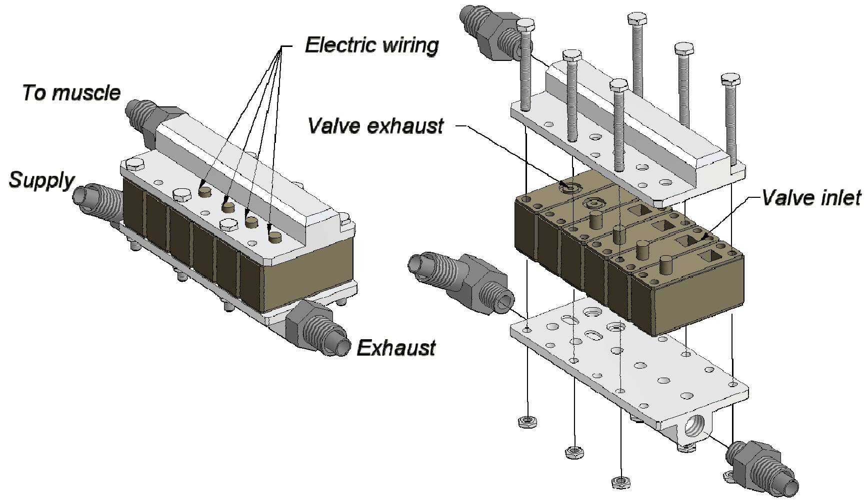

Figure 6.6: CAD drawing of the valve island

lowers the exhaust airflow. It is therefore important to use large silencers with good permeable material.

At the joint rotation side, an angular position limiter is provided. This device is equipped with two screws which can be regulated separately in order to set the joint rotation range. The limits of the angular position are provided to avoid singular joint configurations in the pull rod and leverage mechanism. Such configuration occurs when the axis of the muscle is aligned with the joint rotation point and the muscle attachment point in the leverage mechanism. In this situation the muscle can seriously damage the leverage mechanism when increasing pressures would by required by the controller. Secondly, this angular position limiter is used to bound the muscle contraction range. As was argued in chapter 2, this range lies between 5 and 35 %. Finally, this limiter can be also used to create a joint locking state by means of one muscle driving the joint to its extreme position. This can be exploited for example in the knee during stance, in order to induce a simple inverted pendulum motion over the stance foot [Wisse, 2004; Pratt, 2000]. Figure 6.8 shows a photograph of the modular unit.

6.2.2 Electronic design

Each modular unit has its own low-level control hardware in order to control joint position and stiffness. An overview of this hardware and its function is given in figure 6.9. The pressure PI controller and the bang-bang pressure controller (see 4.4.4) are implemented on a local micro-controller unit, which exchanges data with a central PC. Pressures are measured with absolute pressure sensors and the angu-

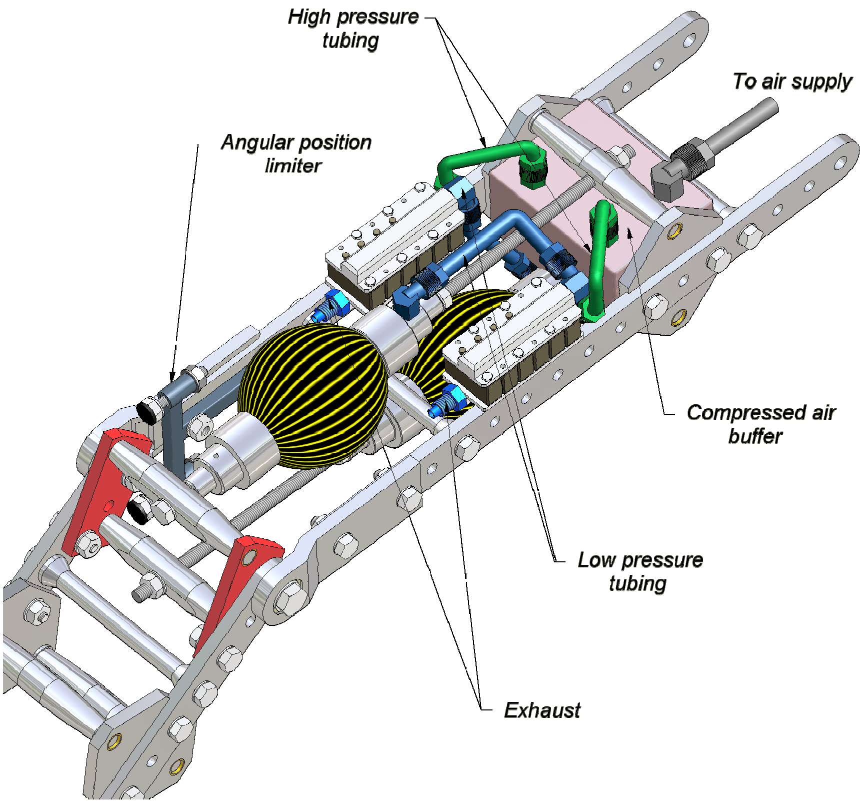

Figure 6.7: CAD drawing of the complete modular unit

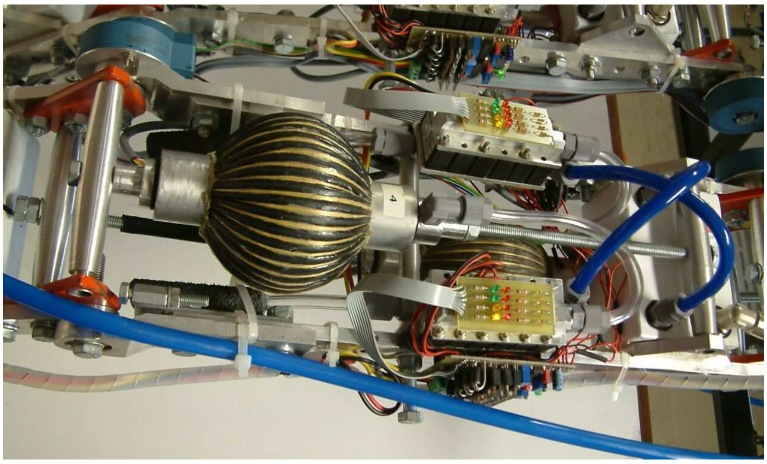

Figure 6.8: Photograph of a modular unit

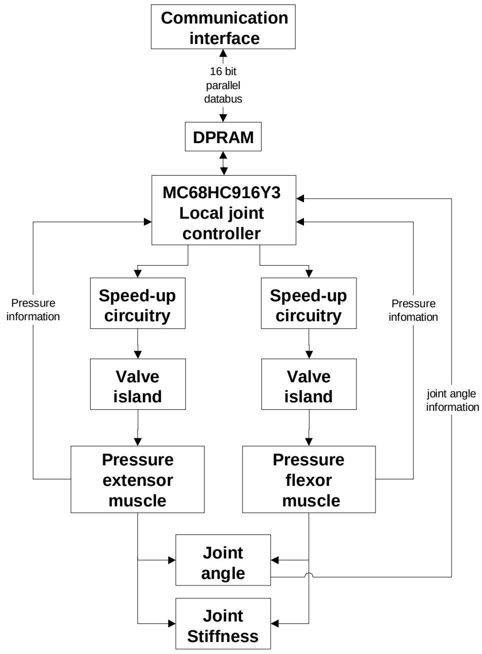

Figure 6.9: Overview of the low-level control hardware

lar position is captured with an incremental encoder. The valves of the two valve islands are controlled by digital micro-controller signals after being transformed by the speed-up board in order to enhance switching speed of the valves. In the next sections detailed information is given about the different elements of the low-level control hardware.

Pressure sensor

To have a good dynamic pressure measurement, the sensor is positioned inside the muscle (see figure 6.10). Since this sensor is inside the muscle volume, an absolute pressure sensor is provided. In order to pass through the entrance of a muscle, the size of the sensor and its electronics has to be small (12 mm). An absolute pressure sensor, CPC100AFC, from Honeywell has been selected for this purpose. The sensor measures absolute pressure values up to 100 psi (6.9 bar) and has an accuracy of about 20 mbar.

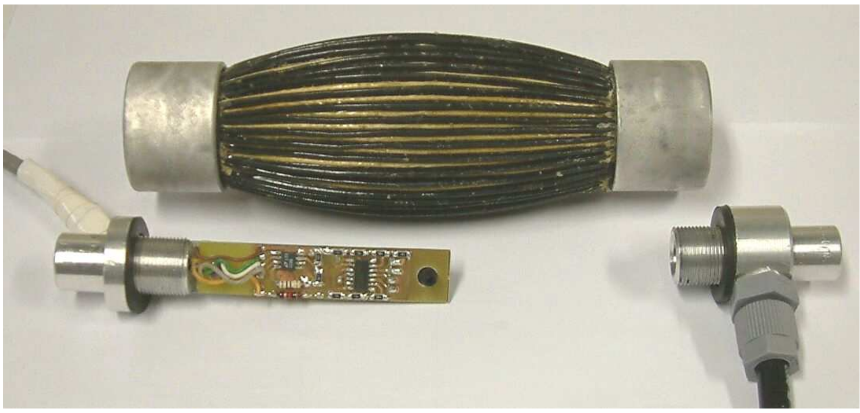

Figure 6.10: Pressure sensor to be positioned inside the muscle

The principe of the electronics, which conditions the millivolt output of the pressure sensor, is depicted in figure 6.11. The complete electronic scheme can be found in appendix D.3. The output of the pressure sensor is amplified by a differential amplifier, and in order to avoid as much as possible noise disturbance, the amplified pressure signal is immediately digitized by a 12 bit analog to digital converter. This chip communicates with the micro-controller unit by a serial peripheral interface (SPI), which is typically used for communication between chips and micro-controllers. A comparator is provided to generate an alarm signal in order to protect the muscle against pressure overload and consequently extend its lifespan. This alarm signal is not treated by a logic controller, but immediately acts on the central pressure supply valve (see 6.3.2). Whenever the muscle gauge pressure exceeds approximately 4.2 bar, the pressure supply is cut-off.

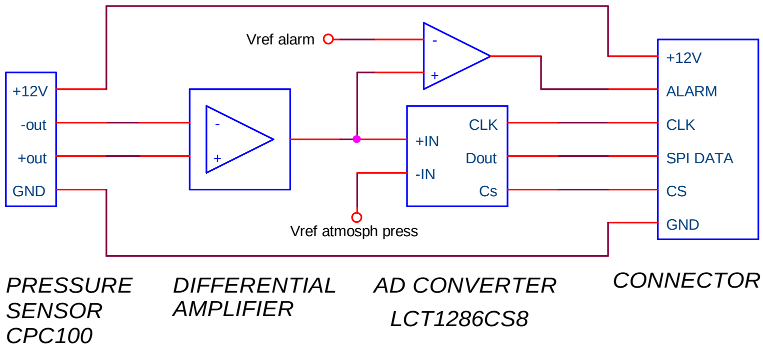

Figure 6.11: Essential scheme of the pressure sensor electronics

Valve system speed-up circuitry

In order to enhance the opening time of the Matrix valves, the manufacturer proposes a speed-up in tension circuitry. With a temporal 24 V during a period of 2.5 ms and a remaining 5 volts, the opening time of the valve is said to be 1 ms. But during practical tests the opening times were twice as slow, in certain ranges of pressure difference over the valves. The opening voltage is therefore increased, but the time during which this voltage is applied is decreased, as such that the valves get not overheated. Figure 6.12 gives the basic electronic scheme of the speed-up circuitry, a complete scheme can be found in appendix D.2. The micro-controller

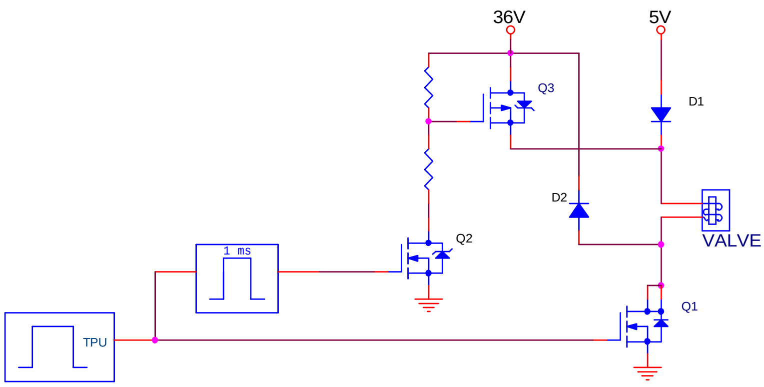

Figure 6.12: Essential scheme of valve speed-up circuitry

commands the valves via discrete 5 V on/off signals. These signals directly activate mosfet Q1 in order to apply 5 V over the valve. A timing unit ensure switches of mosfet Q2 and Q3 in order to apply temporally an increased voltage. Whenever the micro-controller commands the valve to close, by disabling mosfet Q1, the discharge path is connected to the increased supply source via diode D2. This provides a fast discharge of the electromagnetic energy of the valve, which results in a faster closing time. Several practical tests, for which are referred to [Van Ham et al., 2002], have resulted in an opening and closing times of about 1 ms. An increased opening voltage of 36 V is being applied during 1 ms. Figure 6.13 gives a photograph of the speed-up circuitry with its valve island. Four circuits, such as in 6.12, are provided. Two circuits control separately the two inlet valves and another two control the exhaust valves. Hereby three valves are controlled simultaneously by one circuit.

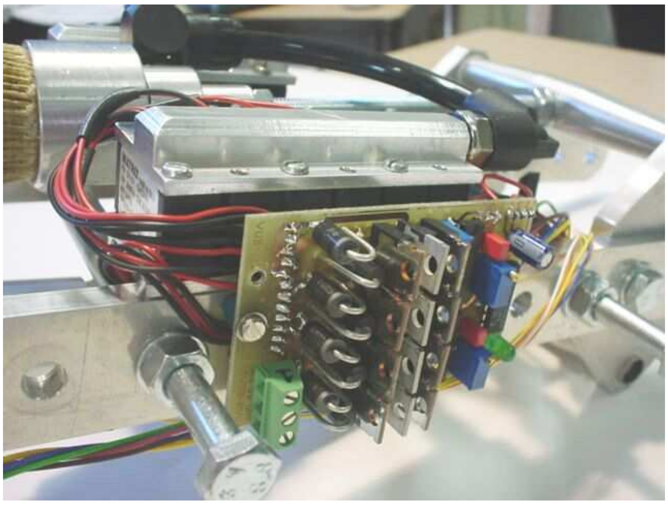

Figure 6.13: Valve speed-up circuitry

Joint micro-controller unit

The trajectory generator, inverse dynamics controller and delta-p units are implemented on a central PC since these controllers require substantial computational effort. The PI controller and the bang-bang controller are locally implemented on micro-controller units. The bang-bang controller requires logic computations, while the PI controller only needs few arithmetic calculations. Therefore a 16 bit processor was chosen over an 8 bit and 32 bit processor. The former is not suited for arithmetics, while the latter is an overkill for the fairly simple local feedback control implementation. The chosen micro-controller is the MC68HC916Y3 of Motorola. This controller has a 16 Mhz clock rate and an internal 100 kB flash EEPROM. A separate timer processor unit (TPU) can process sensor information, such as encoder reading, and control outputs without disturbing the CPU.

The basic scheme of the micro-controller board is depicted in figure 6.14. A complete electronic scheme of this board is given in appendix D.1. The basic task of the micro-controller consists of reading the pressure, register encoder signals, control the on/off valves of the two valve islands and communicate with the central PC. Hereby performing the local PI and bang-bang control scheme. The pressure is read via the SPI interface of the micro-controller and the valves are commanded through the TPU output. The joint angular position is captured with a HEDM6540 incremental encoder from Agilent Technologies which has 2000 pulses per revolution, resulting in one detectable flank each 0.045°. The micro-controller board provides

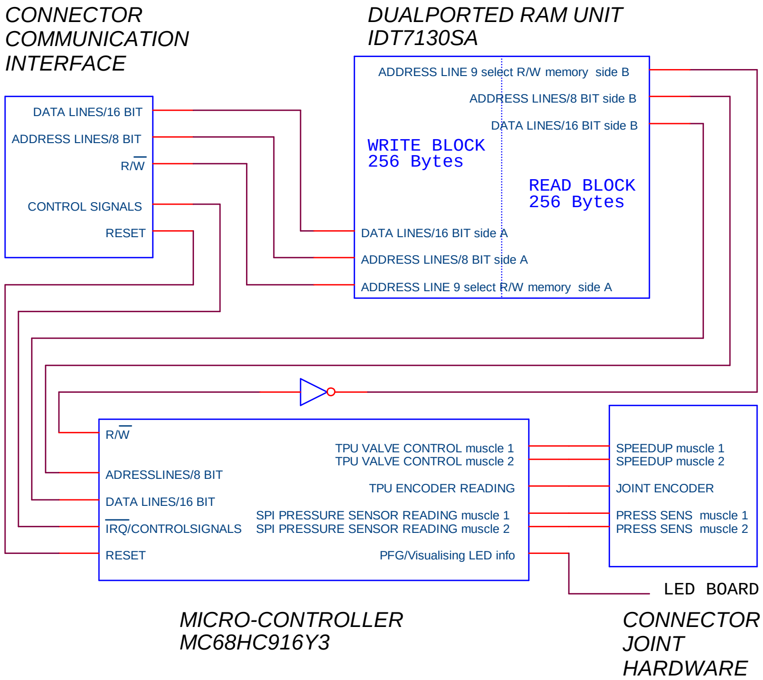

Figure 6.14: Essential scheme of micro-controller board

a quasi real-time local control of the robot joints. It performs the local feedback control loop and communicates with a central PC at a refresh rate of 2000 Hz. In order to ensure the real-time operation, the 16 bit parallel communication lines are buffered via a dual ported RAM structure. The memory of this structure is physically divided into an input and output section of each 256 bytes, by applying the external $r/\overline{w}$ signal to the higher address lines of the dual ported RAM unit. Additionally, several control lines are linked with the IRQ input/output interface of the micro-controller. The communication interface (see 6.3.2) uses these control lines to master the communication protocol and reset the different micro-controllers. Figure 6.15 shows a picture of the micro-controller board with its dual

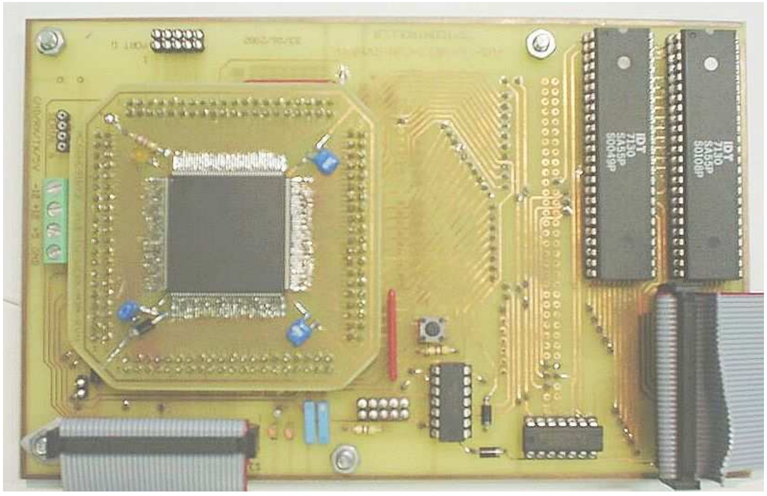

Figure 6.15: Micro-controller board

ported RAM communication interface.

6.3 Complete biped

6.3.1 Mechanical design

Integrating the modular units

Six modular units, as discussed in the previous sections, are integrated to create the complete biped. A CAD drawing of the mechanical configuration of the complete robot is given in figure 6.17. Figure 6.18 gives a photograph of the real robot, including the electronic components. The upper body of the robot consists of two modular units which are rigidly connected to each other. The left and right antagonistic muscle pairs of the upper body drive the left and right hip joint respectively. Each leg has two modular units, which form the upper leg and the lower leg. The muscle pair of the modular unit in the upper leg actuates the knee joint and the muscles in the lower leg drive the ankle joint. The latter forms the connection to the foot, which is the only link with a configuration different from the modular unit setup. The feet do not have any form of toes and do not explicitly have a heel shape rounding at the rear. Thus currently, "Lucy" can only walk with the feet kept parallel to the ground at touch-down and foot lift-off. This has been done in order not to complicate control trajectory generation and tracking control strategies. Performance of rolling over a rounded heel shape at touch-down and usage of an extra toe link at foot lift-off, after all introduces two extra intermediate phases in the walking cycle. At control level, this means that for these two phases an additional DOF has to be taken into account in the dynamic model of the robot.

Figure 6.16 gives an overview of the pneumatic circuit, which is used to control the different muscles of the robot. The pneumatic scheme shows the 6 identical pneumatic circuits of which each of them drives one antagonistic flexor/extensor muscle pair. This scheme contains the local reservoir from which the two valve islands are supplied with compressed air. The valve island is depicted with separately inlet and exhaust, which each of them are represented by two "2/2 electrically actuated" valve symbols. These two symbols represent the 2 reaction levels of the valve system. The number of actual valves which are included in each configuration are depicted as well. Note that closing of the inlet valves is not done by a return spring but by the pressure of the supply air.

All reservoirs of the modular units are connected to the pressure regulating unit at the central pneumatic distributor by separate tubes. The pressure regulating unit consists of two supply circuits with different pressure levels. One for the normal operating high pressure supply and an other for a lower reference pressure supply. The latter circuit is used for the calibration of the pressure sensors (6.2.2) each time the robot is initialized. Two mechanical pressure regulating units determine the pressures in the high and low pressure circuits respectively, and each circuit is interrupted with an electrically actuated valve. The reference circuit uses a 2/2 valve, while the high pressure circuit is interrupted by a 3/2 valve. The exhaust of this high pressure valve is connected to an electrically actuated 2/2 depressurizing valve in order to deflate the complete robot. The air supply is buffered with a large central reservoir and an airflow sensor is positioned in the supply line of this reservoir.

Since the robot can only walk in the sagittal direction, a kind of supporting structure has to be provided to avoid turning over in the frontal plane. Several configurations can be used for this purpose. One such configuration is a rotating boom mechanism attached to the hip and a central rotating point as was used for e.g. the biped "Rabbit" in France [Chevallereau et al., 2003] and "Spring Flamingo" at MIT [Pratt and Pratt, 1998]. This solution requires a lot of space since the boom mechanism has to be large in order to mimic planar walking. Another possible configuration are laterally extended feet, such that the projection of the COG on the ground in the lateral plane lies within the supporting feet area. This has for example been used for the robot "Bart-UH" in Germany [Lorch et al., 2002]. The extended feet however require a large distance between the legs such that they can never hit each other and some positions of the feet are not possible anymore. For "Lucy", it has been decided to use a vertically positioned XY-frame, to which the hip points of the robot are attached with two sliding bearings. The XY-sliding mechanism is of high quality for smooth sliding of the frame, in order not to disturb too much the robot motion in the sagittal plane. Such supporting configuration allows the use of a treadmill, which is currently under construction. A picture with a leg of "Lucy" attached to the XY-frame is given in figure 6.19.

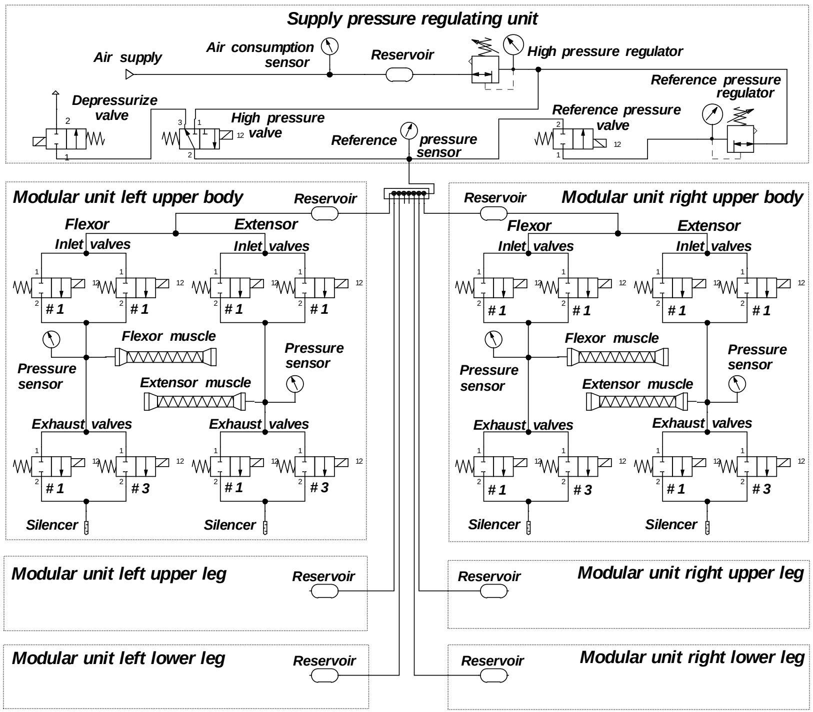

Figure 6.16: Schematic overview of the complete pneumatic circuit

Joint characteristics

The kinematics of a joint have been described in section (3.2). Essential parameters for joint design have been linked to contraction and torque characteristics in function of the specific joint angle. In figure 6.20 these joint design parameters are marked on the CAD drawing of a modular unit. As was discussed in section 6.2.1, the joint design allows easy reconfiguration. The parameters b_1 and b_2 are fixed and the parameter l_b in theory can be altered in discrete steps by moving the fixed attachment part of the muscles. But with all components such as valve islands and speed-up circuitry mounted on the robot frame, there is not much space left to manoeuver. The essential parameters which can be altered to change the specific joint characteristics are d_1, d_2, α_1 and α_2. These changes are made with the connection plates of the joint rotation system. Furthermore are also adaptable the muscle contraction parameter ϵ^c which is defined at a chosen mid angle θ^c. This parameter is associated with the length of the threaded rods which form the interface between muscle and leverage mechanism. This length can be altered with the nuts that cling the rods to the rotary muscle axes (see figure 6.4). Of course, the muscle dimensions also influence the joint torque characteristics, but currently

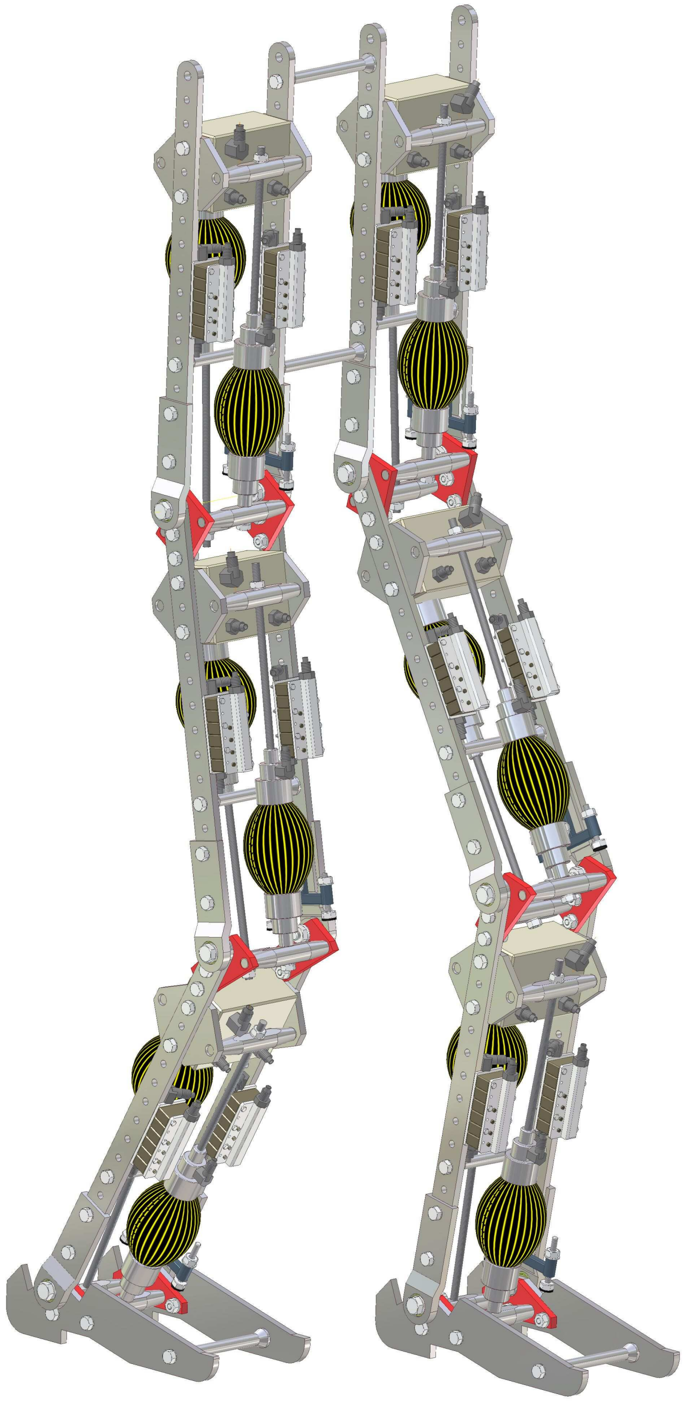

Figure 6.17: CAD drawing of the robot "Lucy"

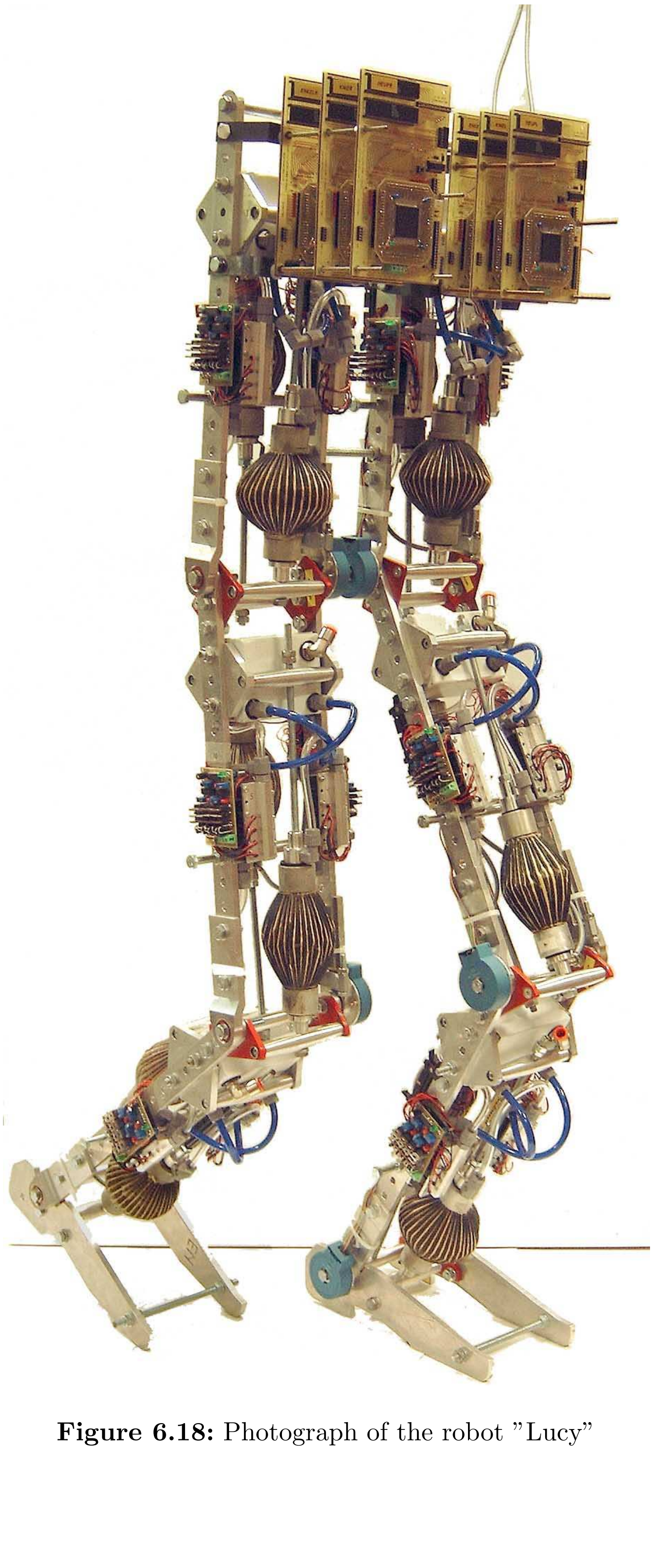

Figure 6.18: Photograph of the robot "Lucy"

Figure 6.19: Photograph of the leg of "Lucy" attached to the guiding vertical XY-frame

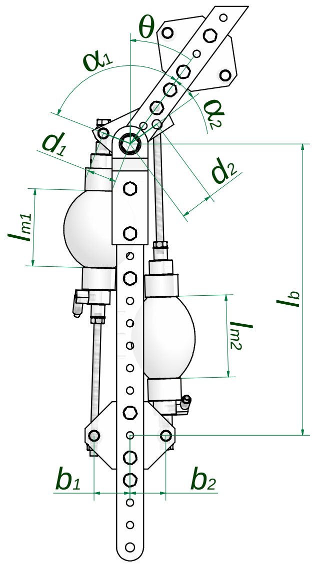

Figure 6.20: CAD drawing with side view of a modular unit, showing the kinematical joint design parameters

all muscles of the robot have the same dimensions, which were discussed in chapter 2.

When designing the joint characteristics, a lot of requirements should be taken into account. Such as static torques required for standing still and more important, dynamic torque values for walking. Of course, the latter are strongly related to the walking speed and control strategies. And, in combination with the torque values, the ranges of angular motion should be determined as well, these also depends on the various movements the robot should perform. In case of this biped, another design factor, associated with natural dynamics, has to be taken into account. The kinematic joint parameters in combination with muscle dimensions determine the range in which the compliance of the joint can be altered. And of course, if this compliance variation is intended for energy minimization, the range in which it should vary depends on the walking motion and on the specific control strategy. This all clearly indicates that a good joint design is hard to make at once. The versatility in the joint configuration by allowing easy changes to the leverage mechanism is therefore provided. During the future experimental and theoretical evolution concerning the different aspects of controlling "Lucy", the design parameters will be altered corresponding to the gained insights in this complex matter.

Currently, the first design of the parameters has been made rather intuitively and roughly based on simulations performed by Vermeulen [2004] and some analogy with human walking. In figure 6.21 the specific oriented relative ankle, knee and hip angles are defined (counterclockwise positive). The ankle angle β_1 varies symmetrical with respect to the lower leg between $-25°$ and $25°$. The knee is not able to stretch completely and the specific joint angle ranges from $15°$ to $65°$. The upper body should be able to rotate more to the front than to the rear as is the same for humans. The range of angular motion for the hip joint is therefore set between $-35°$ and $15°$.

The generated torque at 3 bar is designed to be able to generate 70 to 80 Nm at the extreme positions, which generally require the largest joint torques for static postures. In the first design attempt, the torque generation is taken symmetrical for both flexor and extensor muscle of a joint. This is not always necessary, e.g. the flexor of the knee joint generally does not require the same large torques as the extensor muscle. The knee extensor muscle has to carry the weight of the robot, while the flexor is for example required to lift the lower leg when the specific leg is in a swing phase. So the torque characteristics where designed with 3 bar gauge pressure, but it is taken into account that higher pressures until a 4.2 bar can be set in the muscles (see alarm pressure sensor in 6.2.2). So whenever the tracking controller demands higher torques, it can apply higher pressures in the specific muscle. The actual torque characteristics currently determined for "Lucy" are depicted in figure 6.22, 6.23 and 6.24. The graphs on these figures give extensor and flexor torques respectively for ankle, knee and hip at 1, 2 and 3 bar muscle gauge pressure. The muscle contraction range associated with the angle range for each joint are approximately situated between 7 and 30 %. This means that the

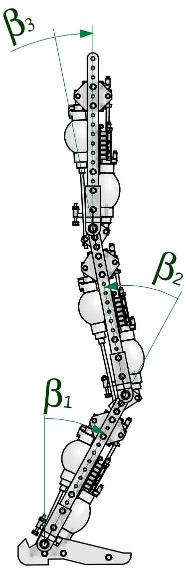

Figure 6.21: Definition of the oriented relative joint angles (counterclockwise positive)

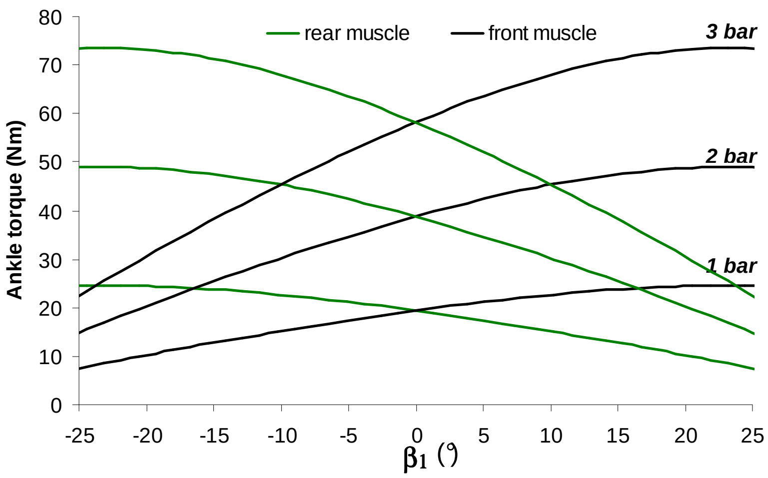

Figure 6.22: Generated flexor and extensor torque in the ankle joint for 1, 2 and 3 bar

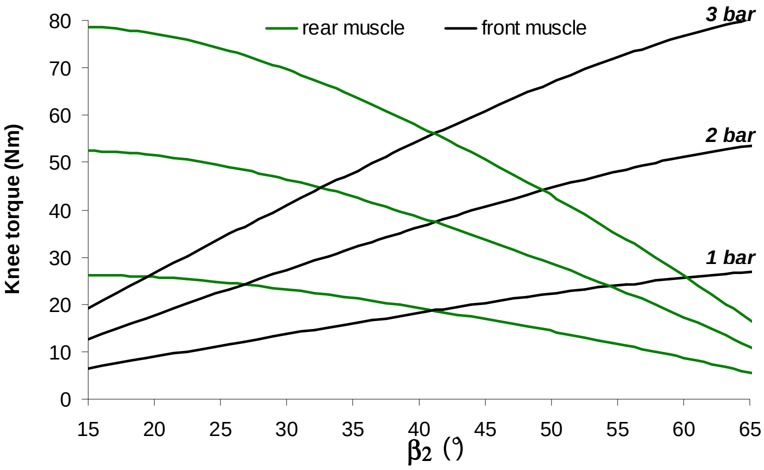

Figure 6.23: Generated flexor and extensor torque in the knee joint for 1, 2 and 3 bar

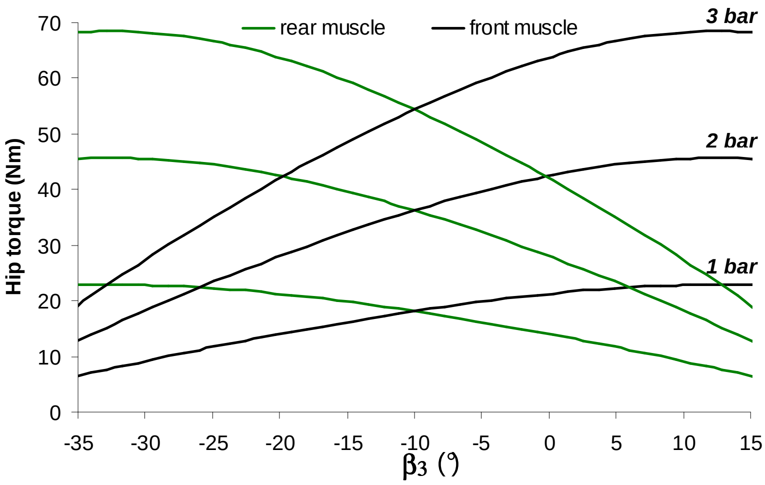

Figure 6.24: Generated flexor and extensor torque in the hip joint for 1, 2 and 3 bar

angular ranges still can be extended when required, the nuts of the angular position limiters in the joints can be fine-tuned to fix exact ranges.

6.3.2 Electronic design

Figure 6.25 gives an overview of the complete electronic hardware. The central PC hosts the graphical user interface (GUI) and performs the calculations for a large portion of the control scheme. This includes the trajectory generator, computed torque and delta-p unit since these require substantial computational power. The

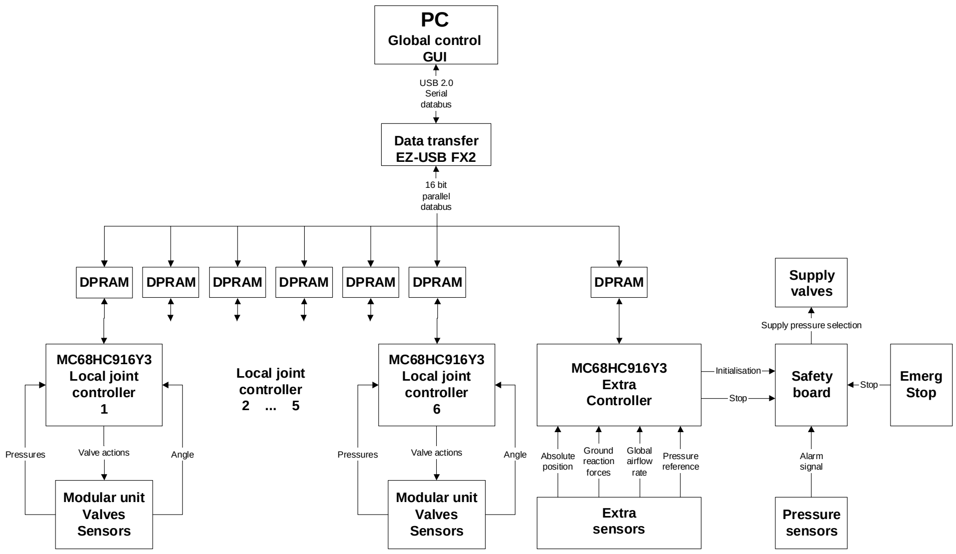

Figure 6.25: Schematic overview of the robot electronics

PC exchanges data with the different dual ported RAM units of the low-level control boards through a data exchange agent which is implemented on an extra micro-controller. This controller distributes the serial USB 2.0 bulk data transfer, originating from the PC, over the several 16 bit parallel data lines going to the dual ported RAM units of the local micro-controllers, and the other way around. Besides the 6 micro-controllers, of which each of them masters a modular unit, an extra controller is provided to read additional sensor information and control the supply valves via a safety board. Extra sensor information concerns absolute robot position, ground reaction forces, air consumption, and supply pressure level. The safety board controls the supply valves and depressurizes the supply tubes whenever a muscle pressure sensor gives an overload pressure alarm signal, or whenever an emergency bottom is activated. In the next sections detailed information about this global electronic scheme is given.

Communication hardware and protocol

Since a lot of extensive calculations are required due to the model based control algorithms, a central PC is used. Therefore a fast communication line between PC and robot hardware is provided. A fast communication line could be an extension of the internal PC bus by means of a parallel data communication, but this kind of communication is only suitable for short distance applications. For larger distances (several meters) serial communication protocols are preferable. The most popular serial protocol in the past was the RS232, but this is only suitable for slow data transfer (20 to 115 Kbit/s). Nowadays, several other serial protocols, used to branch to computers, have much higher transfer rates: USB (up to 480 Mbit/s), FireWire (standard IEEE-1394: 400Mbit/s and IEEE-1349b: 3.2 Gbit/s) and Ethernet connections (up to 1 Gbit/s). Since USB is a widely used standard, which is available at all modern computers, and since a micro-controller was found, which incorporates a USB 2.0 interface, USB was chosen as communication system. Over time the USB standard has evolved from USB 1.1 (1.5 or 12 Mbit/s) to the current USB 2.0 (up to 480 Mbit/s). For normal control operation the communication line should only transfer pressures and angle information, but in the experimental setup much more information such as control parameter values, valve actions and several status information is transferred. A total set of 226 bytes are transferred in bulk. Therefore the fastest USB 2.0 protocol is preferred in order to have a reasonable sampling rate.

Since the local Motorola controllers (6 joint controllers+1 extra controller) have a 16 bit parallel communication bus via the dual ported RAM units, the serial USB bulk data block has to be divided into 7 blocks of 16 bit parallel data. Therefore

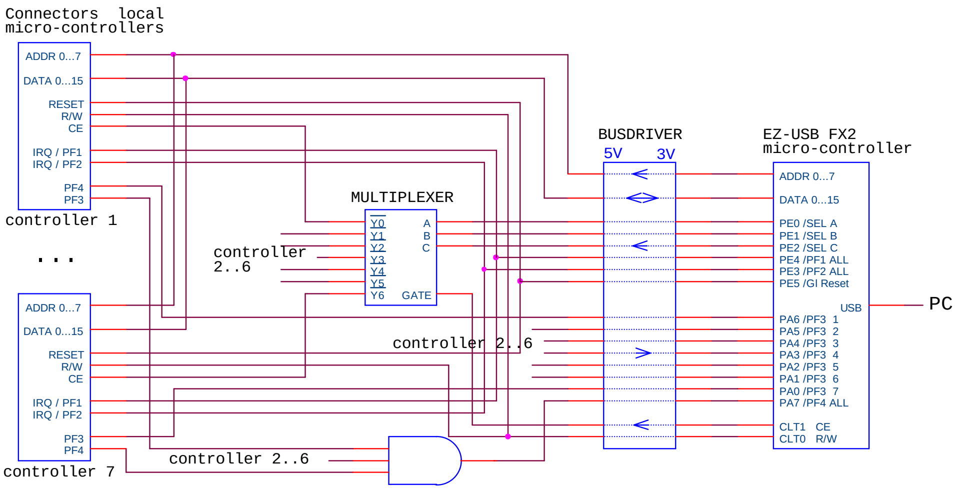

Figure 6.26: Communication interface overview scheme

an extra micro-controller, EZ-USB FX2 from Cypress Semiconductors, is provided to act only as data transfer agent. This controller runs at 48 Mhz and is able to transfer the serial data block of 226 bytes to the peripheral 16 bit data bus in less than 50 μs. Additional to the Cypress development board, an electronic interface has been created to connect the peripheral bus of the Cypress micro-controller to the different dual ported RAM units. An overview of the communication interface is given in figure 6.26, a detail of the expanding electronics can be found in appendix D.4. This interface mainly converts the different voltage levels of address and data lines and connects the Cypress controller, which is the bus master, to the interrupt driven ports PF of the several Motorola micro-controllers. Through the first three pins on port PE, the Cypress controller selects a specific slave micro-controller via a multiplexer. It can generate common interrupts on pins PF1 and PF2 of the different micro-controllers and command a global reset of these controllers, such that a software reset of the complete robot can be ordered by the PC. In the other direction each slave controller can communicate separately or all together, via an AND gate, with the pins of port PA of the Cypress bus master. All these lines are used to exchange communication acknowledgement signals. A photograph of the complete communication interface is given in figure 6.27.

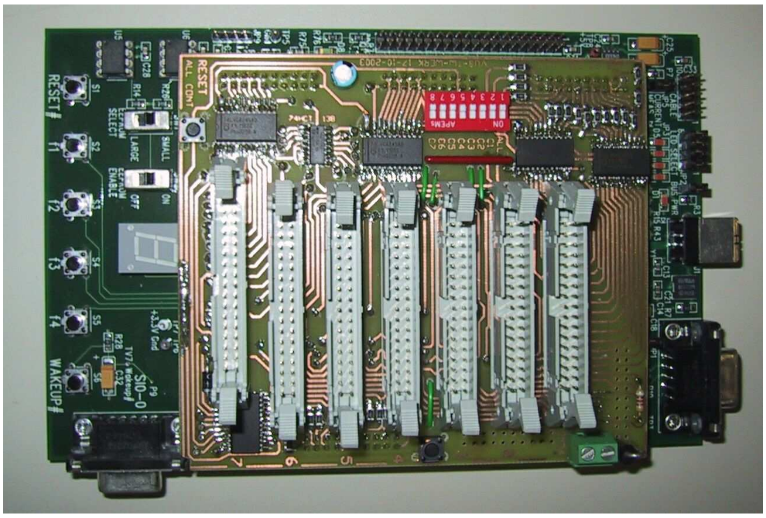

Figure 6.27: EZ-USB FX2 communication interface

Due to the use of a Windows operating system the refresh rate for the control calculations, implemented on the PC with high priority, is currently set to 2000 Hz, which is the same as the refresh rate of the local micro-controller units. The timing of the communication refresh rate is controlled by the USB Cypress micro-controller. The local micro-controllers ensure low-level, quasi real-time, control of the joints, and in order to prevent control disturbance of missed torque calculations by the central PC, the incoming data of the local units are buffered via the dual ported RAM hardware. So whenever the central PC does not succeed to perform the necessary calculations within the sampling time, the local control units use the previously sent data, which are stored in the dual ported RAM structure. One should also remark in the context of this refresh rate, that the delay time of the valves is about 1 ms, which suggests that the communication frequency of 2000 Hz is high enough.

Extra sensor implementation and safety board

Besides the 6 micro-controller boards, an analogous micro-controller board is provided. This micro-controller is responsible for handling additional sensor information and control of a safety board. The controller board is the same as for the joint controllers (6.2.2), except that the connections for the valves and sensors differ. The TPU of this controller reads three additional encoder signals which are of the same type as for the joints. The encoders measure the horizontal and vertical position of the hip point, which moves together with the guiding XY-frame, and measure the absolute rotation of the upper body. These signals fully determine absolute position of the robot since it can only move in the sagittal plane. Two extra sensors, air flow and reference pressure sensor, are positioned in the pressure regulating circuit. The standard analogue signals of these sensors are transformed with the same electronic scheme as for the pressure sensor inside the muscles (6.2.2). So they are captured by the SPI interface of the extra micro-controller. The flow sensor is required to have an indication of the air consumption, which becomes crucial when dealing with experiments regarding exploitation of natural dynamics. This sensor is a SD6000 flow meter from IFM Electronic and measures airflows in a range from 4 to 1250 Nl/min. It has a built in accumulator which gives total air consumption. The reference pressure sensor is required to calibrate all 12 pressure sensors inside the muscles, whenever the robot is initialized. This reference sensor is a PN2024 gauge pressure sensor also from IMF electronics. It measures in a range from -1 to 10 bar gauge pressure with accuracy smaller then $\pm 0.6\%$ of the range. Four additional force sensors will have to be provided to measure ground reaction forces in the foot. Each foot requires two such sensors, one in the front and one at the rear, in order to determine the ZMP position during single support. This information is required to evaluate dynamic stability of the robot and will be used to create a ZMP feedback structure to compensate for errors of the model based feedforward trajectory generation. These sensors and the feedback structure are not specified yet.

The safety board consists of electronic hardware, which commands the three valves of the supply pressure regulating unit (figure 6.16). This board handles all the alarm signals, originating from the pressure sensors inside the muscles and several emergency stops. Whenever an alarm signal is activated, the supply valves of the two pressure regulating pneumatic circuits are closed, while the depressurizing valve is opened in order to deflate the complete robot. Opening or closing of the supply valves in the pressure regulating circuits can be commanded by the 7th micro-controller, if the valve commands are not overruled by the electronic hardware during an emergency case. Since this controller is attached to the PC via the USB and dual ported RAM communication structure, selection of the proper supply pressure circuit and depressurization of the robot can be commanded by the central control and GUI. The complete electronic scheme of the safety board can be found in appendix D.5.

6.4 Preliminary tracking experiments

Currently, most parts and electronic hardware of the robot are assembled, apart from the absolute robot position encoder measurements and the force sensors in the foot. The USB communication with a central PC is established and a GUI is designed to guide the experimental process. The feedforward trajectory tracking control algorithm, as proposed for the single support phase, has been programmed and is currently being tested on the real robot. The tests that are carried out so far, only regard leg motions while the robot is suspended with both feet in the air. A full dynamic walking motion can not be achieved yet since double support control strategies are not yet implemented and the required treadmill, for steady state experiments, is still in its development phase.

In order to quickly evaluate the tracking performance, the proposed single support feedforward control structure is implemented on the robot, while it mimics essential walking motions. Thereby the upper body is always in an upright, fixed position and the feet move in the air as if there was a single and double support phase while walking at a speed of about 0.5 km/h. A video of this motion is found at the following internet address: http://lucy.vub.ac.be/movies.htm. Although the practical implementation has not yet been thoroughly examined, already satisfactory results are generated. Some graphs, characterizing these first achievements, are given in figures 6.28 to 6.31.

Figure 6.28 gives the desired and measured angle for the ankle, knee and hip joint of one leg. The depicted angles correspond to the definition of the relative joint angles β_i of figure 6.21. The presented graphs depict two walking cycles and clearly show the effectiveness of the control strategy. Note that the presented graphs include two double support phases and four single support phases of both legs. Tracking errors are bounded within a maximum of one to two degrees. Although the actual stability can not be evaluated yet, these results already give an indication that promising future experiments may be expected.

Figures 6.29 and 6.30 depict required and measured pressure values for the knee. Both pressure courses of front and rear knee muscle are shown for two walking cycles. The mean pressure p_m is set at 2.5 bar, which results in a sum of both

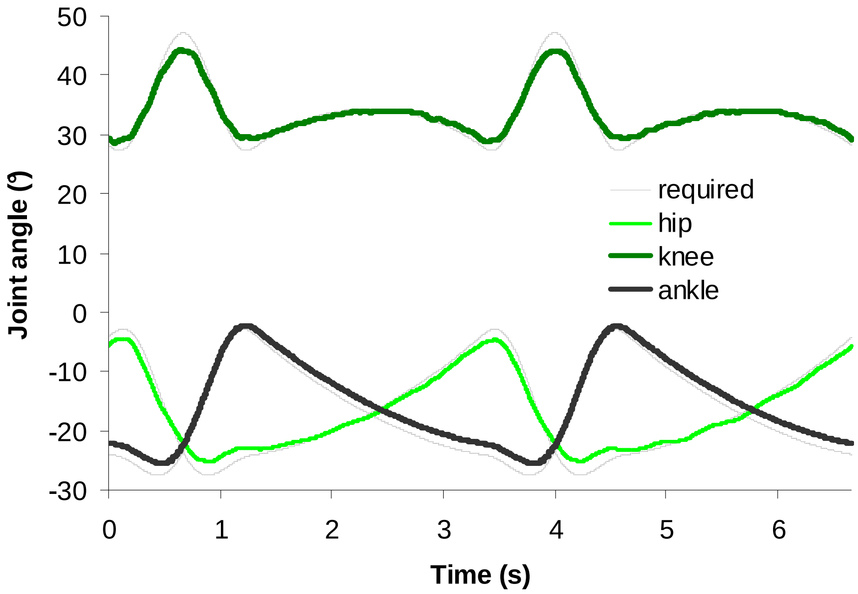

Figure 6.28: Desired and measured angles β_i (°) for the ankle, knee and hip joint

pressures of approximately 5 bar. Additionally, both graphs show the valve activity which is for this movement only switching of one inlet or outlet valve. Analogous to the simulation of chapter 5, the valve switching is rather nervous since the tracking controller, at this stage, is just been implemented without any kind of optimization. In order to have clearer view on the pressure control behaviour, figure 6.31 gives a detail of the pressure course and valve switching for the front muscle in the knee for the time interval 1 to 2 s. From 1 to approximately 1.2 ms the knee is stretching, which means that the knee angle is decreasing. Consequently, the volume of the front muscle in the knee is increasing. This explains the pressure drops with closed muscles for this time interval. On the contrary, after 1.2 ms the knee is flexing, although with a smaller slope. Thus it is expected that this would induce pressure rises when the valves are closed. But, the graph shows that the pressure stays about the same when a valve is closed, which is explained by the existence of small air leaks in the muscles and the tube connections.

These first experimental tests show the effectiveness of the pneumatic tracking system and its control structure. In combination with the real-time trajectory generator, the tracking system should lead to a dynamically stable walking motion of the robot "Lucy". The next step in the experimental process will be the implementation of the double support phase tracking control strategy and the provision of a speed controlled treadmill to perform continuous walking experiments. During these experiments a more profound study of the results will be made in order to tune the several parameters. Therefore, the simulation model can be used as a

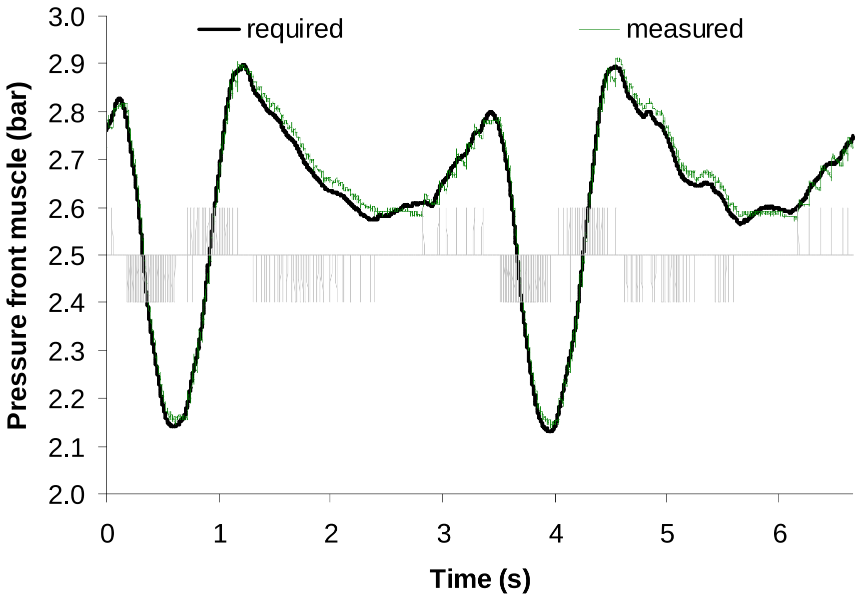

Figure 6.29: Required and measured pressure (bar) in the front muscle for the knee joint

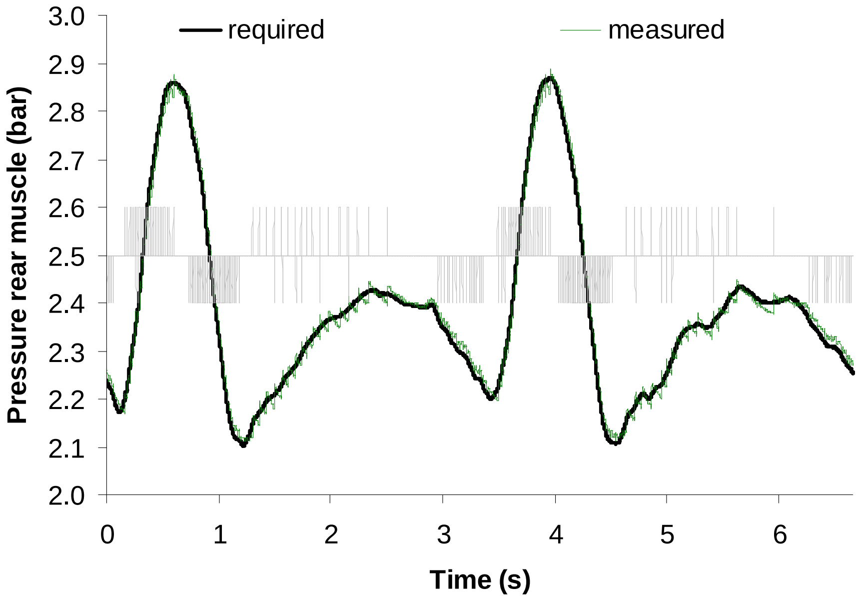

Figure 6.30: Required and measured pressure (bar) in the rear muscle for the knee joint

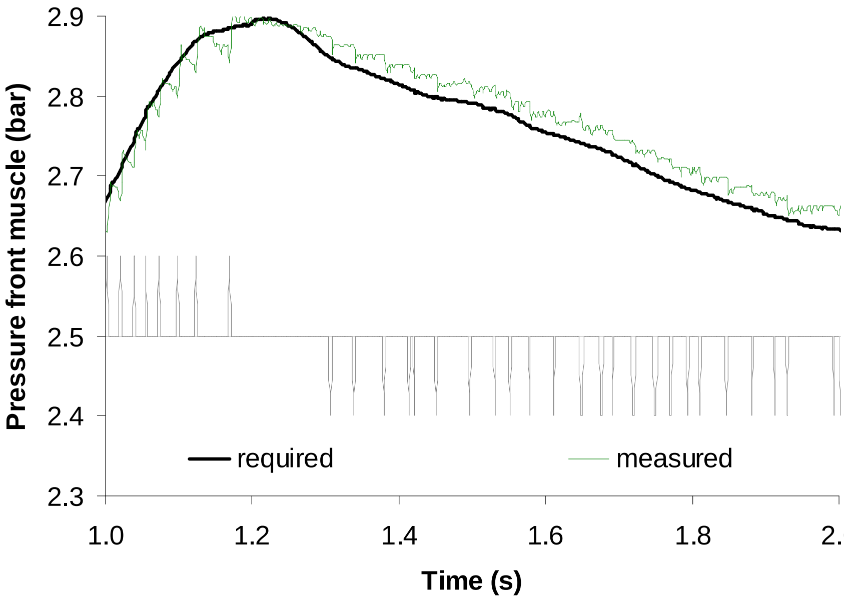

Figure 6.31: Detail of required and measured pressure (bar) in the front muscle for the knee joint

tool to give the qualitative influence of the different control parameters. As was shown with the experimental results concerning pressure, it might also be necessary to adapt the simulation model according to the experimental data, e.g. by incorporating leakage of the pneumatic system.

6.5 Conclusion

In this chapter the construction of the biped "Lucy" was presented. It was shown that the robot has a modular design, meaning that each essential robot part, such as lower leg and upper leg has the same layout. The modularity is provided mechanically as well as electronically. Each modular unit has its basic frame with two antagonistically positioned muscles driving the next modular unit by a leverage mechanism. Six such modular units are brought together to create the complete biped. Four units are used for the two legs and 2 units are attached parallel to each other to form the upper body. The two antagonistic muscle systems of the latter actuate the two hip joints, while the muscles in an upper leg actuate a knee and those of a lower leg an ankle joint. The feet are designed such that the robot can only walk with the feet parallel to the ground at foot touch-down and lift-off. Due to the one dimensional rotation of the joints, the robot can only walk in the sagittal plane, so the robot is attached to a XY-guiding frame, in order to prevent tipping over in the frontal plan. Special in the mechanical design of the modular units, is the flexibility towards changes of the joint torque characteristics. These can be altered by easy changes in the muscle leverage mechanism or by replacing the muscles with different ones. The provision of this versatility allows to make easy changes during the experimental and theoretical evolution. Due to complexity of the biped concept and its control strategy regarding natural dynamics it is not possible to find "good" joint actuation characteristics at the first design.

The pressure in each muscle is controlled by its own valve island, which consists of several fast switching on/off valves. Special attention was given to the design of the pressure regulating unit, valves and pressure sensor, to enhance control performance. The two valve islands of each modular unit are controlled by a separate micro-controller unit. This unit also reads the pressure sensors, which are positioned inside each muscle, and reads the encoder signal to determine joint position. The low-level PI and bang-bang pressure controller are implemented on these micro controller units, which communicate with a central PC, on which the inverse dynamics and the delta-p control units are hosted. The communication between PC and the micro-controllers of the modular units is controlled by a separate micro-controller. This controller communicates with the PC via a USB 2.0 serial line and transfers data to and from the other micro-controllers via a 16 bit parallel communication interface. This results in a global communication rate of 2000 Hz.

Apart from the 6 identical micro-controllers, which drive the modular units, a 7th analogous controller is provided to read extra sensory information such as absolute robot position, ground reaction force, air consumption and reference pressure of the pneumatic supply regulating circuit. This pneumatic circuit is divided into a high pressure and a lower reference pressure circuit. The latter is used to calibrate the 12 pressure sensors inside each muscle whenever the robot is initialized. The valves, which select between the two pneumatic circuits, are commanded via the safety board. This board controls the supply pressure and directly reacts on possible alarm signals that can be generated by the pressure sensors in the muscles. Whenever the pressure in a muscle exceeds a threshold of about 4.2 bar gauge pressure, the signal is generated and the robot automatically depressurizes.

Currently, the robot is assembled and its hardware is functioning properly. The first tracking experiments have been carried out while the robot is suspended with both feet in the air. The feedforward control structure, as was designed for single support, has already been implemented. The first preliminary tests, with this controller, shows promising results. Currently, a treadmill is being constructed in order to perform steady-state walking motion. Once this is finished, extensive experiments with the robot can start, and the complete dynamic control structure, as was presented in this work, can be evaluated thoroughly.

Chapter 7

General conclusions

This thesis reports on the development and the control of the robot "Lucy". This robot is a planar walking biped with six joints each actuated by a pair of pleated pneumatic artificial muscles (PPAM). The main purpose of the biped project is to evaluate the implementation of these muscles and to develop some specific control strategies related to legged locomotion with compliant actuators. Pneumatic artificial muscles have some interesting characteristics which can be beneficial towards actuation of legged locomotion. These actuators have a high power to weight ratio and they can be coupled directly without complex gearing mechanism. Due to the compressibility of air, a joint actuated with pneumatic drives shows a compliant behaviour, which can be employed to reduce shock effects at touch-down of a leg. Moreover, in a joint setup with two muscles positioned antagonistically, the joint compliance can be adapted while controlling the position. This joint compliance adaptation can be used to influence the natural frequencies of the system in order to create more flexibility towards exploitation of natural dynamics. The ultimate control idea intended for "Lucy" is to combine exploitation of natural dynamics with joint trajectory control. A trajectory generator calculates joint trajectories which ensure dynamically stable walking, and the different joint controllers track the imposed trajectories while adapting the joint compliance, as such that the natural regimes correspond as much as possible to the reference trajectories. This can significantly reduce control effort and energy consumption, while continuously ensuring global dynamical stability.

Currently the biped "Lucy" is assembled and its hardware components are tested. The first developments of the control architecture for "Lucy" focus on trajectory control and dynamic stability, which is studied in the framework of this thesis. A nonlinear tracking controller for a single and double support phase is proposed in combination with a joint trajectory generator, developed by Vermeulen [2004]. A hybrid simulation model, combining the robot link dynamics with actuator thermodynamics, is developed to evaluate the proposed control strategy, and to provide a tool for future research on exploitation of natural dynamics. The control architecture for the biped does not yet incorporate optimization towards control activity and energy consumption, but a discussion on the basic concepts of exploiting natural dynamics, with the proposed pneumatic tracking system, is given. Additionally, a contribution is made to the development of a second generation muscle prototype of the PPAM.

Chapter 2 discusses this new PPAM, which is an adaptation of the first prototype in order to extend the muscle lifespan and to simplify the construction process. Essential changes are made to the pleated muscle membrane. The stiff Kevlar fabric, used in the first prototype, is replaced by a discrete number of Kevlar yarns which are positioned in each crease of the pleated membrane. The latter is made out of a more flexible polyester material which improves the equal unfurling of the folds when the muscle is inflated. The new layout significantly increases the lifespan, the muscles currently implemented in the biped "Lucy" can easily perform a few hundred thousand cycles. The mathematical model describing the muscle characteristics, introduced for the first prototype, is reformulated as a function of the new membrane layout. The theoretical force characteristic is validated with static load tests, performed on the new type of muscle. These tests show a good resemblance between model and measurements but reveal a moderate hysteresis. This hysteresis will influence joint control performances, and a quantitative description of the measured hysteresis is incorporated in the simulation model of chapter 5.

Chapter 3 describes basic concepts associated with a one-dimensional joint setup. Since pneumatic artificial muscles can only generate forces in one direction, two muscles are positioned antagonistically in order to drive a joint bidirectionally. With a formal description of the joint kinematics it was shown that joint position is influenced by differences in both muscle pressures, while the compliance of a joint, with closed muscles, is set by a weighted sum of pressures. The presented basic control structure therefore includes two controllable variables which separately affect the pressure difference and the sum of pressures. This control structure is implemented in a simulation model for the motion of a simplified leg configuration. This simulation model is used to illustrate the influence of natural dynamics while tracking a prescribed knee trajectory with the proposed control structure. The strong influence of proper stiffness selection on control activity and energy consumption is clearly visualized by means of simulation results. A mathematical formulation is given to select an appropriate value of this control variable as a function of the imposed trajectory. For simplification it is assumed that the stiffness variable remains constant. This works well for the studied configuration in this chapter, but it will be more suitable to consider varying stiffness when dealing with the complete biped. As a consequence, new strategies based on the simplified calculations in this chapter, will have to be explored in future research.

After presenting a basic tracking control scheme for the one-dimensional setup in chapter 3, this control scheme is extended for the complete biped in chapter 4. The proposed nonlinear tracking controller consists of multiple stages which deal with the system's nonlinearities at separate levels. An inverse dynamic control block calculates the torques required to track the desired joint trajectories, while taking into account single support and double support phase dynamics separately. The computed torques are translated into required pressure levels for each joint by a so-called delta-p controller, using the nonlinear torque/angle relation. The required pressures are locally adjusted by a PI position feedback controller, before two multilevel bang-bang pressure controllers command the several on/off valves to set the pressure in the respective muscles of a joint. The stiffness variable of each joint is not yet controlled and therefore given a constant value. The proposed tracking controller is used in combination with the trajectory generator developed by Vermeulen [2004]. This trajectory planning unit generates joint motion patterns based on two specific concepts, namely the use of objective locomotion parameters, and the exploitation of the natural upper body dynamics by manipulating the angular momentum equation. The objective locomotion parameters are average forward speed of the hip, step-length, step-height and intermediate foot-lift. The proposed strategy requires only small ankle torques during the single support phase which locates the zero moment point in the vicinity of the ankle joint, resulting in dynamically stable walking. A recapitulation of this trajectory generator is given in chapter 4 and the concept of small ankle torques is incorporated in the design of the inverse dynamics controller for the double support phase.

Chapter 5 describes a hybrid simulation model of the biped which is used to evaluate the trajectory control architecture as proposed in chapter 4. The simulation model combines robot link dynamics with the thermodynamic effects which take place in the muscle/valves systems. Moreover, the simulator incorporates three different phases: a single support phase, an impact phase and a double support phase. The several differential equations representing the mechanics and pneumatics are discussed, followed by an overview of the complete simulator with special emphasis on the equations regarding the antagonistic muscle/valve actuation system. Some hardware limitations associated with the robot "Lucy", such as sampling time and valve delay time, are taken into account in the simulation model. An elaborate discussion of a specific walking motion is given. It is verified that tracking performance is adequate at the cost of control activity, because optimization of control parameters and exploitation of natural dynamics is not yet considered. The main conclusion points out that dynamic stability, as prescribed by the trajectory generator, is still guaranteed with the proposed pneumatic actuation system and some introduced parameter estimation errors. The errors considered are estimation errors on the inertial parameters used by the inverse dynamics control block. Moreover, the measured hysteresis of the muscle force function is incorporated. The latter has a strong negative influence on the performance of the delta-p control unit. It is expected that exploitation of natural dynamics will become a crucial factor to achieve faster motions and that some design parameters will have to be recalculated. In this context the simulation model proves to be an important tool for future parameter optimization and will give a qualitative insight of the complex behaviour of the system in order to facilitate the formulation of extended control strategies.

Chapter 6 gives an elaborate description of the design and construction of the biped "Lucy". The main focus during the design process was modularity and the creation of a flexible experimental platform, which incorporates versatility towards possible joint design changes. The latter is very important to allow changes in actuator characteristics as a function of the developed control strategies. It is expected that proper exploitation of natural dynamics will require specific joint torque characteristics. Due to the modular structure each elementary unit, such as a lower leg, an upper leg and an upper body, is almost identical from a mechanical and electronic point of view. Each modular element is controlled by its own control hardware such that these elements have identical types of signal flows. Moreover, the global communication protocol allows easy reconfiguration of the experimental setup. The flexibility towards mechanical changes to the experimental platform is foreseen at joint torque level and recombination of the modular units. The joint torque characteristics can easily be altered by either replacing the pneumatic artificial muscles or by changing the actuator connecting interface. Furthermore, the frame of the robot has been designed in a straightforward way to facilitate machining and it also allows easy attachment of additional parts. Special attention was drawn to the design of the pneumatic valve system, consisting of several fast on/off valves placed in parallel, for which electronics have been designed to enhance switching times of the valves. Pressures are measured by specially designed pressure sensors which are positioned inside the muscles in order to have a reliable dynamic measurement. The valves are controlled by separate micro-controller units for each joint. These units incorporate the local PI feedback and bang-bang pressure controller, and they communicate with the PC via an extra micro-controller which serves as a data transfer agent. Between this agent and the several micro-controller units a sixteen bit parallel data bus is provided, and the communication with an external PC is done via a USB 2.0 interface. The complete setup allows a sampling frequency of about 2000 Hz, while the trajectory generator, the inverse dynamics and the delta-p tracking control units are implemented on a central PC under a Windows operating system. The biped "Lucy" is assembled and its hardware components are tested. Preliminary tracking results, with the biped suspended in the air, show satisfactory behaviour of the proposed trajectory tracking controller in combination with the sophisticated control hardware of the robot "Lucy". Additional visual information on the robot "Lucy" and its current walking motions can be found at the following internet address: http://lucy.vub.ac.be/.

In the near future the simulations of the reduced configuration as developed in chapter 3 should be evaluated. Therefore a reduced configuration of the real robot should be established. The practical tests will be used for a first validation of the simulation model towards un-modelled effects such as friction and air leakage, and will allow for fine-tuning of some estimated model parameters. By means of the air consumption sensor, it will be possible to evaluate the real influence of adapted compliance and validate the proposed mathematical formulation concerning the proper stiffness parameter estimation.

The first findings of these practical tests should be taken into account in the simulation model of the complete robot. And extensive experimental testing on the robot should allow for further optimization of the simulation model.

Currently, a treadmill is being constructed which is an essential element in order to evaluate the proposed trajectory control architecture with experiments. After implementing the double support control strategies, the first preliminary walking tests can be performed. A proper evaluation of the dynamic stability will be possible after installing the necessary force sensors in the feet in order to estimate the location of the ZMP. Another validation of the modelling will be carried out on the ZMP placement. Control parameter values will have to be fine-tuned in order to match the expected ZMP with the measured one. Currently, the trajectory generator only focusses on steady-state motions, possibly combined with only small, gradually performed deviations in the cyclic motion. Thus strategies to begin and end the walking motion of the robot will have to be added to the trajectory generator unit.

The validated simulation model will be used to search for new strategies concerning exploitation of natural dynamics. The strategy of stiffness selection as was proposed in this thesis will be reformulated, and optimization loops on the joint design parameters will have to be done in order to find suitable torque characteristics as a function of exploitation of natural dynamics. Additionally, a study on the trajectory generator towards energy efficient combinations of the objective locomotion parameters should be carried out.

Furthermore, it is believed that these actuators and the knowledge which is gathered from the biped project can be extended towards other applications. Currently, a project is being carried out on a robot arm for manipulation tasks of heavy loads, in direct interaction with an operator [Van Damme et al., 2004]. The robot arm is designed to carry a large portion of the load and it is meant to sense the direction in which the operator is guiding the robot arm. The advantage of using pneumatic artificial muscles is that the directing forces imposed by the operator are estimated with simple pressure measurements in the muscles in combination with angular positions measurements in the joints, thus without any force sensors. Moreover, the compliance of the muscles creates safe operating conditions towards the operator. The same concept can, for instance, be applied in a human exoskeleton for the lower limbs. Such a device could be used to train paraplegic persons during their revalidation process. An exoskeleton, which carries the patient on a treadmill, then performs position controlled leg motions for training. The adaptable stiffness of the joints can be used to influence the amount in which the patient has to be assisted in the walking motion. High stiffness would mean a large support of the exoskeleton in the walking motion, a decreasing joint stiffness means that the patient is more and more performing the walking motion on his own.

In sum, this thesis illustrates some theoretical issues of robotics combined with pneumatics, which are being implemented in a real biped model. An elaborate tracking control strategy is developed and forms the basis for future research on exploitation of natural dynamics in combination with trajectory control. Therefore an important simulation tool has been created. Furthermore, it demonstrates that several applications, such as exoskeleton rehabilitation, will be accessible in the future thanks to the practical and conceptual know-how that has already been and will be gathered further during research on "Lucy".

Appendix A

Dynamic model of the basic leg configuration

In this section the equation of motion for the model depicted in figure (A.1) is derived. A Newton-Lagrange formulation of the equation of motion is used for this

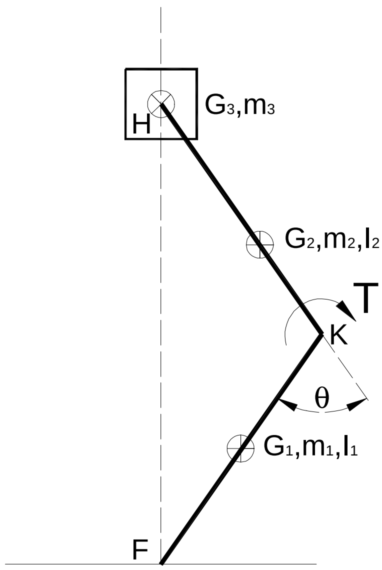

Figure A.1: schematic overview of the studied model

purpose. Since the foot stays on the ground, the model has only one DOF θ:

$$\frac{d}{dt}\left\{\frac{\partial K}{\partial \dot{\theta}}\right\} - \frac{\partial K}{\partial \theta} + \frac{\partial U}{\partial \theta} = Q_\theta \tag{A.1}$$

K is the total kinetic energy and U the potential energy. Q_θ is the generalized force associated with the knee.

If the origin is placed in the foot the kinematic expressions for the positions and velocities of the centers of mass for the different links are given by:

$$O\bar{G}_1 = L\left(\alpha\sin\frac{\theta}{2}, \alpha\cos\frac{\theta}{2}\right)^T \tag{A.2}$$

$$O\bar{G}_2 = L\left((1-\beta)\sin\frac{\theta}{2}, (1+\beta)\cos\frac{\theta}{2}\right)^T \tag{A.3}$$

$$O\bar{G}_3 = L\left(0, 2\cos\frac{\theta}{2}\right)^T \tag{A.4}$$

$$\bar{v}_{G_1} = \frac{L}{2}\left(\alpha\cos\frac{\theta}{2}\dot{\theta}, -\alpha\sin\frac{\theta}{2}\dot{\theta}\right)^T \tag{A.5}$$

$$\bar{v}_{G_2} = \frac{L}{2}\left((1-\beta)\cos\frac{\theta}{2}\dot{\theta}, -(1+\beta)\sin\frac{\theta}{2}\dot{\theta}\right)^T \tag{A.6}$$

$$\bar{v}_{G_3} = \frac{L}{2}\left(0, -2\sin\frac{\theta}{2}\dot{\theta}\right)^T \tag{A.7}$$

The total potential energy of the robot is equal to:

$$U = m_1 g Y_{G_1} + m_2 g Y_{G_2} + m_3 g Y_{G_3} \tag{A.8}$$

which results in:

$$U = gL\left(\alpha m_1 + (1+\beta)\, m_2 + 2m_3\right)\cos\frac{\theta}{2} \tag{A.9}$$

The partial derivative becomes:

$$\frac{\partial U}{\partial \theta} = -g\frac{L}{2}\left(\alpha m_1 + (1+\beta)\, m_2 + 2m_3\right)\sin\frac{\theta}{2} \tag{A.10}$$

The kinetic energy K_i of link i is given by:

$$K_i = \frac{1}{2}m_i v_{G_i}^2 + \frac{1}{2}I_i\omega_i^2 \tag{A.11}$$

with ω_i the angular velocity of link i. For the three links this becomes:

$$K_1 = \frac{1}{8}\left(I_1 + m_1\alpha^2L^2\right)\dot{\theta}^2 \tag{A.12}$$

$$K_2 = \frac{1}{8}\left(I_2 + m_2\left(1+\beta^2\right)L^2 - 2m_2\beta L^2\cos\theta\right)\dot{\theta}^2 \tag{A.13}$$

$$K_3 = \frac{1}{8}\left(4m_3L^2\sin^2\frac{\theta}{2}\right)\dot{\theta}^2 \tag{A.14}$$

The total kinetic energy is the sum of these three terms:

$$K = \frac{1}{8}\Bigg(I_1 + I_2 + m_1\alpha^2L^2 + m_2\left(1+\beta^2\right)L^2$$
$$+2m_3L^2 - 2L^2\left(m_2\beta + m_3\right)\cos\theta\Bigg)\dot{\theta}^2 \tag{A.15}$$

Now the different derivatives of the kinetic energy can be calculated:

$$\frac{d}{dt}\left\{\frac{\partial K}{\partial\dot{\theta}}\right\} = \frac{1}{4}\Big(I_1 + I_2 + m_1\alpha^2L^2 + m_2\left(1+\beta^2\right)L^2$$
$$+2m_3L^2 - 2L^2\left(m_2\beta + m_3\right)\cos\theta\Big)\ddot{\theta}$$
$$+\frac{1}{2}L^2\Big(\left(m_2\beta + m_3\right)\sin\theta\Big)\dot{\theta}^2 \tag{A.16}$$

and

$$\frac{\partial K}{\partial\theta} = \frac{1}{4}L^2\Big(\left(m_2\beta + m_3\right)\sin\theta\Big)\dot{\theta}^2 \tag{A.17}$$

The torque T applied in the knee represents the generalized force. So the equation of motion for this model can be summarized as followed:

$$D\big(\theta\big)\ddot{\theta} + C\big(\theta,\dot{\theta}\big)\dot{\theta} + G\big(\theta\big) = T \tag{A.18}$$

with:

$$D\big(\theta\big) = \frac{1}{4}\big(I_1 + I_2 + m_1\alpha^2L^2 + m_2\left(1+\beta^2\right)L^2$$
$$+\,2m_3L^2 - 2L^2\left(m_2\beta + m_3\right)\cos\theta\big) \tag{A.19}$$

$$C\big(\theta,\dot{\theta}\big) = \frac{1}{4}L^2\left(\left(m_2\beta + m_3\right)\sin\theta\right)\dot{\theta} \tag{A.20}$$

$$G\big(\theta\big) = -g\frac{L}{2}\left(\alpha m_1 + \left(1+\beta\right)m_2 + 2m_3\right)\sin\frac{\theta}{2} \tag{A.21}$$

Appendix B

Thermodynamic model

In this section the first order differential equation describing the pressure changes inside the muscle valve system is formulated. The discussion is based on the works of Daerden [1999] and Brun [1999].

The first law of thermodynamics is applied to a muscle with its valve island of 6 on/off valves. The muscle itself and its tubing until the different input and exhaust valve orifices are taken as control volume V. Figure (B.1) gives a schematic representation where the two inlet valves and the four exhaust valves are respectively depicted as one inlet and one exhaust. The first law is given in its rate form and

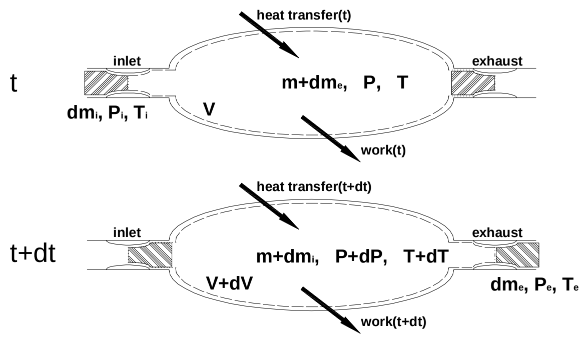

Figure B.1: Muscle and valves on time step t and $t + dt$

expresses that the variation of the total energy of a an amount of fluid is equal to the sum of the work done by the exerted forces and the net heat transfer with the surrounding. Assuming a uniform thermodynamic state inside the control volume the first law of thermodynamics can be written as follows (variation referred to time):

$$dU + dE_k + dE_p = \delta W + \delta Q \tag{B.1}$$

with:

$$
\begin{aligned}
dU &= \text{variation of the fluid's total internal energy} \\
dE_k &= \text{variation of the fluid's total kinetic energy} \\
dE_p &= \text{variation of the fluid's total potential energy} \\
\delta W &= \text{work done by external forces} \\
\delta Q &= \text{the net transfer of heat across the boundary}
\end{aligned}
$$

The pressurized air can be regarded as an ideal gas for which the following relations hold:

$$PV = mrT \tag{B.2}$$

$$u = c_v(T - T_0) \tag{B.3}$$

$$h = c_p(T - T_0) \tag{B.4}$$

$$c_p = c_v + r \tag{B.5}$$

with:

$$
\begin{aligned}
P &= \text{absolute pressure} \\
V &= \text{air volume} \\
m &= \text{air mass} \\
T &= \text{temperature} \\
r &= \text{dry air gas constant} = 287(Jkg^{-1}K^{-1}) \\
u &= \text{specific internal energy} \\
h &= \text{specific enthalpy} \\
c_v &= \text{constant volume specific heat} = 718(Jkg^{-1}K^{-1})\text{for dry air at 300K} \\
c_p &= \text{constant pressure specific heat} = 1005(Jkg^{-1}K^{-1})\text{for dry air at 300K} \\
T_0 &= \text{reference temperature which is taken zero}
\end{aligned}
$$

To calculate the different variations in equation B.1 for the open muscle-valve system, the constant mass $(m + dm_i + dm_e)$ is studied at two instant time steps t and $t + dt$ as depicted in figure (B.1). At time t, pressurized air with mass dm_i is about to enter the control volume V while mass $m + dm_e$ is inside this volume. At $t + dt$ mass dm_e is leaving while the mass inside the control volume is $m + dm_i$.

Evaluating equation B.3 between the two time steps results in:

$$dU = \left[\left(m + dm_i\right) c_v \left(T + dT\right) + dm_e c_v T_e\right] - \left[\left(m + dm_e\right) c_v T + dm_i c_v T_i\right] \quad \text{(B.6)}$$

And while neglecting second order terms, equation B.6 leads to:

$$dU = mc_v dT + dm_i c_v (T - T_i) + dm_e c_v (T_e - T) \quad \text{(B.7)}$$

Neglecting furthermore the kinetic energy of the air inside the muscle against the kinetic energy of the inlet and exhaust, the variation of kinetic and potential energy becomes:

$$dE_k = dm_e \frac{C_e^2}{2} - dm_i \frac{C_i^2}{2} \quad \text{(B.8)}$$

$$dE_p = dm_e g z_e - dm_i g z_i \quad \text{(B.9)}$$

The work exchanged with the environment, while assuming reversibility, is expressed as:

$$dW = -PdV + P_i dV_i - P_e dV_e \quad \text{(B.10)}$$

with the first term, the work done by the muscle and the other two terms associated with the work needed to transport dm_i and dm_e in and out the muscle volume.

Combining the first law of thermodynamics (B.1) with equations (B.7), (B.8), (B.9) and (B.10) gives:

$$\begin{aligned} mc_v dT + c_v T \left(dm_i - dm_e\right) = &-PdV \\ &+ dm_i \left(c_v T_i + P_i v_i + \frac{C_i^2}{2} + g z_i\right) \\ &- dm_e \left(c_v T_e + P_e v_e + \frac{C_e^2}{2} + g z_e\right) + \delta Q \end{aligned} \quad \text{(B.11)}$$

with v_i and v_e the specific volume of inlet and exhaust. Taking into account conservation of mass and the definition of enthalpy:

$$dm = dm_i - dm_e \quad \text{(B.12)}$$

$$h = u + Pv \quad \text{(B.13)}$$

Differentiating the perfect gas law (B.2) gives:

$$d\left(PV\right) = PdV + VdP = mrdT + rTdm \quad \text{(B.14)}$$

Using (B.14), equation (B.11) can be transformed to:

$$\frac{c_v}{r} d\,(PV) = -PdV + dm_i \left(h_i + \frac{C_i^2}{2} + gz_i \right) - dm_e \left(h_e + \frac{C_e^2}{2} + gz_e \right) + \delta Q \tag{B.15}$$

Flows through small orifices, such as valves and tubes, are assumed to be adiabatic and since no mechanical work is exchanged with the surroundings, for these situations is stated:

$$h + \frac{C^2}{2} = constant \tag{B.16}$$

Thus for inlet and exhaust can be written:

$$h_i + \frac{C_i^2}{2} = h_s = c_p T_s \tag{B.17}$$

$$h_e + \frac{C_e^2}{2} = h = c_p T \tag{B.18}$$

with h_s and T_s the enthalpy and temperature of the pressurized air supply buffer, h and T are the enthalpy and temperature of the pressurized air inside the muscle volume. For equations (B.17) and (B.18) kinetic energy is neglected since the considered volumes are assumed large enough. Taking into account these two equations and the definition $\gamma = c_p/c_v$ and relation (B.5), the energy balance (B.15) can be rewritten in the following form, if potential energy of the air masses is neglected:

$$dP = -\frac{\gamma}{V} \left(PdV + rT_s dm_i - rTdm_e + (\gamma - 1)\delta Q \right) \tag{B.19}$$

If furthermore an adiabatic process is considered, $\delta Q = 0$, equation (B.19) becomes:

$$dP = \frac{\gamma}{V} \left(-PdV + rT_s dm_i - rTdm_e \right) \tag{B.20}$$

Expression (B.20) is valid for the so called isentropic process, where adiabatic and reversibility conditions are assumed. The non-ideal conditions can be represented in analogy with the polytropic process, by substituting γ with a polytropic coefficient n in equation (B.20):

$$dP = \frac{n}{V} \left(-PdV + rT_s dm_i - rTdm_e \right) \tag{B.21}$$

with dm_i and dm_e determined by air flows through the different inlet and exhaust valves and dependend on the number of valves that are opened.

Appendix C

Kinematics and Dynamics of the biped "Lucy" during a single support phase

C.1 Kinematics

The biped model during a single support phase is depicted in figure C.1. For the following derivations it is supposed that both legs are identical. Hereby assuming all inertial properties and the length of the upper and lower leg to be pairwise equal.

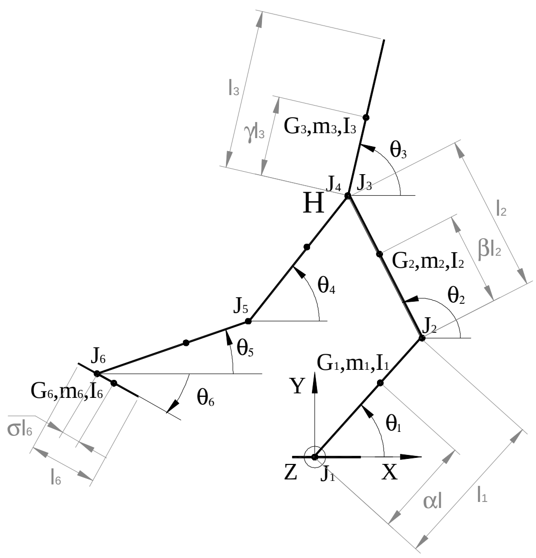

Figure C.1: Model of the biped during a single support phase with l_i, m_i and I_i respectively the length, mass and moment of inertia with respect to the local COG G_i of link i. The location of the COG's G_i are given by $J_1G_1 = J_6G_5 = \alpha l_1$, $J_2G_2 = J_5G_4 = \beta l_2$ and $J_3G_3 = \gamma l_3$ and for the foot $J_6G_6 = \sigma l_6$ where $0 < \alpha, \beta, \gamma, \sigma < 1$. The position of each link i is given by the angle θ_i, measured with respect to the horizontal axis.

The hip takes a central position, so the location of the different COG's is calculated with reference to this point.

$$X_H = l_1 \cos\theta_1 + l_2 \cos\theta_2 \tag{C.1a}$$

$$Y_H = l_1 \sin\theta_1 + l_2 \sin\theta_2 \tag{C.1b}$$

The vectors defining the position of the local COG's of each of the five links are calculated as:

$$\overline{OG}_1 = (X_H, Y_H)^T - (1-\alpha)\, l_1 (\cos\theta_1, \sin\theta_1)^T - l_2 (\cos\theta_2, \sin\theta_2)^T \tag{C.2a}$$

$$\overline{OG}_2 = (X_H, Y_H)^T - (1-\beta)\, l_2 (\cos\theta_2, \sin\theta_2)^T \tag{C.2b}$$

$$\overline{OG}_3 = (X_H, Y_H)^T + \gamma l_3 (\cos\theta_3, \sin\theta_3)^T \tag{C.2c}$$

$$\overline{OG}_4 = (X_H, Y_H)^T - (1-\beta) l_2 (\cos\theta_4, \sin\theta_4)^T \tag{C.2d}$$

$$\overline{OG}_5 = (X_H, Y_H)^T - (1-\alpha)\, l_1 (\cos\theta_5, \sin\theta_5)^T - l_2 (\cos\theta_4, \sin\theta_4)^T \tag{C.2e}$$

$$\begin{aligned}\overline{OG}_6 = {} & (X_H, Y_H)^T + \sigma l_6 (\cos\theta_6, \sin\theta_6)^T \\ & - l_1 (\cos\theta_5, \sin\theta_5)^T - l_2 (\cos\theta_4, \sin\theta_4)^T\end{aligned} \tag{C.2f}$$

The position of the global COG of the robot, stance foot not included, is given by:

$$\overline{OG} = (X_G, Y_G)^T \tag{C.3}$$

with:

$$\begin{aligned}X_G = X_H &+ a_1 \cos\theta_1 + a_2 \cos\theta_2 + a_3 \cos\theta_3 \\ &+ a_4 \cos\theta_4 + a_5 \cos\theta_5 + a_6 \cos\theta_6\end{aligned} \tag{C.3a}$$

$$\begin{aligned}Y_G = Y_H &+ a_1 \sin\theta_1 + a_2 \sin\theta_2 + a_3 \sin\theta_3 \\ &+ a_4 \sin\theta_4 + a_5 \sin\theta_5 + a_6 \sin\theta_6\end{aligned} \tag{C.3b}$$

and:

$$a_1 = -(1-\alpha)\, \eta_1 l_1$$

$$a_2 = -\big[\eta_1 + (1-\beta)\, \eta_2\big] l_2$$

$$a_3 = \gamma\eta_3 l_3$$

$$a_4 = -\big[\eta_1 + \eta_6 + (1-\beta)\,\eta_2\big] l_2$$

$$a_5 = -\big[\eta_6 + (1-\alpha)\,\eta_1\big] l_1$$

$$a_6 = \sigma\eta_6 l_6$$

and:

$$\eta_i = \frac{m_i}{2(m_1+m_2)+m_3+m_6}$$

The first and second derivative of (C.3a) and (C.3b), which are required for the derivation of the dynamic model and the ZMP, are straightforward and thus not explicitly listed here.

C.2 Dynamics

With the swing foot included, the robot has 6 DOF during the single support phase if the robot is assumed to move only in the sagittal plane. These degrees of freedom are represented by the 6-dimensional vector:

$$\mathbf{q} = \big[\theta_1\,\theta_2\,\theta_3\,\theta_4\,\theta_5\,\theta_6\big]^T \tag{C.4}$$

The dynamics are represented by 6 equations of motion of which the i th equation can be written with the Lagrange formulation as:

$$\frac{d}{dt}\left\{\frac{\partial K}{\partial \dot{q}_i}\right\} - \frac{\partial K}{\partial q_i} + \frac{\partial U}{\partial q_i} = Q_i \quad (i = 1\ldots 6) \tag{C.5}$$

with K and U, respectively the total kinetic and gravitational energy of the robot, Q_i are the generalized forces associated with the generalized coordinates q_i.

The total kinetic energy can be found by the summation of the separate kinetic energy values of each link:

$$K = \sum_{i=1}^{6} K_i = \frac{1}{2}\sum_{i=1}^{6}\left(m_i v_{G_i}^2 + I_i\dot{\theta}_i^2\right) \tag{C.6}$$

with $\bar{v}_{G_i} = \left(\dot{X}_{Gi}, \dot{Y}_{Gi}\right)^T$ the velocity of the COG of link i and $\dot{\theta}_i$ the angular velocity. The expression of the total kinetic energy is quite large and is not explicitly listed here.

The gravitational (potential) energy is given by:

$$U = MgY_G \tag{C.7}$$

The generalized forces are the different net torques acting on each link of the robot (see figure C.2):

$$\mathbf{Q} = \boldsymbol{\tau} = \begin{bmatrix} \tau_1 \\ \tau_2 \\ \tau_3 \\ \tau_4 \\ \tau_5 \\ \tau_6 \end{bmatrix} = \begin{bmatrix} \tau_{K_S} - \tau_{A_S} \\ \tau_{H_S} - \tau_{K_S} \\ -\tau_{H_S} - \tau_{H_A} \\ \tau_{H_A} - \tau_{K_A} \\ \tau_{K_A} - \tau_{A_A} \\ \tau_{A_A} \end{bmatrix} \tag{C.8}$$

The H, K and A stands for "Hip", "Knee" and "Ankle" respectively, a stands for "air", and s for "stance". Expression (C.8) gives the relations between net torques and applied joint torques.

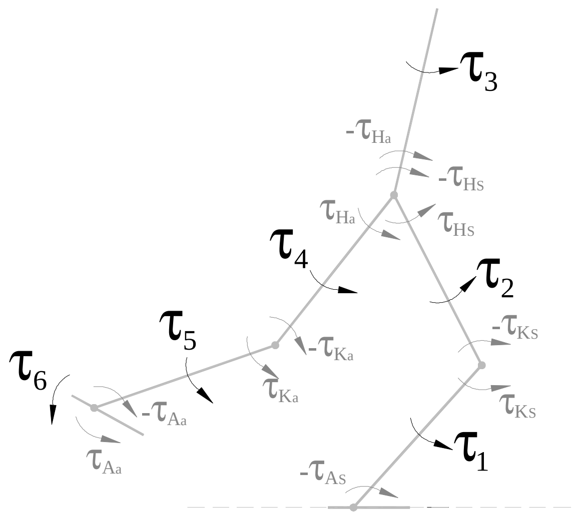

Figure C.2: Definition of net torques and joint torques

The 6 equations of motion (C.5) can be written in the following form [Spong and Vidyasagar, 1989]:

$$D(\mathbf{q})\ddot{\mathbf{q}} + C(\mathbf{q}, \dot{\mathbf{q}})\dot{\mathbf{q}} + G(\mathbf{q}) = \boldsymbol{\tau} \tag{C.9}$$

with $D(\mathbf{q})$ the inertia matrix, $C(\mathbf{q}, \dot{\mathbf{q}})$ the centrifugal/coriolis matrix, $G(\mathbf{q})$ the gravitational torque vector and $\boldsymbol{\tau}$ the net torque vector.

The inertia matrix can be calculated with the following relation to the kinetic energy:

$$K = \frac{1}{2}\,\dot{\mathbf{q}}^T D(\mathbf{q})\dot{\mathbf{q}} \tag{C.10}$$

The elements of the centrifugal/coriolis matrix c_{kj} can be found with the following expression [Spong and Vidyasagar, 1989]:

$$c_{kj} = \sum_{i=1}^{6} c_{ijk}\dot{\theta}_i = \sum_{i=1}^{6} \frac{1}{2}\left\{\frac{\partial d_{kj}}{\partial \theta_i} + \frac{\partial d_{ki}}{\partial \theta_j} - \frac{\partial d_{ij}}{\partial \theta_k}\right\}\dot{\theta}_i \tag{C.11}$$

with c_{ijk} the so called Christoffel symbols and d_{ij} the elements of the inertial matrix $D(\mathbf{q})$. The elements of the gravitational torque vector g_i are given by:

$$g_i = \frac{\partial U}{\partial q_i} \tag{C.12}$$

As a result all the parameters of the dynamic model are given below:

- Inertia matrix $D(\mathbf{q})$:

$$d_{11} = I_1 + l_1^2\left[\left(1+\alpha^2\right)m_1 + 2m_2 + m_3 + m_6\right]$$

$$d_{12} = l_1 l_2\left[m_1 + (1+\beta)\,m_2 + m_3 + m_6\right]\cos\left(\theta_1 - \theta_2\right) = d_{21}$$

$$d_{13} = l_1 l_3 \gamma m_3 \cos\left(\theta_1 - \theta_3\right) = d_{31}$$

$$d_{14} = l_1 l_2\left[(\beta - 1)\,m_2 - m_1 - m_6\right]\cos\left(\theta_1 - \theta_4\right) = d_{41}$$

$$d_{15} = l_1^2\left[(\alpha - 1)\,m_1 - m_6\right]\cos\left(\theta_1 - \theta_5\right) = d_{51}$$

$$d_{16} = l_1 l_6 m_6 \sigma \cos\left(\theta_1 - \theta_6\right) = d_{61}$$

$$d_{22} = I_2 + l_2^2\left[m_1 + \left(1+\beta^2\right)m_2 + m_3 + m_6\right]$$

$$d_{23} = l_2 l_3 \gamma m_3 \cos\left(\theta_2 - \theta_3\right) = d_{32}$$

$$d_{24} = l_2^2\left[(\beta - 1)\,m_2 - m_1 - m_6\right]\cos\left(\theta_2 - \theta_4\right) = d_{42}$$

$$d_{25} = l_1 l_2\left[(\alpha - 1)\,m_1 - m_6\right]\cos\left(\theta_2 - \theta_5\right) = d_{52}$$

$$d_{26} = l_2 l_6 m_6 \sigma \cos\left(\theta_2 - \theta_6\right) = d_{62}$$

$$d_{33} = I_3 + \gamma^2 l_3^2 m_3$$

$$d_{34} = 0 = d_{43}$$

$$d_{35} = 0 = d_{53}$$

$$d_{36} = 0 = d_{63}$$

$$d_{44} = I_2 + l_2^2\left[m_1 + (1-\beta)^2\, m_2 + m_6\right]$$

$$d_{45} = l_1 l_2\left[(1-\alpha)\,m_1 + m_6\right]\cos\left(\theta_4 - \theta_5\right) = d_{54}$$

$$d_{46} = -l_2 l_6 m_6 \sigma \cos(\theta_4 - \theta_6) = d_{64}$$

$$d_{55} = I_1 + l_1^2 \left[m_1(1-\alpha)^2 + m_6\right]$$

$$d_{56} = -l_1 l_6 m_6 \sigma \cos(\theta_5 - \theta_6) = d_{65}$$

$$d_{66} = I_6 + l_6^2 m_6 \sigma^2$$

- Centrifugal/coriolis matrix $C(\mathbf{q}, \dot{\mathbf{q}})$:

$$c_{11} = 0 = c_{22} = c_{33} = c_{44} = c_{55} = c_{66}$$

$$c_{12} = l_1 l_2 \left[m_1 + (1+\beta)m_2 + m_3 + m_6\right] \sin(\theta_1 - \theta_2)\,\dot{\theta}_2$$

$$c_{13} = l_1 l_3 \gamma m_3 \sin(\theta_1 - \theta_3)\,\dot{\theta}_3$$

$$c_{14} = -l_1 l_2 \left[m_1 + (1-\beta)m_2 + m_6\right] \sin(\theta_1 - \theta_4)\,\dot{\theta}_4$$

$$c_{15} = -l_1^2 \left[(1-\alpha)\,m_1 + m_6\right] \sin(\theta_1 - \theta_5)\,\dot{\theta}_5$$

$$c_{16} = l_1 l_6 m_6 \sigma \sin(\theta_1 - \theta_6)\,\dot{\theta}_6$$

$$c_{21} = -l_1 l_2 \left[m_1 + (1+\beta)m_2 + m_3 + m_6\right] \sin(\theta_1 - \theta_2)\,\dot{\theta}_1$$

$$c_{23} = l_2 l_3 \gamma m_3 \sin(\theta_2 - \theta_3)\,\dot{\theta}_3$$

$$c_{24} = -l_2^2 \left[m_1 + (1-\beta)m_2 + m_6\right] \sin(\theta_2 - \theta_4)\,\dot{\theta}_4$$

$$c_{25} = -l_1 l_2 \left[(1-\alpha)\,m_1 + m_6\right] \sin(\theta_2 - \theta_5)\,\dot{\theta}_5$$

$$c_{26} = l_2 l_6 m_6 \sigma \sin(\theta_2 - \theta_6)\,\dot{\theta}_6$$

$$c_{31} = -l_1 l_3 \gamma m_3 \sin(\theta_1 - \theta_3)\,\dot{\theta}_1$$

$$c_{32} = -l_2 l_3 \gamma m_3 \sin(\theta_2 - \theta_3)\,\dot{\theta}_2$$

$$c_{34} = 0 = c_{35} = c_{43} = c_{53} = c_{63} = c_{36}$$

$$c_{41} = l_1 l_2 \left[m_1 + (1-\beta)m_2 + m_6\right] \sin(\theta_1 - \theta_4)\,\dot{\theta}_1$$

$$c_{42} = l_2^2 \left[m_1 + (1-\beta)m_2 + m_6\right] \sin(\theta_2 - \theta_4)\,\dot{\theta}_2$$

$$c_{45} = l_1 l_2 \left[(1-\alpha)\,m_1 + m_6\right] \sin(\theta_4 - \theta_5)\,\dot{\theta}_5$$

$$c_{46} = -l_2 l_6 m_6 \sigma \sin(\theta_4 - \theta_6)\,\dot{\theta}_6$$

$$c_{51} = l_1^2 \left[(1-\alpha)\,m_1 + m_6\right] \sin(\theta_1 - \theta_5)\,\dot{\theta}_1$$

$$c_{52} = l_1 l_2 \left[(1-\alpha)\, m_1 + m_6 \right] \sin(\theta_2 - \theta_5)\, \dot{\theta}_2$$

$$c_{54} = -l_1 l_2 \left[(1-\alpha)\, m_1 + m_6 \right] \sin(\theta_4 - \theta_5)\, \dot{\theta}_4$$

$$c_{56} = -l_1 l_6 m_6 \sigma \sin(\theta_5 - \theta_6)\, \dot{\theta}_6$$

$$c_{61} = -l_1 l_6 m_6 \sigma \sin(\theta_1 - \theta_6)\, \dot{\theta}_1$$

$$c_{62} = -l_2 l_6 m_6 \sigma \sin(\theta_2 - \theta_6)\, \dot{\theta}_2$$

$$c_{64} = l_2 l_6 m_6 \sigma \sin(\theta_4 - \theta_6)\, \dot{\theta}_4$$

$$c_{65} = l_1 l_6 m_6 \sigma \sin(\theta_5 - \theta_6)\, \dot{\theta}_5$$

- Gravitational torque vector $G(\mathbf{q})$:

$$g_1 = \left[(\alpha+1)\, m_1 + 2m_2 + m_3 + m_6 \right] g l_1 \cos\theta_1$$

$$g_2 = \left[m_1 + (\beta+1)\, m_2 + m_3 + m_6 \right] g l_2 \cos\theta_2$$

$$g_3 = \gamma m_3 g l_3 \cos\theta_3$$

$$g_4 = \left[-m_1 + (\beta-1)\, m_2 - m_6 \right] g l_2 \cos\theta_4$$

$$g_5 = \left[(\alpha-1)\, m_1 - m_6 \right] g l_1 \cos\theta_5$$

$$g_6 = g l_6 m_6 \sigma \cos\theta_6$$

Appendix D

Details of the electronics

D.1 Joint micro-controller board

Figure D.1 gives a detailed overview of the micro-controller board which is provided for each modular unit. This micro-controller board executes the low-level PI controller and regulates muscle pressure with the bang-bang control structure. Furthermore, it handles sensory inputs originating from two pressure sensors and an encoder, and provides a buffered interface between the central PC and the local micro-controller. The same board architecture is also used for an extra micro-controller, which handles additional sensory information such as absolute robot position, supply pressure conditions and ground reaction forces.

The core of the joint controller board is the MC68HC916Y3 micro-controller of Motorola. It has a 16 bit central processor unit, CPU, and a separate processor, TPU, which is designed to handle sensory input and control output without disturbing the CPU.

The micro-controller unit can be debugged and programmed via the serial SDI interface which is a commercially available device. A 10 pin connector is provided to link the essential pins to the SDI debugger module. This interface has only been used during the development of the micro-controller board. Currently, the micro-controllers are programmed via the 16-bit communication interface.

This interface is created with a dual ported RAM unit. This unit provides a buffered structure which communicates with the Cypress micro-controller communication interface board (see D.4). Two dual ported ram chips IDT7130SA (8 bit wide) are used to create the 16-bit parallel bus interface. Each chip has 1 Kbyte of memory, the first chip is used to store the lowest byte of the 16-bit data, while the other stores the highest byte. The memory is physically divided into a read data block and a write data block by connecting the $R/\overline{W}$ signal to address line number 8 of the dual ported RAM memory. The highest address line is not used, which means that two memory storage places are provided for 256 16 bit wide data. Due to the divided structure into a read and write block, it is never possible to access a memory place from both sides simultaneously, therefore the BUSY and INT pins of the dual ported RAM units are not used.

The connector to the USB interface board redirects the pins of port PF which can be used to generate interrupts on the CPU (MC68HC916Y3) and give acknowledge signals to the communication master. E.g. the Cypress USB micro-controller, which is the communication master controlling the communication sampling rate, generates an interrupt on the CPU of all the Motorola micro-controllers each communication sample. Furthermore these pins are used to reset all the Motorola CPUs and in the other direction, to acknowledge to the communication master that the specific Motorola CPU is ready for a read or write action.

One connector is provided for the interface to the sensors and the valves. These valves are controlled by several TPU signals. The micro-controller board provides 6 separate signals to control the 6 valves of a valve island, but currently only 4 of them are used since three exhaust valves are switched together. The 3 incremental encoder channels are also connected with the TPU, which presents a position signal to the CPU without demanding any processor time. Additionally, one of the two main channel of the encoder are linked with a secondary TPU pin in order to estimate angular joint rotation speed. This speed is determined by time measurement between two neighboring encoder flanks. The 12-bit digital signals of the two pressure sensors are linked to the micro-controller via the serial SPI interface. Finally, port G is connected with 8 LEDs which are used to visualize the different operation modes of the robot.

Resetting the controller can be done by a local button on the micro-controller board or by the USB micro-controller via the dual ported RAM units. The local reset and micro-controller initialization scheme uses an AND-port (chip 4023) structure as clearly explained in the data sheets. Furthermore are provided an oscillation circuit to generate the clock for the CPU, two RS232 interfaces and a flash EEPROM programming circuit, all described in the data sheets.

The communication software is programmed into the flash EEPROM and works with two essential modes: program and run mode. These modes are selected by the first word of the communication data block, which come with 32 bytes each sample. Program mode is selected to load the micro-controller with the specific low-level controller program, such as e.g. the bang-bang controller, and in the run mode this downloaded program is executed while exchanging necessary control data with the central PC. So there is no fixed controller design programmed in the controller but it is downloaded each time the robot is initialized. This creates a fast an flexible experimental low-level control board for which different controller strategies can be implemented easily.

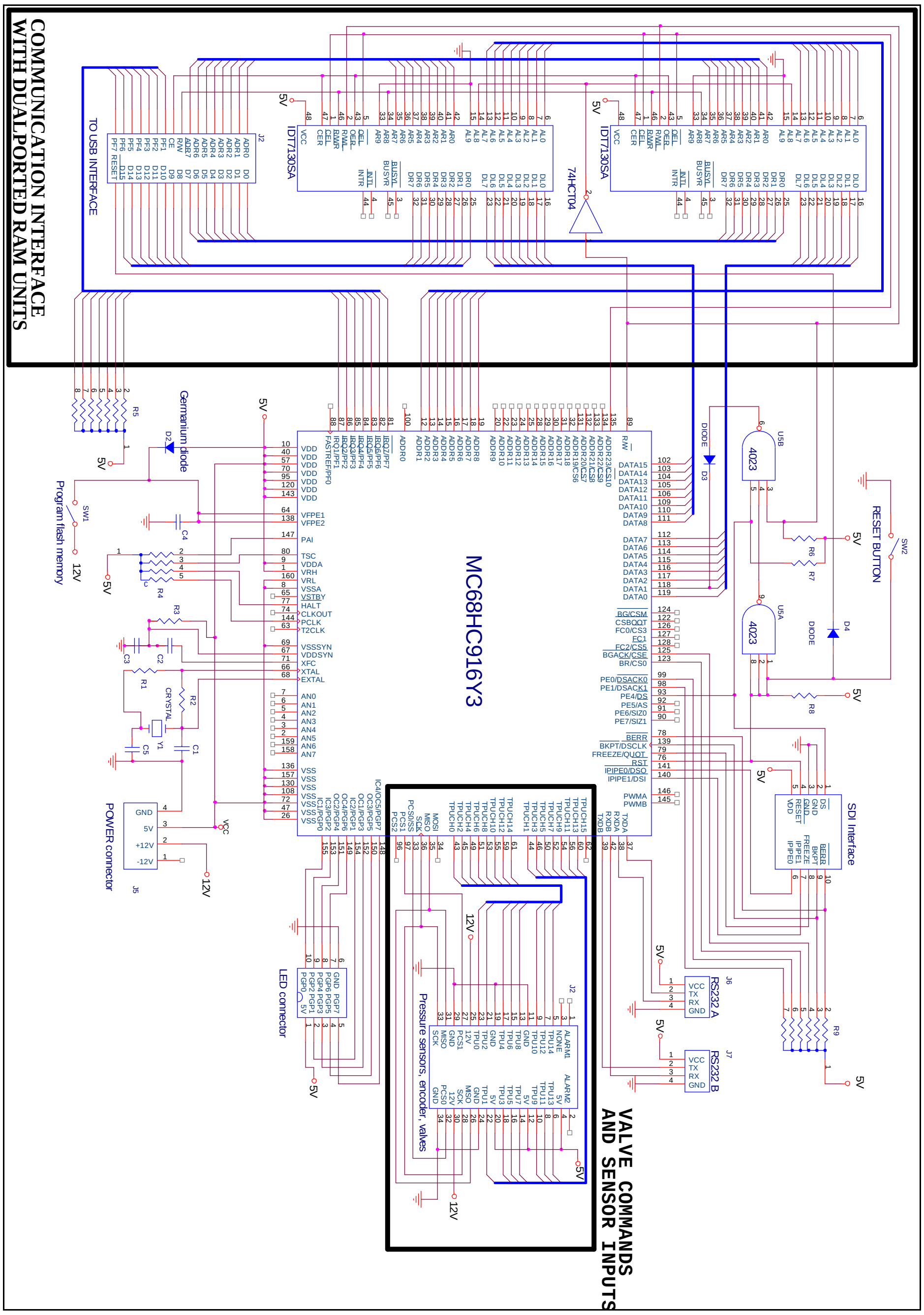

Figure D.1: Electronic scheme of joint microcontroller board

D.2 Speed-up circuitry

In order to enhance the opening time of the Matrix valves, the manufacturer proposes a speed-up in tension circuitry. With a temporal 24 V during a period of 2.5 ms and a remaining 5 volts the opening time of the valves is said to be 1 ms. But during practical tests more than double values for the opening time were recorded. The opening tension is therefore increased to 36 V, but the time during which this voltage is applied is decreased to the actual opening time of 1 ms, such that the valves do not get overheated.

Figure D.2 gives the complete electronic scheme of the speed-up circuitry. Four identical schemes are provided, two for inlet and two for exhaust valves, of which one circuit commands three exhaust valves to open and close simultaneously. For each circuitry two LED's are provided in order to visualize valve action, one of them only lights up when the increased voltage is applied. These LEDs are important to check if the pressure control block is properly working. For each circuitry, the microcontroller commands a valve via discrete 5 V on/off signals. These signals directly activate mosfet Q1 (IRF530) in order to apply 5 V over the valve. The same signal passes parallel through a one-shot (74LS123) in order to increase the applied voltage over the valve during the first 1 ms of valve activation. The output of the one-shot therefore temporally activates mosfet Q2 (IRF610) which on its turn commands mosfet Q3 (IRF9540) to branch the 36 V supply to a valve. Whenever the microcontroller commands a valve to close, by disabling mosfet Q1, the discharge path is connected to the increased supply source via diode D2. This provides a fast discharge of the electromagnetic energy stored in the valve, which results in a faster closing time.

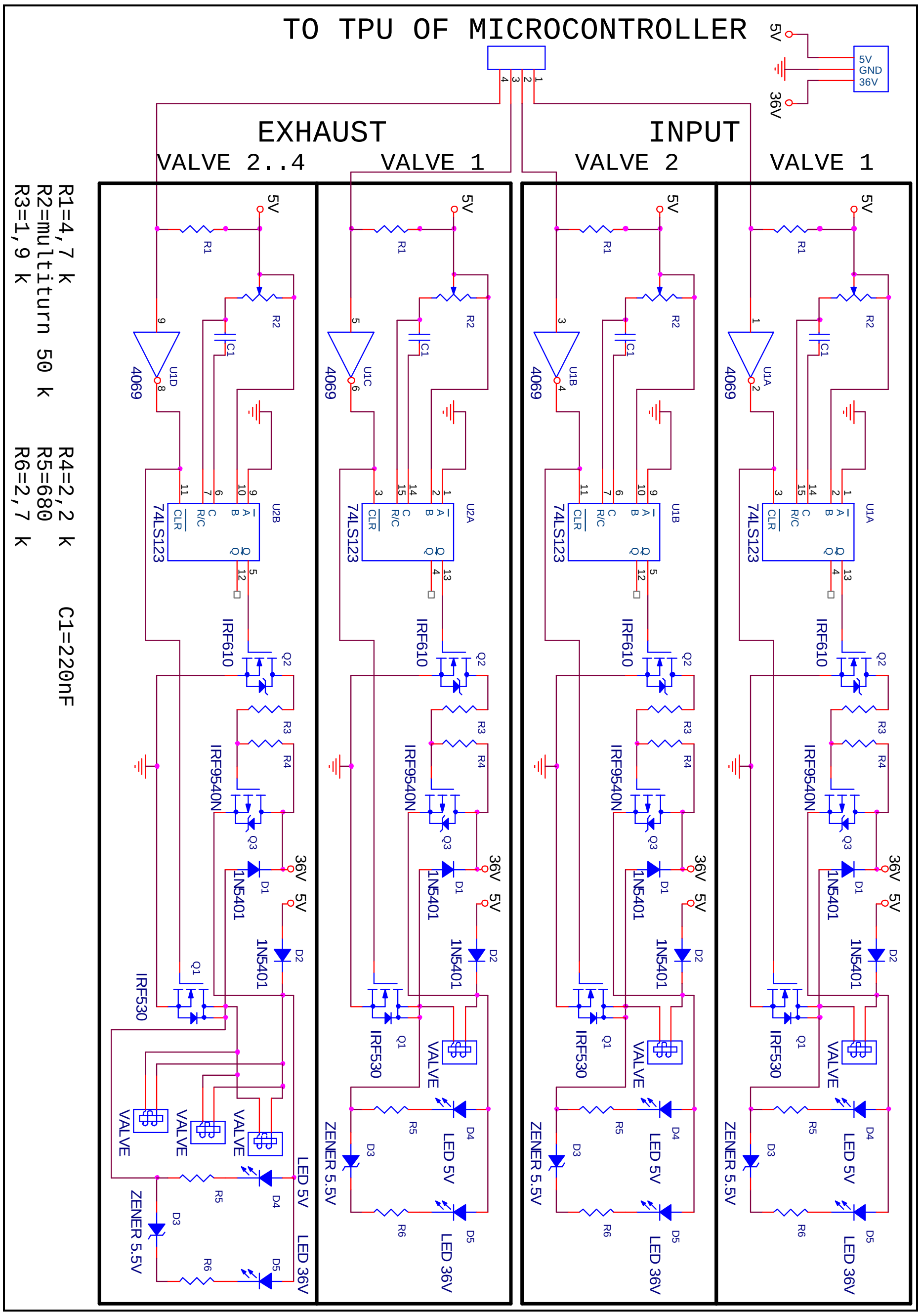

Figure D.2: Electronic scheme of the speed-up circuitry

D.3 Pressure sensor

To have a good dynamic pressure measurement, the sensor is positioned inside the muscle. Since this sensor is inside the closed muscle volume, an absolute pressure sensor is provided. In order to pass through the entrance of a muscle, the diameter of the sensor and its electronics has to be small (12 mm). An absolute pressure sensor, CPC100AFC, from Honeywell has been selected for this purpose. The sensor measures absolute pressure values up to 100 psi (6.9 bar) and has an accuracy of about 20 mbar. Approximately 100 mV for each 100 PSI is generated, meaning 14.5 mV for 1 bar.

Figure D.3 depicts the electronic scheme which conditions the pressure sensor signal. The output of the pressure sensor is amplified by a differential amplifier. The gain of this amplifier is approximately 63.2. In order to avoid as much as possible noise generation, the amplified pressure signal (V_0) is immediately digitized by a 12 bit analog to digital converter. A stable reference voltage for this converter is locally generated by a cascade circuit of two zener diodes. The negative input (-IN) of the AD-converter is augmented with a fixed voltage to roughly compensate atmospheric pressure. The AD-converter chip communicates with the micro-controller unit by a serial SPI interface. Which is typically used for communication between chips and micro-controllers. A comparator is provided to generate an alarm signal in order to protect the muscle against pressure overload. This signal is not treated by a logic controller, but immediately acts on the central pressure supply valve (see 6.3.2). Whenever the muscle gauge pressure exceeds approximately 4.2 bar, the pressure supply is cut-off. The pressure sensor circuit is calibrated each time the robot is initialized. This calibration is performed via an extra pneumatic calibration circuit with an additional pressure sensor.

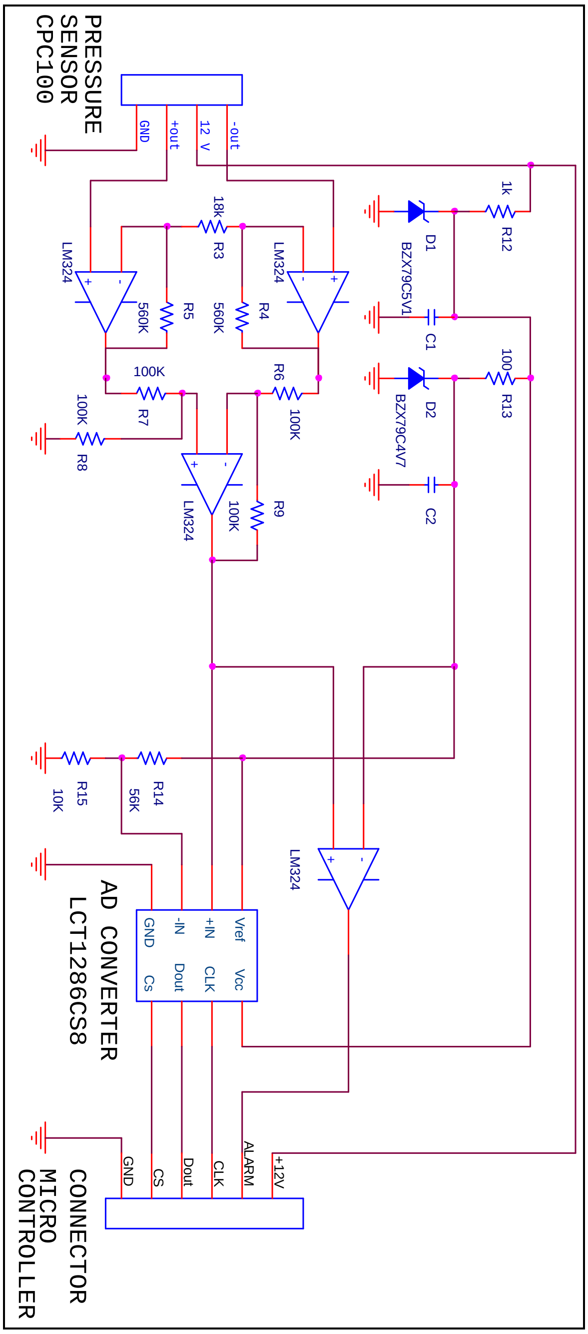

Figure D.3: Electronic scheme of the pressure sensor

D.4 Cypress communication interface

Since a lot of extensive calculations are required due to the model based control algorithms, a central PC is used. Therefore a fast communication line between PC and robot hardware is provided. A fast communication line could be an extension of the PC bus by means of a parallel data communication, but this kind of communication is only suitable for short distance applications. For larger distances (several meters) serial communication protocols are preferable. For this application it was chosen to use a USB 2.0 communication interface, which has a data transfer rate of 480 Mbit/s. Since the local Motorola controllers (6 joint controllers+1 extra controller) have a 16 bit parallel communication bus via the dual ported RAM units, the serial USB bulk communication data blocks have to be divided into 7 blocks of 16 bit parallel data. Therefore an extra micro-controller, EZ-USB FX2 from Cypress Semiconductors, is provided to act only as data transfer agent. This controller runs at 48 Mhz and is able to transfer the serial data block of 226 bytes to the peripheral 16 bit data bus in less than 50 μs. Additional to the Cypress development board, an electronic interface has been created to connect the peripheral bus of the Cypress micro-controller to the different dual ported RAM units. Figure D.4 gives the electronic scheme of the interface. Since the Cypress controller works at 3 V supply voltage level and the dual ported RAM units at 5 V, all lines connecting both parts are buffered via octal supply translating transceiver chips, 74LVC4245. These have a tristate when not enabled, this is important especially for connecting the data lines FD[i] of the Cypress controller to data lines D[i] of the dual ported RAM units. Two chips, U1 and U2, are foreseen for the 16 bit data lines, which work in both directions. The address lines are buffered with U3 which only translates in one direction as is the same for chip U4. The latter connects port PE of the Cypress controller to the other micro-controllers in order to give communication commands. These are: selection of a specific dual ported RAM unit by means of the line decoder chip U6, directing the R/W signal, global reset by software via pin PE5 and two extra general purpose control pins connected to PF1 and PF2 of the Motorola controller. These PF port pins can be controlled interrupt driven. In the other direction, pins PF3 of all the Motorola micro-controllers are connected separately to port PA of the Cypress controller. And PF4 of all Motorola controllers are connected together via an AND gate to pin PA7. These signals are used as communication acknowledgement signals, knowing that the Cypress controller is the bus master. Furthermore, a dip switch is provided to act on pin PF5 in order to select between two working modes. Finally, a general purpose interrupt can be generated manually on pin PF7 of all controllers and a manual global reset button is also provided.

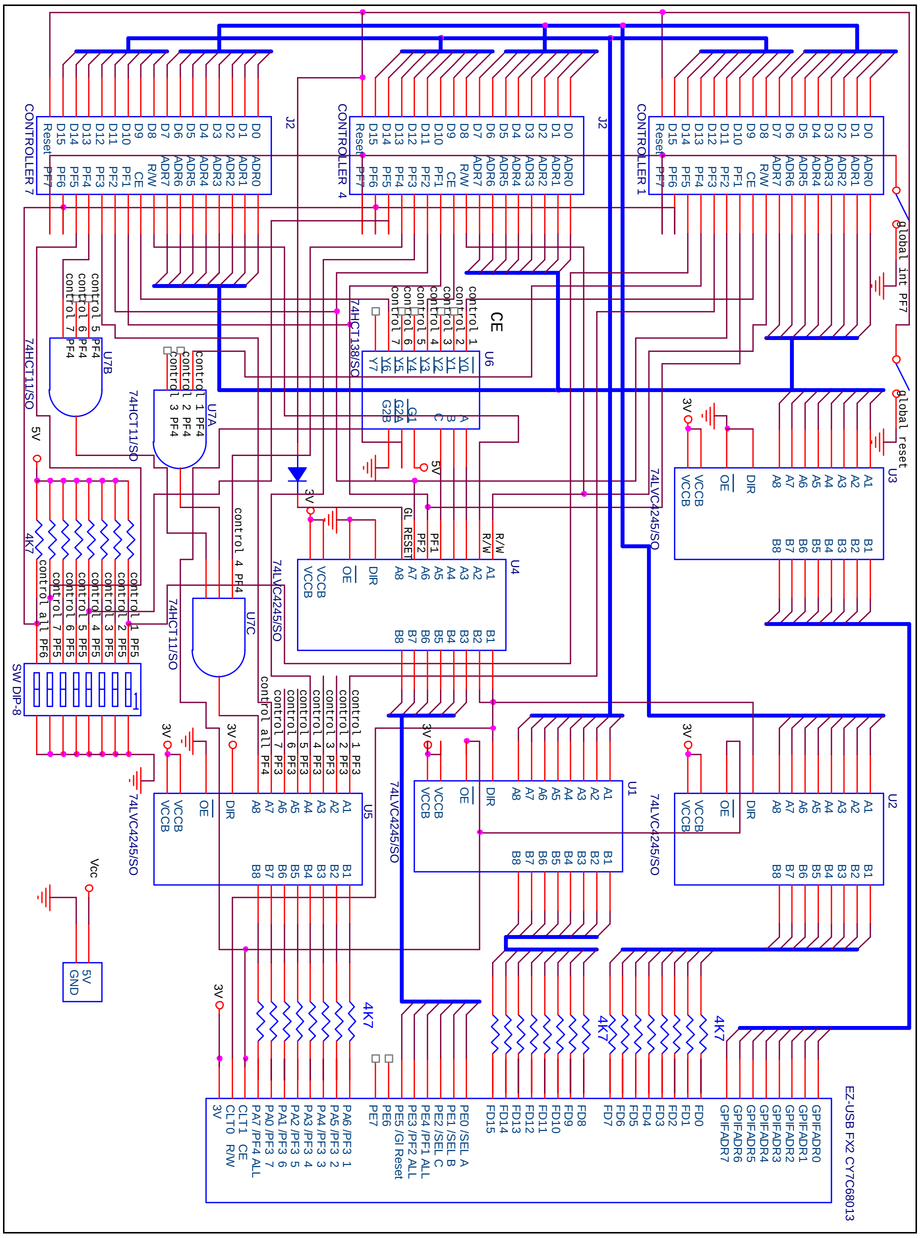

Figure D.4: Electronic scheme of the cypress communication interface

D.5 Safety board

The safety board is provided in order to control the supply pressure flow. It will cut-off the supply pressure in case an emergency situation is met. It can also select a lower calibration supply pressure required for the calibration of the 12 muscle pressure sensors. Figure D.5 shows the electronic scheme of the safety board. There are three valves which control the supply pressure. Opening valve 1 connects the robot to the high supply pressure and valve 2 introduces a lowered calibration pressure. Both valves are activated by a transistor circuit for which signals S1 or S2 have to be logic zero in order to open valve 1 or valve 2 respectively. If these signals are high, than valve 3 is opened in order to depressurize the robot. This happens when the robot is not working or when a pressure alarm or emergency stop is activated. A pressure alarm is induced by the pressure sensors in the muscles, whenever the pressure exceeds approximately 4.5 bar gauge pressure. In this case a rising flank on the alarm signal switches the output of a D flip-flop to low logic state. The flip-flop is used to remember this emergency state and close the pressure valve until a manual reset is given on the safety board. All alarm signals have their own flip-flop structure with an additional LED such that is can be easily detected in which muscle the alarm signal was generated. An OR structure on all the flip-flop outputs in combination with 4 mechanical emergency stops depressurizes the robot whenever one of them alerts for a dangerous situation. Selection between the high or initialization pressure is done by two external signals, which are commanded by the extra Motorola micro-controller.

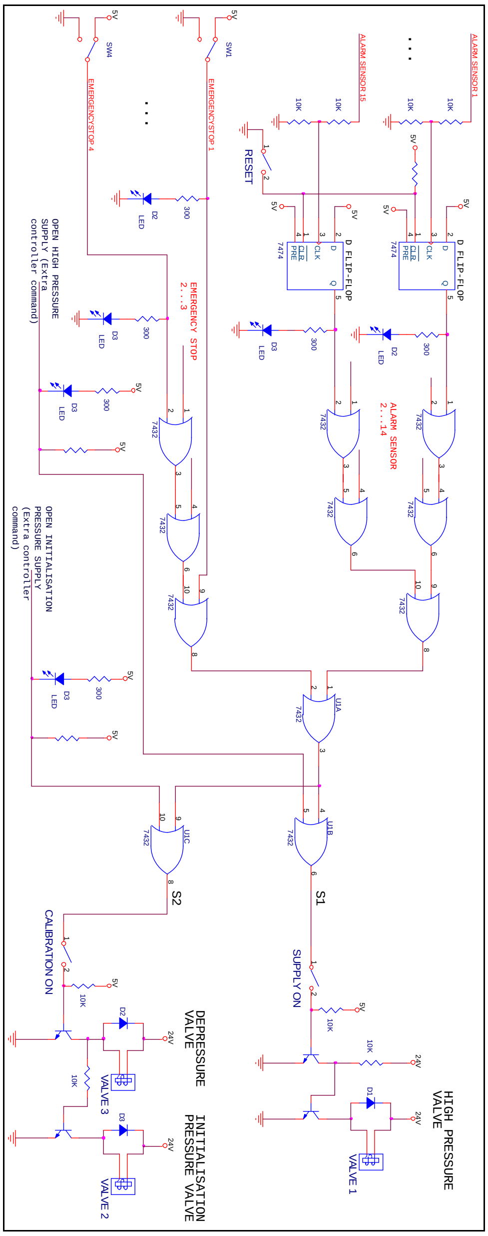

Figure D.5: Electronic scheme of the safety board

Bibliography

Albiez, J., Kerscher, T., Grimminger, F., Hochholdinger, U. and Berns, K. [2003]. PANTER-prototype for a fast running quadruped robot with pneumatic muscles, *Proceedings the 6th International Conference on Climbing and Walking Robots and the Support Technologies for Mobile Machines*, Catania, Italy, pp. 617–624.

Artrit, P. and Caldwell, D. G. [2001]. Single support balancing of a pneumatic biped, *Proceedings of the 4th International Conference on Climbing and Walking Robots, from Biology to Industrial Application*, Karlsruhe, Germany, pp. 835–842.

Asano, F., Yamkita, M. and Furuta, K. [2000]. Virtual passive dynamic walking and energy-based control laws, *Proceedings of the IEEE/RSJ International Conference on Intelligent Robots and Systems*, pp. 1149–1154.

Baldwin, H. A. [1969]. Realizable models of muscle function, *Proceedings of the First Rock Biomechanics Symposium*, New York, USA, pp. 139–148.

Bares, J. and Wettergreen, D. S. [1999]. Dante II: Technical description, results and lessons learned, *The International Journal of Robotics Research* **18**(7): 621–649.

Berns, K., Albiez, J., Kepplin, V. and Hillenbrand, C. [2001]. Airbug insect-like machine actuated by fluidic muscle, *Proceedings of the 4th International Conference on Climbing and Walking Robots, from Biology to Industrial Application*, Karlsruhe, Germany, pp. 237–244.

Brockmann, W. and Huwendiek, O. [1998]. From a pneumatically actuated robot-arm to a pneumatically actuated walking machine, *Proceedings of the 1st International Symposium on Climbing and Walking Robots*, Brussels, Belgium, pp. 203–208.

Brun, X. [1999]. *Commendes Linéaires et Non Linéaires en Electropneumatique, Méthodologies et Applications*, PhD thesis, Institut National des Science Appliquees de Lyon.

Caldwell, D. G., Medrano-Cerda, G. A. and Goodwin, M. J. [1995]. Control of pneumatic muscle actuators, *IEEE Control Systems Magazine* **15**(1): 40–48.

Carbonell, P., Jiang, Z. P. and Repperger, D. [2001]. Comparative study of three nonlinear control strategies for a pneumatic muscle actuator, *Proceedings of the 5th IFAC Symposium "nonlinear Control Systems"*, Vol. 3, St Petersburg, Russia, pp. 1129–1135.

Chestnutt, J., Kuffner, J., Nishiwaki, K. and Kagami, S. [2003]. Planning biped navigation strategies in complex environments, *Proceedings of the IEEE International Conference on Humanoid Robots*, Karlsruhe, Germany.

Chevallereau, C., Abba, G., Aoustin, Y., Plestan, F., Westervelt, E., Canudas-de Wit, C. and Grizzle, J. [2003]. RABBIT: A testbed for advanced control theory, *IEEE Control Systems Magazine* **23**(5): 57–79.

Chevallereau, C. and Aoustin, Y. [2001]. Optimal reference trajectories for walking and running of a biped robot, *Robotica* **19**: 557–569.

Chou, C.-P. and Hannaford, B. [1996]. Measurement and modeling of McKibben pneumatic artificial muscles, *IEEE Transactions on Robotics and Automation* **12**(1): 90–102.

Clark, J. E., Cham, J. G., Bailey, S. A., Froehlich, E. M., Nahata, P. K., Full, R. J. and Cutkosky, M. [2001]. Biomimetic design and fabrication of a hexapedal running robot, *Proceedings of the IEEE International Conference on Robotics and Automation*, Seoul, Korea.

Colombo, G., Joerg, M., Schreier, R. and Dietz, V. [2000]. Treadmill training of paraplegic patients using a robotic orthosis, *Journal of rehabilitation Research and Development* **37**(6): 693–700.

Cooke, D. S., Hewer, N. D., White, T., Galt, S., Luk, B. L. and Hammond, J. [1998]. Implemnetation of modularity in robug IV, *Proceedings of the 1st International Symposium on Climbing and Walking Robots*, Brussels, Belgium, pp. 185–191.

Cupec, R., Lorch, O. and Schmidt, G. [2003]. Vision-guided humanoid walking-concepts and experiments, *Proceedings of the 12th International Workshop on Robotics in Alpe-Adria-Danube Region*, Cassino, Italy.

Dabrowski, T., Feja, K. and Granosik, G. [2001]. Biologically inspired control strategy of pneumatic driven walking robot, *Proceedings of the 4th International Conference on Climbing and Walking Robots from Biology to Industrial Application*, Karlsruhe, Germany, pp. 687–694.

Daerden, F. [1999]. *Conception and Realization of Pleated Pneumatic Artificial Muscles and their Use as Compliant Actuation Elements*, PhD thesis, Vrije Universiteit Brussel.

Daerden, F., Lefeber, D. and Kool, P. [1998]. Using free radial expansion pneumatic artificial muscles to control a 1DOF robot arm, *Proceedings of the 1st International Symposium on Climbing and Walking Robots*, Brussels, Belgium, pp. 209–214.

Daerden, F., Verrelst, B., Lefeber, D. and Kool, P. [1999]. Controlling motion and compliance with folded pneumatic artificial muscles, *Proceedings of the 2nd International Symposium on Climbing and Walking Robots*, Portsmouth, UK, pp. 667–677.

Dasgupta, A. and Nakamura, Y. [1999]. Making feasible walking motion of humanoid robots from human motion capture data, *In Proceedings of the IEEE International Conference on Robotics and Automation*, Detroit, USA, pp. 1044–1049.

Davis, S. T. and Caldwell, D. G. [2001]. The bio-mimetic design of a robot primate using pneumatic artificial muscle actuators, *Proceedings of the 4th International Conference on Climbing and Walking Robots, from Biology to Industrial Application*, Karlsruhe, Germany, pp. 197–204.

Davis, S., Tsagarakis, N., Canderle, J. and Caldwell, D. [2003]. Enhanced modelling and performance in braided pneumatic muscle actuators, *The International Journal of Robotics Research* **22**(2-3): 213–227.

De Man, H., Lefeber, D., Daerden, F. and Faignet, E. [1996]. Simulation of a new control algorithm for a one-legged hopping robot (using the multibody code mechanica motion), *Proceedings of the International Workshop on Advanced Robotics and Intelligent Machines*, Manchester, UK.

De Man, H., Lefeber, D. and Vermeulen, J. [1998]. Design and control of a robot with one articulated leg for locomotion on irregular terrain, *Proceedings of the 12th Symposium on Theory and Practice of Robots and Manipulators*, Paris, France, pp. 417–424.

Delcomyn, F. and Nelson, M. [2000]. Architectures for a biomimetic hexapod robot, *Robotics and Autonomous Systems* **30**: 5–15.

Denk, J. and Schmidt, G. [2001]. Walking primitive synthesis for an anthropomorphic biped using optimal control techniques, *Proceedings of the 4th International Conference on Climbing and Walking Robots from Biology to Industrial Application*, Karlsruhe, Germany, pp. 819–826.

Einstein, J. and Pawlik, G. [1995]. Feasibility of bipedal locomotion in robotic systems: Pneumatics vs. electronics, *Proceedings of the 5th International Symposium on Measurement and Control in Robotics*, Smolenice, Slovakia, pp. 453–458.

Eskiizmiler, S., Tondu, B. and Darlot, C. [2001]. Motor control of a limb segment actuated by artificial muscles, *Proceedings of the 23th IEEE/EMBS Annual Conference*, Istanboul, Turquie.

Festo [2004]. Fluidic muscle MAS, *Festo Brochure Fluidic Muscle* .

Figliolini, G. and Ceccarelli, M. [2003]. Novel binary pneumatic actuation for EP-WAR3 biped robot, *Proceedings of the 6th International Conference on Climbing and Walking Robots and the Support Technologies for Mobile Machines*, Catania, Italy, pp. 853–860.

Fujitsu [2001]. Fujitsu introduces miniature humanoid robot, HOAP-1, *Press Release September 10, 2001* .

Garcia, M., Chatterjee, A., Ruina, A. and Coleman, M. [1998]. The simplest walking model: Stability, complexity, and scaling, *ASME Journal of Biomechanical Engineering* **120**: 281–288.

Gorce, P. and Guihard, M. [1998]. On dynamic control of pneumatic bipeds, *Journal of Robotic Systems* **15**(7): 421–433.

Goswami, A. [1999]. Postural stability of biped robots and the foot-rotation indicator (FRI) point, *The International Journal of Robotics Research* **18**(6): 523–533.

Gregorio, P., Ahmadi, M. and Buehler, M. [1997]. Design, control, and energetics of an electrically actuated legged robot, *IEEE Transactions on Systems, Man and Cybernetics* **27B**(4): 626–634.

Guccione, S., Muscato, G. and Spampinato, G. [2003]. Modelling and control strategies for bipedal locomotion-experiments with anthropometric robot leg, *Proceedings of the 6th International Conference on Climbing and Walking Robots and the Support Technologies for Mobile Machines*, Catania, Italy, pp. 517–526.

Guihard, M. and Gorce, P. [2001]. Dynamic control of a biomechanical inspired biped-BIPMAN, *Proceedings of the 4th International Conference on Climbing and Walking Robots, from Biology to Industrial Application*, Karlsruhe, Germany, pp. 39–45.

Guihard, M., Gorce, P. and Fontaine, J. G. [1995]. SAPPHYR: Legs to pull a wheel structure, *Proceedings of the International Conference on Systems, Man and Cybernetics*, pp. 1303–1308.

Habumuremyi, J. and Doroftei, I. [2001]. Mechanical design and MANFIS control of a leg for a new demining walking robot, *In Proceedings of the 4th International Conference on Climbing and Walking Robots, from Biology to Industrial Applications*, Karlsruhe, Germany, pp. 457–464.

Harada, K., Kajita, S., Kanehiro, F., Fujiwara, K., Kaneko, K., Yokoi, K. and Hirukwa, H. [2004]. Real-time planning of humanoid robots gait for force controlled manipulation, *Proceedings of the IEEE International Conference on Robotics and Automation*, New Orleans, USA.

Hardt, M., Kruetz-Delgado, K., Helton, J. and Stryck, O. V. [1999]. Obtaining minimum energy biped walking gaits with symbolic models and numerical optimal control, *Proceedings of the Workshop- Biomechanics Meets Robotics, Modelling and Simulation of Motion*, Heidelberg, Germany, pp. 1–19.

Hesselroth, T., Sarkar, K., van der Smaght, P. P. and Schulten, K. [1994]. Neural network control of a pneumatic robot arm, *IEEE Transactions on Systems, Man and Cybernatics* **24**(1): 28–38.

Hirai, K., Hirose, M., Haikawa, Y. and Takenaka, T. [1998]. The development of honda homanoid robot, *Proceedings of the IEEE International Conference on Robotics and Automation*, Leuven, Belgium, pp. 1321–1326.

Hirose, M., Haikawa, Y., Takenaka, T. and Hirai, K. [2001]. Development of humanoid robot ASIMO, *Proceedings of the IEEE/RSJ International Conference* *on Intelligent Robots and Systems*, Maui, USA.

Honda [2004]. Honda reveals technologies next-generation ASIMO, *Press Release December 15, 2004* .

Hurst, W., Chestnutt, J., E. and Rizzi, A., A. [2004]. An actuator with physically variable stiffness for highly dynamic legged locomotion, *In Proceedings of the IEEE International Conference on Robotics and Automation*, New Orleans, USA, pp. 4662–4667.

Immega, G. B. [1987]. Romac actuators for micro robots, *Proceedings of the IEEE Micro Robotics and Teleoperators Workshop*, Hyannis, Massachusetts.

Inoue, K. [1987]. Rubbertuators and applications for robotics, *Proccedings of the 4th International Symposium on Robotics Research*, pp. 57–63.

International Standard ISO6358 [1989]. Pneumatic fluid power - method of test - determination of flow rate characteristics of components using compressible fluids.

Jalón, J. G. and Bayo, E. [1994]. *Kinematic and Dynamic Simulation of Multibody Systems: The Real-Time Challenge*, Springer-Verlag.

Kagami, S., Kitagawa, T., Nishiwaki, K., Sugihara, T., Inaba, M. and Inoue, H. [2002]. A fast dynamically equilibrated walking trajectory generation method of humanoid robot, *Autonomous Robots* **12**: 71–82.

Kajita, S., Kanehiro, F., Kaneko, K., Yokoi, K. and Hirukawa, H. [2001]. The 3d linear inverted pendulum mode: A simple modelling for a biped walking pattern generation., *Proceedings of the IEEE International Conference on Intelligent Robots and Systems*, Maui, Hawai, pp. 239–246.

Kajita, S., Matsumoto, O. and Saigo, M. [2001]. Real-time 3d walking pattern generation for a biped robot with telescopic legs, *Proceedings of the IEEE International Conference on Robotics and Automation*, Seoul, Korea, pp. 2299–2306.

Kanehiro, F., Hirukawa, H., Kaneko, K., Kajita, S., Fujiwara, K., Harada, K. and Yokoi, K. [2004]. Locomotion planning of humanoid robots to pass through narrow spaces, *Proceedings of the 2004 IEEE International Conference on Robotics and Automation*, New orleans, USA, pp. 604–609.

Kaneko, K., Kanehiro, F., Kajita, S., Hirukawa, H., Kawasaki, T., Hirata, M., Akachi, K. and Isozumi, T. [2004]. Humanoid robot HRP-2, *Proceedings of the IEEE International Conference on Robotics and Automation*, New Orleans, USA, pp. 1083–1090.

Kato, I., Mori, Y. and Masuda, T. [1972]. Pneumatically powered artificial legs walking automatically under various circumstances, *Proceedings of the 4th International Conference on External Control of Human Extremities*, pp. 458–470.

Kawashima, K., Sasaki, T., Miyata, T., Nakamura, N. Sekiguchi, M. and Kagawa, T. [2004]. Development of robot using pneumatic artificial rubber muscles to operate machinery, *Journal of Robotics and Mechatronics* **16**(1): 8–16.

Kerscher, T., Albiez, J. and Berns, K. [2002]. Joint control of the six-legged robot

AirBug driven by fluidic muscles, *Proceedings of the 3th International Workshop on Robot Motion and Control*, Bukowy, Poland, pp. 27–32.

Kerscher, T., Albiez, J., Zoellner, J. M. and Dillmann, R. [2004]. AirInsect- a new innovative biological inspired six-legged walking machine driven by fluidic muscles, *Proceedings of IAS 8th Conference on Intelligent Autonomous Systems*, Amsterdam, Netherlands.

Kikuchi, F., Ota, Y. and Hirose, S. [2003]. Basic performance experiments for jumping quadruped, *Proceedings of the IEEE/RSJ International Conference on Intelligent Robots and Systems*, LAs Vegas, US, pp. 3378–3383.

Kingsley, D. A., Quinn, R. D. and Ritzmann, R. E. [2003]. A cockroach inspired robot with artificial muscles, *Proceedings of the International Symposium on Adaptive Motion of Animal and Machines*, Kyoto, Japan.

Klute, K. G., Czerniecki, J. M. and Hannaford, B. [2002]. Artificial muscles: Actuators for biorobotic systems, *The International Journal of Robotics Research* **21**(4): 295–309.

Kuo, A. [1999]. Stabilization of the lateral motion in passive dynamic walking, *The International Journal of Robotics Research* **18**(9): 917–930.

Kuroki, Y., Ishida, T., Yamagushi, J., Fujita, M. and Doi, T. [2001]. A small biped entertainment robot, *Proceedings of the IEEE/RAS International Conference on Humanoid Robots*, pp. 184–186.

Lee, T.-T. and Liao, J.-H. [1988]. Trajectory planning and control of a 3-link biped robot, *Proceedings of the IEEE International Conference on Robotics and Automation*, New York, USA, pp. 820–823.

Löffler, K., Gienger, M. and Pfeiffer, F. [2002]. Trajectory control of a biped robot, *Proceedings of the 5th International Conference on Climbing and Walking Robots and the Support Technologies for Mobile Machines*, Paris, France, pp. 437–444.

Lorch, O., Albert, A., Denk, J., Gerecke, M., Cupec, R., Seara, J., Gerth, W. and Schmidt, G. [2002]. Experiments in vision-guided biped walking, *Proceedings of the IEEE/RSJ/GI International Conference on Intelligent Robots and Systems*, Lausanne, Switserland, pp. 2484–2490.

Matsuoka, K. [1980]. A mechanical model of repetitive hopping movements, *Biomechanisms* **5**: 251–258.

Mattiazzo, G., Mauro, S., M., V., Beomonte Zobel, P. and T., R. [1998]. Force control of a one d.o.f. manipulator actuated by rubber muscles, *Proceedings of the 29th International Symposium on Robotics*, Birmingham, UK, pp. 333–336.

McGeer, T. [1990]. Passive dynamic walking, *International Journal of Robotics Research (Special Issue on Legged Locomotion)* **9(2)**: 62–82.

McGhee, R. B. and Frank, A. A. [1968]. On the stability properties of quadruped creeping gaits, *Journal of Mathematic Biosciences* **3**: 331–351.

Merlin Systems Coorporation [2003]. Merlin actuators: Automation, animatronics and artificial creatures, *Brochure Merlin Actuators* .

Mitobe, K., Capi, G. and Nasu, Y. [2004]. A new control method for walking robots based on angular momentum, *Mechatronics* **14**: 163–174.

Nadjar-Gauthier, N., Cherrid, H. and Cadiou, J.-C. [2002]. A new second order sliding mode control for the experimental walking of an electro-pneumatic biped robot, *Proceedings of the 5th International Conference on Climbing and Walking Robots and the Support Technologies for Mobile Machines*, Paris, France, pp. 93–100.

Nishiwaki, K., Sugihara, T., Kagami, S., Kanehiro, F., Inaba, M. and Inoue, H. [2000]. Design and development of research platform for perception-action integration in humanoid robot : H6, *Proceedings of IEEE/RSJ International Conference on Intelligent Robots and Systems*, Takamatsu, Kagawa, Japan, pp. 1559–1564.

Osuka, K. and Saruta, Y. [2000]. Development and control of new legged robot QUARTET III-from active walking to passive walking, *Proceedings of the 2000 IEEE/RSJ International Conference on Intellegent Robots and Systems*, pp. 991–995.

Pfeiffer, F., Löffler, K. and Gienger, M. [2003]. Humanoid robots, *Proceedings of the 6th International Conference on Climbing and Walking Robots and the Support Technologies for Mobile Machines*, Catania, Italy, pp. 505–516.

Plustech [2004]. The walking forest machine concept, *Timberjack Brochure: Walking Technology* .

Pomiers, P. [2003]. Modular robot arm based on pneumatic artificial rubber muscles (PARM), *Proceedings of the 6th International Conference on Climbing and Walking Robots and the Support Technologies for Mobile Machines*, Catania, Italy, pp. 879–886.

Pratt, G. A. and Williamson, M. M. [1995]. Series elastic actuators, *Proceedings IEEE-IROS Conference*, Pittsburg, USA, pp. 399–406.

Pratt, G., Williamson, M., Dillworth, P., Pratt, J. and Wright, A. [1995]. Stiffness isn't everything, *Proceedings of the Fourth International Symposium on Experimental Robotics*, Stanford, California, USA, pp. 253–262.

Pratt, J. E. [2000]. *Exploiting Inherent Robustness and Natural Dynamics in the Control of Bipedal Walking Robots*, PhD thesis, Massachussetts Institute of Technology (MIT), Massachussets, USA.

Pratt, J. E. and Pratt, G. [1998]. Exploiting natural dynamics in the control of a planar bipedal walking robot, *Proceedings of the 36th Annual Allerton Conference on Communication, Control, and Computing*, Monticello, Illinois.

Quinn, R. D., Nelson, G. N., Bachmann, R. J., Kingsley, D. A., Offi, J. and Ritzmann, R. E. [2001]. Insect design for improved robot mobility, *Proceedings of the 4th International Conference on Climbing and Walking Robots from Biology to Industrial Applications*, Karlsruhe, Germany, pp. 69–76.

Quinn, R. D. and Ritzmann, R. E. [1998]. Construction of a hexapod robot with cockroach kinematics benefits both robotics and biology, *Connection Science* **10**(3-4): 239–254.

Raibert, M. [1986]. *Legged Robots That Balance*, MIT Press, Cambridge, Massachussetts.

Rao, C. and Mitra, S. [1971]. *Generalized Inverse of Matrices and its Applications*, John Wiley & Sons, Inc, New York.

Raparelli, T., Beomonte Zobel, P. and Durante, F. [2001]. The design of a 2-dof robot for functional recovery therapy driven by pneumatic muscles, *Proceedings of the 10th International Workshop on Robotics in Alpe Adria Danube Region*, Vienna, Austria.

Raparelli, T., Mattiazzo, G., Mauro, S. and Velardocchia, M. [2000]. Design and development of a pneumatic anthropomorphic hand, *Journal of Robotic Systems* **17**(1): 1–15.

Regele, R., Bott, W. and Levi, P. [2003]. Pro-robot: Predictions for the future development of humanoid robots, *Robocup 2003 Symposium*, Padova, Italy.

Ridderström, C. [1999]. Legged locomotion control - a literature study, *Technical Report 27*, Mechatronics Lab, Departement of Machine Design, Royal Institute of Technology, Stockholm, Sweden.

Rogers, G. and Mayhew, Y. [1992]. *Engineering Thermodynamics, Work and Heat Transfer*, John Wiley & Sons, New York, USA.

Schröder, J., Kawamura, K., Gockel, T. and Dillmann, R. [2003]. Improved control of humanoid arm driven by pneumatic actuators, *Proceedings of the IEEE International Conference on Humanoid Robots*, Karlsruhe, Germany.

Schulte, H. F. [1961]. The characteristics of the McKibben artificial muscle, *The Application of External Power in Prosthetics and Orthotics*, number Publication 874, National Academy of Sciences–National Research Council, Lake Arrowhead, pp. 94–115.

Seara, J. F., Strobl, K. H. and Schmidt, G. [2003]. Path-Dependent Gaze Control for Obstacle Avoidance in Vision Guided Humanoid Walking, *Proceedings of the IEEE International Conference on Robotics and Automation*, Taipei, Taiwan.

Shadow Robot Company [2003]. Design of a dextrous hand for advanced CLAWAR applications, *Proceedings of the 6th International Conference on Climbing and Walking Robots and the Support Technologies for Mobile Machines*, Catania, Italy, pp. 691–698.

Shih, C.-L. and Gruver, W. [1992]. Control of a biped robot in the double-support phase, *IEEE Transactions on Systems, Man and Cybernetics* **22**(4): 729–735.

Slotine, J. J. E. and Li, W. [1991]. *Applied Nonlinear Control*, Prentice-Hall, Cambridge, MA.

Song, S.-M. and Waldron, K. [1989]. *Machines That Walk: The Adaptive Sus-*

pension Vehicle, MIT Press, Cambridge, Massachussetts.

Spong, M. and Vidyasagar, M. [1989]. *Robot Dynamics and Control*, JohnWiley and Sons, Inc.

Takanishi, A., Ishida, M., Yamazaki, Y. and Kato, I. [1985]. The realization of dynamic walking by the biped walking robot WL-10RD, *Proceedings of the International Conference on Advanced Robotics*, pp. 459–466.

Thompson, C. and Raibert, M. [1989]. Passive dynamic running, *Proceedings of the International Symposium of Experimental Robotics*, pp. 74–83.

Tondu, B., Boitier, V. and Lopez, P. [1994]. Natural compliance of robot-arms based on McKibben artificial muscle actuators, *European Robotics and Intelligent Systems Conference*, Malaga, pp. 783–797.

Toyota [2004a]. Toyota announces overview of "toyota partner robot", *Press Release March 11, 2004* .

Toyota [2004b]. Toyota group announces plans for EXPO 2005 AICHI, JAPAN pavilion performance, *Press Release December 3, 2004* .

Tzafestas, S., Raibert, M. and Tzafestas, C. [1996]. Robust sliding-mode control applied to a 5-link biped robot, *Journal of Intelligent and Robotic Systems* **15**: 67–133.

Van Damme, M., Daerden, F. and Lefeber, D. [2004]. Design of a pneumatic manipulator in direct contact with an operator, *Proceedings of the 35th International Symposium on Robotics*, Paris, France.

van der Linde, R. [2001]. *Bipedal Walking with Active Springs, Gait Synthesis and Prototype Design*, PhD thesis, Technische Universiteit Delft.

van der Linde, R. Q. [1998]. Active leg compliance for passive walking, *Proceedings of the IEEE International Conference on Robotics and Automatisation*, Leuven, Belgium, pp. 2339–2344.

van der Linde, R. Q. [1999]. Design, analysis and control of a low power joint for walking robots, by phasic activation of mckibben muscles., *IEEE Transactions on Robotics and Automation* **15**(4): 599–604.

Van Ham, R., Daerden, F., Verrelst, B., Lefeber, D. and Vandenhoudt, J. [2002]. Control of pneumatic artificial muscles with enhanced speed up circuitry., *Proceedings of the 5th International Conference on Climbing and Walking Robots and the Support Technologies for Mobile Machines*, Paris, France, pp. 195–202.

Vermeulen, J. [2004]. *Trajectory Generation for Planar Hopping and Walking Robots: An Objective Parameter and Angular Momentum Approach*, PhD thesis, Vrije Universiteit Brussel.

Vermeulen, J., Lefeber, D. and Verrelst, B. [2003]. Control of foot placement, forward velocity and body orientation of a one-legged robot, *Robotica* **21**: 45–57.

Vermeulen, J., Lefeber, D., Verrelst, B. and Vanderborght, B. [2004]. Trajectory planning for the walking biped lucy, *Proceedings of the 7th International Conference* *on Climbing and Walking Robots*, Madrid, Spain.

Vermeulen, J., Verrelst, B., Lefeber, D., Kool, P. and Vanderborght, B. [2005]. A real-time joint trajectory planner for dynamic walking bipeds in the sagittal plane, *Robotica* . to be published.

Verrelst, B., Daerden, F., Lefeber, D., Van Ham, R. and Fabri, T. [2000]. Introducing pleated pneumatic artificial muscles for the actuation of legged robots: a one-dimensional set-up, *Proceedings of the 3th International Conference on Climbing and Walking Robots and the Support Technologies for Mobile Machines*, Madrid, Spain, pp. 583–590.

Villard, C., Gorce, P., Fontaine, J. G. and Rabit, J. [1993]. RALPHY: A dynamic study of a quadruped robot, *Proceedings of the International Conference on Systems, Man And Cybernetics*, pp. 106–111.

Vukobratovic, M. [1975]. *Legged Locomotion Robots and Anthropomorphic Mechanisms*, Mihailo Pupin Institute, Beograd.

Vukobratovic, M. and Borovac, B. [2004]. Zero-moment point - thirthy five years of its life, *International Journal of Humanoid Robotics* **1**: 157–173.

Wisse, M. [2001]. Biologically inspired biped design, *Symposium of the Int. Soc. For Postural and Gait Research*, Maastricht, The Netherlands, pp. 900–903.

Wisse, M. [2004]. *Essentials of Dynamic Walking : Analysis and Design of Two-Legged Robots*, PhD thesis, Technische Universiteit Delft.

Wisse, M., Schwab, A. L. and vd. Linde, R. Q. [2001]. A 3d passive dynamic biped with yaw and roll compensation, *Robotica* **19**: 275–284.

Wisse, M. and van Frankenhuyzen, F. [2003]. Design and construction of mike: A 2d autonomous biped based on passive dynamic walking, *Proceedings of the Conference on Adaptive Motion of Animals and Machines*, Kyoto, Japan.

Yamguschi, J., Nishino, D. and Takanishi, A. [1998]. Realization of dynamic biped walking varying joint stiffness using antagonistic driven joints, *Proceedings of the IEEE International Conference on Robotics and Automatisation*, Leuven, Belgium, pp. 2022–2029.

Yokoi, K. and al. [2003]. Humanoid robot's applications in HRP, *Proceedings of the IEEE International Conference on Humanoid Robots*, Karlsruhe, Germany.

Yokoi, K., Kajita, S., Saito, H. and Tanie, K. [2004]. A stable foot teleoperation method for humanoid robot, *Proceedings of the IEEE International Conference on Robotics and Automation*, New orleans, USA.

Yokoi, K., Kanehiro, F., Kaneko, K., Fujiwara, K., Kajita, S. and Hirukawa, H. [2001]. A honda humanoid robot controlled by AIST software, *Proceedings of the IEEE/RAS International Conference on Humanoid Robots*, Tokyo, Japan, pp. 259–264.

Zheng, Y. and Hemami, H. [1985]. Mathematical modeling of a robot collision with its environment, *Journal of Robotic Systems* **2**(3): 289–307.